Modelling and evaluation of high-power light-emitting diodes for general lighting

Arno KEPPENS

Jury:
Prof. dr. ir. Paul Van Houtte, president
(MTM, K.U.Leuven)
Prof. dr. ir. Geert Deconinck, promotor
(ESAT, K.U.Leuven)
Prof. dr. Peter Hanselaer, promotor
(Light & Lighting Lab, KaHo St.-Lieven)
Prof. dr. ir. Martine Baelmans, assessor
(MECH, K.U.Leuven)
Prof. dr. ir. Roel Baets, assessor
(INTEC, UGent)
Prof. dr. ir. Ronnie Belmans
(ESAT, K.U.Leuven)
Prof. dr. ir. Patrick Rombauts
(ETEC, VUB)
Dr. Rudy Geens
(Havells-Sylvania)

Dissertation presented in partial fulfilment of the requirements for the degree of Doctor in Engineering.

September, 2010

ISBN 978-94-6018-256-3
D/2010/7515/9

Cover image: Cree LED package on printed circuit board, Cree Inc.

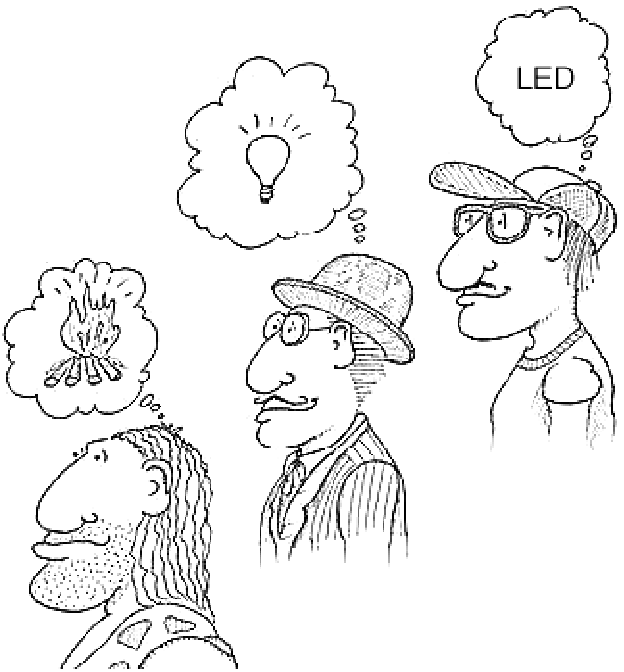

EVOLUTION OF HAVING AN IDEA

Preface

This work is the result of a Ph.D. thesis at the Light & Lighting Laboratory (Gent, Belgium), affiliated with the ELECTA research group at K.U.Leuven (Belgium). The thesis has the intention to narrow the comprehension gap between diode manufacturers and luminaire designers in two ways. First, designers of general lighting products are provided with models that allow estimating diode performance in practical lighting applications. Next to that, measurement results that have been used for model construction are utilized for an extended evaluation of the present LED technology status as well. Related recommendations for best practice are additionally presented.

Scientific research of any kind is impossible without decent funding. First and foremost, I would therefore like to thank the five Belgian lighting manufacturers and their representatives that have made this work possible. These companies are – in alphabetical order – EREA, Havells-Sylvania, Massive (Network Philips Consumer Luminaires), R-Tech (Schréder group), and Toplight (now renamed LUNOO). The representatives attended four-monthly meetings that provided me with crucial knowledge of the present LED technology and market status. The first-hand research output was presented to them in return.

My very special thanks go to the thesis promotors. Prof. Geert Deconinck was the final responsible of this work, while Prof. Peter Hanselaer almost daily guided me through the difficulties I met during the past four years. Both trusted upon my efforts and encouraged me in taking specific research paths. By doing this, they really managed to introduce me into the academic research, which still enormously pleases me. I could additionally rely on the professional knowledge of assessors Prof. Martine Baelmans (K.U.Leuven) and Prof. Roel Baets (UGent). They also contributed to the examination commission, whose members I have to thank for their evaluation vocation and role in optimizing the contents of this book.

It would be unfair not to mention all past and present colleagues from the Light & Lighting Laboratory. Bart, Catherine, Filip, Frederic, Frederik, Guy, Jan, Jan, Jonas, Kevin, Sam, Sandra, Stefaan, Steven, Sven, Toon, Wim, and Wouter have contributed in their own way to this work or – maybe even much more important – the friendly atmosphere on the work site. Nevertheless, it is appropriate to peculiarly mention Wim De Geest and Mario Wyns, who have provided me with custom-made hardware and software, respectively. Although contacts have been much less frequent with the administration staff of the K.U.Leuven Engineering Faculty and Arenberg Doctoral School, I would like to thank those people as well for their very personal assistance.

Four master thesis students have taken the opportunity to contribute to the research described herein. I thank – in order of appearance – David De Smeyter, Joeri Van Rentergem, Pieter Lindeboom, and Steven Denijs for their sincere enthusiasm and persisting work efforts. For the same reason I would especially like to thank visiting scholars Huanting Chen (China) and Paula Catalina Acuña Roncancio (Colombia). I hope I have been able to give them a valuable research experience in return.

Great thanks go to Yuqin Zong and Yoshi Ohno of the National Institute of Standards and Technology (Gaithersburg, MD, USA). Through FWO funding, they have given me the chance to work during one month as a guest researcher at one of the most reputable LED lighting technology laboratories worldwide. Further internationalisation has been made possible thanks to Jesús Maria Quintero Quintero and Fernando Augusto Herrera Leon, who have invited me as a guest lecturer to the National University of Colombia (Bogotá, Colombia).

The role of my parents in the realization of this work and the preceding educational path I have followed cannot be overestimated. They have never ceased to encourage me while making choices for life and they have always supported me in all possible ways to obtain the goals I pursued.

Lots of thanks are also due to my close friends who were able to offer me plenty more than qualitative relaxation whenever appropriate. I am very lucky to say that mentioning all of them would unfortunately result in too long a list to include here. If I just bring up the refreshing sports activities, exciting parties, relaxing evening drinks, frank laughs, and unforgettable journeys we have shared, they most probably know who I have in mind.

Liesbeth, keeping the most important for the end, I tremendously have to thank you for everything you have meant to me the past years. Although having both a scientific background we are able to relativate love, I am convinced that we have found a high local optimum of mutual happiness. Sometimes, a simple expression of your interest or an encouraging word was the most effective working stimulus I could get.

Arno Keppens
Gent, 2010

Brief summary

Due to the complexity and current implementation obstacles of high-power light-emitting diodes (LEDs), lighting companies are generally short of experience with these light sources and depend on the often misleading information of diode manufacturers. The work at hand has the intention to narrow this technological comprehension gap in two ways. First, integration of high-power diodes in general lighting implies providing product designers with models that allow performing maximum LED characterization from a minimum number of measurements and estimating diode performance in practical lighting applications. User-relevant characteristics as electrical input power, radiant flux, spectrum, and colour pattern are modelled. For the scientific community, the construction of such semi-empirical LED models, based on both physics theories and experimental data, is the most important research contribution. Determination of LED characteristics through simulations immediately makes model validation possible. Secondly, measurement results that have been used for model construction can be utilized for an extended evaluation of the present LED technology status as well, including binning, efficiency, and diode quality. The academic research approach as applied in this work is however different from its practical use. Related recommendations for best practice are therefore provided.

Korte samenvatting

Omwille van de complexiteit en huidige implementatieproblemen van hoogvermogen light-emitting diodes (LED's) hebben verlichtingsbedrijven typisch weinig ervaring met deze nieuwe lichtbronnen. Hierdoor zijn zij afhankelijk van de dikwijls misleidende informatie van diodeproducenten. Dit doctoraatsonderzoek heeft als doel deze technologische begripskloof op twee manieren te reduceren. Enerzijds impliceert de integratie van hoogvermogen diodes in algemene verlichting het aanbieden van modellen die maximale LED-karakterisatie aan de hand van een minimum aantal metingen en bovendien het inschatten van LED-prestaties in verlichtingstoepassingen mogelijk maken. Gebruikersrelevante eigenschappen als ingangsvermogen, stralingsstroom, spectrum en kleurpatroon worden gemodelleerd. Deze constructie van semi-empirische modellen, die zowel op theorie als experimentele data zijn gebaseerd, is de belangrijkste onderzoeksbijdrage voor de academische wereld. Simulatie van LED-karakteristieken achteraf maakt validatie van de modellen mogelijk. Anderzijds kunnen de meetresultaten die voor het modelleren werden gebruikt ook voor een uitgebreide evaluatie van de huidige LED-technologie worden toegepast. Deze evaluatie behandelt aspecten van binning, rendement en diodekwaliteit. De academische onderzoeksbenadering verschilt echter van zijn toepassing in de praktijk. Daarom worden ook aanbevelingen voor *best practice* verstrekt.

Samenvatting

De voorbije jaren hebben light-emitting diodes – beter bekend als “LED’s” – zowel voor Jan met de pet als in de onderzoekswereld enorm aan populariteit gewonnen. Omwille van de complexiteit en huidige implementatieproblemen van hoogvermogen LED’s hebben verlichtingsbedrijven echter weinig ervaring met deze nieuwe lichtbronnen. Hierdoor zijn zij afhankelijk van de informatie van diodeproducenten, die dikwijls eerder misleidend is. Doel van het hier beschreven onderzoek is deze technologische begripskloof tussen LED- en armatuurproducenten op twee manieren te reduceren.

In de eerste plaats worden modellen opgesteld die maximale LED-karakterisatie aan de hand van een minimum aantal metingen en het inschatten van LED-prestaties in verlichtingstoepassingen mogelijk maken. Door vergelijking met andere model- en simulatietechnieken werd de *gray-box*-benadering gekozen tot beste optie voor dit werk. De constructie van semi-empirische modellen, die zowel op theorie als experimentele data zijn gebaseerd, is meteen de belangrijkste onderzoeksbijdrage voor de academische wereld. Simulatie van LED-karakteristieken achteraf maakt onmiddellijke validatie van de modellen mogelijk.

Meetresultaten die voor het modelleren werden gebruikt kunnen daarnaast ook voor een uitgebreide evaluatie van de huidige LED-technologie worden toegepast. Het integreren van hoogvermogen LED’s in algemene verlichting kan dus beschouwd worden als het eindproduct van meting, modellering, simulatie en validatie, in deze specifieke volgorde. Deze academische onderzoeksbenadering kan echter verschillen van zijn toepassing in de praktijk. Daarom worden ook aanbevelingen voor *best practice* verstrekt.

In combinatie met commerciële vermogensbronnen, meetapparatuur en een oven werden twee integrerende sferen and twee goniofotometers gebruikt voor alle experimenten. Eén van de sferen heeft een diameter van 50 cm en werd speciaal voor dit werk ontworpen, gebouwd en gekarakteriseerd. Het typische hemisferische stralingspatroon van LED’s werd daarbij benut om de nauwkeurigheid van de metingen te verhogen. Recentelijk in de literatuur voorgestelde technieken zoals een externe referentiebron en spectrale detectie werden bovendien gecombineerd met een specifieke poortgeometrie en een geminimaliseerde oppervlakte van de *baffle*, zodat een zeer uniforme sfeerrespons werd verkregen. De directionele respons van de detector werd gebruikt om deze sfeerrespons te verifiëren. Stralingsstromen zijn in zeer goede overeenstemming met waarden verkregen met een goniofotometer.

Stroom-spanning-karakteristieken van tien commerciële *single-die* hoogvermogen LED’s werden opgemeten bij zes verschillende temperaturen tussen 295 en 400 K. Voor LED’s gebaseerd op InGaN halfgeleiderlegeringen konden duidelijk drie

stroomgebieden onderscheiden worden. Het intermediaire stroomgebied werd als gebruikelijk gemodelleerd met de experimentele Shockley-vergelijking. De idealiteitsfactor bleek daarbij weinig afhankelijk van de junctietemperatuur. Aangezien stroom-spanning-karakteristieken niet louter door een diffusie- of recombinatiestroom kunnen verklaard worden, werd de idealiteitsfactor ook expliciet in de uitdrukking van de saturatiestroom geïntroduceerd. Daarnaast werd ook de temperatuursafhankelijkheid van de verboden energiezone in rekening gebracht. Uit dit model kan het lineaire gedrag van de voorwaartse spanning in functie van junctietemperatuur voorspeld worden, maar slechts voor een gelimiteerd stroombereik. Metingen bevestigen de theorie met fittingcoëfficiënten hoger dan 0.99 voor alle geteste LED-samples. Bijkomende stroom-spanning-karakteristieken van tien *multi-die* LED's bij verschillende temperaturen lieten toe het voorwaartse spanningsmodel te verifiëren voor een veralgemeende junctietemperatuur. Daarbij konden de idealiteitsfactoren en interne serieweerstanden gerelateerd worden aan diegene van de individuele diodes.

Voor zowel *single-die* als *multi-die* LED's werd het oorspronkelijke spannings-model uitgebreid met de temperatuursafhankelijkheid van de interne serieweerstand. Meetresultaten tonen aan dat de weerstand een negatieve exponentiële afhankelijkheid van de junctietemperatuur vertoont, maar deze wordt in praktijk dikwijls door een lineair gedrag benaderd. Bij nominale stuurstromen gaat ongeveer 10 tot 35 % van het ingangsvermogen ten gevolge van de interne serieweerstand aan warmte verloren. Dat maakt deze weerstand de tweede grootste reden voor opwarming van de diodejunctie.

Gedeeltelijk gebaseerd op het spanning-temperatuur model werd uit de thermische weerstandsdefinitie voor LED's een uitdrukking voor de junctietemperatuur in functie van de stuurstroom opgesteld. De variatie van het elektrische ingangs-vermogen en de stralingsflux met stroom en junctietemperatuur werd experimenteel bepaald voor negen commerciële LED's. Zowel voor de flux als het ingangsvermogen werd een kwadratische afhankelijkheid van de stroom en een lineair verband met de temperatuur gevonden. Het combineren van deze afhankelijkheden leidt tot simpele uitdrukkingen voor het elektrische en radiometrische vermogen en hun verschil in functie van stroom en temperatuur. Mits kennis van de thermische weerstand kunnen deze modellen gebruikt worden om de junctietemperatuur te berekenen uit de stuurstroom in praktische LED-toepassingen. In- en uitgangsvermogens kunnen dan ook meteen voor elke stroominstelling bepaald worden. Deze methode werd gevalideerd door gemeten resultaten met gesimuleerde data te vergelijken. De maximale afwijkingen tussen beide benaderingen bleken niet groter dan enkele procenten.

De spectrale stralingsstroom van zeven commerciële hoogvermogen LED's afkomstig van twee producenten werd gemeten met de zelfontworpen integrerende sfeer bij verschillende junctietemperaturen tussen 290 en 340 K. Met frequentie of

energie in plaats van golflengte als onafhankelijke variabele werd uit de metingen een model voor enkelkleurige spectra geconstrueerd (bij 300 K). De variatie van de initiële modelparameters met junctietemperatuur werd daarna onderzocht. In tegenstelling tot een aantal louter wiskundige modellen uit de literatuur, werden daarbij het exponentiële Boltzmann-gedrag en de shift van de verboden energiezone met temperatuur expliciet in het model opgenomen. Voor het merendeel van de modelparameters konden bovendien de waarden voor AlGaInP halfgeleiders onderscheiden worden van diegene van InGaN diodes. Een Gaussiaanse functie met temperatuurafhankelijke piekwaarde, piekfrequentie en breedte bleek voldoende om fluorescentiespectra te modelleren en te simuleren. Zeer hoge fittingcoëfficiënten werden gevonden, wat wijst op een goede overeenkomst tussen de modellen en experimentele data. Beide modellen werden gevalideerd door vergelijking van flux en kleurcoördinaten van gemeten en gesimuleerde spectra bij een junctietemperatuur van 340 K. Afgezien van een rode LED met een duidelijke spectrale afwijking werden respectievelijk verschillen kleiner dan 2.5 % en kleiner dan de straal van een driestap MacAdam ellips gevonden.

Tien commerciële LED's met een *proximate* of *remote* vlakke fosfor werden gemeten met een goniofotometer. De resultaten werden gebruikt voor het modelleren van de ruimtelijke kleurvariaties van deze lichtbronnen. Voor alle geteste LED's veranderden de kleurcoördinaten langs een rechte lijn in het CIE chromaticiteitsdiagram, waarbij beide kleurwaarden toenamen met de kijkhoek. Als gevolg hiervan kon het modelleren van de ruimtelijke kleurverdeling worden gereduceerd tot het modelleren van de geel-blauw-verhouding in het spectrum en de verandering ervan in functie van de kijkhoek. Deze verhouding kon worden gerelateerd aan de relatieve schijnbare fosfordikte. Een bijkomende modelparameter werd ingevoerd om het model uit te breiden tot fosforwitte LED's met eenvoudige optieken. Een zeer goede overeenkomst tussen meting en simulatie met alle fittingcoëfficiënten groter dan 0.94 werd gevonden.

Het vooropgestelde model laat toe de zichtbaarheid van ruimtelijke kleurverschillen en dus de relevantie van kleurbinning aan het einde van LED-productielijnen te evalueren. Een eenvoudige lineaire benadering toont aan dat een maximaal kleurverschil in overeenstemming met een vierstap MacAdam ellips optreedt van zodra de primaire modelparameter gelijk is aan 0.6.

Meetresultaten die werden gebruikt voor de constructie van wiskundige modellen werden ook aangewend om de huidige LED-technologie grondig te evalueren. Deze evaluatie focust op drie aspecten, zijnde de betrouwbaarheid van LED-datasheets, studie van vermogensverliezen in LED's en een voorstel tot het hanteren van een kwaliteitsschaal voor LED-toepassingen.

De binning van spanning, lichtstroom en kleur aan het einde van LED-productielijnen werd geverifieerd met behulp gepulste metingen onder gelijkaardige

stroom- en temperatuurcondities. Resultaten werden bovendien vergeleken met metingen in thermisch evenwicht. Daarbij werden twaalf fosforwitte en twee rode diodes van in totaal drie producenten (Cree, Nichia en Seoul Semiconductor) onderzocht.

Hoewel Cree geen binning volgens voorwaartse spanning doorvoert, werden de spanningswaarden voor alle fabrikanten succesvol geverifieerd. In thermisch evenwicht bleef echter enkel de binning van Seoul Semiconductor (SSC) geldig.

De binning van lichtstroom blijkt een grote moeilijkheid te vormen voor diodeproducenten. Omwille van de selectie van zeer nauwe fluxbins slaagden zowel Cree als Nichia packages er niet in om aan de eigen binningsvereisten te voldoen. Enkel LED's van producent SSC stemden overeen met de opgegeven fluxbin tijdens de gepulste meting. Voor werking in thermisch evenwicht zakten alle lichtstromen echter onder de ondergrens vermeld in de datasheet.

Het is opmerkelijk dat, in tegenstelling tot de zeer goede resultaten voor spanning en lichtstroom, SSC LED's typisch niet aan hun kleurspecificaties voldoen. Kleurcoördinaten van Cree en Nichia packages situeren zich daarentegen wel in de respectievelijke bins. Diodeproducenten hebben het dus blijkbaar zeer moeilijk met het gelijktijdig vervullen van alle drie de binningsvereisten. Voor fosforwitte LED's zijn de kleurveranderingen tengevolge van een veranderende junctietemperatuur echter nog steeds kleiner dan de ruimtelijke kleurvariaties waarvan eerder sprake.

Verschillende verliesfactoren die aanwezig zijn in hoogvermogen LED-packages werden geëvalueerd voor een selectie van stromen en junctietemperaturen. Het vermogensverlies in de interne serieweerstand bleek daarbij de voornaamste oorzaak voor de dalende diode-efficiëntie met toenemende stroom. De externe kwantum-efficiëntie is de dominante verliesfactor, die bovendien voor witte LED's gerelateerd is aan de kleurtemperatuur. De absorptie van fotonen in de fosfor is het inderdaad grootst voor warmwitte LED's. De externe kwantumefficiëntie is eveneens verantwoordelijk voor de dalende specifieke lichtstroom met stijgende junctie-temperatuur. Verliezen ten gevolge van de Stokes-shift bedragen ongeveer 2 tot 5 % van het ingangsvermogen. Hoewel het conversieverlies per foton groter is voor warmwitte LED's, lijkt dit effect gecompenseerd te worden door het kleinere aantal uitgestuurde fotonen. Voor fosforwitte LED-spectra is het resterende zichtbare gedeelte van de ouput steeds net iets kleiner dan het visuele verlies.

De fosfortemperatuur van *remote* fosforwitte LED's neemt evenredig met de pompflux en junctietemperatuur toe. De stijging hangt af van de kwantumefficiëntie van de fosfor en de thermische weerstand tussen de fosfor en de diodejunctie. De effectieve kwantumefficiëntie (EQE) van drie LED-modules werd berekend uit spectrale fluxmetingen. In typische werkingsomstandigheden is de daling van de EQE met de pompflux (ongeveer 0.1 %/W) verwaarloosbaar in vergelijking met het effect van een toenemende fosfortemperatuur (ongeveer 0.03 %/K).

De efficiëntie-evaluatie van LED's werd in vijf stukken onderverdeeld. In eerste instantie werd de efficiëntie van RGB (rood-groen-blauw) en fosforwitte packages op twee manieren vergeleken. Zowel de benadering met constante junctie-temperatuur als diegene met vast koelelement toonde aan dat – voor een gelijke lichtstroom en kleur – de specifieke lichtstroom van fosforwitte LED's tot meer dan het dubbele van de overeenkomstige RGB-combinatie bedraagt.

De dalende efficiëntie van fosforwitte LED's met afnemende kleurtemperatuur werd verklaard aan de hand van de vorm van het spectrum. Om een lagere kleurtemperatuur te verkrijgen moet namelijk zowel de relatieve bijdrage als de piekgolflengte van het fluorescentiespectrum toenemen.

Om een vergelijking tussen LED-efficiënties van verschillende producenten zo eerlijk mogelijk te maken, werden enkel *single-die* packages bij een stuurstroom van 350 mA en een junctietemperatuur van 330 K beschouwd, en dit voor twee productieperiodes (2006-2007 en 2008-2009). In vergelijking met de eerste periode stegen de specifieke lichtstromen van producenten Cree, Lumileds en SSC met ruwweg een derde tegen 2008-2009. Toch werden zelfs voor de meest bekende hedendaagse LED-producenten zeer grote efficiëntieverschillen gevonden.

Verlichtingstoepassingen met LED's zouden een pak efficiënter kunnen gemaakt worden door elke package met nominale stuurstroom te vervangen door een schakeling van diodes met gereduceerde sturing. Alternatief kan een *single-die* package vervangen worden door een *multi-die* package waarbij het initiële ingangsvermogen wordt verdeeld over de verschillende *dies*. Dit statement werd geverifieerd met behulp van simulaties en experimenten.

De lichtstroom van vier LED-lampen en zes LED-*engines* (met hun bijhorende koelelementen) werd bepaald in thermisch evenwicht. Voor alle lampen werden specifieke lichtstromen tussen 35 en 45 lm/W gemeten. Fosforwitte LED-*engines* vertonen gelijkaardige efficiënties, wat erop wijst dat praktische toepassingen met LED's nu vergelijkbaar zijn met compact fluorescentielampen (CFL's).

Uit alle voorgaande onderzoek werden tien modelparameters geselecteerd die nauw verbonden zijn met de diodekwaliteit. Daar werden drie parameters aan toegevoegd om ook de lichtstroomdegradatie in functie van de tijd in rekening te brengen. De efficiëntie van voorschakelapparatuur en secundaire optieken zullen een bijkomende invloed hebben op de performantie van de finale LED-applicatie. Dit brengt het totaal aantal kwaliteitsparameters op vijftien. Het is aan toekomstige designers van verlichtingstoepassingen om een aantal LED-types te selecteren op basis van vooropgestelde ontwerpcriteria en om deze daarna te vergelijken voor elke kwaliteitsparameter afzonderlijk of een gewogen functie.

Alle werk ter modellering en evaluatie van LED's zou geen weerslag vinden als het niet kon worden gebruikt door diegenen waarvoor het werd bedoeld. Daarom werd aan de verschillende onderzoeksonderdelen een *best practice* toegevoegd die typisch bestaat uit een beschrijving van minimale model-, simulatie- en evaluatie-

inspanningen of richtlijnen voor het bekomen van optimale LED-prestaties. Een overkoepelende *best practice* voor de integratie van hoogvermogen LED's in algemene verlichting werd daar aan toegevoegd.

Voldoende nauwkeurige bepaling van de junctietemperatuur is enkel mogelijk als ten minste twee spanning-temperatuur calibratiemetingen worden uitgevoerd. Om te controleren of de meetstroom zich voor alle relevante temperaturen in het intermediaire stroominterval bevindt, moeten twee stroom-spanning-karakteristieken bij ongeveer de uiterste temperatuurwaarden opgemeten worden.

Hoewel minder exact kan een lineair spanning-temperatuur verband ook worden toegepast bij nominale stromen. In praktische toepassingen verschilt de meetstroom echter typisch van de stuurstroom. De spanningsmeting mag in dat geval slechts een milliseconde (of minder) duren om het effect ervan op de junctietemperatuur te minimaliseren.

De junctietemperatuur en het elektrische en optische vermogen van geïntegreerde LED's kunnen ook rechtstreeks uit de stroom berekend worden. Daarvoor zijn vier calibratiemetingen vereist: drie integrerende sfeermetingen en één meting van het ingangsvermogen in thermisch evenwicht op een vast koelelement. De simulatie van LED-prestaties door verlichtingsdesigners zou echter sterk vereenvoudigd worden indien modelparameters en thermische weerstanden op voorhand gekend zouden zijn. Sommige diodeproducenten vermelden reeds experimentele data van de vermogensvariatie in functie van stroom en temperatuur in hun datasheets, maar expliciete vermelding van modelparameters zou handig zijn.

Het modelleren en simuleren van een diodespectrum voor elke junctietemperatuur vereist twee spectrale fluxmetingen. De eerste meting dient daarbij als referentie. Voor enkelkleurige spectra kunnen vier van de zeven modelparameters bepaald worden uit een exponentiële benadering van de lage en hoge energiezijde van het spectrum. Voor de lage energiezijde kunnen echter vaste coëfficiënten van $22.5\ 10^{-14}$ Hz^{-1} en $7.5\ 10^{-14}$ Hz^{-1} voor respectievelijk AlGaInP- en InGaN-diodes gehanteerd worden. Het verschil tussen de combinatie van de exponentiëlen en het gemeten referentiespectrum wordt gemodelleerd met een Gaussiaanse functie. Fluorescentie-spectra kunnen rechtstreeks door een Gaussiaan benaderd worden.

Lineaire approximaties bleken voldoende om de temperatuursafhankelijkheid van de initiële modelparameters te beschrijven. Daarom is slechts één bijkomende spectrale fluxmeting nodig om het gedrag van een LED-spectrum in functie van de junctietemperatuur te voorspellen.

Door de verandering van de schijnbare fosfordikte in functie van de kijkhoek, vertonen vlakke fosforen in bichromatische witte LED's een onvermijdelijke ruimtelijke kleurspreiding. In praktijk zijn voor Lambertiaanse stralers twee spectrale intensiteitsmetingen voldoende om de relatieve verandering van de geel-

blauw-verhouding in het spectrum voor alle kijkhoeken te kennen. Voor fosforwitte LED's met een evenredig bundelende optiek is daarvoor minstens één bijkomende intensiteitsmeting nodig.

Er werd een hoge correlatie tussen de primaire modelparameter C_1 en de maximale kleurspreiding ΔE_{uv} waargenomen met R^2 = 0.92. Een maximaal kleurverschil dat overeenkomt met een vierstap MacAdam ellips of typisch één kleurbin wordt verkregen voor de LED's met $C_1 \approx 0.6$. Deze waarde kan dus ook als een kleurevaluatiecriterium worden gehanteerd. Voor LED's met $C_1 > 0.6$ is kleurbinning volgens een vierstap MacAdam ellips enkel geldig voor een deel van de bundel en dus irrelevant voor de volledige lichtoutput. Het gebruik van *remote* sferische fosforverdelingen is de beste optie om tot minimale ruimtelijke kleurverdelingen te komen.

Vanuit commercieel oogpunt focust een evaluatie van de huidige LED-technologie typisch op betrouwbaarheidstesten voor binning door producenten en vergelijking van producten op een kwaliteitsschaal. Vermogensverliezen en efficiënties kunnen echter met behulp van hetzelfde beperkte aantal metingen berekend en vergeleken worden.

Twee integrerende sfeermetingen bij verschillende junctietemperaturen zijn nodig en voldoende voor het testen van de betrouwbaarheid van LED-specificaties. Dezelfde data kunnen gebruikt worden voor de berekening van alle vermogensverliezen en hun verandering met temperatuur. Minstens één bijkomende meting bij een afwijkende stroom is vereist om het gedrag van deze verliezen in functie van het ingangsvermogen te kennen. Deze metingen moeten herhaald worden voor een ruimere selectie van LED's om efficiëntievergelijking mogelijk te maken.

Acht van de tien geselecteerde kwaliteitsparameters kunnen bepaald worden uit twee stroom-spanningsmetingen en drie integrerende sfeermetingen. Daarnaast laten twee vermogens- en intensiteitsmetingen toe respectievelijk de thermische weerstand en het kleurevaluatiecriterium C_1 voor fosforwitte LED's vast te leggen. Om de kwaliteitsschaal verder uit te breiden tot LED-lampen of volledige armaturen is nog minstens één meting van de lichtstroom nodig. Daaruit kunnen de efficiënties van voorschakelapparatuur en secundaire optieken worden berekend.

De voorgaande paragrafen tonen aan dat het modelleren, karakteriseren en evalueren van LED's kan uitgevoerd worden met behulp van een zeer beperkte hoeveelheid meettoestellen. Indien een verlichtingproducent zelf een middelmatige commerciële versie van elk van deze toestellen wil bemachtigen bedraagt de initiële totaalkost ruwweg 60 000 euro.

Naast de reproduceerbaarheid die gerelateerd is aan de variatie die optreedt tussen resultaten van metingen van eenzelfde testobject, moet bij karakterisatie van LED-toepassingen ook rekening gehouden worden met de reproduceerbaarheid die het gevolg is van het optreden van verschillen tussen LED's van eenzelfde type of bin. Bovendien kunnen modelparameters die initieel gelijk zijn na verloop van tijd

toch van elkaar afwijken. Verlichtingsontwerpers moeten hiervan op de hoogte zijn wanneer zij het gedrag van hun toepassingen op basis van modelparameters gaan simuleren.

Niet enkel de specifieke lichtstromen van commerciële LED-toepassingen zijn op dit moment van dezelfde grootteorde als die van compact fluorescentielampen. Kleurverschuivingen ten gevolge van veranderingen van de junctietemperatuur zijn vergelijkbaar met de kleurveranderingen van CFL's tijdens de opstartperiode. Aangezien daarnaast ook de kleurweergave-indices van LED's en CFL's equivalent zijn, kan besloten worden dat beide technologieën in dezelfde mate voor algemene verlichtingstoepassingen geschikt zijn. Uiteraard heeft elke technologie echter zijn eigen optimale applicatiedomeinen.

Een belangrijk nadeel van een LED ten opzichte van een CFL is zijn dikwijls zichtbare ruimtelijke kleurspreiding. Het gebruik van *remote* sferische fosforen moet dit euvel in de toekomst verhelpen. Dit maakt de gelijkenis tussen beide technologieën nog groter.

Ondanks de reeds zeer bevredigende outputkarakteristieken van LED's, is het van belang nogmaals de gereduceerde performantie bij nominale stuurstromen te benadrukken. De interne kwantumefficiëntie daalt zienderogen met toenemende stroom en ongeveer 10 tot 35 % van het ingangsvermogen gaat onmiddellijk verloren in de interne serieweerstand. Men kan de efficiëntie van LED-toepassingen tot 50 % verhogen door elke diode bij nominale stuurstroom te vervangen door een aantal diodes met gereduceerd verbruik. Zoals zo vaak zal men in de toekomst de verhoogde initiële kostprijs van dit alternatief moeten afwegen tegenover de gerelateerde winst.

List of symbols and abbreviations

D	absolute (phosphor) thickness (m)
E_a	activation energy (eV)
AC	alternating current
AlGaInP	aluminium-gallium-indium-phosphide
(α, β)	angles indicating a direction of view (rad.)
$f(\theta, \varphi)$	angular variation (of responsivity)
D_a	apparent (phosphor) thickness (m)
$B(\lambda)$	asymmetrical line width
E_g	band gap energy (eV)
k	Boltzmann constant = $8.617\ 10^{-5}$ eV/K
T_c	carrier temperature (K)
T_Φ	characteristic temperature of flux (K)
T_R	characteristic temperature of internal series resistance (K)
T_l	characteristic temperature of light output degradation (K)
CCD	charge-coupled device
COB	chip-on-board
(x, y)	CIE colour coordinates in x, y colour space
(u', v')	CIE colour coordinates in u', v' colour space
R^2	coefficient of determination
a_D to d_D	coefficients of dissipated power variation with current and temperature
α_F, β_F	coefficients of flux variation with current
a_F to d_F	coefficients of flux variation with current and temperature
γ_F, δ_F	coefficients of flux variation with temperature
γ, δ	coefficients of forward voltage variation with temperature
α_P, β_P	coefficients of input power variation with current

a_P to d_P	coefficients of input power variation with current and temperature
γ_P, δ_P	coefficients of input power variation with temperature
ΔE_{uv}	colour difference in CIE-u',v' colour space
CRI	colour rendering index
CIE	Commission Internationale de l'Eclairage
CFL	compact fluorescent lamp
CCT	correlated colour temperature
I	current (A)
C_l	degradation constant (fitting parameter)
α_l	degradation rate
W_D	depletion region width (m)
I_D	diffusion saturation current (A)
DC	direct current
(θ,φ)	direction in space indicated by spherical coordinates (rad.)
P_d	dissipated power (W)
N_D, N_A	donor and acceptor concentrations
N_C, N_V	effective density of states at conduction-band and valence-band edges
η_{eff}	effective quantum efficiency
η_s	efficiency of step s in efficiency scheme
η_R	efficiency related to internal series resistance
N_n, N_p	electron and hole concentrations
D_n, D_p	electron and hole diffusion constants (s^{-1})
τ_n, τ_p	electron and hole minority-carrier lifetimes (s)
e	electron charge = $1.602\ 10^{-19}$ C
E	energy (eV)
I_S	experimental saturation current (A)
η_{EQ}	external quantum efficiency

ΔP_{EQ}	external quantum loss (W)
η_{ext}	extraction efficiency
ΔP_{vis}	eye sensitivity loss (W)
FOV	field of view
C_1, C_2	fitting parameters for spatial colour distribution
U_f	forward voltage (V)
ν	frequency (Hz)
FWHM	full width at half maximum
GaAsP	gallium-arsenic-phosphide
GaN	gallium-nitride
ν_G	Gaussian peak frequency (Hz)
b	Gaussian peak width (Hz)
HID	high-intensity discharge
n	ideality factor
$pump$	index for quantities related to (blue) pump spectrum
src	index for quantities related to a (light) source
$phos$	index for quantities related to phosphor spectrum
rad	index for radiative related transitions
r	index for reference quantities
$trap$	index for trap related transitions
InGaN	indium-gallium-nitride
P	input power as product of current and voltage (W)
η_{IQ}	internal quantum efficiency
R_S	internal series resistance (Ω)
N_i	intrinsic carrier concentration
T	junction temperature (K)
LASTIP	Laser Technology Integrated Program
t_l	lifetime (s or h)

LED	light-emitting diode
Lum.	Lumileds
K_m	luminous efficacy maximum at 555 nm = 683 lm/W
η_v	luminous efficacy of a device (lm/W)
K	luminous efficacy of radiation (lm/W)
Φ_v	luminous flux (lm)
I_v	luminous intensity (cd)
MFR	manufacturer
π	mathematical constant $\approx$ 3.14159265
NIST	National Institute of Standards and Technology
I_n	normal drive current specified by datasheet (A)
L_n , L_p	n-type and p-type semiconductor diffusion lengths
N_s	number of particles for step s in efficiency scheme
N	number or concentration
OLED	organic light-emitting diode
POB	package-on-board
ν_p	peak frequency (Hz)
λ_p	peak wavelength (nm)
η_{phos}	phosphor external quantum efficiency
S_{phos}	phosphor spectrum peak value (W)
h	Planck constant = $4.136\ 10^{-15}$ eV s
ΔP_R	power loss due to internal series resistance (W)
ΔP_s	power loss of step s in efficiency scheme (W)
m	power of degradation rate variation with current
P_s	power of step s in efficiency scheme (W)
Prol.	Prolight Opto
x	proportionality index for compound semiconductors
$\propto$	proportionality symbol

PWM	pulse-width modulation
f_{pump}	pump light leakage fraction
C_D, C_R, C_S	quasiconstant fore factors for diffusion, recombination, and experimental saturation currents
C_L	quasiconstant luminescence factor
η_e	radiant efficiency
Φ_e	radiant flux (W)
I_e	radiant intensity (W/sr)
Φ_0	radiant or luminous flux at $t = 0$ (initial value)
R	radius (m)
τ	recombination lifetime
I_R	recombination saturation current (A)
RGB	red-green-blue
ρ	reflectance
n_{amb}	refractive index of ambient
n_{phos}	refractive index of phosphor
$\Delta\mathrm{YB}(\theta)$	relative YB variation as a function of viewing angle θ
RMS	root mean square (i.e. quadratic mean)
n	semiconductor with excess number of electrons
p	semiconductor with excess number of holes
SSC	Seoul Semiconductor
SiC	silicon-carbide or carborundum
S_0 to S_3	single-colour spectrum peak values (W)
α'	slope of band gap energy variation with temperature (eV/K)
c_T	slope of carrier temperature variation with junction temperature
γ_G	slope of Gaussian peak frequency variation with temperature (Hz/K)
γ_p	slope of peak frequency variation with temperature (Hz/K)
γ_b	slope of rooted double Gaussian variance variation with temperature (Hz/K)

SSL	solid-state lighting
SRDF	spatial response distribution function
I_0	specific constant current (A)
T_0	specific constant temperature (K)
S_λ	spectral detector response
$E_{e,\lambda}$	spectral irradiance (W/m²/nm)
$V(\lambda)$	spectral luminous efficiency
$L_{e,\lambda}$	spectral radiance (W/m²/nm)
$\Phi_{e,\lambda}$ or $\Phi_{e,\nu}$	spectral radiant flux (W/nm)
$I_{e,\lambda}$ or $I_{e,\nu}$	spectral radiant intensity (W/sr/nm)
$\Re_\lambda$	spectral responsivity at normal incidence
a	spectrum's low energy slope (s)
c	speed of light (in vacuum) = 299792458 m/s
η_S	Stokes shift efficiency
ΔP_S	Stokes shift power loss (W)
A	surface (m²)
SMD	surface-mount device
ΔT	temperature difference (K)
R_T	thermal resistance (K/W)
$R_{T,j-x}$	thermal resistance between junction and point x (K/W)
TH	through-hole
t	time (s)
TCO	total cost of ownership
P_t	total input power from grid (W)
η_t	total luminous efficacy (lm/W)
°	unit of angle in degrees
C	unit of charge in coulomb
A	unit of current in ampere

eV	unit of energy in electron-volt
lm	unit of flux in lumen
Hz	unit of frequency in hertz
m	unit of length in meter
W	unit of power in watt
Ω	unit of resistance in ohm
sr	unit of space angle in steradian
°C	unit of temperature in degrees celsius
K	unit of temperature in kelvin
h	unit of time in hours
s	unit of time in seconds
V	unit of voltage in volt
α_V , β_V	Varshni parameters
η_{vis}	visibility efficiency
Φ_{vis}	visible flux (W)
ΔU_f	voltage drop due to internal series resistance (V)
λ	wavelength (nm)
YB	yellow-blue ratio (of a phosphor-white spectrum)
YB_0	yellow-blue ratio in forward direction

Table of contents

1. Introduction

Light-emitting diodes (LEDs) have become very popular and certainly have proven their usefulness in a wide variety of applications. These include applications requiring narrow-band colour spectra [Tamulaitis, 2004] [Harbers, 2007] and indicative, decorative and signal lighting [Freyssinier, 2004]. It cannot be denied that especially the high-power LED technology is developing very quickly and may be considered a promising alternative for general (public, industrial, private) lighting applications as well [Mottier, 2009]. Next to important efficiency improvements, the total luminous flux per device is increasing by combining different dies into one package and by allowing larger drive currents [Bierhuizen, 2007]. However, the real breakthrough of LEDs in general lighting is still subject of discussion. Main obstacles are the moderate total system efficiency and luminous flux, the need for narrow colour binning regions when combining several devices, and the production price [Narendran, 2004] [Bierhuizen, 2007] [Liu, 2007]. Furthermore, optical and electrical characteristics strongly depend on the diode junction temperature, which in turn is determined by the forward current, heat sink size and ambient temperature [Chou, 2008]. Low junction temperatures are especially favourable regarding flux, efficiency and lifetime, while high temperature operation strongly reduces the overall diode performance [Deshayes, 2005] [Krames, 2007] [Meneghini, 2007] [Hu, 2008]. Additionally, the present lack of international standardization regarding the optical and electrical characterization of LEDs is compromising a successful implementation.

An extended overview and comparison of existing general lighting technologies and commercial high-power LEDs in particular is given in chapter 2. Design history, current manufacturing, nomenclature, technology benefits and bottlenecks, and market trends of high-power light-emitting diodes are discussed in detail.

Due to the complexity and current implementation obstacles of LEDs, lighting companies are generally short of experience with these light sources and depend on the often misleading information of diode manufacturers. The idea for the doctoral research work at hand arose from the recognition of this technological comprehension gap between high-power LED package manufacturers and application designers or end-users by its later promoters. This project has the intention to narrow the comprehension gap in two different ways.

First and foremost, research on the integration of high-power light-emitting diodes in general lighting implies providing manufacturers and product designers with models that allow performing maximum LED characterization from a minimum number of measurements and estimating diode performance in practical lighting applications. For the scientific community, this construction of semi-empirical light-emitting diode models, based on both physics theories and

experimental data, is the most important research contribution. Chapters 4 to 7 are dedicated to this modelling. In each chapter, determination of diode characteristics through simulations immediately makes model validation possible.

Secondly, measurement results that have been used for model construction can be utilized for an extended evaluation of the present LED technology status as well. This evaluation is discussed in chapter 8.

Integration of high-power light-emitting diodes in general lighting can thus be considered the final product of measurement, modelling, simulation, validation, and evaluation, in this specific order. The academic approach to this research cycle as applied in this work is however different from its practical use. Related recommendations for best practice have to be provided. Therefore, at the end of each chapter a more industry-friendly measurement and simulation approach is proposed. Once available, models of course don't have to be reconstructed in practice.

Chapter 3 has the intention to provide the reader with an outlook on the approaches that have been used to work towards the intended research contributions. By comparison with other modelling and simulation techniques, the gray-box modelling approach has been found to be the best option. In the same chapter, all measurement equipment setups are described in detail. Next to commercial voltage and power source-measure systems, two integrating spheres and two goniophotometer setups are used. One of the spheres has been especially custom-made for this doctoral research.

Integrating spheres are widely used for determining optical characteristics of materials and light sources [Yu, 2006]. Traditional integrating sphere photometry is based on the substitution method in which a test lamp is measured in comparison with a standard lamp [CIE, 1989]. Measurements suffer from limited accuracy if spectral characteristics and angular intensity distributions of test source and reference source are dissimilar. Consequently, test lamps should only be measured against standard lamps of the same or similar types, as recommended in standard practices [CIE, 1989] [Rea, 2000].

For the new custom-made integrating sphere, the most was made of the typical hemispherical radiation of power LEDs to increase the accuracy of flux determination. Recently developed measurement techniques are combined with a very particular port geometry and a minimized baffle area. This results in a uniform spatial response distribution function (SRDF), which guarantees an accurate radiant and luminous flux determination, irrespective of the spatial intensity distribution of the LED package or luminaire [Ohno, 1999]. Furthermore, the effect of the directional response of the detector head on the SRDF is explored.

Due to chip encapsulation, in situ junction temperature determination is not possible for commercial LED packages [Lee, 2009]. Many research groups and light-emitting diode manufacturers are therefore doing efforts to develop proper junction temperature measurement techniques. In 2004, Lee proposed a progressive

technique using nematic liquid crystal thermography with laser illumination [Lee, 2004]. Also Gu and Narendran developed a non-contact method for determining junction temperature of phosphor-converted white light-emitting diodes in 2004 [Gu, 2004]. Similar non-contact methods have been developed subsequently [Cho, 2005] [Vaitonis, 2008]. Xi *et al.* published an article about junction and carrier temperature measurements in deep-ultraviolet light-emitting diodes using three different methods [Xi, 2005]. One of these methods uses voltage-temperature calibrations for junction temperature determination. This method has been described in more detail by Xi and Schubert [Xi, 2004] [Chhajed, 2005] and generalized by Ryu *et al.* [Ryu, 2005] afterwards. A practical voltage-temperature calibration method has been developed by Zong and Ohno [Zong, 2008].

In contrast to the methods described above, LED application manufacturers in general still stick to the most popular junction temperature measurement technique. This technique uses a thermistor or thermocouple to measure the temperature of the ambient or a specific external system component, such as slug, printed circuit board, and heat sink. Given the thermal resistance of the material(s) between the LED junction and the measuring point, one can estimate the junction temperature [Lumileds, 2001] [Nichia, 2003] [Huber, 2006].

Chapter 4 shows that junction temperature measurements of packaged light-emitting diodes can be performed more precisely without the need of complex equipment setups. The method consists of a rather simple forward voltage measurement, which is directly related to junction temperature. The difference between the method of Xi and Schubert [Xi, 2004] lies in the way the forward voltage dependence of junction temperature is derived and applied to measurement data. Indeed, current-voltage measurements at different junction temperatures are modelled, and the numerical coefficients are explained in terms of basic semiconductor characteristics. This approach is first utilized for single-die packages, and verified for multi-die packages afterwards. The forward voltage model is then extended to include the internal series resistance and its junction temperature dependence. The model is applicable for all practical current values as a result.

Partially based on the models constructed in chapter 4, the fifth chapter demonstrates that the junction temperature and electrical and optical power of LEDs can be determined from forward current directly. A current-temperature relation is constructed from the thermal resistance definition for LED packages, linking the diode's junction temperature and dissipated power. The latter is modelled by examining the electrical power, radiant flux, and their difference as a function of current and temperature.

As a consequence of the power modelling, accurate input power and flux simulations can be performed. Similar modelling and simulation efforts have been reported by other researchers [Baureis, 2005] [Deshayes, 2005] [Salsbury, 2007] [Hui, 2009] [Moolman, 2009] [Li, 2010], but never before a simple expression for electrical power and flux variation with both current and junction temperature has

been provided. Such comprehensive models can easily be used by manufacturers to predict solid-state lighting performance [Salsbury, 2007].

The spectral radiant flux is all lighting devices' primary optical characteristic, determining luminous flux and colour. A lot of effort has been attributed to model the LED spectral flux and its variation with junction temperature. One of the first attempts consisted of a rather simple LASTIP (Laser Technology Integrated Program) simulation of previously measured LED and laser spectra [Kuo, 2000]. In 2005 however, a Gaussian spectrum model appeared more successful [Uchida, 2005] and this model simplified incorporation of the peak wavelength variation with junction temperature [Chhajed, 2005]. Very soon afterwards, a double Gaussian model has been presented [Ohno, 2005], which is nowadays still used for lighting calculations by the International Commission on Illumination. A more general approach based on the double Gaussian model has been published in 2006 [Man, 2006]. In 2008 a variant of the split Gaussian function with a different exponential behaviour on each side of the maximum has been reported to be a more simplified approach, still containing the junction temperature as a free parameter [Chou, 2008]. More recently an evaluation of several LED spectrum approximations has been published [Reifegerste, 2008], but due to the large number of fitting parameters an easy-to-use modelling approach is not provided. Furthermore, most spectral radiant flux models that have been published so far are purely mathematical and any link with underlying physical principles is missing. Integration of the junction temperature variation into the initial model parameters often results in piecewise defined and complex models.

In chapter 6, a spectrum model is constructed where the Boltzmann exponential behaviour with carrier temperature variation, band gap energy shift and the increase of the non-radiative recombination rate with junction temperature are included explicitly. In a first step, an experimental spectrum at a particular temperature is modelled with two exponentials and a Gaussian function, using frequency as the main variable. Afterwards, peak frequency, absolute spectrum power and spectrum skewness variation with temperature are implemented. The model allows for very accurate simulations of single-colour and phosphor-white LED spectra at any temperature.

Although less known by luminaire designers or end-users, another major drawback of current LED technology is its colour variation as a function of the viewing angle. This spatial colour variation is negligible for single-colour emitters, but this is not the case for bichromatic white LEDs using phosphor for wavelength conversion. As the latter diode types are most often used for high colour rendering applications [Narendran, 2002] [Mirhosseini, 2009], a quantitative description of this colour variation is necessary.

In contrast to the spatial (luminous) intensity distribution of high-power LEDs, little effort has been made to examine the spatial colour distribution of these light

sources [Moreno, 2008]. According to literature, only two research groups have been studying this colour variation with viewing angle of bichromatic white LEDs. The first group focussed on the effect of phosphor thickness, phosphor concentration and phosphor particle size on the colour distribution [Wenzl, 2008] [Sommer, 2009], while the second group simulated and examined the yellow-blue ratio of phosphor-white LED devices for different package configurations and phosphor locations [Liu, 2008-2] [Liu, 2009-2].

Despite the increasing colour homogeneity by using new package configurations and phosphor distributions, spatial colour changes appear to be inevitable. The seventh chapter has the intention to model and evaluate these colour variations, which should allow making appropriate design improvements. As non-conformal phosphor distributions vary significantly for different manufacturers, only packages containing a planar phosphor have been considered.

Measurement results that have been used for model construction in chapters 4 to 7 can be utilized for an extended evaluation of the present LED technology status as well. This evaluation is discussed in chapter 8 and focuses on three major aspects:

Due to the lack of related standards, the reliability of datasheet information is often doubtful. In a first part of the evaluation, binning by manufacturers at pulsed operation is hence verified. The relevance of this binning for diode operation in practice is discussed directly afterwards.

Numbers quoted for (luminous) flux, and consequently for efficiency of LEDs, are very sensitive data as they are used to impress and push the LED market. Nowadays, specification data can be misleading as the measurement conditions are often not well defined. Therefore, efficiency measurements and output comparison, including the current and temperature dependence of the results, are of major importance in current high-power light-emitting diode research [Krames, 2007]. In literature however, often only very specific efficiency measurements are discussed, e.g. the diode extraction efficiency [Boroditsky, 1997] or the relative luminous efficacy [Narendran, 2000]. More recently, there is a trend towards more combined efficiency determination. Examples of the latter are [Krames, 2007], [Liu, 2007] and [Chen, 2008]. Nevertheless, none of these papers has the intention to unite a maximum number of efficiency measurements in one setup, which allows connecting power and loss calculations by use of the energy conservation relation. Such an extended efficiency study is performed in the second part of the technology evaluation. The study is subdivided in an examination of power loss mechanisms in solid-state lighting applications and a LED efficiency comparison on five different levels. These levels are RGB versus phosphor-white technology efficiency, dependence of efficiency on correlated colour temperature for phosphor-white emitters, efficiency dissimilarities between manufacturers, single-die versus multi-die component efficiency, and comparison of efficiency values obtained for LED lamps and engines in practice.

The evaluation is completed by a proposal for a light-emitting diode quality scale. This scale is constructed from modelling parameters that have been found to be closely related to device quality. Comparing such parameters for different LEDs allows making a technology ranking according to the lighting designer's or end-user's needs.

The general conclusions of this doctoral research work are summarized in chapter 9. Scientific contributions and guidelines for best practice are discussed separately. Reflections on possibilities for improvement of the results and continuation of the research are added. This chapter is finally followed by the bibliography and appendices.

2. Light-emitting diode: a promising youngster of the Lighting family

2.1. Goals

Just as the first cars looked like deformed horse coaches, the first LED lamps appeared to many as somewhat weird incandescent bulbs as well. This did however not mean that the innovations were ineffective. This chapter has the intention to show that SSL with high-power LEDs indeed is a promising illumination approach. Next to that, it serves as a concise introduction to the technology that is focussed in this work.

An overview and comparison of the existing general light sources, with particular focus on diodes, is given. Due to the large number of components involved, some supplementary LED nomenclature clarification is required. A brief development history of this semiconductor device cannot lack either. The look on the past is followed by a discussion of the present LED technology, including benefits and drawbacks, manufacturing and binning issues, and current market trends.

2.2. The Lighting family

2.2.1. Overview of commercial light sources

Light is defined as the form of electromagnetic radiation to which the human eye is sensitive and on which our visual awareness of the universe and its contents relies [Daintith, 2009]. Controllable sources of light have been of human concern from the prehistoric era when open fire was used to illuminate caves. Plenty of safer and more efficient illumination alternatives have been developed ever since. In many forms, as torches, oil lamps, candles, and others, fire remained the only human-controlled light source until by the end of the nineteenth century the incandescent light bulb has been invented and commercialised [Rea, 2000].

Incandescence is still one of the three major technologies that constitute the electrical Lighting family nowadays. It is defined as the emission of light by a material that is heated to high temperatures, typically higher than 750 °C [Schubert, 2006]. Two incandescent lamp types are commonly used, called standard bulbs and halogen sources (see Table 2.1 and Fig. 2.1). Despite their low luminous efficacies, incandescent lighting is still utilized for applications requiring a high colour rendering or for creating warm atmospheres [Rea, 2000].

A second artificial lighting technology is being developed since the early 19th century and is based on the electrical discharge of ionized gases or plasmas. Radiation is thereby created through relaxation of atoms or molecules that have been excited by collisions with free electrons [Krames, 2007] [Daintith, 2009]. Depending on their shape, electrode distance, filling mixture, and internal gas pressure, different discharge lamp types are distinguished. Most familiar are fluorescent tubes and compact fluorescent lamps (CFL) based on a low pressure mercury filling, metal halide lamps based on high pressure mercury, low and high pressure sodium lamps, and high-intensity discharge (HID) lamps incorporating for example xenon gas [Rea, 2000]. Gas-discharge lamps allow obtaining high fluxes within a wide variety of luminous efficacies, up to 200 lm/W (see Table 2.1). They are therefore most often used in public, workplace, street, and shop lighting [Rea, 2000]. However, with the increasing awareness of the need for reducing energy consumption, the discharge technology is now gaining popularity in private lighting as well [Bodart, 2010].

Only by the end of the twentieth century, high-power solid-state devices emerged as a third technology for general lighting applications (see Fig. 2.1 and section 2.4). Although the inorganic types have a certain lead, also organic LED devices (OLEDs) are still in full development nowadays. The solid-state lighting technology is based on a physical process called electroluminescence, i.e. the emission of electromagnetic energy due to electrons returning to a lower energy state [Daintith, 2009]. For both LEDs and OLEDs, the electrons are typically injected into a semiconductor alloy through constant current operation (see next section for details). Because of their narrow-band spectra, solid-state light sources are now mainly used for indicative, decorative and signal lighting [Freyssinier, 2004]. Nevertheless, LED technology is already considered a proper alternative for several general lighting applications as well [Mottier, 2009]. The projections in Fig. 2.1 show that the high-power diode indeed is a promising youngster of the Lighting family.

Table 2.1: Overview of the most common technologies within the electrical Lighting family. Lamp types and typical luminous efficacy values η_v (including driver electronics) are gathered in columns two and three, respectively [Rea, 2000] [Mottier, 2009] [Navigant, 2009] [Bodart, 2010].

technologies	lamp types	typical η_v (lm/W)
incandescent	standard incandescent (Edison bulb)	about 10 to 15
	halogen	about 20 to 30
discharge	low pressure mercury (fluorescent and CFL)	80-90 for fluorescent, 30-70 for CFL
	low pressure sodium (street lighting)	up to 200
	high pressure mercury (metal halide)	about 70 to 110
	high pressure sodium (outdoor and shops)	up to 150
	high-intensity discharge (HID, e.g. xenon)	about 80
solid-state	(inorganic) LED	to be discussed in chapter 8
	organic LED (OLED)	about 20 to 30

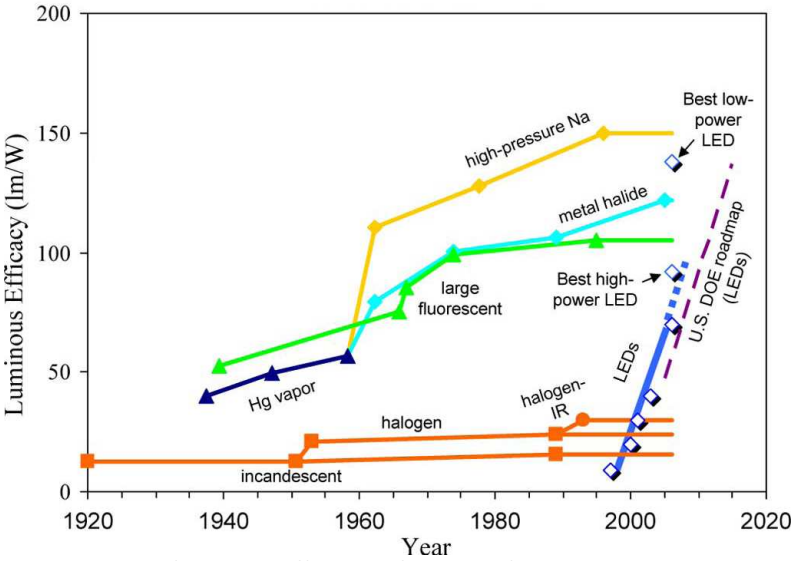

Fig. 2.1: Evolution of luminous efficacy performance of commercial white light sources. High-power LED performance is indicated by the points along the solid blue curve. The USA Department of Energy (DOE) projections for white LEDs are indicated by the dashed purple line [Krames, 2007].

2.2.2. Light-emitting diodes

According to its definition, a LED is a semiconductor device that converts electrical energy into electromagnetic radiation through electroluminescence (see preceding section) [Daintith, 2009]. For this conversion always a junction of p-type and n-type (compound) semiconductors is required. These are materials that contain an excess number of free charge carriers, being holes or electrons, due to doping with acceptor and donor atoms, respectively. Although free electrons and holes are separated by a forbidden energy zone or band gap, a p-n homojunction in the absence of a forward voltage (zero bias) forms a depletion region where positive and negative carriers are compensated. The resulting potential difference between both sides of the junction prevents further electron-hole recombination (see Fig. 2.2) [Schubert, 2006].

When a forward voltage is applied to the homojunction (forward bias), the steady-state potential difference is reduced. As a consequence, free electrons will diffuse from the n-type into the p-type semiconductor, while free holes will migrate in the opposite direction. This leads to radiative electron-hole recombinations for some of the carriers. Such recombinations have a certain lifetime τ and create quanta of electromagnetic radiation (photons) with an energy $h\nu$ that is closely related to the band gap energy (see Fig. 2.2).

In order to enlarge quantum yields, heterojunction instead of homojunction LEDs are manufactured for practical use. Heterojunction diodes contain at least two

different semiconductor alloys. By placing a material with lower band gap in between high gap counterparts, free carriers are confined into the heterojunction energy barriers or quantum well during forward bias operation (see Fig. 2.2). In comparison with the freely diffusing carriers in homojunctions, this confinement significantly increases the electron-hole recombination probabilities. Commercial high-power LED devices generally incorporate a large sequence of heterojunctions, as diodes' external quantum efficiency is proved to increase with the number of quantum wells [Hunt, 1992].

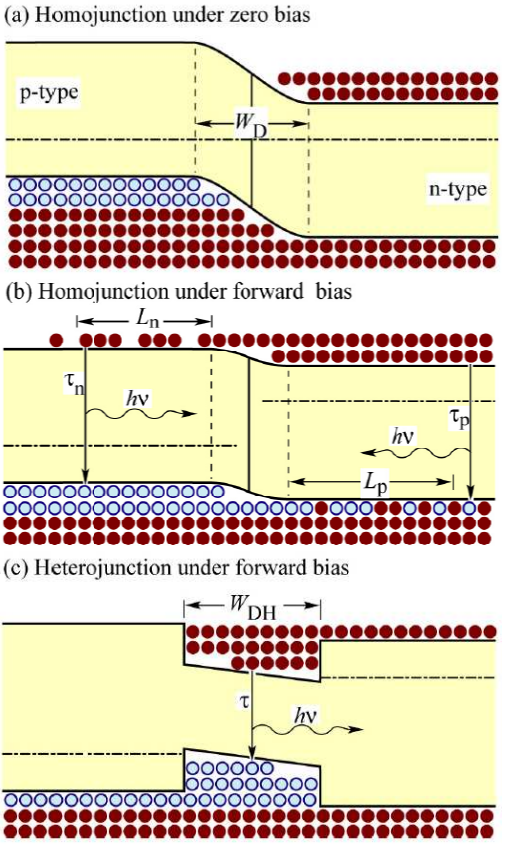

Fig. 2.2: Homojunction under (a) zero and (b) forward bias and heterojunction under forward bias (c). Carriers (red for electrons and blue for holes) diffuse on average over the diffusion lengths L_n and L_p in homojunctions, while they are confined by the heterojunction barriers. Homojunction and heterojunction depletion widths are indicated by W_D and W_{DH}, respectively. The yellow regions represent the forbidden band gap. According to an electron-hole recombination lifetime τ, photons with energy $h\nu$ are created [Schubert, 2006].

As the photon energy of a LED is determined by the band gap of the semiconductor, different alloys are used to acquire different light colours. Most commonly, indium-

gallium-nitride (InGaN) and aluminium-gallium-indium-phosphide (AlGaInP) compounds are utilized for constructing blue and green, and red and amber emitters, respectively [Schubert, 2006]. The emission colour of one semiconductor alloy can thereby be varied by changing the proportionality of the elements within (see also chapter 8). This fine-tuning of the forbidden energy zone is called band gap engineering.

White LED light can be obtained by combining red, green, and blue emitters. For some applications requiring more smooth spectra, other colours (e.g. amber) are added. White light is however created through phosphor-conversion as well (see chapters 7 and 8). Usually blue LEDs are covered with a yellowish phosphor, but some manufacturers apply ultraviolet emitters in combination with red-green-blue (RGB) phosphors instead. Phosphor-white diodes are particularly suited for high colour rendering purposes, but combinations of single-colour emitters have the important benefit of allowing dynamic colour control [Mottier, 2009]. Efficiency differences between both approaches are discussed in chapter 8.

2.3. Nomenclature

The abbreviation “LED” is already to a large extent integrated into general language. It is however often unclear what is exactly meant by this denomination. The semiconductor junction, electrical component, and complete lamp are regularly given the same name by laymen. Some nomenclature clarification may therefore be required at the beginning of this work.

Despite the general language, the spelled out form of “LED” precisely indicates what this epithet stands for: A light-emitting diode is in fact nothing more than a contact of two semiconductors that generates electromagnetic radiation during current injection (see preceding section) [Schubert, 2006]. For all derivative applications, “LED” is typically used a prefix: LED-package, LED-module, LED-lamp, etc. These concepts are explained in detail below (also see Fig. 2.3). Nevertheless, the prefix is frequently omitted and the term “LED device” is generally used for all products related to or containing LEDs.

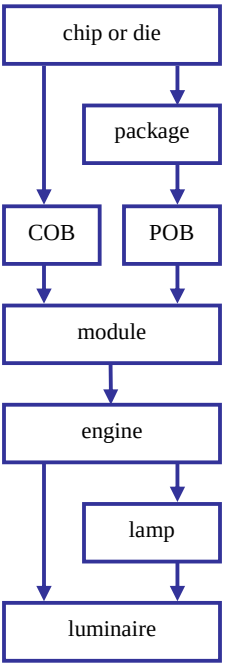

Fig. 2.3: Schematic overview of all components or production steps for obtaining a LED luminaire.

The LED-chip or LED-die is the small solid block of compound semiconductor crystals that incorporates the light-emitting diode junction and is thus considered the basic entity of each LED application (see Figs. 2.3 and 2.4). The light colour depends on the semiconductor type(s) this entity is made of (see section 2.2).

At this moment, two possibilities for further integration of the chip exist. Firstly, the chip can be placed directly on a piece of printed circuit board (PCB). This approach is called chip-on-board technology (COB, see Figs. 2.3 and 2.5). Alternatively, a LED-chip can be incorporated into a solderable LED package. Depending on the number of chips per package, single-die packages (one die) and multi-die packages (multiple dies) are distinguished, where the latter allow combining different chip types for applications with changeable colours. Next to that, a distinction between surface-mount devices (SMD) and through-hole (TH) packages is made [Schubert, 2006]. Although soldering on top or at the back of the board has nothing to do with chip quality, SMD packages typically allow for a better heat conduction, which is favoured (see chapter 4). In correspondence with the term “COB”, also “POB” (package on board) is utilized for a package soldered to a PCB (see Figs. 2.3 and 2.5). The combination of several packages on one board is also referred to as a LED array [Navigant, 2009].

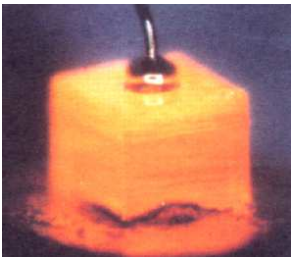

Fig. 2.4: Amber coloured LED chip with about 0.25 mm length of each side [Schubert, 2006].

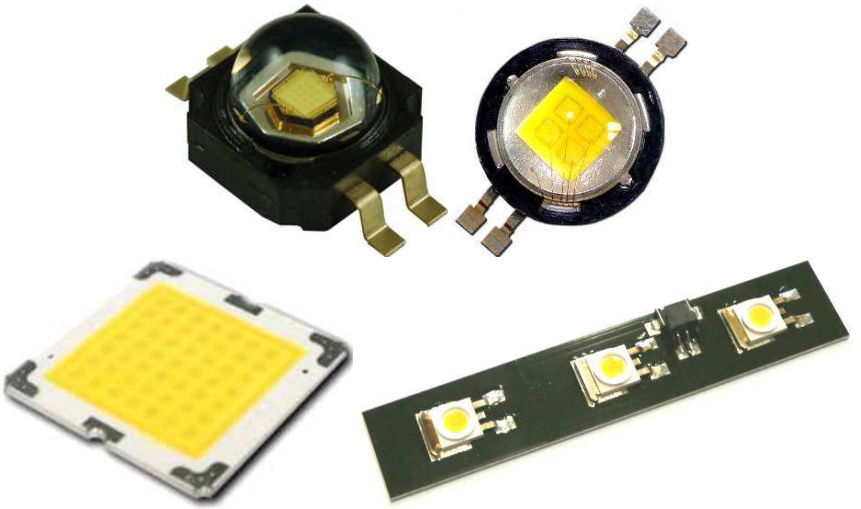

Fig. 2.5: single-die package (top left), multi-die package (four dies, top right), COB (49 dies, bottom left) en POB array (bottom right) [Edison, 2007] [Lumileds, 2007] [SSC, 2008].

On the level of the integrated chip (package or board) LED devices are divided into different types according to their luminous flux and power consumption. Low-power LEDs typically consume less than one watt, while high-power diodes have an input power of one watt or above. Devices with a flux between 50 and 250 lm are called high-brightness LEDs. The denomination “ultra-high-brightness” has been created for light outputs above 250 lm [Mottier, 2009]. Note however that the input power and luminous flux of a final application can be remarkably different from the values suggested by the categorical names of the package(s) or board(s) within.

The next two steps in the production process of a lighting application with LEDs are the LED module and LED engine (see Figs. 2.3 and 2.6), and this for both the COB and POB technology. A LED module consists of a board with chips or packages mounted on a heat sink and provided with secondary optics (e.g. a reflector or lens) [Navigant, 2009]. If necessary, the board is equipped with electronic components and wiring as well. In a next step, a LED engine is created by adding a driver to the module. The engine can hence be considered a rough version of the final lighting product that can already be attached to the power grid.

Fig. 2.6: LED module (left) en LED engine (right) [Philips, 2009].

Starting from the LED engine, again two methods are applied to obtain a LED luminaire. The engine can be designed in such a way that a LED lamp with standard fitting emerges. This lamp can be easily implemented in an existing luminaire (see Fig. 2.7). Another option that is employed more often for the current LED technology is the construction of a complete luminaire from a LED engine directly (see Figs. 2.3 and 2.7). A major drawback of this approach is that in case of catastrophic light source failure the entire luminaire has to be replaced.

Fig. 2.7: LED luminaire starting from a LED engine (left), LED lamp (centre) and existing luminaire that can be used for operation of a LED lamp (right) [Elation, 2006] [Sunview, 2008].

The discussion above shows that the current confusion regarding the nomenclature of LED devices is not very surprising. Moreover, the distinction between different parts or steps in de production process is sometimes fuzzy, even for diode and application manufacturers. These manufacturers therefore also tend to divide the SSL production process into different levels, ranging from level zero for the compound semiconductor wafer to level three representing the final LED lighting system [Mottier, 2009].

2.4. Brief light-emitting diode design history

In 2007, while this doctoral research was in full development, the centennial anniversary of the LED has been celebrated worldwide. Henry Joseph Round, a British electrical engineer, had reported a “curious phenomenon” exactly hundred years earlier [Round, 1907]. This phenomenon appeared to be the first observation

of electroluminescence from a SiC (silicon-carbide or carborundum) light-emitting diode. Until the 1940s, various crystalline materials were observed to exhibit the same rectifying behaviour when a sharp metal point contact was applied to the surface, but the rectification was unstable, not reproducible, and hardly understood [Dupuis, 2008].

The first accidental discovery of the semiconductor p-n junction was made in a silicon crystal by Russell Ohl while working at Bell Labs (Holmdel, NJ, USA) on February 23, 1940 [Riordan, 1997]. However, the fundamental understanding of the operation of this device was limited until 1947 when Bardeen and Brattain invented the transistor (also at Bell Labs) and Bardeen first described the process of minority-carrier injection [Bardeen, 1949]. Immediately afterwards, William Shockley published his theoretical analysis of the p-n junction [Shockley, 1949]. This new understanding of semiconductor diode operation initiated the development of the first commercial infrared LEDs in 1950 [Schubert, 2006]. Technologies regarding material growth and device design and fabrication were further developed in the subsequent decade [Dupuis, 2008].

The key to the advancement towards visible LEDs was the creation of direct band gap III-V alloy semiconductors from the 1960s onwards [Dupuis, 2008]. New techniques for growing and combining thin films of compound semiconductors were developed, leading to the invention of the first LED based on a GaAsP (gallium-arsenic-phosphide) semiconductor by Holonyak and Bevacqua in 1962 [Holonyak, 1962]. This device emitted red light with a luminous efficacy of approximately 0.1 lm/W [Yam, 2005]. Fig. 2.8 shows the advance of (commercial) visible LEDs' luminous efficacy values ever since.

For the first time in 1968, red GaAsP diodes were fabricated in large numbers for commercial purposes. This technological milestone was followed by a rapid progress in LED performance which can mainly be attributed to the improvement of semiconductor alloys and their growth technique, as well as the use of novel chip structures resulting in higher external quantum efficiencies [Yam, 2005] [Mottier, 2009]. By 1985, the LED luminous efficacy had increased by almost a factor hundred, up to around 10 lm/W. The additional development of AlGaInP compound semiconductors in 1992 caused the efficacy to surpass typical incandescent lamp values [Schubert, 2006] (see Fig. 2.8). Since 1993, the performance of red and orange commercial diodes has been gradually increasing [Bürmen, 2008].

At the end of the 1980s, due to the rising use of red LEDs in various applications, the lighting world was vastly looking forward to the emergence of green and blue emitters. Such devices would finally allow creating solid-state white light (see section 2.2.2). The waiting did not take long anymore. In 1990, Amano and Akasaki demonstrated stimulated emission from GaN (gallium-nitride) films grown on sapphire, establishing that this approach could be used for LEDs as well [Amano, 1990]. Shortly thereafter, Shuji Nakamura, who was working at Nichia Corporation (Japan), constructed a GaN blue LED for the first time [Nakamura, 1991]. In the next few years, workers at Nichia and other labs, notably Cree

Research Inc. (USA), Osram (Germany), Hewlett-Packard Optoelectronics (now Philips Lumileds Lighting Co., USA), and Toyoda Gosei (Japan), developed high-volume production systems for the growth of high-performance blue and green LEDs [Dupuis, 2008]. Blue InGaN diodes are used to create phosphor-white LEDs since 1996 [Schubert, 2006].

Benefiting from the preceding technology learning process of red LEDs, InGaN green and blue emitters have developed very quickly since 1994 (see Fig. 2.8). After just about four years, high-power AlGaInP and InGaN devices were already successfully combined in public traffic lights. Finally, by 2002, the commercial fabrication of phosphor-white high-power LEDs for general lighting was no longer fiction [Schubert, 2006] [Mottier, 2009].

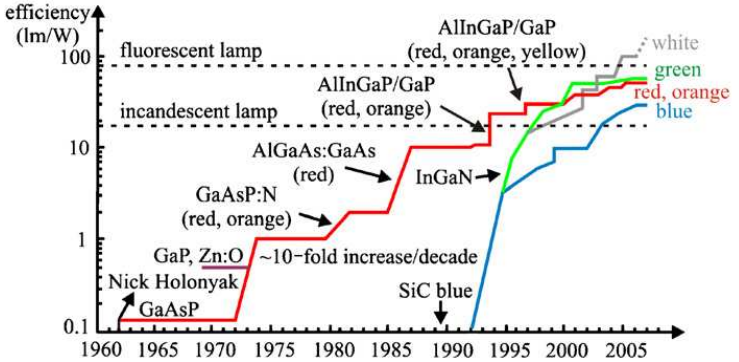

Fig. 2.8: Development of (commercial) LEDs in terms of luminous efficacy over the last 50 years. Typical incandescent and fluorescent lamp efficacies have been added for comparison [Bürmen, 2008].

Although this has not been explicitly mentioned in the brief history above, LED package design improvements have been of key importance for the technological growth of solid-state lighting as well. Especially the packages' thermal conductivity has been considered throughout the past decades. Indeed, the heat generated within the LED chip during diode operation needs to be optimally extracted in order to keep the junction temperature as low as possible (see chapter 8). This can be achieved by reducing the thermal resistance of the package as much as possible. Fig. 2.9 shows that subsequent packaging improvements resulted in a thermal resistance decrease from about 250 K/W forty years ago to only a few K/W nowadays [Jayasinghe, 2006] [Schubert, 2006]. The use of surface-mount devices with heat sink slug and their mounting on a PCB with metal core are the main causes for the present low thermal resistance values.

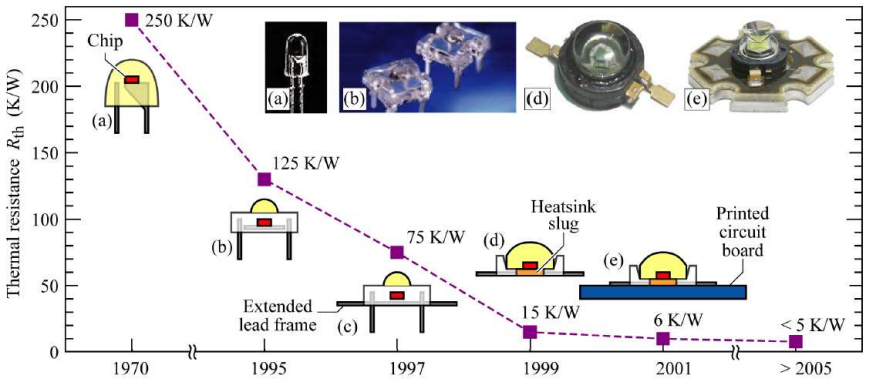

Fig. 2.9: Evolution of the thermal resistance of LED packages over the last 40 years [Schubert, 2006]: (a) low-power TH package, (b) low-power TH package with low-profile, (c) low-profile package with extended lead frame, (d) SMD package with heat sink slug, and (e) SMD package mounted on a PCB with metal core.

2.5. Present LED technology

2.5.1. Technology status

During the past decade, a large number of improvements have been made on the high-power light-emitting diode technology. Although packaging, secondary optics, and driver electronics have a significant effect as well, the major efficiency breakthroughs have been obtained on the diode chip. Without going in detail, the most important steps forward can be summarized as follows: a better control of semiconductor layer deposition (see section 2.5.2) and treatment, an enhanced current injection and current spreading, changes in die shape and surface texture that allow for a higher photon extraction rate, and the use of transparent substrates or mirror layers for supplementary extraction of back-scattered photons [Schubert, 2006] [Krames, 2007] [Mottier, 2009]. All related research efforts would certainly not have taken place if LEDs did not have some considerable benefits with respect to the classical light source technologies. These advantages are listed below [Schubert, 2006] [Navigant, 2009]:

- Extended lifetime.
- Very saturated colours that allow for efficient colour applications.
- Quasi point source with hemispherical light output. This is especially favourable for the design of secondary optics.
- Large luminaire design flexibility with small electrical components.
- Vibration proof source. In particular vehicles, mobile appliances, and machines require such devices.
- Complete encapsulation allows applications under water or in very dusty environments.

- Low-voltage operation.
- Only few harmful materials are involved.
- Absence of unwanted (infrared or ultraviolet) radiation.
- Immediate switching (see chapter 3).
- Easy dimming through DC diminution, pulse-width modulation, or alternative methods.
- Improved performance in low temperature environments, e.g. fridges or freezers. Note however that this benefit becomes a drawback during high temperature operation (see chapters 5, 6, and 8).

Yet no technology has ever been found to be perfect, and even LEDs cannot escape this fate. Disadvantages of this type of solid-state lighting are the following [Schubert, 2006] [Bürmen, 2008] [Navigant, 2009]:

- Substantial forward current and junction temperature dependence of the light output.
- Hard to predict performance changes over life.
- Binning necessity due to difficult device reproduction (see section 2.5.2).
- Low flux per package and moderate overall system efficiency (see chapter 8).
- Relevant spatial spectral shifts or colour variations for phosphor-white devices.
- Difficult or no replacement of individual packages within a luminaire.
- International lack of related standards.
- High source prices due to the use of rare materials and manufacturing complexity (see next sections).

2.5.2. Manufacturing and binning

Compound semiconductor crystals are manufactured by epitaxial growth on wafers. Epitaxy is the deposition of a layer of one substance on a single crystal of another, such that the crystal structure in the layer is the same as that in the substrate [Daintith, 2009]. When all layers for obtaining a diode have been grown, the wafer is cut to chips that can be mounted on circuit boards or incorporated into LED packages (see section 2.3). The top surface of power dies roughly sizes one square millimetre. For most diode chips, the substrate is removed before integration.

The two main complications regarding large-scale LED chip production for commercial purposes are the critically small substance amounts involved and the occurrence of defects and constraints due to heteroepitaxy, i.e. epitaxy of semiconductor alloys with a different lattice structure. Examples of the latter are dislocations, disorientation of the substrate, and epitaxial and thermal stress [Mottier, 2009]. Light-emitting diode manufacturers therefore have large difficulties in fabricating great numbers of devices with equal specifications. As a consequence,

each component distribution at the end of a production line has to be systematically subdivided into smaller groups with similar performance parameters. This process is called binning and requires an evaluation of each device through a pulsed measurement. Manufacturers in general apply three binning parameters, being the diode's forward voltage, colour, and luminous flux [Bardsley, 2009] [Perkins, 2009].

The obligatory binning measurement of individual diodes and limited availability of specific performances are two of the main reasons for the high unit price of LEDs nowadays. Luminaire manufacturers are therefore suggested to prioritize on just one instead of all three performance criteria [Perkins, 2009]. The last option may lead to a binning yield of only one out of ten devices (see Fig. 2.10).

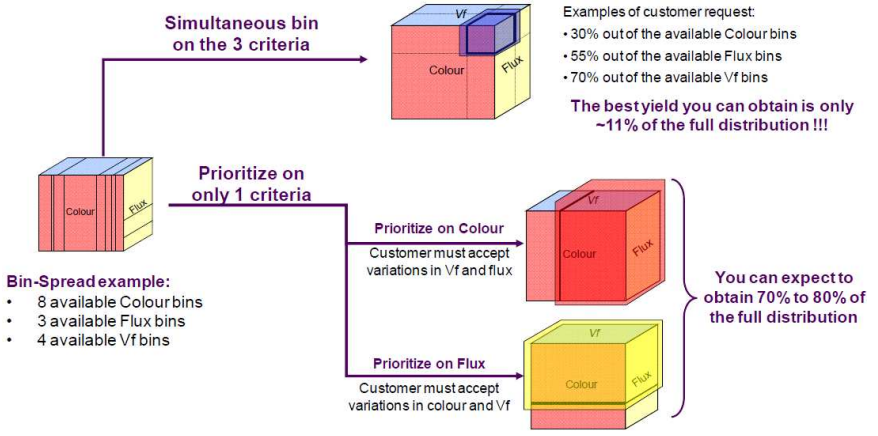

Fig. 2.10: Binning yield losses for LEDs. Prioritizing on only one instead of three criteria strongly increases device availability and hence reduces the product price [Perkins, 2009].

2.5.3. Market status and trends

Technological improvements are always a result of the quest for making our existence more comfortable. These improvements are generally translated into cost reductions and increases of devices' ease-of-use [Tsao, 2002]. Examples of the latter are an extended lifetime and other issues mentioned in the list of SSL advantages in section 2.5.1. Despite their high initial cost, LED sources have the potential to attain lighting cost reductions as well. Fig. 2.11 shows that, if the total cost of ownership (TCO) for illumination is taken into account, LED luminaires are expected to be sufficiently cost-effective to roughly follow the TCO diminution tendency of the last 200 years.

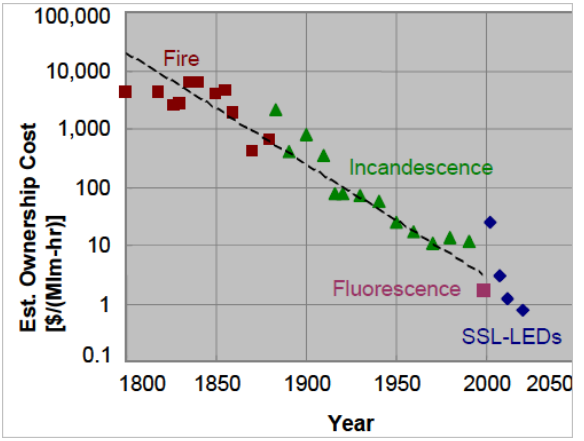

Fig. 2.11: Estimated total cost of ownership (in dollars per megalumen-hour) for illumination based on fire, incandescence, fluorescent lamps, and high-power LEDs [Tsao, 2002].

For future cost reduction of LED lighting, above all the initial device price needs to be decreased. As charges for secondary optics and assembly are relatively small and rather stable, thermal solutions and package manufacturing costs will have to make the biggest price difference with reductions of about 50 % and 80 % respectively by 2015 [Bardsley, 2009].

Based on market data of the past forty years, Haitz's law provides a good view on the diode cost drop off that has been achieved so far (see Fig. 2.12). This law indicates that the LED lighting cost (in dollar per lumen) decreases by about a factor ten per decade, while the light output per package (in lumen) increases by about a factor twenty during the same period [Haitz, 1999]. Although both quantities are expected to asymptotically evolve towards an extreme value in the future, Haitz's law demonstrates that the expected cost reductions might indeed be achieved [Navigant, 2009].

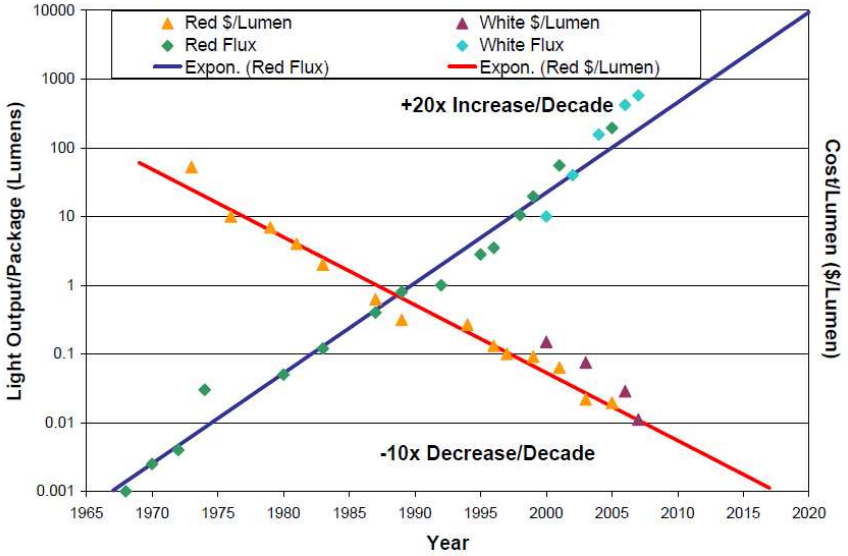

Fig. 2.12: Illustration of Haitz's law which indicates that the light output per LED package increases by about a factor twenty per decade, while the cost per lumen decreases by about a factor ten during the same period [Haitz, 1999] [Navigant, 2009].

The worldwide LED market share amounted about 1.8 billion dollars by the end of 2002, spread over several applications as indicated in Fig. 2.13 [Pelka, 2003]. Mobile appliances, signs, and the automotive sector clearly made up the biggest sales. Although all absolute numbers had been more or less doubled seven years later, the use of LEDs for illumination applications had increased to about 10 % of the total SSL market during the same period [Mottier, 2009]. This increase is expected to be continued and additionally justifies this work on the integration of high-power LEDs in general lighting. By now, the LED market share has surpassed the 10 billion dollar barrier. Some even predict that the 20 billion dollar barrier will be exceeded by the end of 2013 already [Mottier, 2009].

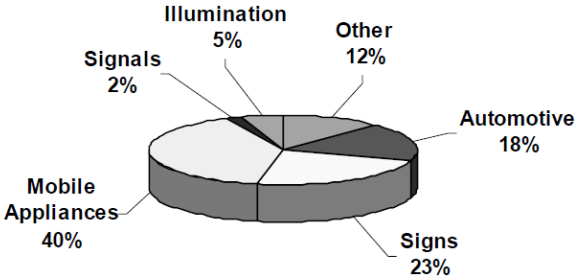

Fig. 2.13: Applications for high-power LEDs by the end of 2002. Others include for example fixed displays, decorative lighting, and medical applications [Pelka, 2003].

2.6. Summary and conclusions

Incandescence, gas-discharge, and solid-state are the three major technologies that constitute the electrical Lighting family nowadays. Solid-state light sources, based on a process called electroluminescence, are now mainly used for indicative, decorative and signal lighting, but LED technology is developing quickly and may be considered a proper alternative for several general lighting applications as well. Emission colours can be varied by changing the semiconductor alloy or through band gap engineering. Phosphor-white diodes are particularly suited for high colour rendering purposes, but RGB combinations of single-colour chips have the important benefit of allowing dynamic colour control.

Due to the large number of components involved, the nomenclature of LED devices has been clarified. Additionally, the diode design history has been briefly sketched, starting from the first observation of electroluminescence by Henry Round in 1907. The key to the advancement towards visible LEDs was the creation of direct band gap semiconductor alloys from the 1960s onwards. For the first time in 1968, red diodes were fabricated in large numbers for commercial purposes. Shuji Nakamura constructed the earliest blue LED in 1991. By 2002, the fabrication of phosphor-white high-power LEDs for general lighting was no longer fiction. Packaging improvements resulted in a thermal resistance decrease from about 250 K/W forty years ago to only a few K/W nowadays.

Benefits and drawbacks of the present LED technology have been considered. Due to the epitaxial growth complexity of compound semiconductors, binning measurements of individual diodes at the end of production lines are necessary. Also the limited availability of specific performances results in high unit prices of LEDs nowadays. The total LED market share amounted about 1.8 billion dollars by the end of 2002, with a 5 % contribution for illumination. By now, the LED market share has surpassed the 10 billion dollar barrier, with a more than 10 % use for general lighting. Some predict that the 20 billion dollar barrier will be exceeded by the end of 2013 already.

3. Modus operandi

3.1. Goals

This chapter has the intention to provide the reader with an outlook on the research approaches that have been used to work towards the integration of high-power light-emitting diodes in general lighting applications. This research implies providing manufacturers and product designers with models that allow estimating LED performance in practical lighting applications. The gray-box modelling approach is described by comparison with other modelling and simulation techniques. The work on recommendations for best practice and an extended technology evaluation resulting from the modelling efforts is explained.

All measurement equipment setups are described in detail. Next to commercial voltage and power source-measure systems, a custom-made integrating sphere and two custom-made goniophotometer setups have been used. Part of the research described herein has been performed with a commercial ambient-temperature controlled integrating sphere, which had been made available at the NIST.

For the custom-made integrating sphere, the most was made of the typical hemispherical radiation of high-power LEDs to increase the accuracy of the flux determination. Recently developed measurement techniques such as the use of an external spectral irradiance standard and an optimised spectral irradiance detection head are combined with a very particular port geometry and a minimized baffle area. This results in a uniform spatial response distribution function (SRDF), which guarantees an accurate radiant and luminous flux determination, irrespective of the spatial intensity distribution of the LED package or luminaire. The effect of the directional response of the detector head on the SRDF is explored. Measurements on LED devices with and without external optics are presented, illustrating the possibilities of the measurement setup.

3.2. Integration approach

3.2.1. Gray-box modelling

Estimating LED technology performance in general lighting applications can be translated into simulation of its user-relevant characteristics. Not taking into account mechanical design aspects, the typical user-relevant characteristics of all lighting sources are (see also Fig. 3.1):

- Light colour and its possible variation with direction of view. Colour is fully determined by the spectrum of the source, which is also related to correlated colour temperature (CCT) and colour rendering index (CRI) [CIE, 1987] [Wyszecki, 2000].
- Total visible light output or luminous flux. For efficiency calculations also the radiant flux is considered.
- Spatial intensity distribution, radiation pattern or emission homogeneity.
- Power consumption or efficiency.
- Lifetime of the source. For LEDs this lifetime is typically indicated by the B50-L70 lumen depreciation [Bullough, 2005]. This means that lifetime has been defined as "the length of time it takes for 50 out of 100 devices (B50), when operated at a specified temperature, to reach 70 % of their initial light output (L70), i.e. close to the threshold at which the human eye can detect a reduction. Moreover, the source or system should not fall outside a four-step MacAdam ellipse (thought to be detectable by well over 99 % of the population) containing the initial colour coordinates (L4M) [MacAdam, 1942]. Where lights are seen side-by-side, as in wall-washing applications, the useful life should be calculated on a higher figure of lumen maintenance, typically 80 % (L80)." Very recently, a proposal has been made to include an additional F10 lifetime definition, corresponding to 10 % complete failures [DOE, 2010].
- Switching time, or the time it takes to reach 90 % of the maximum light output after switch-on.
- Product price. For fair comparison, typically the total cost of ownership (TCO) or price per lumen-hour has to be taken into account.

The radiation pattern of LEDs has already been intensively studied and modelled by Moreno *et al.* and has therefore been omitted in this work [Moreno, 2006] [Chien, 2007] [Moreno, 2008]. Lifetime, switching time, and pricing have not been included either. Switching time is of the order of nanoseconds for LEDs [Hino, 1979] [Ronchi, 2008] and therefore generally an irrelevant issue for end-users. Finally, pricing is considered a commercial topic that did not suit very well within the scientific modelling and simulation approach described herein.

Simulation corresponds to predicting the user-relevant characteristics as a function of various input variables. For light-emitting diodes and their applications, these variables are the forward current, the junction temperature, the direction of view, and time (see Fig. 3.1). Note however that in practical applications the diode's junction temperature is not an independent variable, but changes with both current and ambient temperature. This additional complication is handled in chapter 5. As lifetime and switching time are not examined, time has been excluded as input variable as well.

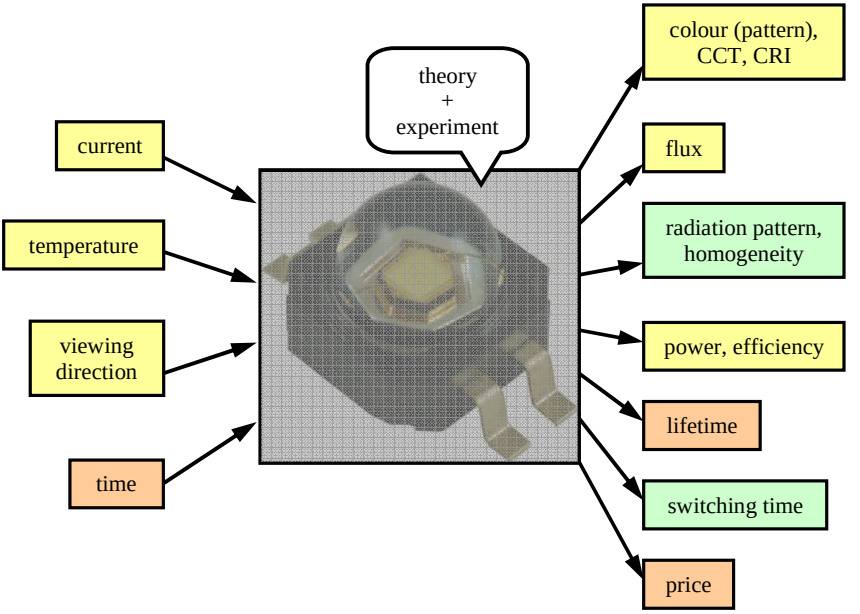

Fig. 3.1: Schematic representation of input variables and user-relevant output characteristics for light-emitting diodes, connected by a gray-box modelling approach. Quantities that have been taken into account are marked with a yellow background. Others that don't need modelling (anymore) or that have been omitted are marked in green and orange, respectively. The centre picture shows a Lumileds K2 LED package [Lumileds, 2007].

Predicting the selected user-relevant LED characteristics as a function of the related input variables requires a suitable modelling approach. One has to take into account here that from the most fundamental point of view, a LED device consists of an initial electron flow that is partially converted into a flux of photons. For systems incorporating any sort of flow, typically three modelling and simulation approaches (or levels) can be employed: micro-level approach by use of finite-element methods, component level approach with ideal resistive, capacitive, and inductive components, and macro-level with black-box approach. Benefits and drawbacks of each approach are summarized in Table 3.1 [García, 2001] [Rencz, 2004] [Baureis, 2005] [Salsbury, 2007] [Hui, 2009] [Liu, 2009-1].

Table 3.1: Overview of flow simulation levels and methods, together with their benefits and drawbacks.

Level	Method	Benefits	Drawbacks
Micro-level	Finite element methods	– Lots of information – Detailed design analysis – Modelling of realistic 3D geometries – Heterogeneous simulations are possible	– Slow – Very device specific – Device structure has to be known – No inclusion of conversions or unknown effects
Component level	Circuits of ideal resistive, capacitive, and inductive components	– Behaviour of components is known – Rough design analysis – Faster than micro-level	– No inclusion of unknown effects – Device structure has to be known – Simplification of real 3D geometries
Macro-level	Black-box approach	– Number and nature of parameters and equations can be adopted – Simplified and fast use – Device structure doesn't need to be known	– Start from measurements only – No design analysis possible – Influence of 3D geometry unknown

Regarding the prospect of providing manufacturers and product designers with models that allow estimating LED performance in practical lighting applications, a generalized simulation approach on the macro-level appears to be the best option. During model construction in this work however, physics-based considerations are taken into account as much as possible. Modelling is thus started from both theory and experiments in order to obtain more accurate and comprehensible results. Additionally, a more profound model validation and a certain degree of design analysis can be achieved. Such a semi-empirical black-box approach is also referred to as gray-box modelling (see Fig 3.1) and is most used for characterizing solid-state lighting performance in literature as discussed further on.

Next to a simulation methodology, also the nature of the simulation model has to be chosen. For flow simulations, a dynamic model using (partial) differential equations or a steady-state model using absolute equations can be utilized. As product designers and end-users are in general only interested in steady-state light source performance, the latter will be brought into play in this work.

3.2.2. Technology evaluation

Integration of high-power LEDs in general lighting includes an extended technology evaluation as well. Using the gray-box modelling approach, measurement results that have been used for model construction can indeed also be utilized for this kind of evaluation. The LED technology evaluation focuses on three major aspects:

- Due to the lack of related standards, the trustworthiness of datasheet information is often doubtful. In a first part of the evaluation, binning by manufacturers at pulsed operation (see chapter 2) is hence verified. The relevance of this binning for diode operation in practice is discussed immediately afterwards.
- An extended efficiency evaluation is performed. This part is subdivided in a study of power loss mechanisms in solid-state lighting applications and a LED efficiency comparison on five different levels. These levels are RGB versus phosphor-white technology efficiency, dependence of efficiency on correlated colour temperature for phosphor-white emitters, efficiency dissimilarities between manufacturers, single-die versus multi-die component efficiency, and comparison of efficiency values obtained for LED lamps and engines in practice.
- The evaluation is completed with a proposal for a light-emitting diode quality scale. This scale is constructed from modelling parameters that are found to be closely related to the diode quality. Comparing such parameters for different LEDs allows making a technology ranking according to the lighting designer's or end-user's needs.

3.2.3. Best practice

All modelling and evaluation work would be useless if not applicable by those it is meant for. Therefore, at the end of each chapter (4 to 8) a method for measurement and simulation or evaluation in practice is proposed. These practical methods usually consist of a description of minimum model reconstruction, simulation and evaluation efforts or guidelines for optimal device performance achievements.

3.3. LED selection

Table A.1 in Appendix 1 contains an overview of all light-emitting diode packages that have been selected for investigation: 92 devices from twelve different manufacturers in total. For each measurable circuit, the following information is shown:

- The first three columns of Table A.1 contain the manufacturer, production year, and part number, respectively. The part number is used for placing orders and datasheet consultation, but its construction is fully determined by the manufacturer. No (inter)national regulations on the structure of these part numbers exists. Therefore, from each part number a four-character code for internal use has been created. These codes have been collected in the fourth column. If more than one LED of the same type has been examined, a number is added to the internal code, separated by an indent.

- The number of semiconductor chips or dies is given in column five. For circuits with more than one die, the number of dies is given by a product of the number of parallel connections and the number of chips per parallel string. Dies marked by an asterisk are low-power emitters which have been combined to create a high-power package.
- The sixth column of Table A.1 shows the typical input power for each device. As only high-power LEDs are considered, this value always exceeds one watt.
- The "colour" column (number seven) is somewhat different for single-colour and phosphor-white LEDs. For single-colour circuits the spectrum's peak wavelength at about 300 K junction temperature is given, while for phosphor-white diodes the CCT (correlated colour-temperature) is shown. This CCT equals the temperature of the Planckian radiator whose perceived colour most closely resembles that of a given stimulus at the same brightness and under specified viewing conditions [CIE, 1987].
- The measurements that have been performed on the selected LEDs are indicated in columns eight to twelve with a gray background. The columns with title "I-$U_f(T)$" and "$R_S(T)$" denote current-voltage characteristic measurements at different temperatures and the internal series resistance measurements described in chapter 4, respectively.
- The column with title "sphere" has a gray background for those LED devices that have been measured with an integrating sphere. Numbers have been added to indicate the number and type of integrating sphere measurements that have been performed. A single number one means that spectral radiant flux has been measured at one constant forward current and junction temperature only. For devices with a product of two numbers in this column, the first number indicates the number of measurements series at constant current, the second digit is the number of sphere measurements at constant junction temperature. When a third digit is added, this represents the number of ambient temperatures for which spectral radiant flux measurements have been executed. Three digits only appear for measurements that have been performed at the National Institute of Standards and Technology. These measurements are described in section 3.7.
- LED packages that have been used for the construction and validation of a current-temperature relation (see chapter 5) are marked in column eleven entitled "$T(I)$".
- Finally, the last column of Table A.1 indicates the devices that have been used for spatial colour distribution measurements (see chapter 7). Although not indicated, only LEDs incorporating a proximate or remote planar phosphor have been considered for colour pattern modelling afterwards.

For the technology evaluation in chapter 8, a number of ready-to-use LED lamps and engines have been examined as well. Table A.2 in Appendix 1 gives an overview of this selection of ten devices from six different manufacturers. For these LED applications only one steady-state goniometer or integrating sphere measurement for efficiency evaluation has been performed. The columns with indication of measurement types are therefore not present. As rather irrelevant and sometimes even unknown, the number of dies is not mentioned either.

A picture of all devices that have been selected for investigation is added in Appendix 2.

3.4. Voltage and power measurements

Forward current-voltage characteristics at constant junction temperature have been determined with a Keithley 2440 5A SourceMeter used in a four-wire set-up and controlled by a LabVIEW 7.1 program. In order to minimize junction heating, millisecond current pulses have been applied. Successive voltage measurements and pulse registration with a Tektronix TDS 210 digital real-time oscilloscope showed that the junction temperature increase during these pulses can indeed be neglected.

Current-voltage characteristics at different temperatures and resulting voltage-temperature calibration curves (see chapter 4) could be constructed by performing pulsed forward voltage measurements in a Heraeus UT6 isothermal oven with active air circulation. The predefined oven temperatures have been precisely measured with a Pt100 thermistor, four-wire connected with a Keithley 2510 TEC SourceMeter. Ambient temperatures have been selected within a range of typical light-emitting diode operation temperatures, i.e. about 300 to 400 K. For each setting, at least twenty minutes delay between the set-temperature and the measurement was respected in order to assure thermal equilibrium between the air in the oven and each diode junction. Thermal equilibrium has been checked by measuring the forward voltage at a small and constant drive current (1 mA) each two minutes.

LED devices under test have also been placed on commercially available heat sinks in a 295 K constant ambient. The Keithley 2440 5A SourceMeter has then been used to apply 150, 250, 350, and 450 mA constant forward currents. When thermal equilibrium was reached (typically after about thirty minutes), corresponding junction temperature and power values have been determined from the voltage-temperature calibration curves.

For power supply and measurement of LED lamps and engines with a typical 50 Hz sinusoidal input of 230 V (RMS), an Agilent 6813B Voltage Source and a Voltech PM1000 Power Analyser have been used, respectively. In order to correspond to practical use, these devices have always been measured during steady-state operation (at least 30 minutes after switch-on) while mounted on their respective

heat sinks. Diode junction temperatures could not be precisely determined as a result, but are estimated to amount between 330 and 400 K.

3.5. Spectral radiant flux measurements

3.5.1. Situation

Integrating spheres are widely used for determining optical characteristics of materials and light sources [Yu, 2006]. When measuring radiant or luminous flux two basic methods can be used, i.e. spatial resolved measurements using a goniometer or spatial integrated measurements using an integrating sphere. Spatial resolved measurements include luminous intensity distribution and suitable software integration. This method requires a complicated measurement facility and is rather time-consuming, but knowledge of the luminous intensity distribution pattern can be advantageous. The measurements can be performed photometrically using an illuminance meter as a detector or spectral radiometric data can be recorded [Shaw, 2008].

Traditional integrating sphere photometry is based on the substitution method in which a test lamp is measured in comparison with a standard lamp [CIE, 1989]. Test and standard lamps are subsequently brought into a sphere coated inside with a white Lambertian non-fluorescent paint, and the illuminance at the sphere wall is measured with a photometer. The light sources are shielded from the photometer with a baffle to avoid direct illumination. Integrating sphere measurements suffer from low accuracy, if spectral characteristics and angular intensity distributions of test source and reference source are dissimilar. Consequently, test lamps should only be measured against standard lamps of the same or similar types, as recommended in standard practices [CIE, 1989] [IES,1993]. Yet, integrating sphere measurements are rather easy and fast and can be used in the spectral resolved mode by replacing the photometric detector by a spectroradiometer. Sometimes, partial flux measurements are used in a manufacturing environment to speed up the measurements [CIE, 2007]. Other approaches with multiple detectors are possible [Szylowski, 2006].

In this work, the most was made of the typical hemispherical radiation of power LEDs to increase the accuracy of flux determination using an integrating sphere. The LEDs are mounted on the inner sphere wall. Recently developed measurement techniques are combined with a specific port geometry and with a minimum baffle area, showing a very uniform spatial response distribution function [Ohno, 1999]. Furthermore, the effect of the directional response of the detector head on the SRDF has been investigated.

3.5.2. Integrating sphere theory

Consider a sphere with radius R. The spectral radiance of a differential source area dA_{src} at a particular location on the sphere characterized by spherical coordinates (θ,φ) and in a particular viewing direction $(\alpha_{src},\beta_{src})$ is called $L_{e,\lambda}(\theta,\varphi,\alpha_{src},\beta_{src})$. This spectral radiance generates a differential spectral irradiance $dE_{e,\lambda}$ at the receiver position on the sphere wall. From the basic relationship between spectral radiance and irradiance, the spectral irradiance at the receiver, located anywhere on the sphere wall is given by:

$$dE_{e,\lambda}(\text{receiver}) = \frac{L_{e,\lambda}(\theta,\varphi,\alpha_{src},\beta_{src})\,dA_{src}}{4R^2} \tag{3.1}$$

The sphere wall itself is not the primary light source. The radiance of the wall is due to reflection of the direct irradiation from a light source inside or outside the sphere and from other parts of the sphere wall. If the spectral radiance of the sphere wall is Lambertian, the spectral radiance $L_{e,\lambda}$ becomes proportional to the local spectral irradiance at the sphere wall $E_{e,\lambda}(\theta,\varphi)$ and independent of the viewing direction:

$$L_{e,\lambda}(\theta,\varphi,\alpha_{src},\beta_{src}) = \frac{\rho}{\pi}E_{e,\lambda}(\theta,\varphi) \tag{3.2}$$

with ρ the spectral reflectance of the sphere wall for diffuse illumination and viewing geometry. Substitution of Eq. (3.2) into Eq. (3.1) gives:

$$dE_{e,\lambda}(\text{receiver}) = \frac{\rho E_{e,\lambda}(\theta,\varphi)\,dA_{src}}{4\pi R^2} \tag{3.3}$$

For a uniform sphere reflectance, integration over the sphere wall results in:

$$E_{e,\lambda}(\text{receiver}) = \frac{\rho}{4\pi R^2}\iint_{\text{sphere wall}} E_{e,\lambda}(\theta,\varphi)\,dA_{src} \tag{3.4}$$

The integral represents the spectral radiant flux incident on the sphere wall. If the spectral radiant flux hitting the sphere wall directly (with exception of the receiver area) is denoted as $\Phi_{e,\lambda}$, Eq. (3.4) can be written as:

$$E_{e,\lambda}(\text{receiver}) = \frac{\rho}{4\pi R^2}\frac{1}{1-\rho}\Phi_{e,\lambda} \tag{3.5}$$

The factor $1-\rho$ appearing in the denominator expresses the subsequent reflections on the sphere wall generating additional contributions to the incident flux. That is why the value of ρ must be considered as the mean reflectance of the sphere wall for a diffuse irradiation geometry, taking into account the presence of the detector area and the open ports.

The irradiance at the receiver is proportional to the incident flux, irrespective of its spatial distribution. This characteristic of the spherical geometry offers the clue for measuring the total flux of a light source. An additional measurement with a calibrated light source eliminates the proportionality factor.

According to Eq. (3.4) and Eq. (3.5), the detector response should be the same if the same flux is introduced in the sphere, irrespective of the location of the direct impact on the sphere wall. This can be tested by using a narrow beam source, such as a laser diode, as a light source. For each orientation of the beam, the same response should be recorded. The relative responsivity as a function of the location (θ,φ) of the beam incident on the sphere wall is called the spatial response distribution function (SRDF) [Ohno, 1998]. In the ideal case, this SRDF is constant.

Eq. (3.5) can be reformulated with photometric quantities instead of spectral radiometric quantities if the mean reflectance is spectrally neutral.

3.5.3. Error sources

The receiver does not only detect the flux originating from the sphere wall, but will normally also respond to the direct radiation coming from the source. This contribution is not taken into account when calculating Eq. (3.5). One can exclude this contribution by placing a baffle between the light source and the receiver. However, this offers a few major problems. The field of view of the detector will not be the complete sphere surface anymore, because of the shielding effect of the baffle. Only the radiance of the sphere wall within the detector field of view and the radiance from the baffle surface faced to the receiver will contribute. The flux hitting the region shadowed by the baffle must undergo at least one additional reflectance before it can contribute to the detector signal. Furthermore, part of the flux of the source hits the face of the baffle oriented to the source, and not the sphere wall. For this flux, again at least a second reflection is needed before it can contribute to the sphere wall radiance, resulting in a decrease of the SRDF for these regions. Since the amount of flux directly hitting the baffle or the shadowed sphere wall is depending on the spatial distribution of the source, the response becomes sensitive to the spatial distribution pattern and yet the mounting position of the source and the baffle. The effects of a baffle on the SRDF and on measurements of light sources with different spatial distribution curves have been simulated extensively [Ohno, 2001].

For centrally mounted hemispherical radiating LEDs, one could argue that by orienting the LED in such a way that direct irradiance of the detector is avoided, a

baffle can be omitted. However, even the printed circuit board of the LED will act as a baffle. Furthermore, for power LEDs extensive heat sinks are required implying large sphere diameters if the LEDs are mounted inside the sphere [Liu, 2008-1].

By placing the baffle very close to the source, the baffle will capture more of the initial flux but the shielded region of the sphere wall within the field of view (FOV) of the detector will be low. Placing the baffle close to the detector will have the opposite effect. Furthermore, in this situation the baffle acts as a mirror enhancing the responsivity of the regions near to the detector. A distance between the baffle and the detector lying between 1/2 and 1/3 of the sphere radius seems to be the best choice [Ohno, 2001].

By applying the substitution method with a test source and reference source having almost the same dimensional and spatial characteristics, baffle effects can be neutralized. If reference and test source are not similar, serious errors will be observed. The variety of luminous and especially spectral radiant flux standards is rather limited. Tungsten lamps are very reliable and widely available, but the spatial and spectral characteristics of tungsten sources can be totally different from LEDs, compromising the accuracy. Until now, LED reference sources are not yet widely available.

The detector head measuring the irradiance or illuminance must be aligned with the sphere wall and must have an ideal cosine response and full hemispherical field of view. Deviation of this requirement is an important error source as explained in literature [Ohno, 2001] and confirmed experimentally (see below). The effect is in fact very analogous to the effect of a baffle resulting in a limited FOV of the detector.

The light source or luminaire mounted into the sphere can also act as an object obstructing and partially absorbing the radiation. Especially luminaries can trap a lot of light which will not reach the sphere wall. These absorption effects have been studied in literature as well [Liu, 2008-1] [Miller, 2001].

The replacement of the test source by the reference source does in fact change the mean reflectance of the sphere, the geometry and the self absorption. This substitution error can be avoided using an auxiliary lamp or by avoiding any change of the sphere while recording the responses of both test and reference signal.

The reflectance of the sphere wall may be wavelength dependent. If an illuminance meter is used as the receiver and photometric quantities are measured directly, sphere reflectance must be spectrally neutral.

Other error sources can be due to the effect of heat on the sphere [Ohno, 2000] and fluorescence of the reflective paint [Zong, 2004].

Advantage will be taken of the hemispherical spatial distribution of a power LED by mounting the LED on the sphere wall, eliminating the need of a central mount baffle.

3.5.4. New developments

In 1994, an absolute detector-based integrating sphere method was proposed [Ohno, 1994]. In this method, the total luminous flux of a lamp inside the sphere is calibrated against the known amount of flux introduced into the sphere from an external irradiance standard through a calibrated aperture, avoiding the need for a radiant or luminous flux standard. Indeed, irradiance or illuminance standards are widely available and the aperture and the distance to the standard define the amount of flux entering the sphere.

Further improvements have been realised by replacing the photometer by an optical fibre which is connected to a spectroradiometer. In this way, the requirement to use a coating which is spectrally neutral within the visible part becomes superfluous as test and reference are compared for each wavelength. Furthermore, spectral mismatch errors of the photometer's spectral responsivity with respect to the eye sensitivity curve are avoided [Ohno, 2006]. Of course, the fibre end connected to the sphere must be provided with a diffuser in order to have the angular responsivity required for irradiance measurements.

The detector-based method was applied to perform luminous flux measurements on low-power LEDs [Miller, 2001]. To include the backward emissions of LEDs, they were mounted inside the sphere and sockets were minimized to reduce near-field absorption in the socket and the LED itself. However, this becomes problematic for high-power LEDs having a large heat sink. Such LEDs could be mounted at the sphere wall where only the LED head is inserted into the sphere while the large heat sink stays outside the sphere [CIE, 2007]. Backward emission, although rather limited for high-power LEDs, can be included using white reflective sheets (see below).

In this chapter, a method is described which combines recent improvements and adds some new features. The main characteristics of this method are:

- Spectral resolved measurements
- Absolute detector-based approach with an external calibrated spectral irradiance source
- Wall-mounted LEDs
- A unique geometry of reference port, detection port and sample port eliminating or at least minimizing the baffle area

These requirements imply some new challenges too:

- The absolute detector-based approach implies the presence of an open port during both the reference and test measurement and a supplementary baffle is needed to avoid any direct escape of radiation from the wall mounted test source.
- The spatial distribution of the narrow reference beam can be very different from the source spatial distribution, which implies severe conditions on the sphere spatial responsivity.

- Although LED radiation is hemispherical to a large extend, back-directed radiation from the top of the LED package must be included.
- A fibre mounted irradiance probe, attributed with a suitable diffusing element to compensate for the limited field of view of a naked fibre, will introduce important losses in transmitted radiation, while spectral resolved measurements need sufficient input signal levels at all wavelengths.

3.5.5. Measurement setup

In Fig. 3.2, the integrating sphere with particular location of the reference port, detection port and sample port is shown. This sphere was custom made by GigaHerz Optik, and coated with a barium-sulphate coating (type ODP97) with a typical reflectance of 97 %. When choosing the diameter of the sphere, a number of issues have to be taken into account. Although large diameter spheres have better integrating characteristics, they will compromise the signal strength, especially if spectral measurements are performed. Additionally, the ratio of the total port area to the sphere area must be kept preferentially below 5 % [Goebel, 1967]. If the sample port diameter, and consequently the diameter of LED packages or LED luminaries is restricted to 11 cm, an inner diameter of 50 cm is certainly a good compromise, the total port to sphere area ratio being less than 2 %.

The reference port is a 2.54 mm port. A spectral irradiance standard (50 W halogen lamp), calibrated at 50 cm normal distance, is placed perpendicular to and at 50 cm from the reference port. The spectral flux entering the sphere can be calculated by multiplying the irradiance with the port area. The flux is entering the sphere as a more or less collimated beam with a divergence of approximately 3°. The reference beam is hitting the sphere wall at the opposite side of the detector port. No baffles are needed to avoid direct incidence on the receiver. A secondary standard can be used which is placed at a shorter distance to provide higher signal levels. The calibration transfer data are realized using the complete measurement setup. The whole installation is placed in a dark room. During the measurement of the test source, the reference port has to remain open to keep the sphere response identical.

The detection port is located very close to the reference port (distance between both centres is about 53 mm or 15°, see Fig. 3.4). The detector head consists of a white diffusing Teflon sheet of 15 mm diameter aligned with the sphere wall. Behind this sheet, a circular quartz fibre bundle (with 3 mm diameter) is mounted at a fixed distance of 6 mm.

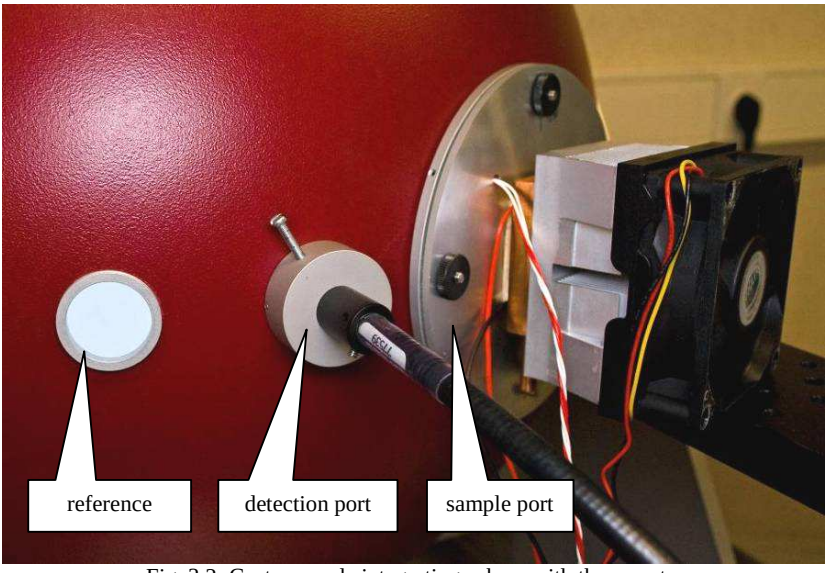

Fig. 3.2: Custom made integrating sphere with three ports.

The rectangular fibre bundle termination is coupled to a 1/4 m focal length spectrometer (Oriel Instruments type 74055 MS260i). The (interchangeable) grating has a line density of 150 lines/mm. At the spectrometer exit plane, a 1 inch Andor back illuminated and cooled (-30 °C) CCD detector (model iDUS DV420A-BU2) is mounted (see Fig. 3.3). With 1024 pixel columns and a slit width of 150 µm, a spectral resolution of approximately 4 nm can be obtained while the complete visible spectrum can be recorded without turning the grating. This bandwidth is sufficiently low to perform accurate measurements of tristimulus and photometric quantities [Ohno, 2007]. Data acquisition with full vertical binning, dark current correction and an integration time set for optimum signal-to-noise ratio is controlled by LabVIEW software.

Fig. 3.3: Spectrometer with CCD detector.

The sample port can be closed with an aluminium plug which can be used as a substrate to mount small LED boards. The plug is adapted to the LED under test: holes are drilled to fix it on the plug and to conduct electrical connections outwards. The interior of the plug is covered with a white Lambertian reflective sheet (GigaHerz Optik ODM98 raw sheet) in order to capture the radiation emitted backwards and to minimize overall absorption [Miller, 2001]. Plug and sheet are renewed when appropriate.

The three ports are located as close as possible together (Figs. 3.2 and 3.4), with the detector port located between sample and reference port. This geometry has a number of advantages.

During LED measurement, the reference port remains open in order to eliminate the substitution error. The open reference port and the detector port must be shielded from the test source by a baffle. The reference port viewed from the centre of the light source represents a solid angle given by 0.002 sr or about 0.03 % of the hemisphere. At the same time, the baffle is automatically shielding the very small detection head, as illustrated in Fig. 3.5. The small solid angle is baffled by an element cut from a white plate (GigaHerz Optik ODM98 raw block), which is easily mounted on the edge of the sample port plug (Fig. 3.6). The baffle can be adapted to the height and width of the LED source. For a naked power LED, a baffle area of only 1×1 cm² is sufficient. If a lens is mounted on the LED, the source becomes much higher but the dimensions of the baffle are still limited to about 2×2 cm². With this particular geometry, the baffle area can be kept very small, introducing only a minimal disturbance from the ideal sphere. In a recent publication [Liu, 2008-1], an integrating sphere method was presented without any baffle present. However, the detector was mounted 90° away from the light source, allowing for direct irradiance from the LED, and the substitution method was adopted without corrections.

Although the solid angle of the reference port as seen from the source is the same whatever the mutual positions of the source and the port, there are yet some

additional advantages attributed to the close location. The flux from the source hitting the baffle directly will be proportional to the source intensity at polar angles of 84° or higher. Even for LEDs with a batwing or side-emitter intensity distribution pattern, the direct flux on the baffle will be very low. In addition, the direct flux incident on the region of the sphere wall shielded by the baffle (Fig. 3.5) is also minimized for the same reason as explained before.

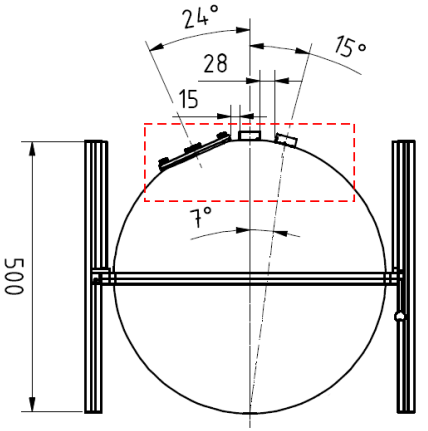

Fig. 3.4: Geometry of the integrating sphere with (from left to right) sample port, detection port, and reference port (top view, dimensions in mm).

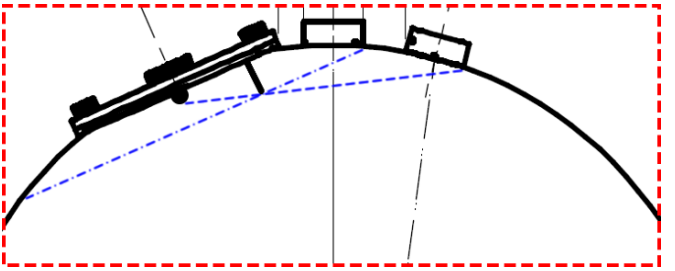

Fig. 3.5: An enlargement of the dashed area in Fig. 3.5 shows the light source and baffle mounted on the sample plate in a configuration avoiding direct light on the detection and reference port (dashed line). The baffle also creates a shadow area which cannot be seen directly from the detection port (dot-dashed line).

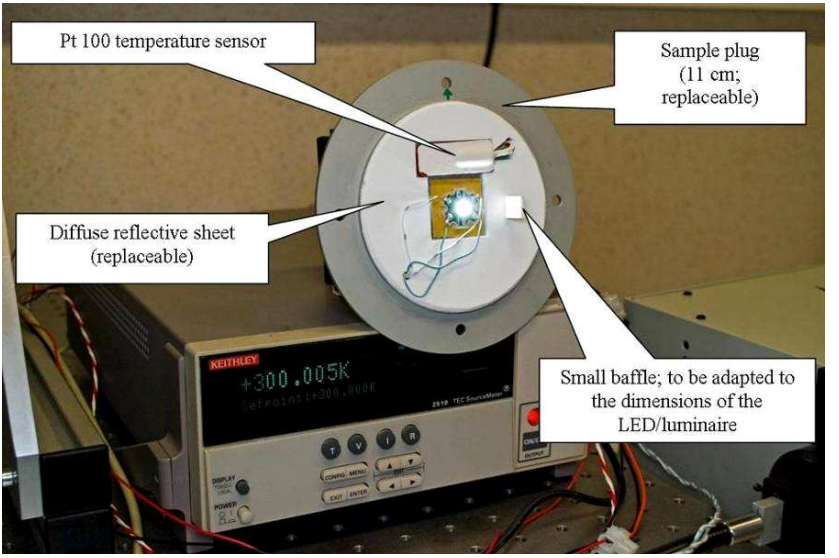

Fig. 3.6: Inner side of the sample port plug with LED, small baffle and Pt100 temperature sensor.

3.5.6. Characterization

The directional response of the combined diffusing sheet and circular quartz fibre bundle acting as the irradiance detector head has been investigated. The detector head has been removed from the sphere and illuminated with a halogen lamp acting as point source at a distance of 90 cm. The response of the spectrometer has been captured for different orientations α of the detection plane with respect to the direction of the source. In this situation, the irradiance is proportional to the cosine of α and so should be the response. All responses have been normalized by the response at normal incidence, corresponding to $\alpha = 0$, and the result is shown in Fig. 3.7. The response of the naked fibre end without diffusing membrane is also shown and a cosine function is given for reference.

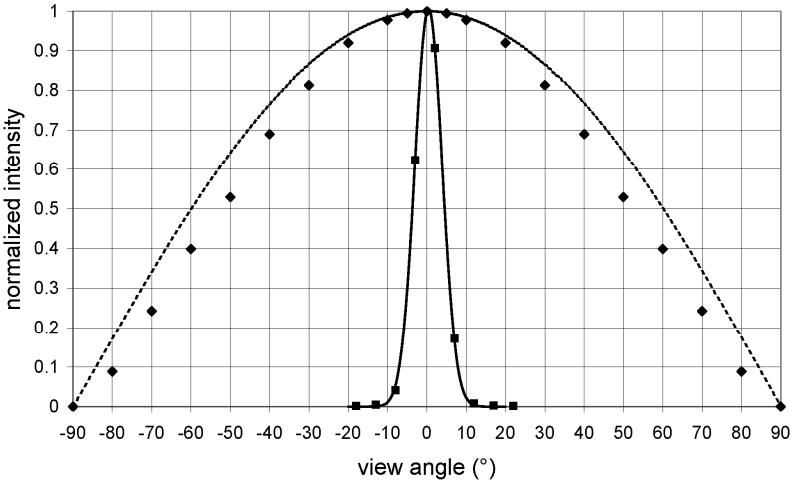

Fig. 3.7: Angular response of naked quartz fibre (squares) with Gaussian fit and of a quartz fibre with diffusing foil (diamonds). A cosine response (dashed line) is shown for reference.

As can be seen, the naked fibre end is certainly not suited as an irradiance detector head. The directional response is in accordance with the theoretical numerical aperture, being approximately 0.22, corresponding to a maximum viewing angle of about 12° from the centre.

If combined with the Teflon sheet, the angular response approximates the ideal cosine response, but at the expense of the signal level being about 30 times smaller. Improving the angular response using thicker membranes (and yet less signal strength) is of course possible, but from the results mentioned below, this angular response seems to be acceptable.

The collimated external beam and the test LED can have very different intensity distributions. Thus a uniform SRDF of the sphere is critical [Zong, 2004]. To determine the SRDF, a laser diode ($\lambda \approx$ 640 nm) was mounted on a rotation stage at the centre of the sample port. The locations of the laser beam hitting the sphere wall are described using spherical coordinates with the origin in the centre of the sphere, with the Z-axis oriented vertically and the X-axis directed to the detector port (see Fig. 3.8). The SRDF is obtained by normalizing the response of the complete measurement system to the maximum recorded value (excluding direct irradiance of the detector). To ensure that fluctuations in the laser's output do not affect the measurement results, the laser was pointed at a fixed position in the sphere between two consecutive measurements [Knee, 1999].

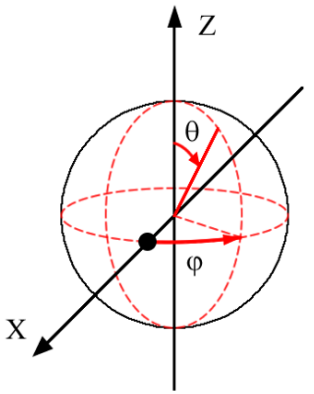

Fig. 3.8: Schematic drawing of spherical coordinates applied to the integrating sphere. The Z-axis is oriented vertically and the X-axis is directed to the detector port (represented by the black dot). θ and φ coordinates are defined.

In Fig. 3.9, the experimental SRDF is shown in the horizontal plane θ = 90°. For φ = 0, a huge relative response of 53 is recorded when the laser hits the detector directly, while no response is recorded at φ = 345°, corresponding to the open reference port. At φ = 90° and φ = 270°, the influence of the hemispherical joints can be clearly observed with a decrease in response of about 4 to 6 % with respect to the maximum value. For all other positions, the SRDF is constant within less than 2 % (see Fig. 3.9), which is an excellent result [Miller, 2004].

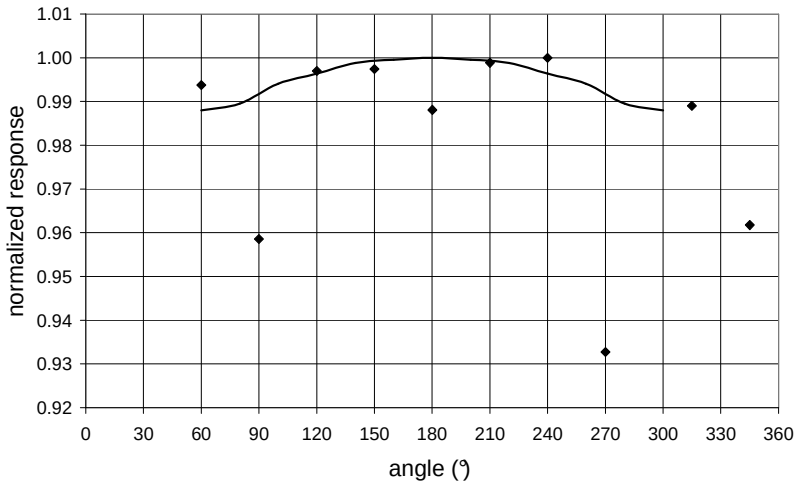

Fig. 3.9: Experimental (diamonds) and calculated (line) normalized SRDF in the horizontal plane of the integrating sphere for different values of φ. At $\varphi = 345°$ the laser is hitting the baffle.

Finally, a little baffle has been mounted to screen the detector and the reference port (see Fig. 3.5 and Fig. 3.6). If the laser hits this baffle directly, the SRDF is measured to be 3.3 % lower from the mean value (φ = 345° in Fig. 3.9). Indeed, the flux must reflect on the baffle first before hitting the sphere wall. Since the reflectance of the baffle material is about 98 %, the loss in SRDF can be mainly attributed to this effect. For a typical Lambertian LED, the flux hitting the small baffle directly is only about 0.26 %. This flux and the flux hitting the shadow region on the sphere wall will be underestimated by 3 %, corresponding to an overall underestimation of approximately $7.9\,10^{-5}$ %. The SRDF has also been measured in a few vertical planes; the values are constant within 2 %.

An additional check of the integrating sphere was done by replacing the fibre detector with an illuminance meter with only the calibration lamp operating. The incident luminous flux has been calculated from the spectral irradiance, eye sensitivity curve and the port area to be 60.45 lm. The illuminance meter response was 1442 lux. From Eq. (3.5), the mean reflectance has been calculated to be 95 %, which is somewhat lower than the 8:d reflectance value of the sphere coating quoted by the manufacturer, being 97 %. This difference can be explained by the presence of the open port, the LED printed circuit board, the hemispherical joints and the diffuse incidence.

When performing luminous flux measurements, the combined measurement uncertainty due to reference port area (0.8 %), reference source (0.8 % according to the datasheet) and CCD readouts (1.2 %) is estimated to be 2.8 %.

3.5.7. Directional detector response and SRDF

The detector response S_λ at a particular wavelength can be written as:

$$dS_\lambda = \Re_\lambda f(\theta,\varphi)\, dE_{e,\lambda}(\text{receiver}) \tag{3.6}$$

with $\Re_\lambda$ the responsivity at a particular wavelength and at normal incidence. $f(\theta,\varphi)$ describes the angular variation of the responsivity. Angular and wavelength dependence are assumed to be independent. Substitution of Eq. (3.6) into Eq. (3.3) and integration gives:

$$S_\lambda = \frac{\rho}{4\pi R^2}\Re_\lambda \iint\limits_{\text{sphere wall}} f(\theta,\varphi)\, E_{e,\lambda}(\theta,\varphi)\, dA_{src} \tag{3.7}$$

The spectral irradiance on the sphere wall is the sum of the direct contribution $E_{e,\lambda,D}$ and the indirect contribution $E_{e,\lambda,IND}$:

$$S_\lambda = \frac{\rho}{4\pi R^2}\Re_\lambda \iint\limits_{\text{sphere wall}} f(\theta,\varphi)\left[E_{e,\lambda,D}(\theta,\varphi)+E_{e,\lambda,IND}(\theta,\varphi)\right]dA_{src} \tag{3.8}$$

When measuring the SRDF, a laser diode is used and the direct irradiance is limited to a small spot such that the variation of $f(\theta,\varphi)$ over the laser spot can be neglected. The first contribution of the integral can be written as:

$$\iint\limits_{\text{sphere wall}} f(\theta,\varphi)E_{e,\lambda,D}(\theta,\varphi)\,dA_{src} = f(\theta,\varphi)\Phi_{e,\lambda,laser} \tag{3.9}$$

with $\Phi_{e,\lambda,laser}$ the spectral radiant flux of the laser.

The indirect irradiance in a sphere without baffles can be written in accordance with Eq. (3.5):

$$E_{e,\lambda,IND} = \frac{1}{4\pi R^2}\frac{\rho}{1-\rho}\Phi_{e,\lambda,laser} \tag{3.10}$$

Eq. (3.8) can thus be rewritten as:

$$S_\lambda = \frac{\rho}{4\pi R^2}\Re_\lambda\Phi_{e,\lambda,laser}\left[f(\theta,\varphi)+\frac{\rho}{4\pi R^2}\frac{1}{1-\rho}\iint\limits_{\text{sphere wall}} f(\theta,\varphi)\,dA_{src}\right] \tag{3.11}$$

The SRDF will be proportional to:

$$\text{SRDF} \propto \left[f(\theta,\varphi)+\frac{\rho}{4\pi R^2}\frac{1}{1-\rho}\iint\limits_{\text{sphere wall}} f(\theta,\varphi)\,dA_{src}\right] \tag{3.12}$$

For the mean reflectance, a value of 0.95 has been used as obtained before. From Fig. 3.7, $f(\theta,\varphi)$ can be determined by dividing the response by the cosine of the corresponding angle. If the Z-axis is chosen parallel to the detector normal, the polar angle θ will be twice the viewing angle α because θ is referenced to the centre of the sphere while the detector is positioned at the sphere wall. If the angular response is supposed to be independent of the azimuth angle, Eq. (3.12) becomes:

$$\text{SRDF} \propto \left[f(\theta,\varphi)+\frac{\rho}{2}\frac{1}{1-\rho}\int_{\theta=0}^{\theta=\pi} f(\theta,\varphi)\sin\theta\,d\theta\right] \tag{3.13}$$

Eq. (3.13) has been calculated numerically and normalized to the maximum value. The result is included in Fig. 3.9 and is in accordance with the measurements, except at the hemispherical joints.

The SRDF has also been measured and calculated when the naked quartz fibre without diffuser was used as receiver head. The measured and calculated values are shown in Fig. 3.10. The quantitative correspondence is very nice, pointing to an integrating sphere behaviour which approximates the theoretical predictions.

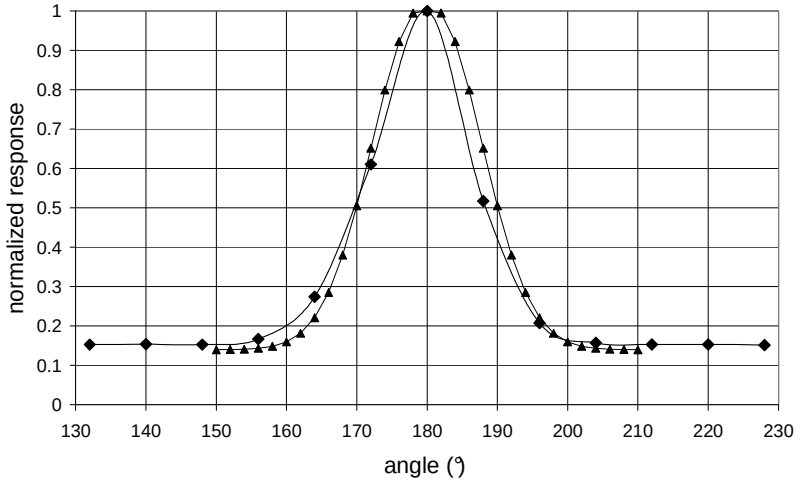

Fig. 3.10: Experimental (diamonds) and calculated (triangles) SRDF values in the equator plane when the naked fibre was used as detector head.

3.5.8. Test measurements

The spectral radiant flux of a power LED (type XREW) has been measured with the new integrating sphere. The LED was mounted on the aluminium port plug by use of thermal adhesive tape. Outside the sphere, a heat sink was mounted onto the plug to keep the junction temperature low. The plug is thermally isolated from the sphere in order to keep the temperature of the reflective inner sphere coating constant. The junction temperature (48.7 °C) has been determined according to the method described in chapter 4. The integration time required to reach a CCD response just below saturation (60 000 counts) was 241.6 ms. When measuring the irradiation standard, the integration time was 23.7 s. The linearity of the CCD response with integration time has been tested to be linear with a correlation index of 0.9998. For each pixel, the counts/s are linked to the incident spectral flux and used as a calibration file. The 1024 spectral values have been converted to values at each nm using a spline interpolation technique. Luminous flux has been calculated numerically and a value of 35.3 lm was obtained. This value is slightly lower than flux number found in the LED datasheet, taking into account the increased junction temperature at thermal equilibrium (38 lm).

The LED configuration was also mounted in a goniometer (see next section). The junction temperature was within a few degrees the same as for the sphere measurement. Luminous intensity values have been integrated over the hemisphere resulting in a luminous flux of 35.0 lm, corresponding to a deviation of only 0.86 %. This result has been obtained after averaging the intensities obtained in four measurement planes.

In a final test, the efficiency of external optics has been determined. A Lambertian LED with a very wide flux distribution (Full Width at Half Max = 120°) is equipped with an external lens with a very small FWHM (10°). The totally different intensity distributions of both sources offer an interesting test for the sphere. The spectral radiant flux with and without external lens is shown in Fig. 3.11. The luminous flux of the LED has been determined to be 34.5 with and 35.3 lm without the lens respectively, resulting in a lens efficiency of 97.8 %. The identical spectral behaviour suggests negligible absorption in the lens material. However, internal reflections in the lens can direct light backwards to the black LED printed circuit board, which might explain the slightly lower flux value.

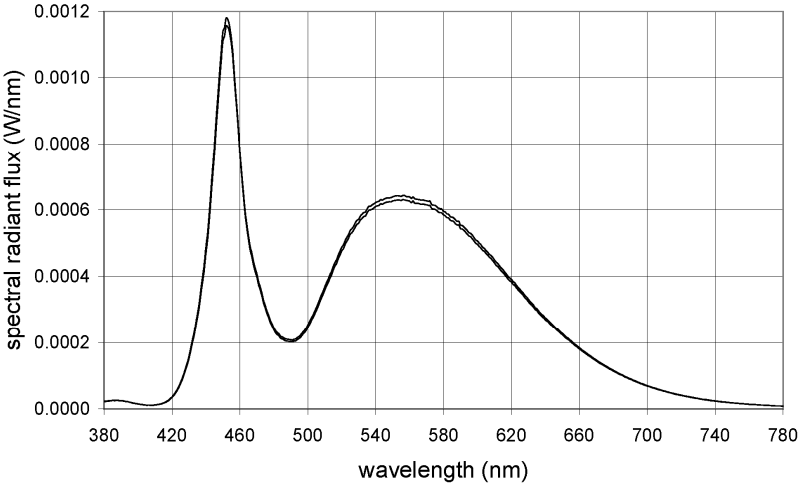

Fig. 3.11: Spectral radiant flux of a white Lambertian LED without (upper curve) and with (lower curve) a clear external narrow beam lens.

3.5.9. Flux measurements at constant current or junction temperature

Each LED package under test has been attached to the sphere surface using an aluminium mounting plate incorporating a Peltier element and a Pt100 thermistor, four-wire connected with a Keithley 2510 TEC SourceMeter. The Peltier element with active air cooling regulates the plate temperature until the thermistor shows the

same temperature as the Keithley set point temperature. Meanwhile, junction temperature is determined with the Keithley 2440 5A SourceMeter in a four-wire set-up by application of the previous voltage-temperature calibration. Because of the thermal resistance between the LED junction and the mounting plate [Jayasinghe, 2006], the thermistor set point temperature must be lowered until the diode junction temperature reaches the desired value.

Using the measurement system described above, radiant flux and electrical input power can be determined simultaneously as a function of constant drive current and junction temperature independently. In practice, the number of data acquisition points has typically been limited to four temperature (300, 320, 340 and 360 K) and four current (150, 250, 350 and 450 mA, or 150, 350, 500, 700 mA) values within a number of constant current measurement series and constant temperature measurement series, respectively. Measurement data obtained for current-temperature couples that had been set during two measurement series (one at constant current and one at constant temperature) served as control points.

3.6. Measuring spatial distributions

Two custom-made goniophotometer setups have been used to determine the radiant spectral intensity $I_{e,\lambda}(\theta,\varphi)$ of a selection of LED devices. The first was designed by Leloup *et al.* and incorporates a freely rotating detector arm of 1.5 m (see Fig. 3.12) [Leloup, 2008]. All single-die packages (typically 1 to 3 W) have been measured with this setup. The second goniophotometer has a fixed Instrument Systems detector; while the sample can be two-dimensionally rotated at a distance of 8.7 m from that detector (see Fig. 3.13). The latter has been used for all multi-die emitters.

Both setups incorporate an Oriel Instruments spectrometer with a 150 lines/mm grating. At the spectrometer exit plane, a 1 inch Andor back illuminated and cooled (-30 °C) CCD detector is mounted, obtaining a spectral resolution of approximately 4 nm while the complete visual spectrum is recorded (also see previous section). Data acquisition with full vertical binning, dark current correction and an automated integration time set for optimum signal-to-noise ratio is controlled by LabVIEW software.

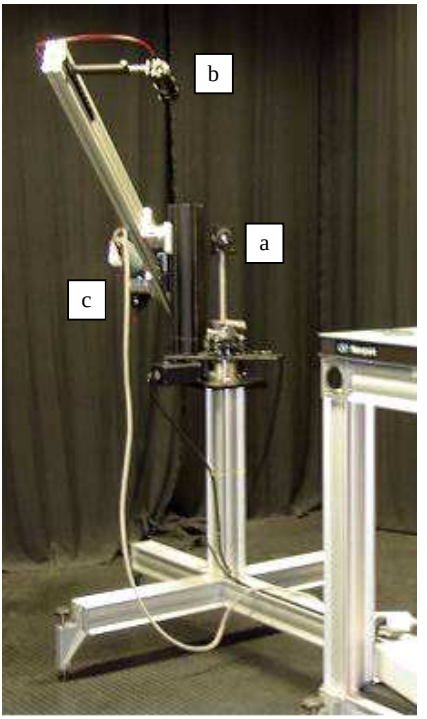

Fig. 3.12: Custom-made goniophotometer setup used for spectral radiant intensity measurements of single-die LEDs. (a), (b), and (c) indicate the sample holder, detector head, and spectrometer with CCD-camera, respectively.

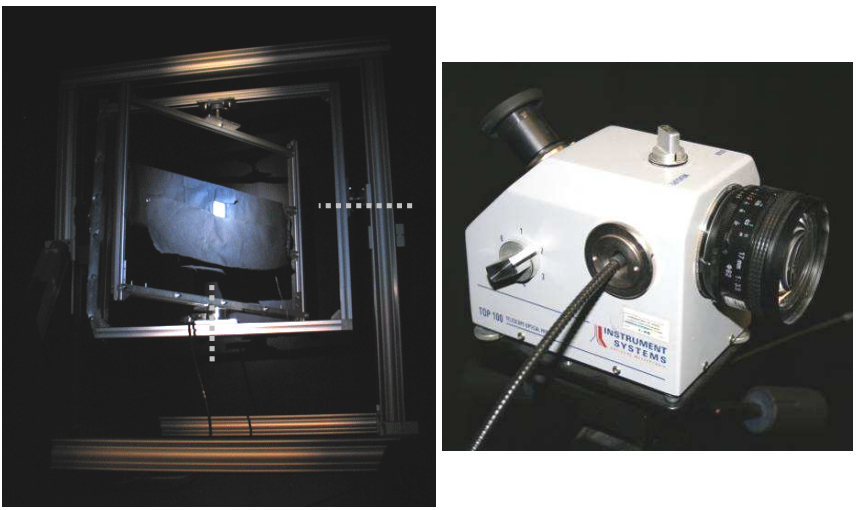

Fig. 3.13: Custom-made goniophotometer setup (left) and detector (right) for spectral radiant intensity measurements of multi-die LEDs. The goniometer's rotating axes are indicated by gray dotted lines.

Using spherical coordinates with $(\theta,\varphi)=(0,0)$ for the forward optical axis of each device, radiant spectral intensity measurements have been performed for θ from 0° to 80° per 10° in four half-planes characterized by φ = 0°, 90°, 180° and 270°. For asymmetric packages, the φ = 0° plane has been chosen along the shortest axis.

3.7. Measurements performed at the NIST

During a five week research visit at the Optical Technology Division of the National Institute of Standards and Technology (NIST, Gaithersburg, MD, USA) a number of experiments have been worked out. Being one of the most reputable LED lighting technology laboratories worldwide, the NIST Optical Technology Division owns a 1 m ambient-temperature-controlled integrating sphere (see Fig. 3.14), which had been made available during the visit. This Sensing SPR-600 Thermostatic Photometric Sphere is particularly designed for the measurement of power LED devices, modules and lamps as required by the NIST. The sphere is connected to an Instrument Systems CAS 140CT-153 spectrometer. Centrepiece of this spectrometer is the Crossed-Czerny-Turner spectrograph incorporating a back-illuminated CCD detector with a 380-1040 nm spectral range at 3 nm resolution.

Research at the NIST focused on the characterization of (remote) phosphor type of LEDs. The junction temperature of each test LED was set by using a 264 TEC Laser Mount temperature-controlled heat sink which is mounted on the sphere surface [Zong, 2008] (see Fig. 3.15). The effects of junction temperature, phosphor temperature, and excitation light density on LED's spectral radiant flux has been studied by first performing flux measurements for pump diode modules without phosphor plate at five forward currents (150, 250, 350, 500, 700 mA) and five junction temperatures (25, 40, 60, 80, 100 °C). The same forward current and junction temperature settings have been used during a second spectral radiant flux measurement series with the remote phosphor plates remounted on their respective pump devices. The phosphor temperature has been recorded using a k-type thermistor connected with thermal paste. Combining the results of both measurement series allowed calculating the effective quantum efficiency of the phosphors afterwards. These experiments have been repeated for three constant sphere temperatures (25, 40, 55 °C). The effect of ambient temperature on phosphor heating and efficiency could be examined as a result. Although the first step had to be skipped, the same research method has been applied to a selection of proximate phosphor type of LEDs as well.

Fig. 3.14: Ambient-temperature-controlled integrating sphere outside (left) and inside (right). The sphere incorporates a camera and control panel with display for lamp control. On the sphere inside the measurement port, baffle, central calibration lamp holder, top and bottom openings for temperature-controlled air flow, and the auxiliary lamp (switched on) can be seen. LED devices are mounted on the right-hand side of the sphere surface.

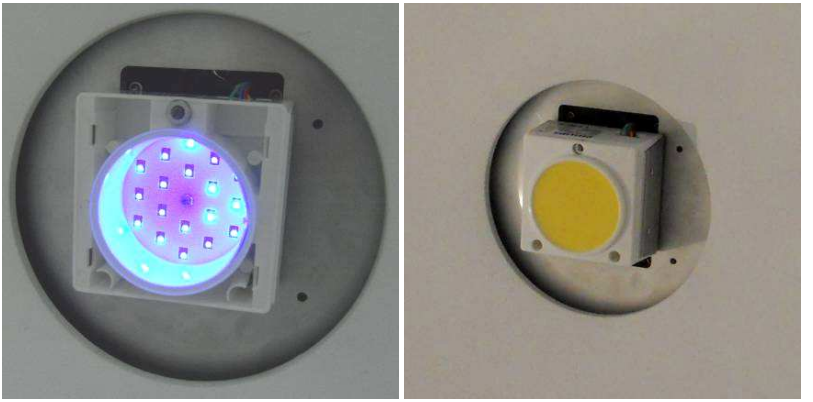

Fig. 3.15: Remote phosphor type of LED mounted on the sphere surface without (left) and with (right) its remote phosphor plate (LED type FOR1).

3.8. Summary and conclusions

By comparison with other modelling and simulation techniques, the gray-box modelling approach has been found to be the best option for the intended research contribution on the integration of high-power LEDs in general lighting applications.

Work on recommendations for best practice and an extended technology evaluation resulting from the modelling efforts has been clarified.

In this chapter, all measurement equipment setups have been described in detail. The typical hemispherical radiation of power LEDs has been exploited to increase the accuracy of the flux determination using a custom-made integrating sphere. Recently proposed measurement techniques such as an external reference source and spectral detection are combined with a specific port geometry of the sphere wall with minimum baffle area, showing a very uniform sphere response distribution function. Furthermore, the sphere response function could be modelled from the directional response of the detector. Luminous flux determination using spatial resolved goniometer measurements are in agreement with the results obtained with the integration sphere. With this measurement setup, the current and temperature dependence of the spectral radiant flux of power LEDs can be studied. This provides essential information for LED manufacturers and end-users and will contribute to the development of LED output models in the subsequent chapters.

4. Forward voltage model

4.1. Goals

Optical and electrical characteristics of power LEDs are strongly dependent on the diode junction temperature. However, direct junction temperature determination is not possible and alternative methods must be developed. Current-voltage characteristics of commercial single-die high-power LEDs are measured at different temperatures ranging from 295 K to 400 K. Modelling these characteristics, including variation of the band gap with temperature, reveals a linear temperature dependence of the forward voltage if the drive current is chosen within a rather limited current range. Theoretically, the voltage intercept can be deduced from the bulk semiconductor band gap. However, experimental results show that accurate junction temperature determination is only possible if at least two calibration measurements at a particular drive current are performed.

The current-voltage characteristics of a variety of multi-die LEDs, ranging from two to a few hundred dies, are recorded at different ambient temperatures as well. The results are used to model the forward voltage as a function of a generalized junction temperature. In multi-die LED modules such models allow analogous junction temperature determination as in single-die packages.

For both single-die and multi-die packages, the initial forward voltage model is extended with the temperature dependence of the diode's internal series resistance. The result can be used directly for power modelling afterwards (see next chapter). Power losses at normal drive currents due to this internal series resistance are evaluated. Apparently, the junction temperature only significantly increases when a certain current level is exceeded, partially depending on the internal series resistance of the complete LED package.

4.2. Situation

Due to chip encapsulation, in situ junction temperature determination is not possible for commercial LED packages [Lee, 2009]. Many research groups and light-emitting diode manufacturers are therefore making efforts to develop proper junction temperature measurement techniques. In 2004, Lee proposed a progressive technique using nematic liquid crystal thermography with laser illumination [Lee, 2004]. Also Gu and Narendran developed a non-contact method for determining junction temperature of phosphor-converted white light-emitting diodes in 2004 [Gu, 2004]. Similar non-contact methods have been developed subsequently [Cho,

2005] [Vaitonis, 2008]. Xi *et al.* published an article on junction and carrier temperature measurements in deep-ultraviolet light-emitting diodes using three different methods [Xi, 2005]. One of these methods uses voltage-temperature calibrations for junction temperature determination. This method has been described in more detail by Xi and Schubert [Xi, 2004] [Chhajed, 2005-1] and generalized by Ryu *et al.* [Ryu, 2005] afterwards. A practical voltage-temperature calibration method has been developed by Zong and Ohno [Zong, 2008].

In contrast to the methods described previously however, LED application manufacturers in general still stick with the most popular junction temperature measurement technique. This technique uses a thermistor or thermocouple to measure the temperature of the ambient or a specific external system component, such as slug, printed circuit board, heat sink, etc. Given the thermal resistance of the material(s) between the LED junction and the measuring point, one can calculate an estimation of the junction temperature [Lumileds, 2001] [Nichia, 2003] [Huber, 2006].

This chapter shows that junction temperature measurements of packaged visible light-emitting diodes can be performed more precisely without the need of complex equipment setups. The method consists of a rather simple forward voltage measurement, which is directly related to the junction temperature. The difference between the method of Xi and Schubert [Xi, 2004] lies in the way the forward voltage dependence of junction temperature is derived and applied to the measurement data. Indeed, current-voltage measurements at different junction temperatures are modelled, and the numerical coefficients are explained in terms of basic semiconductor characteristics. This approach is first utilized for single-die packages, and verified for multi-die packages afterwards. The forward voltage model is then extended to include the internal series resistance and its junction temperature dependence. The model is applicable to all practical current values as a result.

4.2. Experiments

Ten single-die high-power light-emitting diode packages of different types and manufacturers have first been investigated. The selection consists of one blue, two red, two green and five white emitters of 1 W from five important manufacturers. All white LEDs are phosphor based and contain a blue emitter.

Ten multi-die packages of different types and manufacturers have been studied as well. The selection consists of three RGB packages and seven white modules. All white LEDs are phosphor based and contain several blue emitters. The colour circuits of the RGB packages have been measured separately in order to make a distinction between different emitter colours. This brings the total number of multi-die circuits to 16.

Forward current-voltage (I-U_f) characteristics of the LEDs have been determined with a Keithley 2440 5A SourceMeter used in a four-wire set-up and controlled by a LabVIEW 7.1 program. Current-voltage characteristics at different ambient temperatures have been measured by placing the packaged light-emitting diodes in a Heraeus UT6 isothermal oven with active air circulation. The predefined oven temperatures have been precisely measured with a Pt100 thermistor, four-wire connected with a Keithley 2510 TEC SourceMeter. For all single-die packages, six ambient temperatures have been selected within a range of typical light-emitting diode operation temperatures: 295 K, 320 K, 340 K, 360 K, 380 K, and 400 K. The highest value has been omitted for multi-die package measurements.

4.3. Modelling the Shockley behaviour of single-die packages

4.3.2. Current-voltage characteristics

A typical forward current-voltage characteristic at 295 K is shown in Fig. 4.1. Three different regions can be observed.

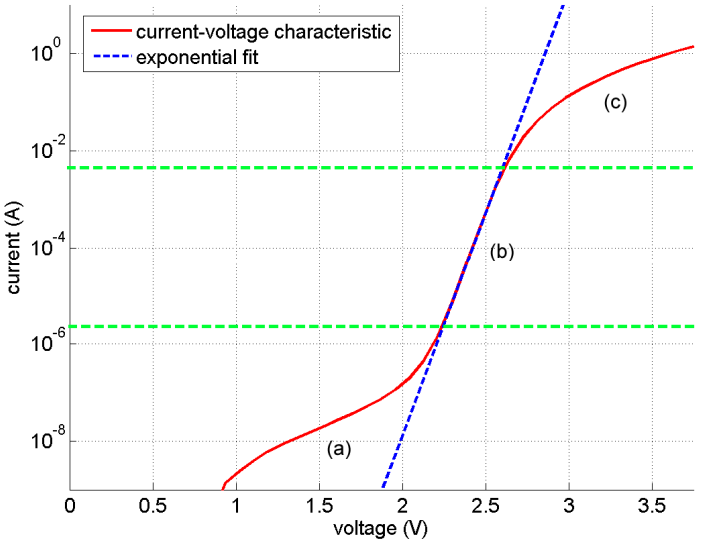

Fig. 4.1: Typical semi-log current-voltage characteristic of a blue InGaN multi quantum-well emitter (LED XREW).

Below about 2 V, excess currents dominate the measured I-U_f characteristic (see region (a) in Fig. 4.1). These currents can be attributed to various leakage currents, including carrier tunnelling transport across the quantum-well structure [Hu, 2008]. When the current exceeds 10 mA, corresponding to a voltage exceeding 2.5 V, a deviation from the exponential fit is observed due to the effect of an internal series resistance (see region (c) in Fig. 4.1) [Chhajed, 2005-1]. Values of this internal resistance typically amount to a few ohms.

For moderate voltages in the range of 2 to 2.5 V, an exponential increase of the current is observed (see region (b) in Fig. 4.1). If the diode current is dominated by diffusion processes, the forward current-voltage characteristic of an ideal p-n junction is given by the Shockley equation [Schubert, 2006]:

$$I = I_D \exp\left(\frac{eU_f}{kT}\right) \tag{4.1}$$

The quantities I_D, e, k and T represent the diffusion saturation current under reverse-bias conditions, the elementary charge, the Boltzmann constant and the junction temperature, respectively. However, if the current is dominated by space charge recombination, the forward current-voltage behaviour should be described by [Chen, 2007]:

$$I = I_R \exp\left(\frac{eU_f}{2kT}\right) \tag{4.2}$$

with I_R the recombination saturation current. Because in practice both current mechanisms are expected to be present at the same time, experimental I-U_f characteristics are commonly modelled by the Shockley equation:

$$I = I_S \exp\left(\frac{eU_f}{nkT}\right) \tag{4.3}$$

where n is the ideality factor of the diode, with a theoretical value between 1 and 2. I_S represents the effective saturation current as a combination of I_D and I_R.

In Fig. 4.2, I-U_f measurements at different junction temperatures are presented. Measurement temperatures have been chosen within a range of typical light-emitting diode operation temperatures. Using Eq. (4.3), the ideality factor and effective saturation current for each LED can be calculated from the exponential fit at each junction temperature. The temperature dependence of these quantities will be examined in the following sections.

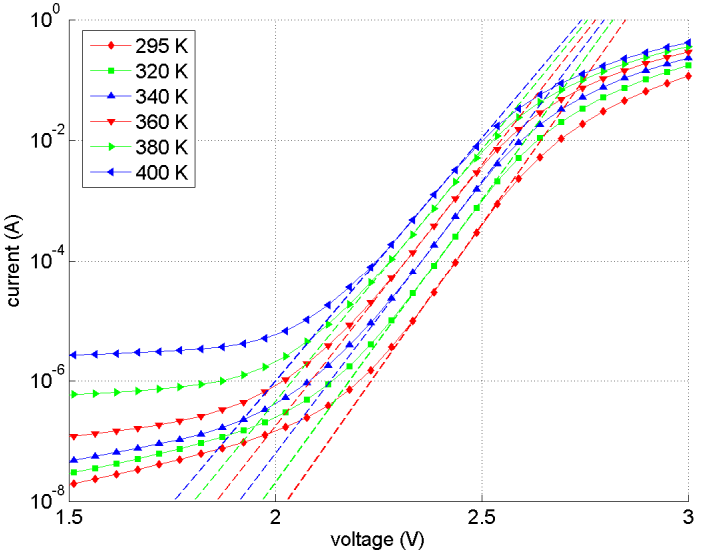

Fig. 4.2: Experimental I-U_f characteristics including exponential fits at six different temperatures for LED XREW.

4.3.2. Temperature dependence of the ideality factor

At room temperature (295 K), the ideality factors n obtained for all light-emitting diode under investigation are ranging from 1.52 to 2.87 (see Table 4.1). For red LEDs, the distinction between the voltage ranges dominated by diffusion and recombination on the one hand (region (b) in Fig. 4.1) and by leakage currents on the other hand (region (a) in Fig. 4.1) is not so clear. As a result, the extraction of the ideality factor and the saturation current is rather inaccurate. Nevertheless, ideality factors of blue emitters $(1 < n < 2)$ seem to be smaller than those of green and red light-emitting diodes $(n > 2)$.

Table 4.1: Experimental ideality factors and effective saturation currents at 295 K junction temperature. The second column contains the two-digit LED codes used in Figs. 4.3 and 4.4.

LED	code	n (295 K)	I_S (295 K) (A)
F51R-0	R1	2.79	$1.52\ 10^{-18}$
LK2R-1	R2	2.18	$4.71\ 10^{-18}$
F51G-0	G1	2.03	$5.07\ 10^{-22}$
LK2G-1	G2	2.87	$1.09\ 10^{-16}$
F51B-0	B1	1.52	$7.70\ 10^{-32}$
NCCW-1	W1	1.70	$2.71\ 10^{-29}$
PW14-1	W2	1.87	$1.68\ 10^{-27}$
W5SM	W3	1.55	$1.29\ 10^{-31}$
W421	W4	1.86	$9.38\ 10^{-27}$
XREW	W5	1.76	$1.80\ 10^{-28}$

The wide spread of measured ideality factors, with values exceeding 2, hampers the identification of a dominant current mechanism in the exponential current region. The occurrence of ideality factor values higher than 2 has been reported in literature and explained by the presence of multiple junctions in series within a single semiconductor chip [Shah, 2003].

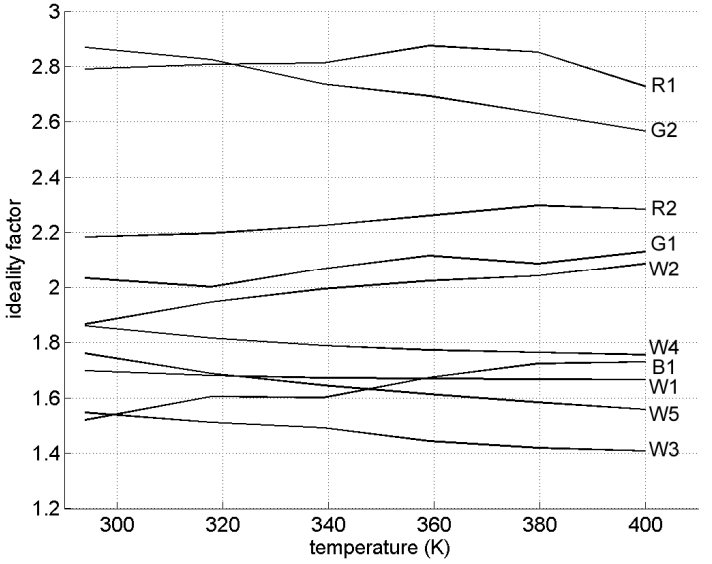

Fig. 4.3: Junction temperature dependence of the light-emitting diode ideality factor for single-die LEDs. The two-digit device codes are explained in Table 4.1.

The ideality factors of the LEDs under investigation appear to have a relatively small, but rather unpredictable temperature dependence (see Fig. 4.3). Constant values are consistent with diffusion current (expecting a constant value of 1) and space charge recombination current (expecting a value of 2) mechanisms.

In literature, ideality factors decreasing with increasing junction temperature have been reported. This behaviour has been attributed to the fact that p-type transport properties generally improve with increasing temperature and the existence of non-uniform diffusion potentials over the junction area [Hanselaer, 1984] [Shah, 2003]. Nevertheless, with respect to the I-U_f characteristic modelling of all light-emitting diodes under consideration, the ideality factors can be assumed to be constant and equal to the ideality factor at 295 K:

$$n(T) \approx n(295\ \mathrm{K}) = n \tag{4.4}$$

4.3.3. Saturation current

It is common practice to describe the temperature dependence of the effective diode saturation current I_S (see Table 4.1) using an activation energy E_a defined by [Chen, 2007]:

$$I_S = C_S \exp\left(-\frac{E_a}{kT}\right) \tag{4.5}$$

with C_S a quasi constant factor combining different physical parameters. This equation can be transformed to

$$\ln(I_S) = \left(-\frac{E_a}{k}\right)\frac{1}{T} + \ln(C_S) \tag{4.6}$$

In Fig. 4.4 the activation plots of $\ln(I_S)$ as a function of T^{-1} are shown for the LEDs under investigation. In this graph one can clearly distinguish the linear behaviour as predicted by Eq. (4.6). From the slope of these curves, the activation energy can be determined (see Table 4.2).

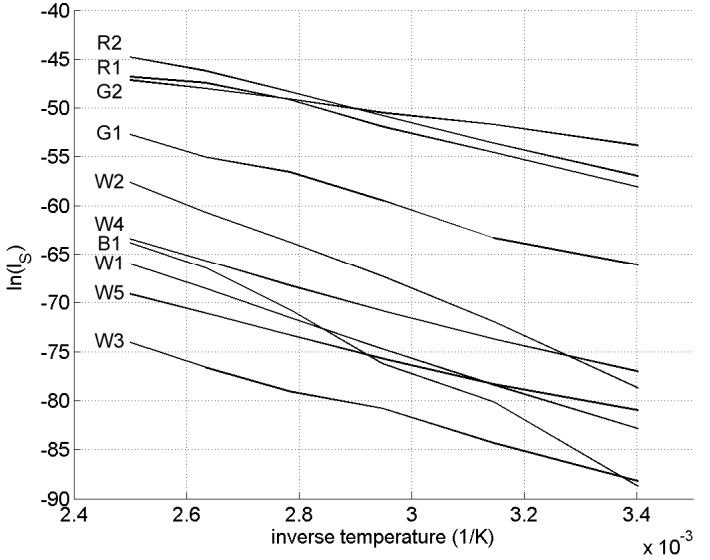

Fig. 4.4: Junction temperature dependence of the light-emitting diode (effective) saturation current. The two-digit device codes are explained in Table 4.1.

If the charge transport mechanism in the current interval with exponential behaviour (part (b) in Fig. 4.1) is dominated by the diffusion current mechanism described by Eq. (4.1), the mathematical expression for the diffusion saturation current, as provided by Shockley, is given by [Xi, 2004]:

$$I_D = eA\left(\frac{1}{N_A}\sqrt{\frac{D_n}{\tau_n}} + \frac{1}{N_D}\sqrt{\frac{D_p}{\tau_p}}\right)N_i^2 \tag{4.7}$$

The donor and acceptor concentrations N_D and N_A are temperature independent semiconductor properties. $D_{n,p}$ and $\tau_{n,p}$ are the electron and hole diffusion constants and the electron and hole minority-carrier lifetimes, respectively. The square of the intrinsic carrier concentration N_i^2 can be written as

$$N_i^2 = N_C N_V \exp\left(-\frac{E_g}{kT}\right) \tag{4.8}$$

with E_g the semiconductor band gap energy and N_C and N_V the effective density of states at the conduction-band and valence-band edges respectively. Although both parameters are explicitly dependent on junction temperature by a power law, this dependency can be neglected with respect to the exponential temperature dependence. This approximation is found in literature as well [Chen, 2007].

Substituting Eq. (4.8) into Eq. (4.7) and combining all temperature independent parameters into a single constant C_D, Eq. (4.7) can be rewritten as

$$I_D = C_D \exp\left(-\frac{E_g}{kT}\right) \tag{4.9}$$

Identification of Eq. (4.9) with Eq. (4.5) results in an activation energy identical to the band gap. However, it is known that the band gap energy is decreasing with increasing temperature [Schubert, 2006]. Taking into account a possible junction temperature range of about 100 K in practice, this temperature dependence will be included into Eq. (4.9).

The temperature dependence of the energy gap of a semiconductor can be expressed by the Varshni formula [Varshni, 1967]:

$$E_g(T) = E_g(0) - \frac{\alpha_V T^2}{T + \beta_V} \tag{4.10}$$

where α_V and β_V are two positive fitting parameters, the so-called Varshni parameters. $E_g(0)$ represents the energy gap for $T = 0$ K. For junction temperatures higher than 295 K however, the Varshni formula can be approximated by a linear expression (see Fig. 4.5). Since the relevant temperatures for the measurements under consideration have a value between about 300 K and 400 K, the Varshni formula in this temperature range may be approximated by

$$E_g(T) \approx E_{g,300} - \alpha'(T - 300) \tag{4.11}$$

with $E_{g,300}$ the band gap at 300 K and α' a positive constant. Typical values for $E_{g,300}$ range from 2.0 to 3.4 eV for InGaN and from 1.3 to 2.3 eV for AlGaInP bulk semiconductor materials. α' is calculated from the corresponding α_V and β_V values [Schubert, 2006]. Numerical values are typical between 0.1 and 0.5 meV/K for InGaN and between 0.3 and 0.4 meV/K for AlGaInP compound semiconductors.

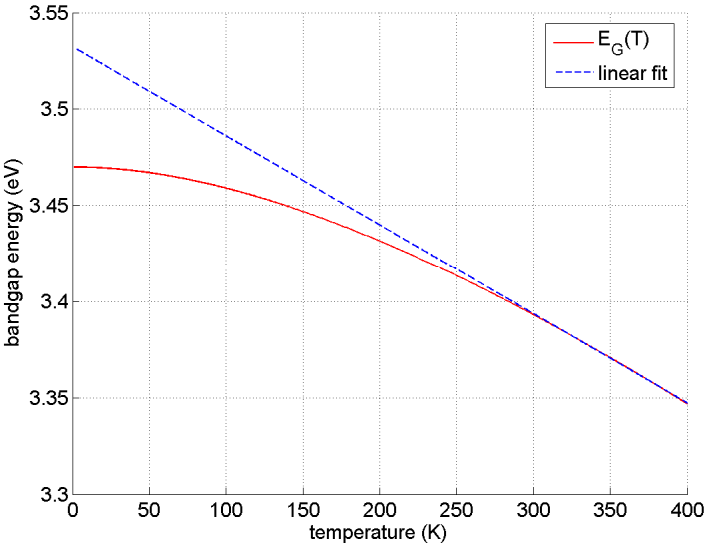

Fig. 4.5: Typical temperature dependence of the light-emitting diode band gap energy (solid line) for a GaN semiconductor lattice. The dashed line represents a linear fit for temperatures above 295 K. Other compound semiconductor materials show similar $E_{g,300}$ curves and fits.

Combining Eqs. (4.9) and (4.11) now yields

$$I_D \approx C_D \exp\left(\frac{\alpha'}{k}\right)\exp\left(-\frac{E_{g,300}+300\alpha'}{kT}\right) \tag{4.12}$$

or

$$\ln(I_D) \approx \left[-\frac{E_{g,300}+300\alpha'}{k}\right]\frac{1}{T}+\left[\frac{\alpha'}{k}+\ln(C_D)\right] \tag{4.13}$$

Identification of Eq. (4.13) with Eq. (4.6) yields the following expression for the energy gap at 300 K:

$$E_{g,300} = E_a - 300\alpha' \tag{4.14}$$

Energy gap values at 300 K calculated from Eq. (4.14) are shown in Table 4.2. A value for α' of 0.3 meV/K has been used for all LED types under consideration. The relative error introduced using this approximation is rather small and negligible in comparison with the energy gap values.

Table 4.2: LED code, ideality factor n, activation energy E_a calculated from Eq. (4.6), $E_{g,300}$ based on Eq. (4.14) (1), $E_{g,300}$ based on Eq. (4.18) (2) and $E_{g,300}$ based on Eq. (4.21) (3).

LED	n	E_a (eV)	$E_{g,300}$ (eV) (1)	$E_{g,300}$ (eV) (2)	$E_{g,300}$ (eV) (3)
F51R-0	2.79	1.221	1.131	2.352	3.318
LK2R-1	2.18	1.181	1.091	2.272	2.490
F51G-0	2.03	1.250	1.160	2.410	2.451
LK2G-1	2.87	0.965	0.875	1.840	2.680
F51B-0	1.52	1.962	1.872	3.833	2.891
NCCW-1	1.70	1.776	1.686	3.463	2.927
PW14-1	1.87	1.739	1.649	3.388	3.156
W5SM	1.55	1.866	1.776	3.643	2.797
W421	1.86	1.603	1.513	3.115	2.892
XREW	1.76	1.692	1.602	3.295	2.890

From Table 4.2 can be observed that values for $E_{g,300}$ (1) are much too low in comparison with literature values. One must conclude that the exponential $I\text{-}U_f$ behaviour for intermediate voltages is not only due to a diffusion current mechanism. This conclusion corresponds to the occurrence of ideality factors n larger than one as described in section 4.3.2.

Though not preferable, the LED current mechanism in the intermediate voltage interval may also be partially due to space charge recombination. Similar to the diffusion saturation current, a mathematical expression can be written for the recombination saturation current [Chen, 2007]:

$$I_R = \frac{eW_D}{2\tau} N_i \tag{4.15}$$

where W_D denotes the width of the depletion region and τ the carrier lifetime. Inserting Eq. (4.8), this expression can be rewritten as

$$I_R = C_R \exp\left(-\frac{E_g}{2kT}\right) \tag{4.16}$$

In analogy with the discussion before, the temperature dependency of the effective density of states N_C and N_V is neglected and all quasi temperature independent parameters have been combined into a single constant C_R.

Substitution of Eq. (4.11) allows rewriting Eq. (4.16) as

$$\ln\left(I_R\right) \approx \left[-\frac{E_{g,300} + 300\alpha'}{2k}\right]\frac{1}{T} + \left[\frac{\alpha'}{2k} + \ln\left(C_R\right)\right] \tag{4.17}$$

This expression once again corresponds to Eq. (4.6). Identification leads to a band gap energy given by

$$E_{g,300} = 2E_a - 300\alpha' \tag{4.18}$$

Energy gap values at 300 K calculated from Eq. (4.18) are gathered in Table 4.2 ($E_{g,300}$ (2)) and found to be, although slightly too high, more realistic. Unfortunately however, no correlation between the bulk semiconductor (InGaN for blue and green and AlGaInP for red) and the activation energy seems to exist. Furthermore, values of $E_{g,300}$ appear to be rather widely spread for the InGaN emitters. Finally, it is unexpected that a recombination current mechanism through mid gap recombination centres, which is known to be non-radiative, is fully responsible for the exponential current-voltage behaviour.

At this point, it seems impossible to explain and model exponential I-U_f characteristics by assuming only a diffusion or recombination current mechanism. Recently other researchers have encountered the same problem and therefore proposed to introduce the LED ideality factor n into the expression of the (effective) saturation current [Chen, 2007]. Indeed, for the diffusion current as well as for the space charge recombination current, the ideality factor of 1 and 2 respectively is also occurring in the denominator of the activation energy. The adaptation can be considered as a generalization of this establishment, in correspondence with the experimental Shockley equation (4.3). If this proposal is adopted, the effective saturation current I_S is modelled by

$$I_S = C_S \exp\left(-\frac{E_g}{nkT}\right) \tag{4.19}$$

with C_S a mathematical combination of C_D and C_R. Similar to Eqs. (4.13) and (4.17), the following expression is now obtained after substitution of Eq. (4.11):

$$\ln(I_S) \approx \left[-\frac{E_{g,300} + 300\alpha'}{nk}\right]\frac{1}{T} + \left[\frac{\alpha'}{nk} + \ln(C_S)\right] \tag{4.20}$$

Comparing to Eq. (4.6), this means in this case the energy gap at 300 K can be written as

$$E_{g,300} = nE_a - 300\alpha' \tag{4.21}$$

The resulting values for $E_{g,300}$ are given in Table 4.2 ($E_{g,300}$ (3)). Remarkably, the inclusion of the ideality factor in the activation energy seems to suppress the spread of $E_{g,300}$ values for all InGaN emitters, which now seem to correspond to

literature values very well. The values of the blue and green emitters have a mean of 2.926 eV and 2.566 eV, respectively, as can be expected. Unfortunately, the $E_{g,300}$ values of the red LEDs are too high and still have a very large spread, but this may be due to the inaccurate determination of the saturation current and ideality factor for red emitters that has been mentioned before.

From now on, Eq. (4.20) is assumed to correspond best to measurements and is used for further modelling.

4.3.4. Forward voltage variation with junction temperature

By combining Eqs. (4.3) and (4.20), the light-emitting diode forward voltage can be modelled as a function of drive current and junction temperature:

$$U_f(I,T) \approx \left[\frac{nk}{e}\ln(I) - \frac{\alpha'}{e} - \frac{nk}{e}\ln(C_S)\right]T + \left[\frac{E_{g,300} + 300\alpha'}{e}\right] \qquad (4.22)$$

From Eq. (4.22), a linear relation between forward voltage and temperature can be expected, with a slope depending on the drive current. For a particular constant current I_0, Eq. (4.22) can be rewritten as:

$$U_f(T) \approx \left[\frac{nk}{e}\ln(I_0) - \frac{\alpha'}{e} - \frac{nk}{e}\ln(C_S)\right]T + \left[\frac{E_{g,300} + 300\alpha'}{e}\right] \qquad (4.23)$$

This equation provides a theoretical base for an often applied, but hardly studied or explained junction temperature measurement technique [Gu, 2004] [Xi, 2004] [Chonko, 2006].

4.3.5. Validation

As Eq. (4.23) is based on modelling of the current-voltage characteristic within the exponential current interval, it is necessary to choose the measurement current I_0 within this interval for all relevant temperatures involved. This is illustrated in Fig. 4.6, obtained from the measurement data plotted in Fig. 4.2. Forward voltage as a function of junction temperature for five different currents applied to the same light-emitting diode (type XREW) is shown. The 10 µA, 100 µA, 1 mA, 10 mA and 100 mA currents correspond to the A, B, C, D and E lines, respectively. For currents below 100 µA, deviations from the $U_f(T)$ linearity occur at high junction temperatures due to leakage current effects. On the other hand, for currents above 1 mA, deviations from linearity occur at relatively low temperatures due to the internal series resistance. A linear relation between voltage and temperature at high nominal

currents – which is frequently used in LED datasheets – can only give a rough approximation of the junction temperature. Consequently, the measurement current I_0 for the LED package under consideration has to be chosen between 100 µA and 1 mA (see Fig. 4.6). In this case, a nice linear temperature behaviour is obtained in agreement with Eq. (4.23). Other diodes show different measurement current limitations. This limitation is however rarely taken into account or even unknown among LED applicators.

For a number of low quality LEDs the exponential current interval cannot be identified for all relevant junction temperatures. For those LEDs, deviations from $U_f(T)$ linearity will occur at all currents, making the junction temperature measurement technique described here less suitable.

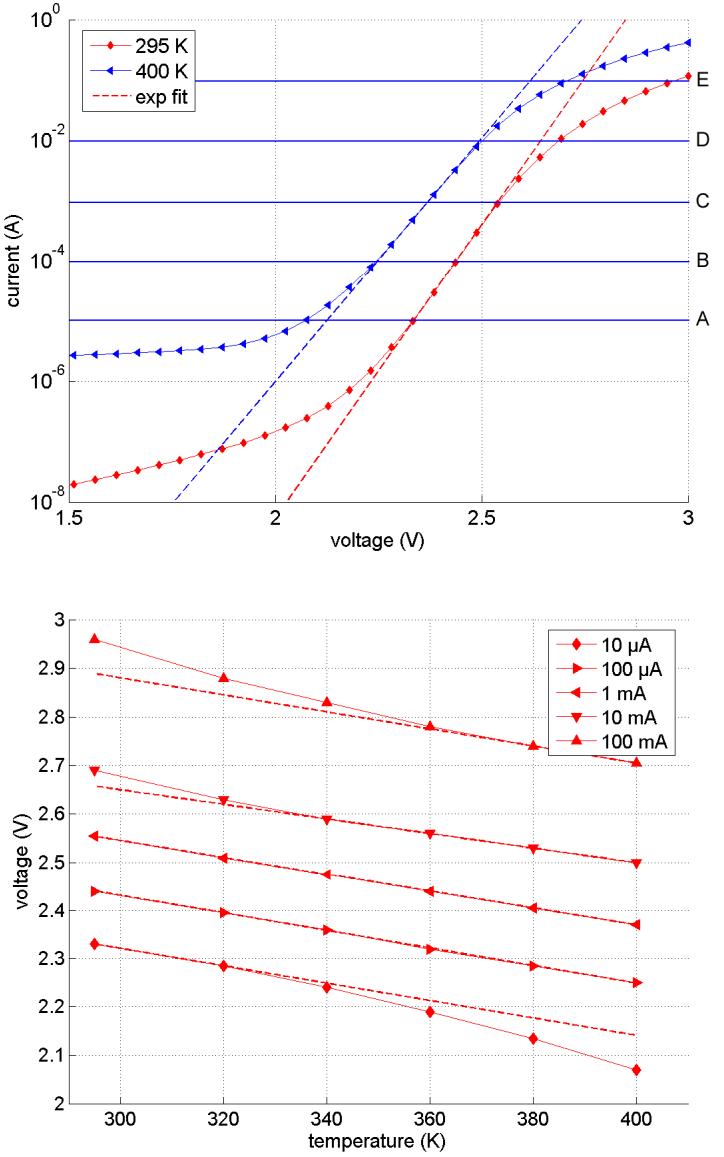

Fig. 4.6: I-U_f measurement data of LED type XREW for the utter temperatures (top) and the corresponding $U_f(T)$ behaviour at different drive currents (bottom). The 10 µA, 100 µA, 1 mA, 10 mA and 100 mA currents correspond with the A, B, C, D and E lines, respectively.

Eq. (4.23) describes a linear $U_f(T)$ behaviour with current dependent slope γ and a current independent intercept δ:

$$U_f(T) \approx \gamma(I_0)T + \delta \tag{4.24}$$

This expression can be easily verified for the linear $U_f(T)$ curves in Fig. 4.6. Linear regression analysis applied to the data corresponding to the 100 µA and 1 mA measurement currents, results in a value for γ equal to -2.0 mV/K and -1.8 mV/K respectively, while δ equals 3.0 V for both curves. I_0 and best fitting γ and δ values for all measured light-emitting diodes are gathered in Table 4.3. Corresponding coefficients of determination have been found to exceed 0.99 for all LEDs.

Table 4.3: LED code, measurement current I_0, $U_f(T)$ slope γ and intercept δ.

LED	I_0 (mA)	γ (V/K)	δ (V)
F51R-0	1.0	-0.003391	3.408
LK2R-1	1.0	-0.002998	2.580
F51G-0	0.3	-0.001466	2.541
LK2G-1	1.0	-0.001767	2.770
F51B-0	1.0	-0.001653	2.981
NCCW-1	0.1	-0.001648	3.017
PW14-1	3.0	-0.002219	3.246
W5SM	4.0	-0.001263	2.887
W421	1.0	-0.001423	2.982
XREW	0.2	-0.001742	2.980

Forward voltage slope values γ vary between -1.2 and -3.4 mV/K. This variation is partially due to the use of different currents, but all values have the same order of magnitude as datasheet values, which typically equal -2.0 mV/K [Lumileds, 2007]. Moreover, the theoretical calculation of γ starting from Eq. (4.23) with I_0 = 200 µA and α' = 0.3 meV/K results in a value of -1.59 mV/K for LED type XREW, which is very close to the experimental value of -1.74 mV/K (see Table 4.3). The intercept values approximate the energy gap values, as one expects from Eq. (4.23) with again α' = 0.3 meV/K. These correspondences justify the previously made assumptions and provide an evidence for Eqs. (4.22) and (4.23).

4.4. Modelling the Shockley behaviour of multi-die packages

4.4.1. Current-voltage characteristics

Fig. 4.7 shows a typical forward current-voltage characteristic of a multi-die LED package containing six dies at 295 K junction temperature. Similar to the single-die packages discussed before, again three different I-U_f regions can be observed.

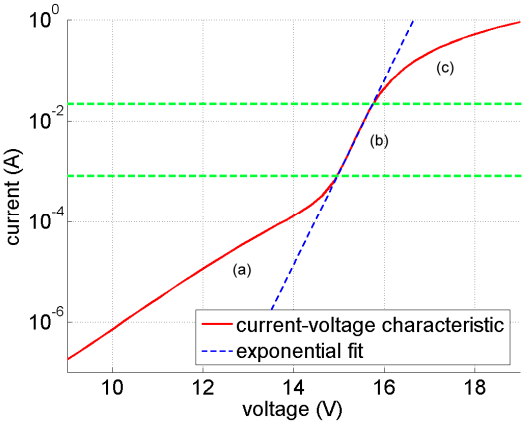

Fig. 4.7: Typical semi-log current-voltage characteristic of a blue InGaN multi-die emitter (LED type E3BN).

Forward current-voltage characteristics of the remaining multi-die circuits have been found to be similar. These measurements show that Eq. (4.3) can be applied to all LEDs under consideration, independent of the number of dies and their series or parallel connection. The corresponding ideality factors have been calculated and are gathered in Table 4.4.

Without going in detail, one can state from Table 4.4 that LED ideality factor values at room temperature generally amount the ideality factor of a single-die emitter, multiplied by the number of dies in series. This corresponds to the occurrence of ideality factors larger than 2 for single-die emitters as explained before. Although an averaging effect is possible, the parallel connection of one or more dies seems to have a rather small effect on the total ideality factor of the module.

In correspondence with all single-die packages, measurement results of forward current-voltage characteristics at five different temperatures show a clear temperature dependent shift (see Fig. 4.8). This should allow constructing $U_f(T)$ calibration curves at fixed drive currents as represented by Eq. (4.24). Mark however that for multi-die circuits the junction temperature represents in fact the generalized junction temperature of all dies in the circuit.

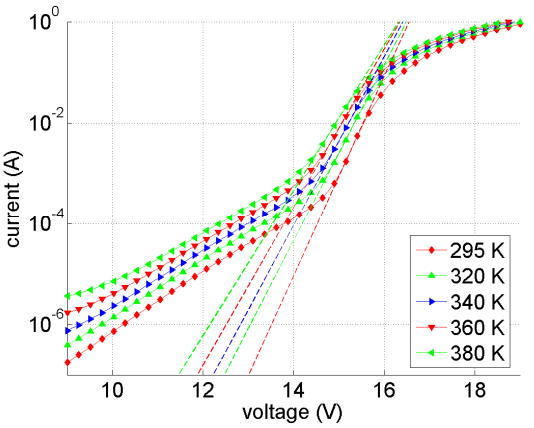

Fig. 4.8: Measurement plot of forward current-voltage characteristics at five different temperatures for a multi-die white light-emitting diode (LED type E3BN).

4.4.2. Model validation

Current-voltage characteristics at five different temperatures as shown in Fig. 4.8 have been measured for all multi-die LEDs. As for single-die LEDs, $U_f(T)$ measurement currents have been chosen within the current region showing an exponential current-voltage behaviour at all junction temperatures. It has been possible to limit the number of constant measurement currents I_0 to two values, being 1 and 10 mA. These constant currents and best fitting γ and δ values for all measured multi-die LEDs are gathered in Table 4.4. Corresponding coefficients of determination have been found to exceed 0.98 for all LEDs, which clearly validates Eq. (4.24) for all devices under test.

Table 4.4: LED code, number of dies in parallel and series connection, ideality factor (295 K), measurement current I_0 and voltage-temperature slope γ and intercept δ. Dies marked by an asterisk are low-power emitters which have been combined to create a high-power package.

LED	# dies	n	I_0 (mA)	γ (V/K)	δ (V)
BL4R	1 × 2	2.63	1.0	-0.0065	5.4208
BL4G	1 × 2	4.92	1.0	-0.0052	6.2341
BL4B	1 × 2	7.41	1.0	-0.0064	7.2349
E3BN	1 × 6	8.68	10.0	-0.0067	17.4587
HSD2-1	2 × 1	2.58	10.0	-0.0028	3.5522
LW6C-1	2 × 2	3.86	1.0	-0.0041	6.3244
NT5R	3 × 3	4.68	10.0	-0.0046	6.8568
NT5G	3 × 3	9.30	10.0	-0.0088	11.0398
NT5B	3 × 3	13.18	10.0	-0.0085	10.4580
NT52	3 × 6	13.45	10.0	-0.0189	22.2536
BL3R	39 × 2*	2.91	1.0	-0.0042	4.4596
BL3G	39 × 2*	5.11	1.0	-0.0053	5.3962
BL3B	39 × 2*	6.06	1.0	-0.0049	6.5186
W114	4 × 1	2.09	1.0	-0.0026	3.2045
NS6W	6 × 1*	1.72	1.0	-0.0015	2.9661
ENEB	7 × 7	14.65	1.0	-0.0128	20.5056

Comparing the $U_f(T)$ slope and intercept values in Tables 4.3 for single-die packages and Table 4.4 for multi-die packages shows that similar conclusions as for the ideality factor can be drawn. Indeed, γ and δ values of multi-die LEDs approximately amount γ and δ values of single-die emitters, multiplied by the number of dies in series. Again, the parallel connection of one or more dies seems to only have an averaging effect. This corresponds to what can be expected from LEDs' current-voltage behaviour: Placing two similar single-die LED devices in series will cause the forward voltage to approximately double. With increasing junction temperature, the voltage decrease will be double as well. On the other hand, placing two single-die LEDs in parallel and applying a double current will roughly result in a forward voltage and forward voltage decrease averaging.

4.5. Effect of internal series resistance

4.5.1. Forward voltage model extension

When the voltage per die exceeds about 2.5 V, for both single-die and multi-die emitters a deviation from the exponential Shockley behaviour is observed due to the

effect of an internal series resistance (see region (c) in Figs. 4.1 and 4.7). Therefore, Eq. (4.3) is adapted as follows [Schubert, 2006]:

$$I = I_S \exp\left[\frac{e\left(U_f - IR_S\right)}{nkT}\right] \tag{4.25}$$

with R_S the internal series resistance. This resistance can be calculated from the measurement data by first performing a fit to the exponential current-voltage region according to Eq. (4.3). By extrapolation of this fit to the internal series resistance region afterwards, one can use Ohm's law to determine R_S :

$$R_S = \frac{\Delta U_f}{I} \tag{4.26}$$

with ΔU_f the difference between the measured forward voltage and the voltage calculated from the exponential fit at the same drive current within the series resistance region. ΔU_f thus represents the voltage drop over the internal series resistance.

For LED PG1A-1 the series resistance is calculated at normal drive current (I_n = 350 mA) to amount about 2.1 Ω . Again by use of Eq. (4.26), this value allows verifying the resistance's character. For an ohmic series resistance the difference between the measured voltage and the exponential Shockley behaviour should equal IR_S for all currents. Good agreement between measured and calculated data shows that this is indeed the case. Internal series resistance values for a selection of LEDs at 295 K junction temperature have been collected in Table 4.5.

Table 4.5: Number of dies in parallel and series connection and internal series resistance at 295 K. Dies marked by an asterisk are low-power emitters which have been combined to create a high-power package.

LED	# dies	R_S (Ω)
F51B-0	1	1.94
F51G-0	1	2.79
F51R-0	1	1.52
LK2R-1	1	2.04
NCCW-1	1	2.42
PG1A-1	1	2.13
XREW	1	1.01
BL4B	1×2	4.12
BL4G	1×2	4.83
BL4R	1×2	2.10
E3BN	1×6	2.91
HSD2-1	2×1	0.40
LW6C-1	2×2	1.58
NT5B	3×3	1.86
NT5G	3×3	1.91
NT5R	3×3	1.02
NT52	3×6	3.37
BL3B	39×2*	1.34
BL3G	39×2*	2.11
BL3R	39×2*	0.83
W114	4×1	0.64
NS6W	6×1*	3.47
ENEB	7×7	3.33

All internal series resistance values in Table 4.5 appear rather randomly spread at first sight. Using the formulas for resistance substitution in series and parallel connections, it is however possible to calculate an approximated value of the internal series resistance of each die separately. Such calculations show that, except for LED type BL3R containing low-power dies, all red AlGaInP emitters have series resistance values between 1.0 Ω and 1.5 Ω at 295 K room temperature. Analogously, if the LED modules containing low-power emitters are once again not taken into account, all InGaN emitters (green, blue and white) have internal series resistance values between 1.0 Ω and 3.0 Ω typically.

For the measured circuits containing low-power emitters (BL3R, BL3G, BL3B and NS6W) internal series resistance values of 16.19 Ω, 41.15 Ω, 26.13 Ω and 20.02 Ω have been found, respectively. These values seem to be abnormally high in comparison with the series resistance values of the individual high-power dies. Until now however, no decent explanation for these results has been formulated.

By use of Eq. (4.26) the internal series resistance of each LED module under consideration has been calculated from its forward current-voltage characteristic measured at five different temperatures. For LED type PG1A-1, measurement results have been plotted in Fig. 4.9. One data point at 400 K has been added in order to decrease the error on the experimental data fit.

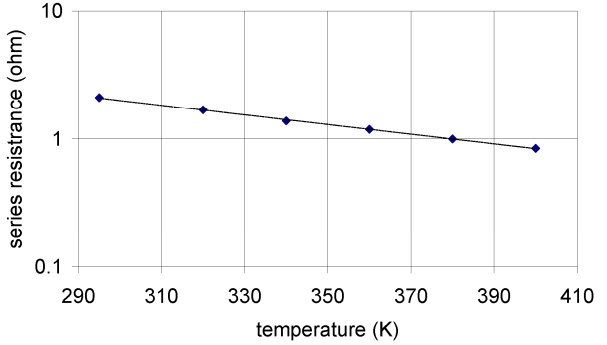

Fig. 4.9: Measured temperature dependence of the internal series resistance (blue diamonds) with exponential fit (solid line) for LED type PG1A-1.

Fig. 4.9 shows that the temperature dependence of the internal series resistance follows a clear negative exponential behaviour. This exponential behaviour has been found experimentally for all LED packages measured, which corresponds to the known temperature dependence of the resistivity of pure and doped semiconductors at relatively high junction temperatures [Kittel, 1996]. Therefore, the internal series resistance of each diode module can be modelled as a function of the (generalized) junction temperature using the following equation:

$$R_S(T) = R_{S,r} \exp\left(-\frac{\Delta T}{T_R}\right) \tag{4.27}$$

with $R_{S,r}$ and T_R the exponential fitting parameters. ΔT equals $T - T_r$, i.e. the difference between the junction temperature and a reference temperature T_r. The denominator T_R can be considered the characteristic temperature of the internal series resistance, in analogy with the experimental characteristic temperature of the LED light output (see chapter 5). $R_{S,r}$ corresponds to the internal series resistance of the diode at T_r. A discussion on these $R_{S,r}$ values would completely similar to that on the measured internal series resistances (for 295 K junction temperature) in section 3.1. The characteristic temperature of the internal series resistance of LED type PG1A-1 is determined to be about 115 K. Considering all LED types that have been selected, the characteristic temperature values are spread over about a decade (100 K to 1000 K).

By combining Eqs. (4.25) and (4.27), the forward voltage model in Eq. (4.22) can be extended in order to be valid for all drive currents chosen within the exponential or series resistance region (regions (b) and (c) in Figs. 4.1 and 4.7):

$$U_f(I,T) \approx IR_{S,r} \exp\left(-\frac{\Delta T}{T_R}\right) + \gamma(I)T + \delta \tag{4.28}$$

This equation describes the diode forward voltage as a function of drive current and (generalized) junction temperature and may be used for modelling both single-die and multi-die packages.

Note that despite the exponential behaviour of the internal series resistance, the forward voltage is often more roughly approximated by a linear expression in the internal series resistance region as well [Gu, 2004] [Xi, 2004] [Chonko, 2006]. Indeed, due to the relatively high characteristic temperature T_R in Eq. (4.27), the junction temperature dependence of the internal series can be expressed as:

$$R_S(T) \approx -\frac{R_{S,r}}{T_R}\Delta T + R_{S,r} \tag{4.29}$$

Taking into account this simplification, the slope of the forward voltage variation with junction temperature becomes $-IR_{S,r}/T_R + \gamma(I)$, while in the intercept the additional term $R_{S,r}$ appears.

4.5.2. Ohmic junction heating

Several LED types have been driven by a wide range of constant drive currents (10 µA, 100 µA, 1 mA, 10 mA, 100 mA, and 350 mA normal drive current). During the first minute of operation, junction temperature of the diode package was determined every 1.5 s by use of the voltage-temperature calibration curves described in the previous sections. Measurement results of the junction temperature increase, i.e. the difference between junction and ambient temperature, for the three highest constant drive currents applied to LED type XREW are plotted in Fig. 4.10.

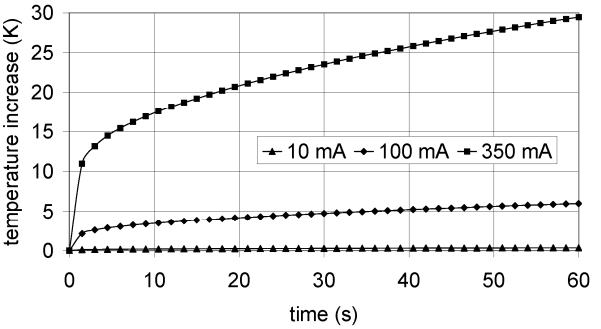

Fig. 4.10: Junction temperature increase for different drive currents applied to LED XREW.

Junction temperature increases by about 1 K, 6 K and 29 K for the 10 mA, 100 mA, and 350 mA drive currents respectively. For all currents below 10 mA, diode junction temperature rise appears to be negligible. This 10 mA drive current approximately corresponds to the upper bound of the exponential current-voltage region of the same diode type in Fig. 4.1. Apparently, junction temperature only significantly increases when a certain current (or input power) level is exceeded, partially depending on the internal series resistance of the complete LED package. Analogous results have been found for other single-die and multi-die packages.

Knowledge of the internal series resistance value allows to determine the power loss due to this resistance at normal drive current I_n. This electrical power loss ΔP_R equals $I_n \Delta U_f$. By use of Eq. (4.26) this can be reformulated as

$$P_R(I,T) = I_n^2 R_S(T) \tag{4.30}$$

Comparing this power loss with the total electrical input power ($P = I_n U_f$) at normal drive current and 295 K, one obtains the relative amount of power guided directly into the internal series resistance, resulting in ohmic junction heating (see Table 4.6).

Table 4.6: Internal series resistance, normal drive current, electrical input power and relative power loss due to the internal series resistance, all at 295 K junction temperature.

LED	R_S (Ω)	I_n (A)	P (W)	$\Delta P_R / P$
F51B-0	1.94	0.350	1.282	0.19
F51G-0	2.79	0.350	1.371	0.25
F51R-0	1.52	0.350	0.859	0.22
LK2R-1	2.04	0.350	1.001	0.25
NCCW-1	2.42	0.350	1.273	0.23
PG1A-1	2.13	0.350	1.310	0.20
XREW	1.01	0.350	1.141	0.11
BL4B	4.12	0.350	2.763	0.18
BL4G	4.83	0.350	2.442	0.24
BL4R	2.10	0.350	1.548	0.17
HSD2-1	0.40	0.700	2.512	0.08
LW6C-1	1.58	0.700	4.960	0.16
E3BN	2.91	0.700	12.959	0.11
NT5B	1.86	1.400	16.727	0.22
NT5G	1.91	1.400	15.268	0.25
NT5R	1.02	1.400	9.857	0.20
NT52	3.37	1.400	32.900	0.20
BL3B	1.34	1.170	9.161	0.20
BL3G	2.11	1.170	9.136	0.32
BL3R	0.83	1.170	5.741	0.20
W114	0.64	1.400	5.320	0.24
NS6W	3.47	0.300	1.141	0.27
ENEB	3.33	2.400	55.200	0.35

From the last column of Table 4.6 can be concluded that at normal drive current between about 10 % and 35 % of the initial electrical input power is directly converted into heat due to the internal series resistance of the complete LED device. This makes the internal series resistance the second biggest loss factor of a LED device (after external quantum efficiency, see chapter 8). These high values are due to the quadratic dependence of electric power loss on the drive current according to Eq. (4.30) and have a large impact on the temperature of the diode junction. Light-emitting diode manufacturers and end-users should know this when applying high (normal) drive currents. E.g. replacing one diode package by three devices at one third of the current should increase the overall light source performance and strongly reduce junction heating (see also chapter 8). Prices and volumes of packages and heat sinks will determine the best design option for LED manufacturers.

4.6. Best practice

4.6.1. Voltage-temperature calibration

Eqs. (4.24) and (4.28) can both be constructed from only two current-voltage measurements at two different but constant junction temperatures. γ and δ can indeed be determined from the Shockley behaviour, whereas $R_{S,r}$ and T_R can be found by fitting the differences between both measured and exponential current-voltage curves. For practical junction temperature measurements however, it is more convenient to stick with Eq. (4.24), valid only within the exponential current-voltage region. This equation can be easily inverted in order to calculate the junction temperature from forward voltage measurements at a fixed drive current:

$$T\left(U_f\right) \approx \frac{U_f - \delta}{\gamma} \tag{4.31}$$

The intercept δ equals about 3 V for the blue emitters. As mentioned before, the δ values of the red LEDs do not correspond very well. Consequently, if one would accept a value of 3 V for blue emitters in general, one single I-U_f characteristic measurement at room temperature (e.g. 300 K) may be sufficient to calculate the forward voltage slope and determine $U_f\left(T\right)$ for all relevant junction temperatures. Eq. (4.24) can indeed also be transformed into

$$T \approx \frac{U_f - 3}{U_f\left(300\right) - 3} 300 \tag{4.32}$$

Unfortunately, this implementation causes unacceptable errors on the temperature in practice. Assuming a typical value for $U_f\left(300\text{ K}\right)$ of 3.5 V with an uncertainty of 200 mV (see B in Table 4), the relative error on temperature can be calculated:

$$\frac{dT}{T} = \left| -\frac{dB}{U_f - B} \right| \approx \frac{0.2}{0.5} = 0.4 \tag{4.33}$$

Another major disadvantage of a single current-voltage measurement at room temperature is the impossibility to verify whether the chosen measurement current I_0 lies within the intermediate current interval for all relevant temperatures (about 300 K to 400 K). Therefore, always two I-U_f measurements at about the most extreme relevant temperatures should be performed in practice. This procedure allows choosing I_0 properly and calculating the corresponding forward voltage slope and intercept immediately from the measurement results as follows:

$$T \approx \frac{T_2 - T_1}{U_f(T_2) - U_f(T_1)} \left[U_f - U_f(T_1) \right] + T_1 \tag{4.34}$$

with T_1 and T_2 the extreme temperatures.

4.6.2. Junction temperature determination

The measurement current I_0 generally differs from the normal drive current in practical applications. In order to minimize the influence of the forward voltage measurement at I_0 on the junction temperature, the drive current has to be lowered to a measurement current only during a millisecond or less. Forward voltage measurements immediately before and after this short step-down period have shown that junction temperature variation due to the measurement pulse is indeed negligible. In order to increase reliability, the forward voltage of a few subsequent measurement pulses (e.g. every 10 s) can be averaged. This drive current time schedule is represented schematically in Fig. 4.11.

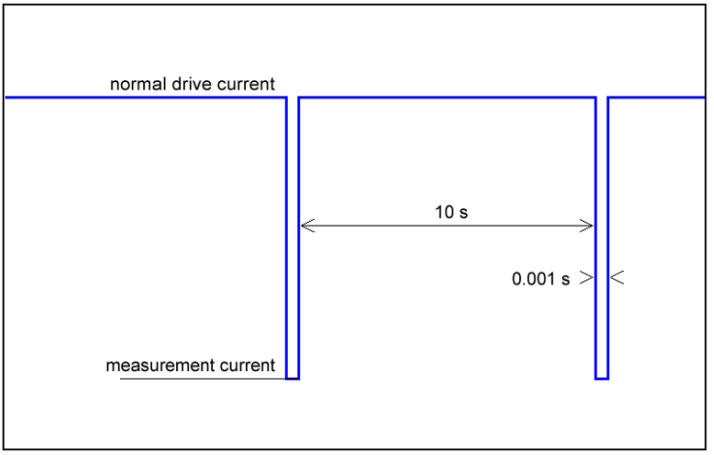

Fig. 4.11: The junction temperature measurement technique for a practical set-up conducted at normal drive current and measured every 10 s by lowering the drive current for about 1 ms.

In LED datasheets, typical maximum junction temperature values of about 400 K can be found. The junction temperature measurement technique described above can thus be used to monitor increasing temperatures in practical applications. In combination with optical measurements, the variation of diode characteristics as flux and efficiency can be studied as a function of junction temperature, or thermal resistances can be precisely calculated. This is shown in the following chapters.

4.7. Summary and conclusions

Current-voltage characteristics of ten commercial single-die high-power LEDs have been measured at six different temperatures ranging between 295 K and 400 K. For InGaN based emitters, three current regions are clearly distinguished. The low current region is dominated by leakage currents, while the high current-voltage region is strongly influenced by the internal series resistance. The intermediate current region is modelled with a generalized Shockley equation using a temperature independent ideality factor which is also included in the expression for the saturation current. Additionally, the variation of the semiconductor band gap with temperature has been included. From this model, a linear relation between the forward voltage and the junction temperature can be expected, but only for a rather limited range of drive currents. These conclusions have been confirmed by measurements, with coefficients of determination exceeding 0.99 for all devices under test.

The current-voltage characteristics of ten multi-die LEDs, ranging from two to a few hundred dies, have been recorded at different ambient temperatures as well. The results allowed validating the forward voltage model using a generalized junction temperature. Light-emitting diode ideality factor and internal series resistance values of multi-die packages could be linked to those of individual dies.

For both single-die and multi-die packages, the initial forward voltage model has been extended with the temperature dependence of the diode's internal series resistance. All internal series resistances show a negative exponential junction temperature dependence. In correspondence with the initial forward voltage model, this exponential behaviour is often approximated by a linear junction temperature dependence.

Apparently, the junction temperature only significantly increases when a certain current level is exceeded, depending on the internal series resistance of the complete LED package. Indeed, due to the internal resistance, about 10 to 35 % of the initial electrical input power is directly converted into heat at normal drive current. The internal series resistance is therefore the second biggest reason for junction heating in LED lighting applications.

For practical use, the voltage intercept could be deduced from the bulk semiconductor band gap at room temperature. However, accurate junction temperature determination is only possible if at least two calibration measurements are performed.

5. Power modelling and junction temperature determination from forward current

5.1. Goals

A junction temperature determination technique from voltage-temperature modelling and calibration measurements has been proposed in the previous chapter. This chapter additionally shows that the junction temperature and input and output power of diode packages can be determined from forward current directly. A current-temperature relation is constructed from the thermal resistance definition for LED packages, linking the diode's junction temperature and dissipated power. The dissipated power is modelled by examining the electrical power, radiant flux, and their difference as a function of current and temperature. Models can be used to simulate the junction temperature as a function of drive current and thermal resistance in practical applications. As a result, electrical input power and optical power can be calculated for each drive current as well. Similar modelling and simulation efforts have been reported by other researchers [Baureis, 2005] [Deshayes, 2005] [Salsbury, 2007] [Hui, 2009] [Moolman, 2009] [Li, 2010], but never before a simple expression for electrical power and flux variation with both current and junction temperature has been provided. Such comprehensive models can be easily used by diode or application manufacturers to predict solid-state lighting performance [Salsbury, 2007].

5.2. Experiments

Nine commercial high-power light-emitting diodes of different types and manufacturers have been selected for examination. The selection consisted of two red, two green, two blue, and three phosphor-white devices. Except for LED E3BN containing six chips, all devices are single-die packages (see Table 5.2).

The LED devices under test have been placed on commercially available heat sinks in a 295 K constant ambient. The Keithley 2440 5A SourceMeter has then been used to apply 150, 250, 350, and 450 mA constant forward currents. When thermal equilibrium was reached (on average after about thirty minutes), corresponding junction temperatures have been determined from the voltage-temperature calibration curves described in chapter 4.

The radiant flux and electrical input power of all LEDs under consideration have been determined as a function of drive current and junction temperature

independently. The number of data acquisition points has been limited to four temperature (300, 320, 340 and 360 K) and four current (150, 250, 350 and 450 mA) values within five measurement series, i.e. three at constant current and two at constant junction temperature, respectively.

5.3. Steady-state temperature conditions

In thermal steady-state, a diode's junction temperature, thermal resistance and power are connected by the following equation (see section 8.3.1 in chapter 8):

$$T = R_{T,j-r}\left(P - \Phi_e\right) + T_r \tag{5.1}$$

where $R_{T,j-r}$ is the thermal resistance between the junction at temperature T and a reference point at temperature T_r. The reference temperature is commonly measured at a particular point on the board or can be coincident with the ambient temperature. Both the reference point and $R_{T,j-r}$ have to be precisely defined after the LED package has been integrated into its final application. The factor $P - \Phi_e$ represents the difference of electrical input power P and radiant flux Φ_e of the LED, often denoted as dissipated power P_d.

A changing drive current will result in electrical power, radiant flux and junction temperature changes. These quantities have been determined independently by use of the methods described before. Measurement results for LED XREW on two different heat sinks in a 295 K ambient are shown in Table 5.1.

Table 5.1: Junction temperature and power measurement results for LED XREW mounted on a small and large heat sink at 295 K ambient temperature.

	small heat sink			large heat sink		
I (A)	P (W)	Φ_e (W)	T (K)	P (W)	Φ_e (W)	T (K)
0.15	0.451	0.102	309	0.455	0.107	302
0.25	0.773	0.159	321	0.785	0.168	307
0.35	1.101	0.209	334	1.127	0.223	313
0.45	1.435	0.250	346	1.476	0.273	320

From the data in Table 5.1 can be concluded that electrical power, radiant flux and junction temperature increase with the drive current. Junction temperature remains lower for the large heat sink, although input power and flux values are higher.

Eq. (5.1) predicts that the thermal resistance can be obtained from the slope of the graph relating junction temperature and dissipated power. This is confirmed by the data in Fig. 5.1. Thermal resistances between junction and ambient have been determined to be 43.1 K/W and 20.8 K/W for LED XREW mounted on the small and large heat sink, respectively.

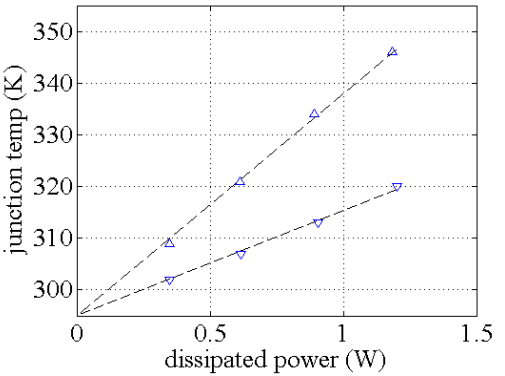

Fig. 5.1: Relationship between junction temperature and dissipated power for LED XREW when using a small (triangles) and large (inverted triangles) heat sink. The dashed black lines represent linear fittings with intercept set to 295 K ambient temperature at zero input power.

The electrical input power P and radiant flux Φ_e in Eq. (5.1) explicitly depend on both forward current and junction temperature. Eq. (5.1) can therefore be considered an implicit equation describing the junction temperature. Solving this equation would allow determining the junction temperature as a function of forward current only. In what follows, the dependence of input power and flux on current and temperature will be investigated.

5.4. Power modelling

5.4.1. Electrical input power

The description of a LED's electrical input power variation as a function of current and junction temperature is started from its more familiar current-voltage (I-U) behaviour. At sufficiently high currents, this behaviour is typically modelled by an ideal diode characteristic with an additional series resistance R_S (see chapter 4):

$$I = C_S \exp\left[-\frac{E_g}{nkT}\right]\exp\left[\frac{e(U - IR_S)}{nkT}\right] \tag{5.2}$$

with E_g the energy gap of the diode's compound semiconductor, n the LED ideality factor, k the Boltzmann constant, e the electron charge, and C_S a quasiconstant combining several physical parameters. By solving Eq. (5.2) for the forward voltage and multiplying by current, one obtains for the electrical power:

$$P(I,T) = I^2 R_S(T) + I\frac{E_g(T)}{e} + \frac{nkT}{e} I \ln\left(\frac{I}{C_S}\right) \tag{5.3}$$

At constant junction temperature, the first two terms of Eq. (5.3) indicate that the electrical input power increases at least quadratically with forward current. As the variation of the logarithmic contribution in the third term only has a minor effect, a second order polynomial function with zero intercept could be proposed. The electrical power at constant junction temperature T_0 can thus be modelled as:

$$P(I,T_0) \approx \alpha_P I^2 + \beta_P I \tag{5.4}$$

Eq. (5.4) is confirmed for all LEDs under consideration at 300 K in Table 5.2 and illustrated by measurement data for LED XREW at two different temperatures in Fig. 5.2. The occurrence of higher current and temperature coefficients for LED E3BN can be attributed to its multi-die nature.

According to Eq. (5.3) and the assumption made above, the coefficient α_P in Eq. (5.4) should be close to the internal series resistance value. At 300 K the fitting parameter α_P of LED XREW equals 1.02 Ω, in very good agreement with the value of 1.00 Ω obtained directly from the corresponding current-voltage characteristic.

Table 5.2: Fitting parameters and corresponding coefficients of determination R^2 for all LEDs' input power and radiant flux as a function of current and junction temperature.

LED	α_P	β_P	R^2	$\gamma_P(10^{-3})$	δ_P	R^2	α_F	β_F	R^2	$\gamma_F(10^{-3})$	δ_F	R^2
XREW	1.02	2.91	1.00	-1.20	1.50	0.99	-0.27	0.78	1.00	-0.51	0.38	0.99
XRCR	0.56	1.85	1.00	-0.84	0.97	0.99	-0.07	0.59	0.99	-0.71	0.41	0.99
XRCG	1.39	3.05	0.99	-1.75	1.77	0.99	-0.48	0.52	1.00	-0.10	0.16	0.96
XRCB	1.22	2.94	1.00	-1.56	1.65	0.99	-0.45	1.06	1.00	-0.67	0.52	0.99
W42D	0.90	2.90	1.00	-1.53	1.59	0.99	-0.16	1.02	1.00	-1.15	0.68	0.99
F51R	1.26	1.90	1.00	-1.04	1.14	0.99	-0.11	0.38	1.00	-0.59	0.32	1.00
F51G	2.66	2.93	1.00	-1.20	1.71	0.99	-0.17	0.25	0.99	-0.18	0.12	0.99
F51B	1.98	2.88	1.00	-0.40	1.37	1.00	-0.19	0.46	1.00	-0.32	0.23	0.99
E3BN	6.99	14.92	1.00	-2.23	6.72	0.99	-1.77	2.59	1.00	-1.51	1.15	0.99

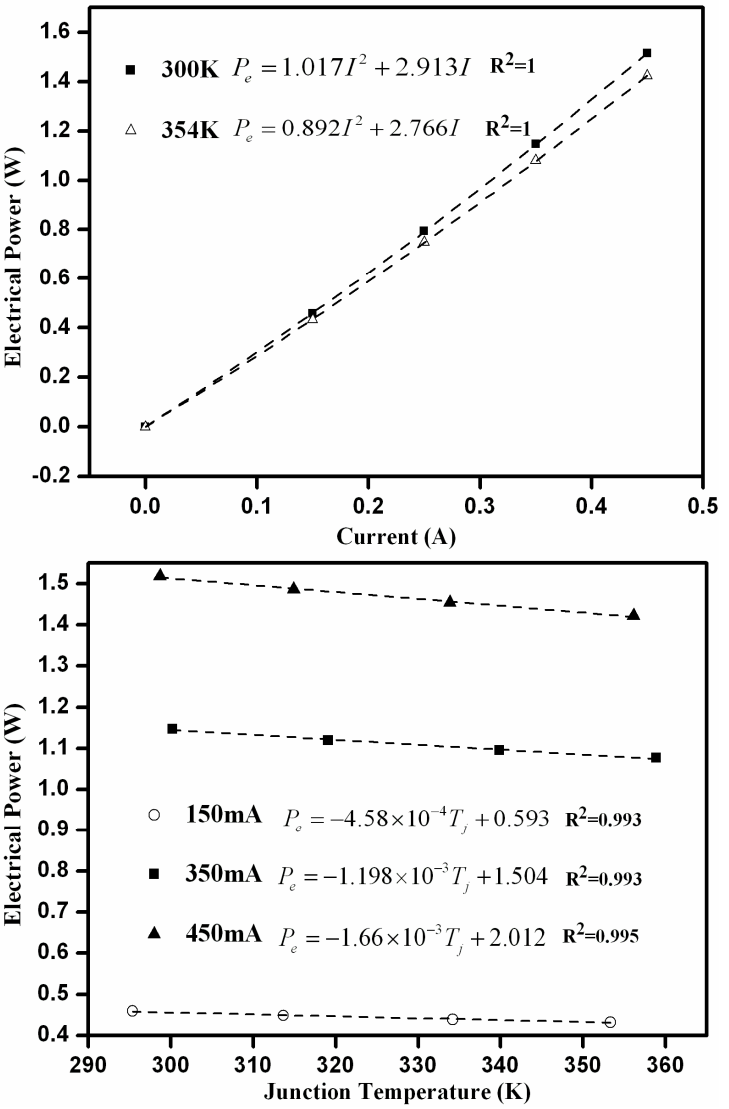

Fig. 5.2: Electrical input power of LED XREW as a function of forward current for two fixed temperatures (top) and as a function of junction temperature for three fixed drive currents (bottom).

The dependence of R_S and E_g on temperature has been written explicitly in Eq. (5.3). For practical temperature ranges, these dependences can be approximated by linear functions, while the variation of the ideality factor with junction temperature can be neglected (see chapter 4). These considerations suggest that for a constant forward current I_0, the electrical input power given by Eq. (5.3) varies more or less linear with temperature:

$$P(I_0,T) \approx \gamma_P T + \delta_P \tag{5.5}$$

The linear behaviour described by Eq. (5.5) is confirmed for all LEDs under consideration at 350 mA in Table 5.2 and illustrated by measurement data for LED XREW at three different currents in Fig. 5.2.

An analytical expression describing the electrical input power at any current or junction temperature within the range under consideration can now be constructed from one measurement series at constant current (e.g. an intermediate value of 350 mA) and one at constant junction temperature (e.g. 300 K). Indeed, as Eqs. (5.5) and (5.4) both represent a polynomial, the electrical input power can be expressed as a function of current and temperature [Carroll, 1961]:

$$\begin{aligned} P(I,T) &\approx \frac{P(I,300\text{ K})\,P(350\text{ mA},T)}{P(350\text{ mA},300\text{ K})} \\ &= \frac{\left(\alpha_P I^2 + \beta_P I\right)\left(\gamma_P T + \delta_P\right)}{P(350\text{ mA},300\text{ K})} \end{aligned} \tag{5.6}$$

with α_P and β_P obtained at 300 K, and γ_P and δ_P obtained at 350 mA. Eq. (5.6) can be rearranged as follows:

$$P(I,T) \approx \left(a_P I^2 + b_P I\right)T + c_P I^2 + d_P I \tag{5.7}$$

Coefficients a_P to d_P of all LEDs have been collected in Table 5.3. A surface plot corresponding to Eq. (5.7) has been constructed for LED XREW in Fig. 5.3. This surface can be compared with the data obtained for the other currents (150 and 450 mA) and temperature (354 K). A very good agreement with deviations smaller than 2 % between measured and calculated data has been found.

Table 5.3: Coefficients of the input power, radiant flux, and dissipated power variation with forward current and junction temperature.

LED	a_P (10^{-3})	b_P (10^{-3})	c_P	d_P	a_F (10^{-3})	b_F (10^{-3})	c_F	d_F	a_D (10^{-3})	b_D (10^{-3})	c_D	d_D
XREW	-1.06	-3.04	1.33	3.82	0.59	-1.69	-0.45	1.28	-1.65	-1.35	1.78	2.54
XRCR	-0.65	-2.16	0.76	2.50	0.25	-2.10	-0.15	1.21	-0.91	-0.06	0.90	1.29
XRCG	-1.97	-4.32	2.00	4.37	0.39	-0.42	-0.62	0.67	-2.36	-3.90	2.61	3.71
XRCB	-1.60	-3.87	1.70	4.10	0.95	-2.26	-0.74	1.75	-2.56	-1.61	2.43	2.35
W42D	-1.22	-3.91	1.27	4.06	0.56	-3.51	-0.33	2.07	-1.78	-0.40	1.60	1.99
F51R	-1.59	-2.41	1.74	2.62	0.43	-1.52	-0.24	0.84	-2.02	-0.89	1.97	1.78
F51G	-2.34	-2.58	3.36	3.71	0.47	-0.69	-0.31	0.46	-2.82	-1.89	3.68	3.25
F51B	-0.63	-1.09	2.17	3.16	0.45	-0.92	-0.32	0.78	-1.08	-0.16	2.49	2.38
E3BN	-2.57	-5.65	7.76	16.57	3.87	-5.49	-2.95	4.31	-6.45	-0.16	10.71	12.27

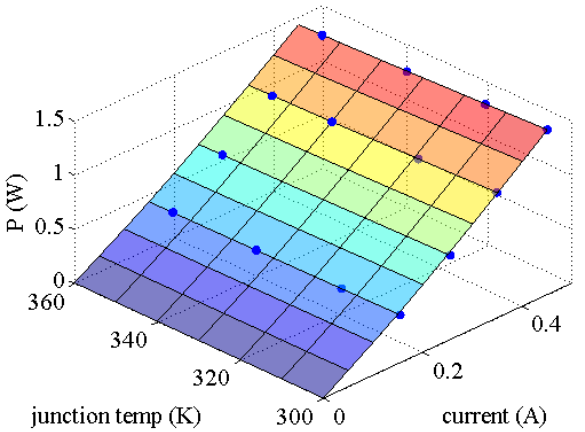

Fig. 5.3: Simulation of electrical input power of LED XREW as a function of forward current and junction temperature. The surface is constructed from the measurement data at 300 K constant junction temperature and 350 mA constant current only. Experimental results are represented by blue dots.

5.4.2. Radiant flux

The behaviour of radiant flux with current is theoretically described by a non-linear and a linear region [Deshayes, 2005]. The non-linear region is only relevant for very small forward currents. For normal drive currents only the linear region has to be considered. This linear behaviour is due to radiative recombination in the active layer and for single-colour emitters described by the following equation:

$$\Phi_e = C_L \times \eta_{EQ} \times I \tag{5.8}$$

with C_L a luminescence factor that can be considered constant and η_{EQ} the total quantum efficiency of the LED [Deshayes, 2005]. This total external quantum efficiency equals the product of internal quantum efficiency η_{IQ} and extraction efficiency η_{ext}. The extraction efficiency majorly depends on the LED chip configuration and is therefore assumed not to change with temperature. The internal quantum efficiency's temperature dependence can be expressed as follows [Schwegler, 1999]:

$$\eta_{IQ}(T) = \left[1 + \left(\frac{N_p \tau_{trap} N_{trap}}{N_n \tau_{rad} N_{rad}}\right) \exp\left(-\frac{E_{trap} - E_{rad}}{kT}\right)\right]^{-1} \tag{5.9}$$

with N_e, N_p, τ_i, N_i, and E_i the electron and hole concentration and lifetimes, concentrations and energies of radiative and non-radiative recombinations, respectively. The indices *trap* and *rad* account for trap and radiative related transitions, respectively.

For practical temperatures values (between about 300 and 400 K), Eq. (5.9) can be approximated by an exponential decrease with increasing temperature, attributed to the increase of non-radiative recombinations. This dependence has also been found experimentally and formulated as [Chhajed, 2005-1] [Schubert, 2006]:

$$\Phi_e(T) \propto \eta_{IQ}(T) \propto \exp\left(-\frac{T}{T_\Phi}\right) \tag{5.10}$$

The denominator T_Φ equals $\left(E_{trap} - E_{rad}\right)/k$ and is called the characteristic temperature of the radiant flux. This characteristic temperature is typically very high (order of 1000 K) and thus implies a weak temperature dependence [Schubert, 2006]. Analogous to the internal series resistance (see chapter 4), the internal quantum efficiency and radiant flux can therefore be approximated by a linear decrease with increasing junction temperature.

Although Eq. (5.10) is valid for single-colour diodes only, experimental results discussed in literature show that the quasi-linear radiant flux behaviour as a function of junction temperature can be considered valid for both single-colour and phosphor-white LEDs [Narukawa, 2007] [Hui, 2009].

The internal quantum efficiency decreases more or less linearly as a function of current as soon as sufficiently high currents are considered, and this for both single-colour and phosphor-white LEDs [Chen, 2008] [Ryu, 2009]. According to Eq. (5.8), a quadratic variation of output power with current is obtained as a result. Similar to Eqs. (5.4) and (5.5), it seems hence obvious to propose the following relationships for radiant flux:

$$\Phi_e\left(I,T_0\right) \approx \alpha_F I^2 + \beta_F I \tag{5.11}$$

$$\Phi_e\left(I_0,T\right) \approx \gamma_F T + \delta_F \tag{5.12}$$

with α_F, β_F, γ_F, and δ_F fitting parameters that can be determined from flux measurements at constant junction temperature and constant forward current, respectively. Similar results have been reported in literature [Deshayes, 2005] [Hui, 2009] [Moolman, 2009].

The validity of Eqs. (5.11) and (5.12) is confirmed for all LEDs under consideration in Table 5.2 and illustrated by measurement data for LED XREW at three different currents and two different temperatures in Fig. 5.4.

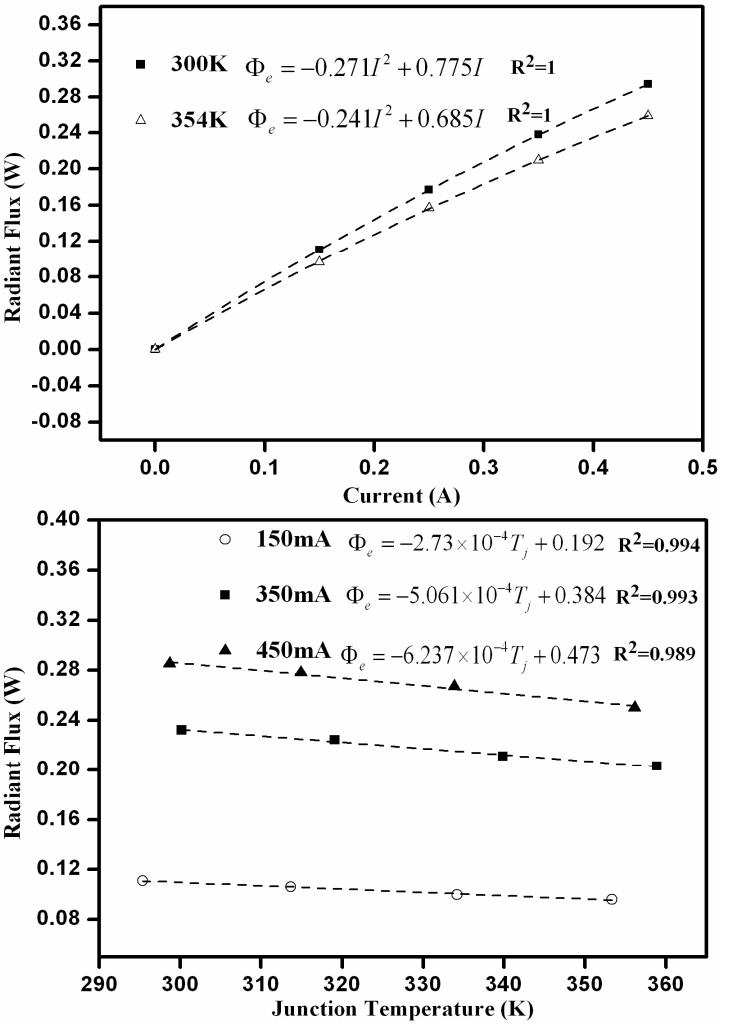

Fig. 5.4: Radiant flux of LED XREW as a function of forward current for two temperatures (top) and as a function of junction temperature for three currents (bottom).

In correspondence with the electrical power, an analytical expression describing the optical power at any current or junction temperature within the range under consideration can now be constructed from one measurement series at constant current and one at constant junction temperature:

$$\Phi_e(I,T) \approx \frac{\Phi_e(I,300\ \mathrm{K})\,\Phi_e(350\ \mathrm{mA},T)}{\Phi_e(350\ \mathrm{mA},300\ \mathrm{K})} = \frac{(\alpha_F I^2 + \beta_F I)(\gamma_F T + \delta_F)}{\Phi_e(350\ \mathrm{mA},300\ \mathrm{K})} \tag{5.13}$$

with α_F and β_F obtained at 300 K and γ_F and δ_F at 350 mA. Eq. (5.13) can be rearranged as

$$\Phi_e(I,T) = (a_F I^2 + b_F I)T + c_F I^2 + d_F I \tag{5.14}$$

Coefficients a_F to d_F of all LEDs have been collected in Table 5.3. In Fig. 5.5, the validity of Eq. (5.14) is checked for LED XREW at currents and temperatures other than 350 mA and 300 K respectively. Again, a very good agreement with deviations smaller than 2 % between measured and calculated data has been found.

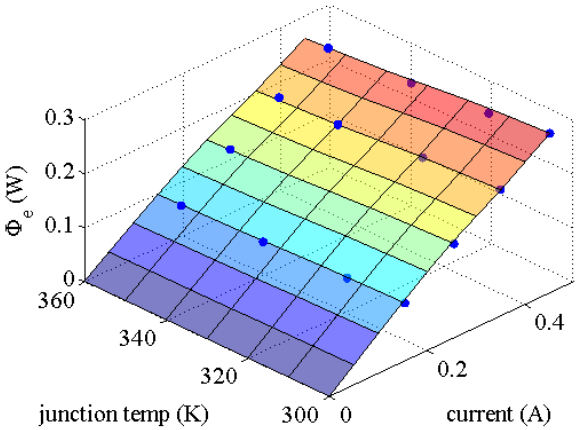

Fig. 5.5: Simulation of radiant flux of LED XREW as a function of forward current and junction temperature. The surface is constructed from the measurement data at 300 K constant junction temperature and 350 mA constant current only. Experimental results are represented by blue dots.

5.5. Junction temperature variation

Having found an expression for the forward current and junction temperature dependence of electrical power and radiant flux separately, one can easily determine an analytical expression for the dissipated power by subtracting Eq. (5.14) from Eq. (5.7):

$$P_d\left(I,T\right)=\left(a_D I^2+b_D I\right)T+c_D I^2+d_D I \tag{5.15}$$

For all devices under test, the coefficients a_D to d_D have been calculated as the difference between the respective input power and radiant flux coefficients (see Table 5.3).

In order to be able to determine the thermal steady-state junction temperature from forward current only, Eq. (5.15) has to be implemented in Eq. (5.1):

$$T \approx R_{T,j-r}\left[\left(a_D I^2+b_D I\right)T+c_D I^2+d_D I\right]+T_r \tag{5.16}$$

This implicit equation can be easily solved for junction temperature:

$$T\left(I\right)\approx\frac{R_{T,j-r}\left[c_D I^2+d_D I\right]+T_r}{1-R_{T,j-r}\left[a_D I^2+b_D I\right]} \tag{5.17}$$

5.6. Validation

Measured junction temperatures have been compared with values calculated by use of Eq. (5.17) for device XREW mounted on the small heat sink with 43.1 K/W thermal resistance between junction and ambient. In order to simplify data comparison, $T-T_r$ has been plotted as a function of forward current in Fig. 5.6, with T_r the ambient temperature. The agreement between measured and simulated data is very good. Deviations amount to a few percent only.

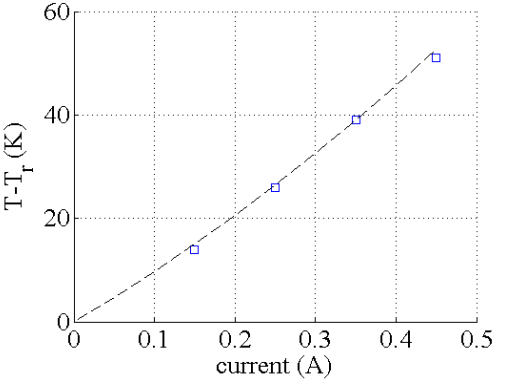

Fig. 5.6: Comparison between measured (blue squares) and calculated (black dashed line) junction temperatures for LED XREW on a fixed heat sink.

Note that all a and b coefficients are roughly a factor 1000 smaller than the corresponding c and d parameters (see Table 5.3). Moreover, the temperature dependencies of input power and flux are partially compensated in coefficient b_D. The second term in the denominator of Eq. (5.17) may be omitted as a result. The parameter values in Table 5.3 show that the junction temperature error introduced by this additional simplification equals about 3 to 4 % at most.

The junction temperature and power models presented have been additionally validated by placing LEDs XREW (single-die) and E3BN (multi-die) on two different heat sinks in a 295 K ambient. Junction-to-ambient thermal resistances have been determined to amount 43.1 and 14.1 K/W, respectively. Given the forward current, junction temperature values have been first calculated by use of Eq. (5.17). Inserting these temperatures and currents in Eqs. (5.7) and (5.14) allowed computing the corresponding electrical powers and radiant fluxes afterwards. Measured and simulated data for 150 and 450 mA forward currents are compared in Table 5.4. Maximum deviations have been found to be of the order of a few percent.

Table 5.4: Measured and simulated data for a 150 and 450 mA forward current applied to devices XREW and E3BN mounted on two different heat sinks.

		measured			simulated		
LED	I (mA)	T (K)	P (W)	Φ_e (W)	T (K)	P (W)	Φ_e (W)
XREW	150	309	0.451	0.102	310	0.454	0.107
	450	346	1.435	0.253	346	1.441	0.263
E3BN	150	322	2.286	0.330	324	2.367	0.342
	450	397	7.710	0.639	396	7.816	0.675

5.7. Best practice

The junction temperature and power variation with forward current of a fixed LED system can be simulated from four calibration measurements only:
From three integrating sphere measurements on the LED package, the a to d coefficients of electrical input power, radiant flux, and the dissipated power can be determined. These three measurements consist of one reference measurement (e.g. at 350 mA and 300 K) and two measurements at a different forward current and junction temperature, respectively (e.g. at 150 mA, 300 K and at 350 mA, 330 K).
When the LED is placed on a heat sink afterwards, one steady-state input power measurement allows calculating the junction temperature from Eq. (5.7). By use of Eqs. (5.1) and (5.15) the junction-to-reference thermal resistance is immediately known as a result. After inserting this thermal resistance value into Eq. (5.17), the junction temperature can be determined at any forward current. Corresponding input power and radiant fluxes of the system can then be calculated from Eqs. (5.7) and (5.14), respectively.

Note that LED performance prediction by application designers would be largely simplified if the power model parameters and thermal resistance values were known in advance. Although some device manufacturers provide experimental figures of the input and output power variation with current and temperature already, explicit inclusion of the above power coefficients in datasheet specifications could be a helpful future option.

5.8. Summary and conclusions

A current-temperature relation has been constructed from the thermal resistance definition for LED packages, linking the diode's junction temperature and dissipated power. Electrical input power and optical radiant flux variations with current and temperature of nine commercial LED packages have been determined experimentally and modelled. For both input power and flux, a quadratic dependence on current and a linear dependence on junction temperature have been found with coefficients of determination exceeding 0.96. Combining these dependencies has lead to simple expressions for the electrical input power, radiant flux, and their difference as a function of forward current and junction temperature. These models can be used to simulate the junction temperature as a function of drive current and thermal resistance in practical applications. As a result, electrical input power and optical power can be calculated for each current as well. The method has been validated by comparing measured and simulated junction temperature and power values of two LEDs mounted on a large and small heat sink, respectively. Maximum deviations have been found to be of the order of a few percent. In practice, the junction temperature and power of integrated LED packages can be determined from forward current directly by performing four calibration measurements only. However, explicit inclusion of the power model coefficients in datasheet specifications could be a helpful future option for diode application designers to predict solid-state lighting performance.

6. Modelling LED spectra and their junction temperature dependence

6.1. Goals

Spectral radiant flux is the primary optical characteristic of a light source, determining the luminous flux and colour. Much research is dedicated to the modelling of LED spectra and their junction temperature dependence, allowing for the simulation of optical properties in various applications. However, most of the spectral radiant flux models that have been published so far are purely mathematical. This chapter has the intention to include physics-based considerations as much as possible.

Spectral radiant fluxes of commercial LED packages have been measured in a custom made integrating sphere at several junction temperatures. For single-colour emitters, a spectrum model at 300 K is constructed where the Boltzmann free carrier distribution and carrier temperature are included explicitly. The model is then extended with the carrier temperature variation and band gap energy shift with junction temperature. As a result, the skewness variation, peak frequency shift, and peak value change of the spectrum with temperature can be predicted. On the other hand, a single Gaussian function with temperature dependent peak value, peak frequency, and peak width appears to be sufficient for fluorescence spectrum modelling. The models are validated by comparing flux and colour coordinates of measured and simulated spectra at 340 K junction temperature.

6.2. Situation

The spectral radiant flux is the primary LED optical characteristic, determining luminous flux and colour. A lot of effort has been attributed to model the LED spectral flux and its variation with junction temperature. One of the first attempts consisted of a rather simple LASTIP simulation of previously measured LED and laser spectra [Kuo, 2000]. In 2005 however, a Gaussian spectrum model appeared more successful [Uchida, 2005] and this model simplified incorporation of the peak wavelength variation with junction temperature [Chhajed, 2005-2]. Very soon afterwards, a double Gaussian model has been presented [Ohno, 2005], which is nowadays still used for lighting calculations by the International Commission on Illumination (CIE). A more general approach based on the double Gaussian model has been published in 2006 [Man, 2006]. In 2008 a variant of the split Gaussian

function with a different exponential behaviour on each side of the maximum has been reported to be a more simplified approach, still containing the junction temperature as a free parameter [Chou, 2008]. More recently an evaluation of several LED spectrum approximations has been published [Reifegerste, 2008], but due to the large number of fitting parameters an easy-to-use modelling approach is not provided. Furthermore, most spectral radiant flux models that have been published so far are purely mathematical and any link with underlying physical principles is missing. Moreover, integration of the junction temperature variation into the initial model parameters often results in piecewise defined and complex models.

In this chapter, a spectrum model is constructed where the Boltzmann exponential behaviour with carrier temperature variation, band gap energy shift and the increase of the non-radiative recombination rate with junction temperature are included explicitly. In a first step, an experimental spectrum at a particular temperature is modelled with two exponentials and a Gaussian function, using frequency as the main variable. Afterwards, peak frequency, absolute spectrum power and spectrum skewness variation with temperature are implemented. The model allows for very accurate simulations of single-colour and phosphor-white LED spectra at any temperature.

6.3. Experiments

Two red, two green, two blue, and one white commercial LED packages have been selected from two manufacturers, being Seoul Semiconductor and Cree. A nominal drive current of 350 mA has been selected, resulting in an input power of about 1 W. The junction temperature has been determined according to the forward voltage method described in chapter 4. The total spectral radiant flux has been measured for each package at five junction temperatures selected between 290 K and 340 K.

6.4. Single-colour spectrum

6.4.1. Spectrum at constant temperature

Two typical experimental single-colour light-emitting diode spectra for the same LED at two junction temperatures are shown in Fig. 6.1. With increasing temperature, a decrease of peak value and an increase of peak wavelength and skewness can be observed.

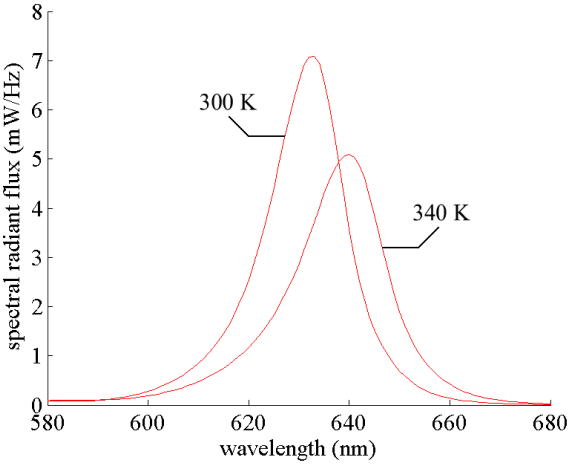

Fig. 6.1: Experimental spectra of LED F51R-1 at two different junction temperatures.

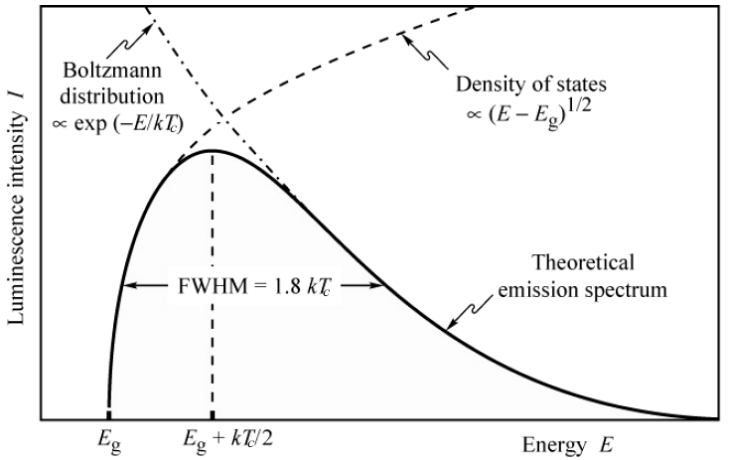

Fig. 6.2: Theoretical light-emitting diode spectrum as a product of the density of energy states above the band gap energy and a Boltzmann distribution [Schubert, 2006].

In theory, the photon energy distribution of a light-emitting diode is determined by the product of the density of energy states within the allowed energy band and a Boltzmann energy distribution (see Fig. 6.2). The Boltzmann distribution is proportional to $\exp(-E/kT_c)$, i.e. the energy distribution of a charge carrier gas of electrons and holes at a carrier temperature T_c. This carrier temperature is typically higher than the diode junction temperature T [Schubert, 2006]. On the other hand, the density of energy states above E_g is proportional to $(E-E_g)^{1/2}$ for bulk semiconductors. This expression should be replaced by a step-function when one degree of freedom for electron propagation is eliminated, but often the $(E-E_g)^{1/2}$

factor is retained as an approximation for the density of energy states for multiple quantum well light-emitting diodes as well [Deshayes, 2005] [Schubert, 2006].

One can easily show that the product of the theoretical expressions for the low and high energy slope of the spectrum has its maximum at $E_g + kT_c/2$, with k the Boltzmann constant. From these theoretical considerations, it seems more appropriate to examine LED spectra taking photon energy or frequency as the main parameter ($E = h\nu$ with h the Planck constant) and using a logarithmic scale [Vaitonis, 2008]. This is illustrated in Fig. 6.3.

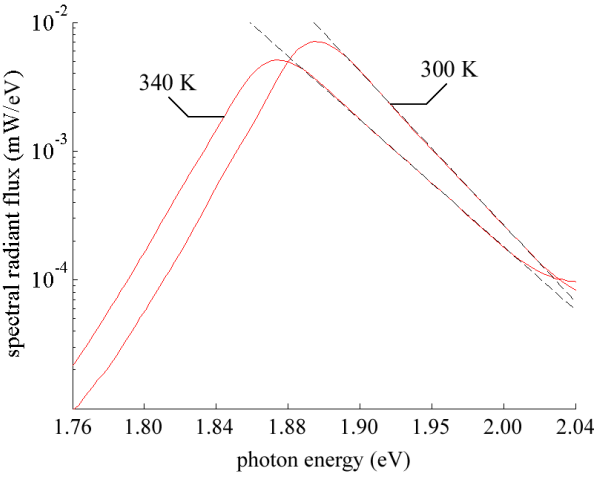

Fig. 6.3: Experimental spectra of LED F51R-1 on a logarithmic scale and with photon energy as main variable. The dashed lines show the Boltzmann exponential behaviour.

In Fig. 6.3, the Boltzmann exponential behaviour beyond the peak energy can be easily recognized and the slope decrease with junction temperature can be predicted as well. The spectrum's FWHM (full width at half maximum) and its temperature dependence are determined by both slopes. However, the sharp spectrum cut-off at the low energy side of the peak frequency as predicted by theory is not observed. The measured spectra show an exponential behaviour even on the low energy slope. Similar results have been reported in literature [Chhajed, 2005-2] [Gessmann, 2003] and have been attributed to thermal agitation of the diode's crystal lattice [Deshayes, 2005]. This behaviour justifies the construction of a spectrum model using frequency as variable and starting from an exponential behaviour on both sides of the spectrum peak. A first modelling attempt containing a combination of two exponentials has been given by [Chou, 2008]:

$$\Phi_{e,\lambda} = \frac{2S_0}{\exp\left[\dfrac{\lambda-\lambda_p}{B(\lambda)}\right] + \exp\left[-\dfrac{\lambda-\lambda_p}{B(\lambda)}\right]} \tag{6.1}$$

with S_0 the spectral intensity at the peak wavelength λ_p and $B(\lambda)$ a piecewise defined asymmetrical line width. It is however clear that the spectrum model in Eq. (6.1) lacks any physics-based background. In order to insert the Boltzmann behaviour explicitly, this equation is adapted as follows:

$$\Phi_{e,\nu} = \frac{1}{S_1 \exp\left[-a\left(\nu-\nu_p\right)\right] + S_2 \exp\left[\frac{h}{kT_c}\left(\nu-\nu_p\right)\right]} \tag{6.2}$$

with ν_p the experimental peak frequency and S_1, S_2 a and T_c four positive fitting parameters. Expression (6.2) does not longer contain any piecewise defined parameters. In practice, S_1 and a on one hand and S_2 and T_c on the other hand are determined from two separate exponential fits to the low energy and high energy tail of the diode spectrum, respectively.

An experimental diode spectrum at 300 K constant junction temperature is plotted in Fig. 6.4, together with the simulation based on Eq. (6.2). This plot shows that the exponential behaviour described by Eq. (2) is not able to model the complete spectrum shape. However, the difference between the experimental curve and the curve according to Eq. (6.2) can be approximated by a Gaussian function. Therefore, a Gaussian function is added, resulting in the following analytical model:

$$\Phi_{e,\nu} = \frac{1}{S_1 \exp\left[-a\left(\nu-\nu_p\right)\right] + S_2 \exp\left[\frac{h}{kT_c}\left(\nu-\nu_p\right)\right]} + S_3 \exp\left[-\left(\frac{\nu-\nu_G}{b}\right)^2\right] \tag{6.3}$$

with S_3, b and the peak frequency of the Gaussian function (ν_G) acting as three additional parameters. Eq. (6.3) can be considered a variant of the double Gaussian model presented by Ohno [Ohno, 2005].

Although seven parameters have to be determined for the description of a diode spectrum, the fitting approach is still very basic. Two parameters are determined from each tail of the spectrum resulting in Eq. (6.2). After subtraction of this equation from the measured spectrum, a Gaussian fit provides the remaining three parameters.

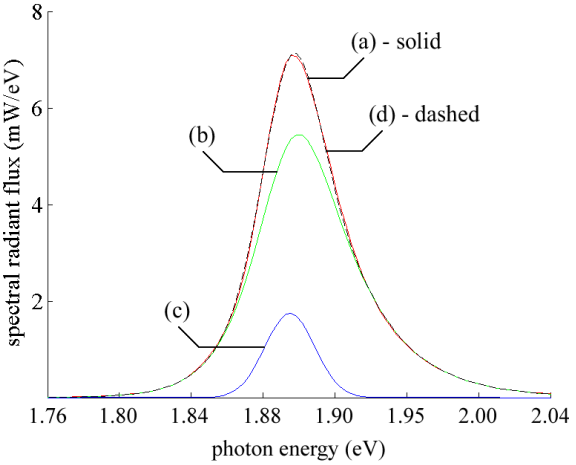

Fig. 6.4: The solid red line (a) corresponds to the measured spectrum of LED F51R-1. The green line (b) represents the spectrum model according to Eq. (6.2), while the blue line (c) represents the Gaussian fit of the difference between (a) and (b). The dashed black line (d) is the simulated spectrum according to the model of Eq. (6.3).

The spectrum model as described by Eq. (6.3) has been applied to all single-colour devices at a constant junction temperature of 300 K. The corresponding fitting parameters have been collected in Table 6.1.

Table 6.1: Experimental peak frequencies and fitting parameters for all LEDs at $T = 300$ K. Coefficients of determination R^2 have been added for the Gaussian fits. For the exponential fits, all R^2 values exceed 0.99.

LED	ν_p (10^{14} Hz)	S_1^{-1} (mW)	a (10^{-14} Hz^{-1})	S_2^{-1} (mW)	T_c (K)
F51R-1	4.736	73.450	22.556	126.200	369.8
XRCR	4.738	10.676	22.370	14.022	322.8
F51G-1	5.701	4.152	7.378	2.248	421.8
XRCG	5.799	9.277	6.809	5.819	588.0
F51B-1	6.664	9.741	7.773	19.770	418.2
XRCB	6.503	30.361	7.971	26.152	481.8

LED	S_3 (mW)	b (10^{14} Hz)	ν_G (10^{14} Hz)	R^2
F51R-1	1.597	0.051	4.721	0.990
XRCR	4.488	0.045	4.731	0.996
F51G-1	-0.219	0.098	5.585	0.873
XRCG	-1.123	0.166	5.724	0.997
F51B-1	-1.301	0.111	6.697	0.973
XRCB	-3.106	0.134	6.468	0.997

As expected, T_c values are always higher than the junction temperature, while ν_G values are found close to the peak frequency ν_p. It is interesting to note that for most of the fitting parameters the values obtained for AlGaInP-based LEDs (red) can be distinguished from the values obtained for InGaN-based emitters (green and blue). The values of T_c, a and b show that the spectrum's FWHM, which typically equals a few kT_c, is larger for InGaN emitters. This may be due to a higher forward voltage and high-energy injection of carriers into the active region [Xi, 2005]. As a consequence, the values of S_3 switch from positive for AlGaInP based LEDs to negative for InGaN based diode chips. Also the numerical value of the low energy slope seems to be characteristic for each compound semiconductor. The value of a equals about 22.5 10^{-14} Hz^{-1} for AlGaInP emitters and 7.5 10^{-14} Hz^{-1} for InGaN diodes.

6.4.2. Spectrum variation with temperature

In the single-colour spectrum model given by Eq. (6.3) , seven fitting parameters appear: S_1, a, S_2, T_c, S_3, b and ν_G. In order to examine and include the junction temperature dependence of these parameters, additional spectra have been measured and modelled at four junction temperatures between 290 K and 340 K.

6.4.2.1. Variation of exponentials

The variation of the carrier temperature T_c with junction temperature has been found to be approximately linear for typical diode junction temperature ranges [Vaitonis, 2008]. Our data, summarized in Fig. 6.5, confirms this behaviour for all LED packages under test.

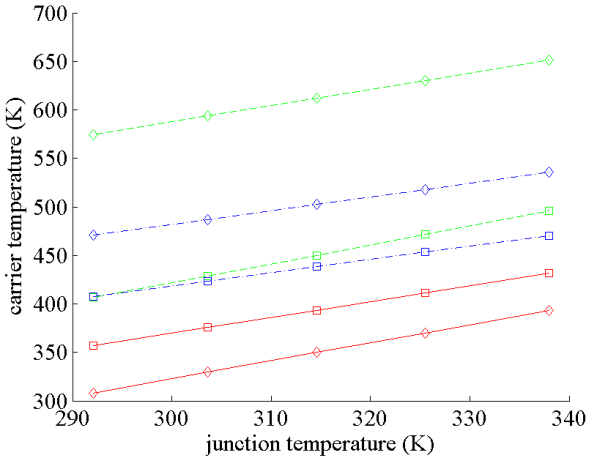

Fig. 6.5: Carrier temperature variation with junction temperature for the red (solid lines) green (dashed lines) and blue (dot-dashed lines) diodes. Squares are used for LEDs from Seoul Semiconductor; diamonds are used for devices from Cree.

Considering the spectrum at 300 K as a reference, the carrier temperature variation can be modelled as follows:

$$T_c(T) \approx c_T (T - T_r) + T_{c,r} = c_T \Delta T + T_{c,r} \tag{6.4}$$

where c_T represents a positive fitting parameter and $T_{c,r}$ equals the carrier temperature at 300 K junction temperature (T_r) as given in Table 6.1. The numerical values of slope c_T are gathered in Table 6.2. With $c_T > 1$, it is clear that the carrier temperature remains always higher than the junction temperature.

The variation with temperature of fitting parameters a (low energy slope) and b (peak width of the additional Gaussian contribution) occurring in Eq. (6.3) has been found to be negligible for all single-colour emitters. This implies that a and b values found in Table 6.1 can be used in the spectrum model for the complete temperature range. Moreover, if a and b are constant, the spectral FWHM and skewness variation with temperature must be attributed to the temperature behaviour of T_c, which is linear. This offers an explanation for the experimental results reported in literature [Chhajed, 2005-2] [Man, 2006].

Table 6.2: Variation of carrier temperature (c_T), total spectrum's peak frequency (γ_p), and Gaussian peak frequency (γ_G) with junction temperature, together with the slope γ_F of the absolute power change with temperature. R^2 values exceed 0.95 for all fits.

LED	c_T	γ_p (10^{14} Hz/K)	γ_G (10^{14} Hz/K)	γ_F (10^{-3} W/K)
F51R-1	1.630	0.001304	0.001152	-0.585
XRCR	1.853	0.001039	0.001012	-0.706
F51G-1	1.945	0.000312	0.000082	-0.182
XRCG	1.677	0.000270	0.000253	-0.100
F51B-1	1.376	0.000397	0.000542	-0.322
XRCB	1.416	0.000413	0.000518	-0.671

6.4.2.2. Peak frequency shift

All light-emitting diode spectra show a downward peak frequency shift with junction temperature as illustrated in Figs. 6.1 and 6.3. In Fig. 6.6, the variation of the peak frequencies ν_p and ν_G with junction temperature is plotted for the LED F51R-1. For both parameters a linear decrease is observed, although with a slightly different slope.

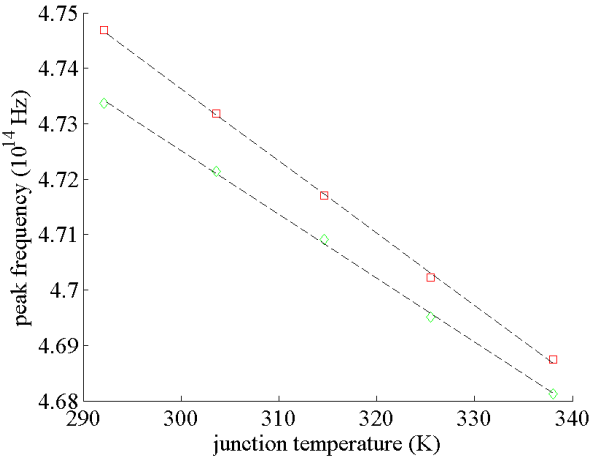

Fig. 6.6: Peak frequency shift (red squares) and shift in ν_G (green diamonds) with junction temperature for the LED F51R-1. The dashed black lines represent linear fits.

The peak frequency shift can be attributed to the variation of the semiconductor's energy gap E_g with temperature, described by the Varshni formula [Varshni, 1967]. For junction temperatures above about 290 K, the Varshni formula may be approximated by a linear expression (see chapter 4):

$$E_g(T) \approx E_{g,300} - \alpha'(T - 300) \tag{6.5}$$

with $E_{g,300}$ the band gap energy at 300 K and α' a positive constant. This linear decrease can explain the linear decrease of the peak frequency as presented in Fig. 6.6. Starting from a reference value at a reference temperature T_r, the position of the peak frequency at any other temperature T can be calculated as:

$$\nu_p(T) \approx \nu_{p,r} - \gamma_p(T - T_r) \tag{6.6}$$

with $\gamma_p = \alpha'/h$. For all single-colour LED spectra, the γ_p values have been summarized in Table 6.2. The values are in accordance with those found in LED datasheets and confirm that the frequency shift for red LEDs is about two to three times higher than the shift for green and blue LEDs. From the values of γ_p, numerical values of α' can be deduced. They agree with values found in literature, and are typically between 0.1 and 0.5 meV/K for bulk InGaN and between 0.3 and 0.4 meV/K for bulk AlGaInP compound semiconductors [Schubert, 2006].

From Fig. 6.6, the relationship between $\nu_G(T)$ and γ_G seems to be completely similar to Eq. (6.6). Experimental γ_G values are also summarized in Table 6.2. Only for LED F51G-1 γ_G is remarkably different from γ_p. This may find its origin in the rather poor Gaussian fits for this device with R^2 below 0.9 (see Table 6.1 for fit at 300 K).

Despite the theoretical and experimental evidence for a linear behaviour of the peak frequency with junction temperature given above, in literature most often the peak *wavelength* is considered to change proportionally with temperature [Hong, 2004] [Cho, 2005] [Xi, 2005]. Although this approximation is valid within a limited temperature range, it would be more correct to state that $\Delta(\lambda^{-1})$ is proportional to the junction temperature variation.

6.4.2.3. Absolute power variation

The total radiant flux variation as a function of junction temperature has been extensively studied in the preceding chapter. A linear dependence on junction temperature with slope γ_F and intercept δ_F has been found. As a result, the variation of the spectrum height with temperature can be taken into account by multiplication of the spectrum by the following factor:

$$\frac{\gamma_F(T - T_r) + \Phi_{e,r}}{\Phi'_{e,r}} \tag{6.7}$$

with $\Phi_e(T_r) = \Phi_{e,r}$ and $\Phi'_{e,r}$ the integral of the reference spectrum over frequency, after having taken into account the temperature dependence of the exponential

slopes and peak frequencies (see next paragraph). γ_F values of all devices under test have been recovered from chapter 5 and collected in Table 6.2.

6.4.2.4. Overall single-colour spectrum model

Combining the previous paragraphs, a semi-empirical model for a single-colour LED spectrum at junction temperature T can be written as follows:

$$\Phi_{e,\nu}(T) \approx \left\{ \frac{1}{S_1 \exp\left[-a\left(\nu-\nu_{p,r}-\gamma_p\Delta T\right)\right] + S_2 \exp\left[\frac{h\left(\nu-\nu_{p,r}-\gamma_p\Delta T\right)}{k\left(c_T\Delta T+T_{c,r}\right)}\right] + S_3 \exp\left[-\left(\frac{\nu-\nu_{G,r}-\gamma_G\Delta T}{b}\right)^2\right]} \right\} \times \left(\frac{\gamma_F\Delta T+\Phi_{e,r}}{\Phi'_{e,r}}\right) \tag{6.8}$$

$\nu_{p,r}$, S_1, a, S_2, $T_{c,r}$, $\nu_{G,r}$, S_3, b and $\Phi_{e,r}$ are determined from one reference spectrum at temperature T_r and $\Delta T = T - T_r$. For the determination of γ_p, γ_G, c_T and γ_F a spectrum obtained at a different temperature has to be available. $\Phi'_{e,r}$ equals the integral of the expression between large braces over frequency.

6.5. Phosphor-white spectrum

6.5.1. Phosphor spectrum at constant temperature

The spectrum of a phosphor-white LED is modelled in two parts, i.e. a pump and a phosphor spectrum. Eq. (6.3) is applied to model the pump spectrum. This spectrum is subtracted from the experimental full white spectrum and the fluorescent contribution is modelled by a single Gaussian function with peak value S_{phos} as proposed by [Uchida, 2005]:

$$\Phi_{e,\nu}^{phos} = S_{phos} \exp\left[-\left(\frac{\nu-\nu_G}{b}\right)^2\right] \tag{6.9}$$

Experimental and simulated white spectra of LED W42D-1 at two different temperatures are shown in Fig. 6.7. The fitting parameters S_{phos}, ν_G, and b corresponding to the 300 K phosphor spectrum equal 1.94 mW, 5.33 10^{14} Hz, and 0.58 10^{14} Hz, respectively. An excellent coefficient of determination exceeding 0.99 has been found.

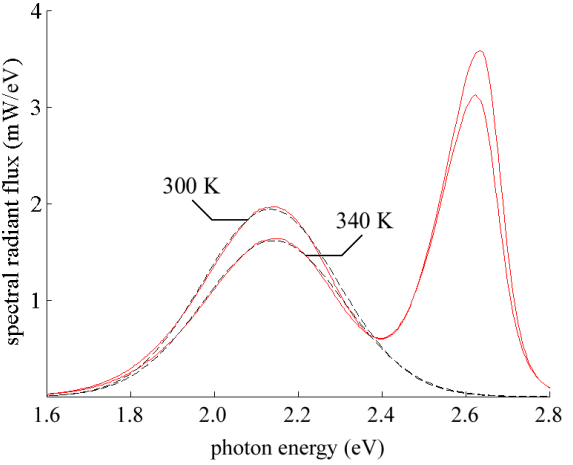

Fig. 6.7: Comparison of measured and simulated phosphor spectrum of LED W42D-1 at 300 K and 340 K junction temperature. The solid red line is the measured spectrum. The dashed black lines represent Gaussian spectrum models.

6.5.2. Temperature dependence of phosphor spectrum

6.5.2.1. Spectrum width and frequency shift

The spectrum width of the fluorescent contribution, represented in Eq. (6.9) by the rooted double Gaussian variance b, is found to increase with temperature (see also Fig. 6.7). The variation is approximately linear as illustrated in Fig. 6.8. This means that in the phosphor model b can be replaced by:

$$b(T) \approx \gamma_b (T - T_r) + b_r \tag{6.10}$$

with γ_b a positive fitting parameter and b_r the value at reference temperature T_r. For the phosphor-white LED under test and T_r = 300 K, γ_b equals 0.000581 10^{14} Hz/K (R^2 = 0.998).

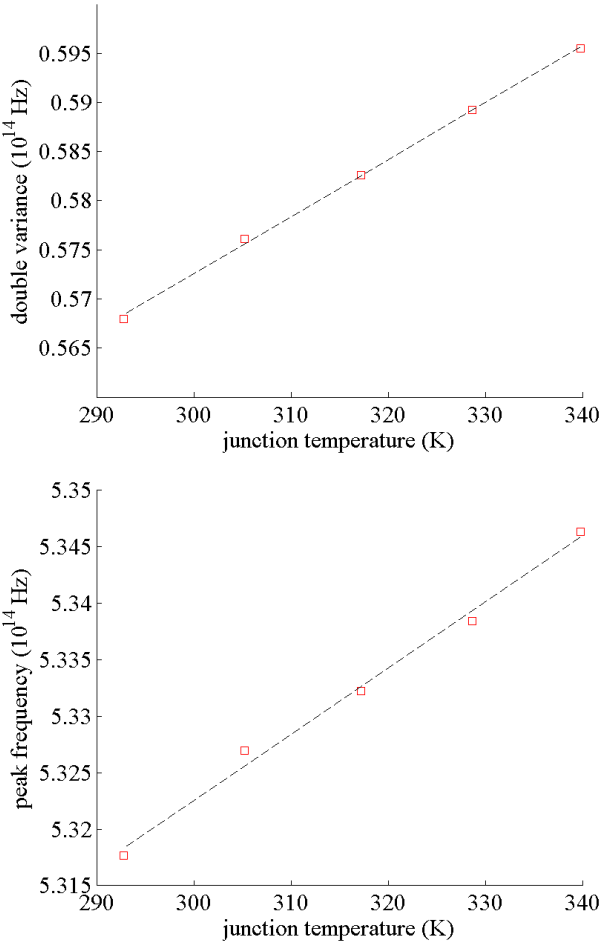

Fig. 6.8: Variation of the rooted double Gaussian variance b (top) and peak frequency shift (bottom) with junction temperature for the fluorescence spectrum of LED W42D-1. The dashed black lines represent linear fittings.

The peak frequency of the fluorescent contribution increases with temperature too. Measurement data gathered in Fig. 6.8 show that the phosphor peak frequency variation with temperature can be considered quasi linear. Thus, although a decent explanation has not yet been found, Eq. (6.6) can be used for the phosphor model as well. For LED W42D-1 a value of $-0.000586\ 10^{14}$ Hz/K has been obtained for γ_G. The corresponding coefficient of determination R^2 equals 0.993.

6.5.2.2. Absolute fluorescent power variation

According to the discussion of the radiant flux variation with temperature in chapter 5, the variation of the phosphor spectrum height with temperature can be taken into account by multiplication of the fluorescence spectrum by the factor in Eq. (6.7) as well. For the phosphor-white emitter under consideration γ_F of the phosphor spectrum only equals -0.813 10^{-3} W/K. This value is remarkably different from the absolute power variation of the corresponding blue pump spectrum with γ_F = $-0.464\ 10^{-3}$ W/K. It is therefore important to always calculate pump and phosphor power variation slopes γ_F separately for spectrum simulations. The sum of both slopes roughly equals the γ_F value of the full spectrum as presented in the preceding chapter.

The variation of the fluorescent contribution with temperature has not yet been fully described in literature. The subject is rather complex because changes in the intrinsic quantum efficiency of the phosphors are combined with variations in the excitation spectrum of the pump diode. The decrease of the fluorescent power of YAG:Ce^{3+} phosphors in terms of quenching processes of the most important transitions has been reported in literature [Zhang, 2008]. A non-radiative decay rate based on a particular activation energy has been proposed and a relative intrinsic fluorescent power decrease of about 0.2 %/K was measured. This is much smaller than the 0.4 %/K observed here, but this difference may be attributed to changes in the pump excitation spectrum.

6.5.2.3. Overall phosphor-white spectrum model

Inserting Eqs. (6.6) and (6.10) into Eq. (6.9) yields for the fluorescence spectrum:

$$\Phi_{e,\nu}^{phos}(T) \approx S_{phos}\left(\frac{\gamma_F \Delta T + \Phi_{e,r}}{\Phi'_{e,r}}\right)\exp\left[-\left(\frac{\nu - \nu_{G,r} - \gamma_G \Delta T}{\gamma_b \Delta T + b_r}\right)^2\right] \qquad (6.11)$$

S_{phos}, $\nu_{G,r}$, and b_r are calculated from one reference spectrum at temperature T_r. For the determination of γ_G, γ_b, and γ_F, a spectrum measured at an additional temperature has to be available.

The temperature dependence of a full phosphor-white spectrum can be modelled and simulated by using Eq. (6.8) for the pump spectrum and Eq. (6.11) for the phosphor spectrum, respectively. Similarly, the variation of any combined spectrum as a function of temperature can be studied by making the sum of all single-colour and fluorescence spectra included [Chhajed, 2005-2].

6.6. Validation

In order to validate the spectrum models presented in Eqs. (6.8) and (6.11), experimental and simulated spectra of red LED F51R-1 and white LED W42D-1 at 340 K junction temperature are shown in Fig. 6.9. Experimental spectra at 300 K have been used as reference spectra. Fitting parameters have been determined from Tables 6.1 and 6.2. For the phosphor-white package, the LED spectrum at 340 K has been determined as the sum of the blue pump spectrum and the fluorescent contribution. Excellent agreements between simulation and measurement with R^2 values always exceeding 0.95 have been found.
Additionally, luminous flux and CIE colour coordinates at 340 K have been calculated from the simulated spectra and compared with measured data for all LEDs in Table 6.3.

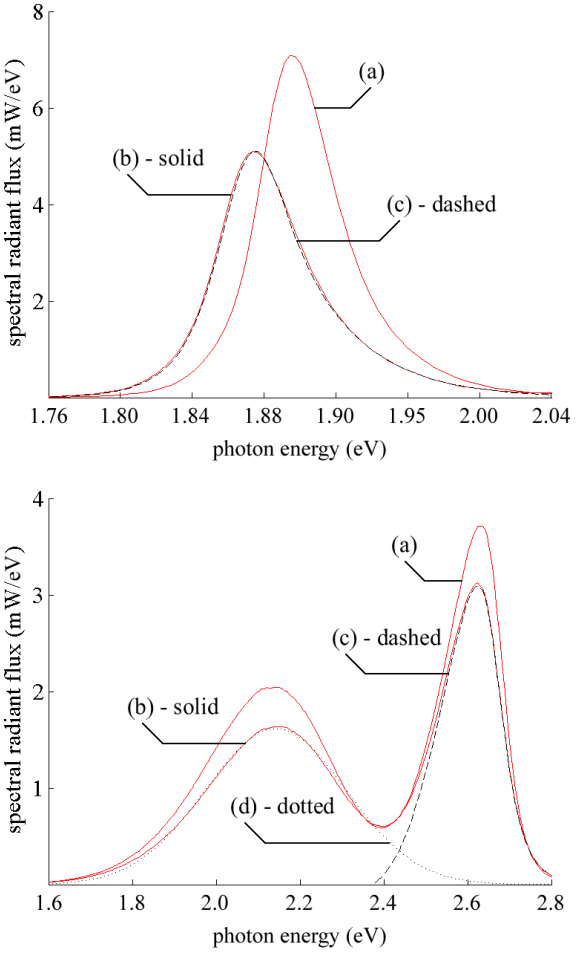

Fig. 6.9: Comparison of measured and simulated spectra for LED F51R-1 (top) and W42D-1 (bottom) at 340 K, starting from reference spectra (a) measured at 300 K. The solid red line (b) is the measured spectrum at 340 K, while the dashed line (c) is the simulated single-colour spectrum. Dotted line (d) represents the simulated fluorescence spectrum at 340 K.

Table 6.3: Comparison between measured and simulated luminous flux Φ_v and CIE x and y colour coordinates at 340 K. Flux and colour deviations $\Delta\Phi_v$ and ΔE_{uv} are added.

LED	measured			simulated			deviation	
	Φ_v (lm)	CIE x	CIE y	Φ_v (lm)	CIE x	CIE y	$\Delta\Phi_v$ (%)	ΔE_{uv}
F51R-1	20.1	0.6939	0.3055	19.6	0.6935	0.3064	2.4	0.0015
XRCR	26.9	0.6941	0.3053	24.5	0.7037	0.2962	8.9	0.0207
F51G-1	29.2	0.2045	0.6714	28.7	0.2049	0.6844	1.7	0.0028
XRCG	55.4	0.1671	0.6679	54.7	0.1709	0.6649	1.3	0.0017
F51B-1	4.5	0.1513	0.0284	4.5	0.1511	0.0270	0.0	0.0038
XRCB	18.0	0.1367	0.0537	17.9	0.1363	0.0534	0.5	0.0007
W42D-1	90.1	0.3006	0.3230	89.5	0.3004	0.3279	0.7	0.0033

The results in Table 6.3 confirm the good agreement between simulation and experiment for all devices under test. Except for LED XRCR, the deviation between simulated and measured luminous flux is smaller than 2.5 % and all CIE-$u'v'$ colour differences ΔE_{uv} (see chapter 7) remain significantly smaller than the typical radius of a three-step MacAdam ellipse ($\Delta E_{uv} \approx 0.006$) [CIE, 2004]. The larger deviations for device XRCR might be due to a small bump in the spectrum close to the $5\,10^{14}$ Hz frequency. Such spectrum deficiencies are of course not incorporated into the model.

6.7. Best practice

In practice, only two spectral radiant flux measurements are needed to accurately model and simulate a diode spectrum at any temperature. The first measurement serves as reference. For single-colour LED spectra, fitting parameters S_1 and a on one hand and S_2 and T_c on the other hand are determined from two separate exponential fits to the low energy and high energy tail of this reference spectrum, respectively. However, for the low energy slope fixed values of 22.5 10^{-14} Hz^{-1} and 7.5 10^{-14} Hz^{-1} could be used for AlGaInP-based and InGaN-based emitters, respectively. The difference between the combination of exponentials and the measured reference spectrum is modelled by a Gaussian function. Reference phosphor spectra can be directly modelled by a Gaussian function. Some multi-phosphor spectra may require a sum of Gaussian functions for precise modelling and simulation.

As linear junction temperature dependencies appeared to be sufficiently accurate for modelling the temperature behaviour of all initial and non-constant model parameters, one additional spectral radiant flux measurement allows calculating the variation of LED spectra with temperature.

6.8. Summary and conclusions

The spectral radiant flux of seven commercial high-power light-emitting diode packages from two manufacturers has been measured with a custom-made integrating sphere at different junction temperatures, ranging between 290 K and 340 K. Considering frequency instead of wavelength as the independent variable, a single-colour spectrum model for one particular temperature (300 K) has been constructed. Afterwards, the variation of all initial model parameters with junction temperature has been examined. In contrast with a number of merely mathematical spectrum models proposed in literature, the Boltzmann exponential behaviour with carrier temperature variation and the band gap energy shift with junction temperature have been included explicitly. For most of the fitting parameters, the

values obtained for AlGaInP-based LEDs could be distinguished from the values obtained for InGaN-based emitters. A Gaussian function with temperature dependent peak value, peak frequency, and peak width appeared to be sufficient for modelling and simulation of fluorescence spectra. Very high coefficients of determination have been found, indicating a good agreement between the models and experimental data. Both models have been validated by comparing flux and colour coordinates of measured and simulated spectra at 340 K junction temperature. Except for one red LED showing a spectrum deficiency, flux and colour deviations between measurement and simulation have been found to be lower than 2.5 % and smaller than the radius of a three-step MacAdam ellipse, respectively. In practice, only two spectral flux measurements are needed to accurately simulate a diode spectrum at any temperature.

7. Spatial colour distribution

7.1. Goals

In contrast to the spatial (luminous) intensity distribution of high-power light-emitting diodes (LEDs), little effort has been made to examine the spatial colour distribution of these light sources, i.e. the values of CIE colour coordinates as a function of direction in space. The spatial colour variation is negligible for single-colour emitters, but this is not the case for bichromatic white LEDs using phosphor for wavelength conversion. As the latter diode types are most often used for high colour rendering applications, a quantitative description of their colour distribution is necessary. Therefore, goniophotometer measurements have been performed on a variety of white light-emitting diodes incorporating a planar (remote) phosphor. Measurement results are used to discuss and model the spatial colour distribution of phosphor-white LEDs. Such LEDs appear to show an intrinsic and inevitable spatial colour variation. Furthermore, the measurement data and constructed model allow evaluating the visibility of spatial colour differences and the relevance of colour binning measurements at the end of LED package production lines. Using insights on spatial colour distribution gathered throughout this work, a design proposal is made to significantly decrease the colour variation of phosphor-white LEDs.

7.2. Colour variation of phosphor-white LEDs

7.2.1. Problem situation

Although less known by luminaire designers or end-users, a major drawback of current LED technology is its colour variation as a function of viewing angle. This spatial colour variation is negligible for single-colour emitters, but this is not the case for bichromatic white LEDs using phosphor for wavelength conversion (see Fig. 7.1). As the latter diode types are most often used for high colour rendering applications [Narendran, 2002] [Mirhosseini, 2009], a quantitative description of this colour variation is necessary. Analogous to spatial (luminous) intensity distribution or radiation pattern, the terms spatial colour distribution and colour pattern have been introduced to describe this phenomenon [CIE, 1987].

Fig. 7.1: Picture (unedited) of a screen illuminated by the collimated beam of a phosphor-white LED. The device's optical axis was positioned perpendicular to the screen, placed at a 20 cm distance. The colour variation is clearly visible.

In contrast to the spatial (luminous) intensity distribution of high-power LEDs, little effort has been made to examine the spatial colour distribution of these light sources, i.e. the values of CIE colour coordinates as a function of direction in space [Moreno, 2008]. According to literature, only two research groups have been studying the colour variation with viewing angle of bichromatic white LEDs based on phosphor conversion. The first group focussed on the effect of phosphor thickness, phosphor concentration and phosphor particle size on the colour distribution [Wenzl, 2008] [Sommer, 2009], while the second group simulated and examined the yellow-blue ratio of phosphor-white LED devices for different package configurations and phosphor locations [Liu, 2008-2] [Liu, 2009-2].

Typically three different phosphor configurations are used in bichromatic white LEDs based on fluorescence (see Fig. 7.2). The proximate non-conformal distribution can be seen as a phosphor droplet on the pump LED chip. This type is more and more abandoned due to the strong colour variation with viewing angle and replaced by the proximate conformal phosphor distribution [Holcomb, 2003]. Mounting the planar conformal coating at a certain distance from the pump chip appeared to even improve the LEDs' light output characteristics. The latter is called a remote phosphor distribution [Kim, 2005].

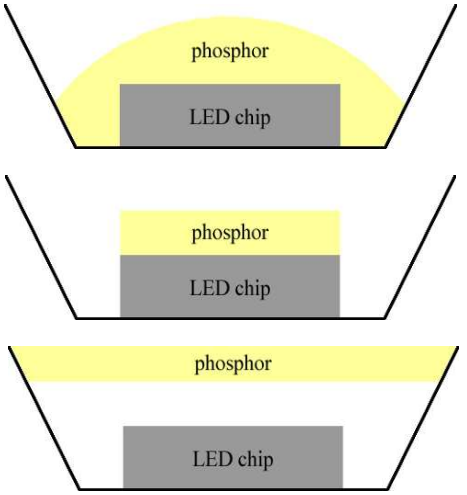

Fig. 7.2: Three different phosphor configurations are typically used in bichromatic white LEDs based on fluorescence: proximate non-conformal phosphor distribution (top), proximate conformal phosphor distribution (middle), and remote phosphor (bottom).

Despite the increasing colour homogeneity by using new package configurations and phosphor distributions, spatial colour changes appear to be inevitable for all three chip-phosphor combinations shown in Fig. 7.2. This chapter has the intention to model and evaluate such colour variations, which should allow making appropriate design improvements. As non-conformal phosphor distributions vary significantly for different manufacturers, only packages containing a planar phosphor, i.e. conformal or remote, have been considered.

7.2.2. Experiments

Ten phosphor-white commercial LED devices have been selected from different manufacturers. Eight out of the ten selected LEDs are planar Lambertian emitters, making direct measurement and modelling of the spatial colour distribution possible. Five of them contain a proximate phosphor distribution (CL3N to XREW in Table 7.1); the other three are remote phosphor devices with pump-phosphor distances ranging between about 0.5 and 3 cm (FOR1, XIC3, and XIC4). Two additional conformal phosphor packages incorporate a beam-shaping lens, allowing examining the effect of optics on the initial colour distribution (NCCW-1 and P1HW, with narrow beam and batwing lens, respectively).

In order to obtain a reliable spatial colour distribution comparison, all LEDs have been tested under conditions similar to general lighting applications. The nominal drive current specified in the datasheet was used for each device. Moreover, by selecting an appropriate heat sink, the steady state junction temperature of each LED was maintained at a fixed value between 50 °C and 70 °C, corresponding to

practical operation conditions. Junction temperatures have been verified by a preceding temperature-voltage calibration as described in chapter 4.

Two custom-made goniophotometer setups have been used to determine the radiant spectral intensity of all LEDs. The first, having a freely rotating detector arm of 1.5 m, has been used for all single-die packages. The second has a fixed detector, while the sample can be two-dimensionally rotated at a distance of 8.7 m from that detector. The latter has been used for all multi-die emitters. Both setups incorporate an Oriel Instruments spectrometer with a 150 lines/mm grating. At the spectrometer exit plane, a 1 inch Andor back illuminated and cooled (-30 °C) CCD detector is mounted, obtaining a spectral resolution of approximately 4 nm while the complete visual spectrum is recorded. Data acquisition with full vertical binning, dark current correction and an automated integration time set for optimum signal-to-noise ratio is controlled by LabVIEW software.

Using spherical coordinates with $(\theta,\varphi)=(0,0)$ for the forward optical axis of each device, radiant spectral intensity measurements have been performed for θ from 0° to 80° per 10° in four half-planes characterized by φ = 0°, 90°, 180° and 270°. For asymmetric packages, the φ = 0° plane has been chosen along the shortest axis.

7.2.3. Measurement results

Three-dimensional models can be used for spatial intensity distributions, i.e. the radiant or luminous intensity as a function of direction in space: $I(\theta,\varphi)$ [Moreno, 2008]. Modelling the variation of colour coordinates with viewing angle however requires a different approach. Two possible data representations of a spatial colour distribution are gathered in Fig. 7.3 for a device with proximate conformal phosphor distribution (PG1A). The first representation shows a part of the CIE chromaticity diagram with indication of (x,y) colour coordinates for different θ angles along two perpendicular axes. The second plot contains CIE x and y values as a function of θ, averaged over the two φ-planes as PG1A-1 is a rotational-symmetric device.

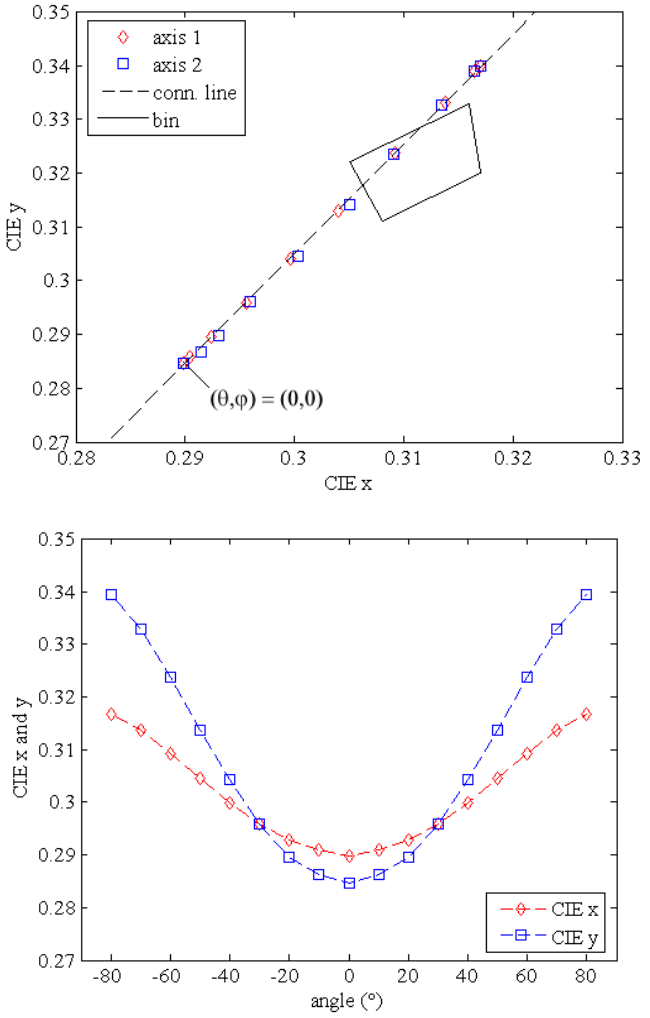

Fig. 7.3: (top) Part of the CIE chromaticity diagram with indication of colour coordinates for different viewing angles along two perpendicular axes for PG1A-1. The line connecting the colour coordinates of pump and phosphor and the colour bin provided in the LED datasheet are added. The colour point along the optical axis of the package is indicated as well. (bottom) CIE x and y colour values as a function of angle θ, averaged over two perpendicular φ-planes.

It is clear from Fig. 7.3 that the spatial colour variation of phosphor-white LED devices cannot be neglected. For the LED PG1A-1 under consideration, the colour variation with viewing angle is about three to four times larger than the binning region specified in the datasheet, which typically corresponds to a four-step MacAdam ellipse. Two additional remarkable facts can be observed:

- In the CIE chromaticity diagram, all (x, y) colour coordinates appear on a single line, independent of the viewing angle. For the given constant input current and junction temperature, this line is found to connect the colour coordinates of the separate pump and phosphor spectra, which have been determined by Gaussian fitting. This implies that individual x and y colour variations can be considered projections of the measured colour variation along this connection line.

- The colour coordinates in forward direction ($\theta = \varphi = 0$) of the full spectrum show the lowest x and y values, meaning that the centre of the beam is most bluish (also see Fig. 7.1). With increasing θ, colour coordinates also increase, getting closer to the yellowish phosphor colour.

Similar results have been found for all LEDs in Table 7.1. According to the Centre of Gravity Law of Colour Mixture on chromaticity diagrams, the colour of a phosphor-white LED with steady state pump and phosphor coordinates changes due to a variation of the yellow-blue ratio (YB) in the full measured spectrum [Hunt, 1998]. This ratio is calculated by dividing the radiant flux contribution of the phosphor spectrum by the corresponding contribution of the pump spectrum. The first observation also shows that the individual pump and phosphor colours do not appreciably change with viewing angle during steady state operation. Only a current or junction temperature variation will influence these colour values, but that effect is not taken into account in this work.

The second observation implies that the YB of each device is lowest for the spectrum measured in forward direction, while its value will increase with increasing viewing angle. This statement is visualised for LED PG1A-1 in Fig. 7.4. Each spectrum is normalized to the pump's peak value, so the yellow-blue ratio equals the height of the phosphor spectrum.

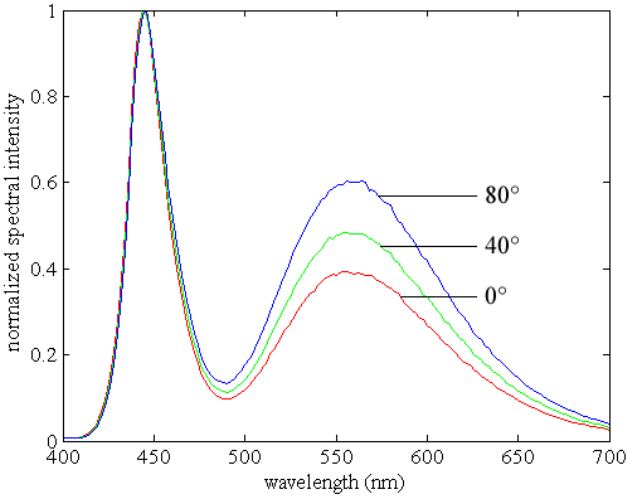

Fig. 7.4: Normalized spectra of LED PG1A-1 at 350 mA forward current for three different viewing angles. With increasing viewing angle, the relative contribution of the phosphor spectrum increases.

The colour coordinates in forward direction (x_0, y_0) and corresponding yellow-blue ratios YB_0 of all measured LEDs have been collected in Table 7.1. The correlation between the second and third column is very clear. For comparable pump and phosphor colours, the resulting colour coordinates increase with increasing yellow-blue ratio.

Table 7.1: x_0 , y_0 and YB_0 values for all LED devices under test.

LED	(x_0, y_0)	YB_0
CL3N	(0.3343 , 0.3796)	1.248
E3BN	(0.3031 , 0.3034)	0.579
ENEB	(0.2943 , 0.2974)	0.503
PG1A-1	(0.2899 , 0.2846)	0.392
XREW	(0.3135 , 0.3276)	0.792
FOR1	(0.3410 , 0.3252)	0.905
XIC3	(0.4259 , 0.4074)	1.887
XIC4	(0.3603 , 0.3612)	0.925
NCCW-1	(0.2732 , 0.2517)	0.301
P1HW	(0.3483 , 0.3865)	1.350

7.3. Modelling YB variation with viewing angle

7.3.1. Theoretical approach

Modelling the spatial colour distribution of phosphor-white LEDs is now reduced to modelling the (relative) yellow-blue ratio variation of the spectrum as a function of viewing angle: $\Delta\mathrm{YB}(\theta)$. According to different publications, YB variations during steady-state diode operation can only be attributed to a variation of the phosphor thickness, a variation of the phosphor concentration, or a combined effect of both variations [Krames, 2007] [Mueller, 2002] [Uchida, 2005] [Kang, 2006] [Ishida, 2008]. However, as phosphor concentrations do not significantly change within conformal or remote phosphor distributions, the detected yellow-blue ratio variations must be due to a variation of the phosphor thickness. Although the absolute phosphor thickness is constant for planar phosphor distributions, the optical path length through the phosphor layer or apparent thickness increases as a function of the viewing angle (see Fig. 7.5).

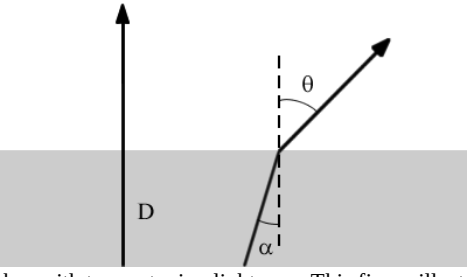

Fig. 7.5: Planar phosphor with two outgoing light rays. This figure illustrates that the apparent phosphor thickness depends on the viewing angle and differs from the absolute phosphor thickness D for all $\theta \neq 0$.

The YB variation as a function of the changing apparent phosphor thickness D_a with viewing angle θ can be described by use of Fig. 7.5, showing that D_a differs from the absolute phosphor thickness D for all $\theta \neq 0$. The relationship between this apparent thickness and the real phosphor thickness is given by:

$$D = D_a \cos\alpha \tag{7.1}$$

with α the angle between the surface normal (perpendicular to the phosphor surface) and the light ray within the phosphor. Thus, the relative change in apparent phosphor thickness can be written as:

$$\frac{D_a - D}{D} = \cos^{-1}\alpha - 1 \tag{7.2}$$

If the typically exponential absorption behaviour is approximated by a linear dependence of thickness, the relative change in apparent phosphor thickness can be considered equal to the relative YB variation $\Delta\mathrm{YB}(\theta)$. The internal angle α and external viewing angle θ of the same light ray are however different due the refractive index difference between phosphor and ambient. Both angles are connected by Snellius' law:

$$\alpha = \arcsin\left(\frac{n_{amb}}{n_{phos}}\sin\theta\right) \tag{7.3}$$

where n_{amb} and n_{phos} represent the refractive indices of the ambient (typically air or a coating) and the phosphor plate, respectively. Combining Eqs. (7.2) and (7.3), an expression for the YB change with viewing angle θ is found:

$$\Delta\mathrm{YB}(\theta) = \left[1-\left(\frac{n_{amb}}{n_{phos}}\right)^2 \sin^2\theta\right]^{-1/2} - 1 \tag{7.4}$$

This final expression is valid for all φ-planes, independent of the package shape. For modelling in practice however, one should have a closer look at Eq. (7.4):

- The proportionality of refractive indices n_{amb}/n_{phos} is usually not known precisely in advance. Moreover, each phosphor or device shows a rather unpredictable diffusing effect leading to a redirection of light rays in the phosphor plate and thus the shape of $\Delta\mathrm{YB}(\theta)$. Phosphors or devices with a larger diffusing capacity are indeed expected to show a reduced spatial colour variation. In Eq. (7.4), this effect may cause the proportionality n_{amb}/n_{phos} to differ from its expected value. It is therefore appropriate to replace n_{amb}/n_{phos} by a parameter C_1 which has to be determined experimentally.
- The spatial colour (and intensity) distribution of LED devices can be easily transformed by using beam shaping optics. For rather simple optical configurations, this may result in a proportional widening or narrowing of the initial YB variation $\Delta\mathrm{YB}(\theta)$. This effect can be included in the theoretical model by scaling the viewing angle θ by a constant C_2.

Taking into account the above remarks, the following equation will be used to model the yellow-blue ratio variation as a function of viewing angle θ:

$$\Delta\mathrm{YB}(\theta) = \left[1-C_1^2\sin^2\left(C_2\theta\right)\right]^{-1/2} - 1 \tag{7.5}$$

with C_1 and C_2 two constant fitting parameters. C_2 is forced to 1 when no beam shaping optics are utilized.

7.3.2. Validation

A custom-made MATLAB program has been used to fit Eq. (7.5) to the measured $\Delta\mathrm{YB}(\theta)$ data. Fitting parameters C_1 and C_2 have been collected in Table 7.2. The corresponding coefficients of determination R^2 have been added as well. For all devices without beam shaping optics, fitting parameter C_2 has been deliberately set to 1. Only parameter C_1 had thus to be fitted for LEDs CL3N to XIC4 in Table 7.2.

Table 7.2: C_1 and C_2 fitting parameters and corresponding coefficients of determination.

LED	C_1	C_2	R^2
CL3N	0.605	1.000	0.943
E3BN	0.819	1.000	0.995
ENEB	0.665	1.000	0.992
PG1A-1	0.809	1.000	0.992
XREW	0.815	1.000	0.977
FOR1	0.583	1.000	0.996
XIC3	0.531	1.000	0.996
XIC4	0.614	1.000	0.994
NCCW-1	0.956	3.159	0.989
P1HW	/	/	/

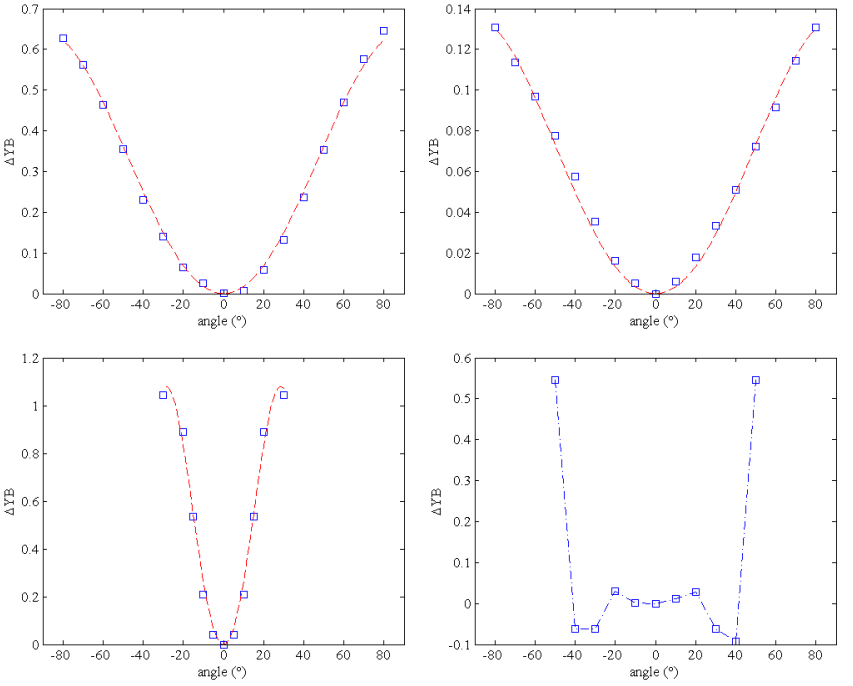

Fig. 7.6: Measured (blue squares) and simulated (red dashed lines) ΔYB colour variation as a function of viewing angle for four LEDs: (upper left) device with proximate phosphor distribution E3BN, (upper right) remote phosphor LED XIC3, (lower left) device NCCW-1 with narrowing lens, and (lower right) device P1HW with batwing lens. For the latter, a blue dot-dashed line simply connects the measured data points.

The data in Table 7.2 show a very good agreement between measurement and simulation according to Eq. (7.5); all coefficients of determination R^2 exceed 0.94. The plots in Fig. 7.6 confirm this statement for the modules E3BN, XIC3, and NCCW-1. The models presented in Eqs. (7.4) and (7.5) can however not be used for devices with special (i.e. not proportionally widening or narrowing) optics. Indeed, the YB variation of LED P1HW with batwing lens could not be simulated, while device NCCW-1 with narrowing lens shows a good agreement between measurement and simulation with $C_2 \approx 3$ (see Table 7.2 and Fig. 7.6). This value corresponds to what can be expected, as the FWHM (full width at half maximum) of the narrowing lens is about 40°, being one third of the FWHM of a Lambertian emitter.

7.4. Best Practice

7.4.1. Colour distribution determination

Although all measurement data has been used for the parameter fittings above, in practice two spectral radiant intensity measurements are sufficient to simulate the $\Delta\mathrm{YB}(\theta)$ or corresponding spatial colour variation of phosphor converted Lambertian LED devices. A first measurement in the forward direction allows calculating YB_0, while a second measurement at a different viewing angle is used for the determination of C_1 in Eq. (7.5). For phosphor-white LEDs with proportionally narrowing or widening optics at least three spectral radiant intensity measurements are needed as in this case $C_2 \neq 1$.

7.4.2. Evaluation of colour variation

The observations made in the previous paragraphs prove that planar phosphor distributions in bichromatic white LEDs lead to an intrinsic and inevitable spatial colour variation due to the changing apparent phosphor thickness with viewing angle θ. The measured colour differences with viewing angle are however very unlike when different LED or phosphor types are considered (see Table 7.2). It is therefore worth having a closer look at the correlation between fitting parameter C_1 and the maximum CIE-$u'v'$ spatial colour difference (see Fig. 7.7), which has been calculated as follows [CIE, 2004]:

$$\Delta E_{uv} = \sqrt{(\Delta u')^2 + (\Delta v')^2} \tag{7.6}$$

with $\Delta u'$ and $\Delta v'$ the maximum coordinate differences in CIE-$u'v'$ colour space (typically between zero and maximum viewing angle θ). This colour difference is definitely visible as soon as a four-step MacAdam ellipse is surpassed, which approximately corresponds to $\Delta E_{uv} > 0.008$. Binning regions provided in LED datasheets therefore have about the same size. C_2 is not taken into account as the absolute spectrum variation does not depend on this parameter.

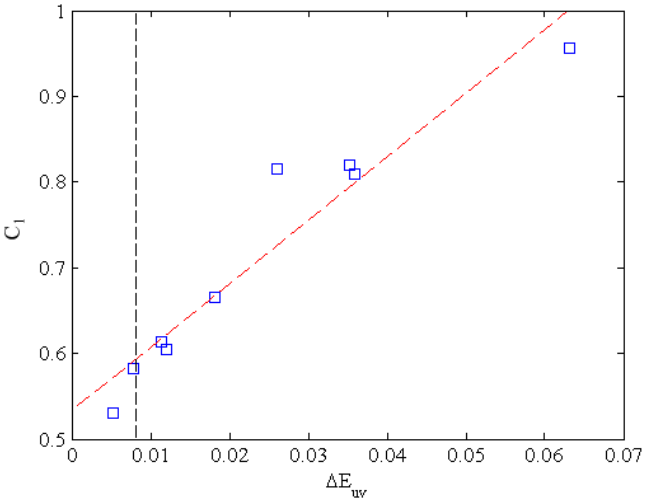

Fig. 7.7: Correlation between maximum CIE-$u'v'$ colour difference and fitting parameter C_1 (blue squares). The red dashed line represents a linear fit, while the vertical dashed line corresponds to the ΔE_{uv} colour difference of a four-step MacAdam ellipse.

The data in Fig. 7.7 show a high correlation between fitting parameter C_1, which is related to n_{amb}/n_{phos} and diffusing effects, and the maximum CIE-$u'v'$ spatial colour difference ΔE_{uv} (R^2 = 0.922). The linear fit shows that a maximum ΔE_{uv} corresponding to a four-step MacAdam ellipse or typically one colour bin is obtained for $C_1 \approx 0.6$. Only two LEDs (FOR1 and XIC3) stay below this value, which can be used as a colour evaluation criterion (see Table 7.2). All other devices under test show a visible colour variation with respect to the forward direction as soon as a certain viewing angle $\theta \leq 80°$ is surpassed. For those LEDs, colour binning according to a four-step MacAdam ellipse can only be valid for part of the beam and is therefore inappropriate for the overall light output.

7.4.3. Phosphor design

By means of the insights on spatial colour distribution gathered throughout this chapter, one can consider the design factors affecting the spatial colour variation of phosphor-white LEDs: the phosphor plate's refractive index and diffusing effect (usually related to its absolute thickness), the pump-phosphor distance, and the phosphor shape [Borbély, 2005]. The first two aspects are related to fluorescent material properties which can hardly be modified in practice, while changing the absolute phosphor thickness will result in a decrease of the LED's correlated colour temperature. Alternatively, one could use additional diffusing layers on top of the

planar phosphor to enhance colour uniformity. However, in that case significant extra light losses have to be taken into account.

The data in Table 7.2 and Fig. 7.7 suggest that spatial colour variations are remarkably smaller for remote phosphor devices in comparison with proximate phosphor distributions. This corresponds to results found in literature and can be attributed to a larger diffusing capacity due to relatively easy re-emission of back-scattered photons for the former [Kim, 2005]. Therefore, although package size does not always allow this, remote phosphor designs are strongly preferred to their proximate counterparts.

Finally, the shape of the fluorescent material has a major influence on the spatial colour distribution of phosphor-white LEDs as well. However, except for some additional diffusing effects, mere adaptation of a planar phosphor can impossibly reduce its spatial colour variation. This is due to the averaging of light rays from each part of the pump-phosphor configuration in each viewing direction. A different colour variation reduction approach has to be utilized as a result: The discussion above shows that the spatial colour distribution of bichromatic white LED light sources is due to the changing apparent phosphor thickness as a function of viewing angle. The most reasonable approach to avoid this shortcoming is the use of spherical phosphor distributions. Indeed, for such configurations the averaged apparent phosphor thickness does not change significantly as a function of viewing direction. Consequently, for phosphor-white LED devices the use of remote spherical phosphors seems to be the best solution for obtaining minimal (i.e. at least invisible) spatial colour variations. Similar conclusions have been drawn by other research groups, mainly based on ray-tracing simulations [Borbély, 2005] [Allen, 2008] [Liu, 2008-2] [Liu, 2009-2].

7.5. Summary and conclusions

Goniophotometer measurements have been performed on ten commercial LED packages incorporating a proximate or remote planar phosphor. The measurement results have been used to discuss and model the spatial colour distribution of these light sources. For all devices under test, the colour coordinates appeared on a single line in the CIE chromaticity diagram and have been found to increase with increasing viewing angle. As a result of these observations, modelling the spatial colour distribution has been reduced to modelling the (relative) yellow-blue ratio variation of the spectrum as a function of viewing angle. After normalizing each spectrum to the pump's peak value, this yellow-blue ratio could be determined as the height of the phosphor spectrum. The YB variation has been modelled starting from its attribution to the relative apparent phosphor thickness change as a function of viewing angle, while Snellius' law has been included to connect internal and external light ray angles. Afterwards, a second parameter has been added to extend the initial model to phosphor-white LEDs with simple narrowing or widening optics.

A very good agreement between measurement and simulation with all coefficients of determination exceeding 0.94 has been found. The measurements and constructed model therefore allowed evaluating the visibility of spatial colour differences and the relevance of colour binning measurements at the end of LED package production lines. Plain linear data fitting showed that a maximum colour difference corresponding to a four-step MacAdam ellipse or typically one colour bin is obtained when the primary modelling parameter equals 0.6. Only two LEDs remain within this constraint that may be used as a colour evaluation criterion. Using the insights on spatial colour distribution gathered throughout this chapter, a design proposal has been made to significantly increase the colour homogeneity of phosphor-white LEDs: Using remote spherical phosphors seems to be the best solution for obtaining minimal (i.e. at least invisible) spatial colour variations.

8. Evaluation of current light-emitting diode technology

8.1. Goals

Measurement results that have been used for model construction in chapters 4 to 7 can be utilized for an extended evaluation of the present LED technology status as well. This evaluation focuses on three major aspects:

- Due to the lack of related standards, the trustworthiness of datasheet information is often doubtful. Voltage, flux, and colour binning by manufacturers at the end of production lines (see chapter 2) is hence verified by performing measurements at similar current and junction temperature conditions. The relevance of this binning for diode operation in practice is discussed directly afterwards.
- Numbers quoted for (luminous) flux and efficiency of LEDs are very sensitive data because they are used to impress and push the LED market. Efficiency measurements and output comparison, including the current and temperature dependence of the results, are therefore of major importance in current high-power light-emitting diode research [Krames, 2007]. An extended efficiency evaluation is performed, subdivided into two parts. The first part studies power loss mechanisms in solid-state lighting applications. Often only very specific loss or related efficiency measurements are discussed in literature [Boroditsky, 1997] [Narendran, 2000], but more recently a trend towards combined efficiency determination comes up. Examples of the latter are given in [Krames, 2007], [Liu, 2007] and [Chen, 2008]. Nevertheless, none of these papers has the intention to unite a maximum number of efficiency measurements in one setup, which allows connecting power and loss calculations by use of the energy conservation relation. In the first efficiency evaluation section, an integrating sphere setup is used to examination the power loss mechanisms in solid-state lighting devices. The second branch handles LEDs' luminous efficacy comparison on five different levels. These are RGB versus phosphor-white technology efficiency, dependence of efficiency on correlated colour temperature for phosphor-white emitters, efficiency dissimilarities between manufacturers, single-die versus multi-die component efficiency, and comparison of efficiency values obtained for LED lamps and engines in practice.
- The technology evaluation is completed with a proposal for a light-emitting diode quality scale. This scale is constructed from modelling parameters

that have been found to be closely related to diode quality. Comparing such parameters for different LEDs allows making a technology ranking according to the lighting designer's or end-user's needs.

8.2. Reliability of datasheet information

8.2.1. Situation

Due to the lack of related standards, the trustworthiness of datasheet information is often doubtful. In this work, the voltage, flux, and colour binning by manufacturers at the end of production lines are hence verified by performing measurements at identical current and junction temperature conditions. For all devices under test (see Table 8.1), binning has been performed at 350 mA normal drive current in a 25 °C ambient (more or less 300 K). Due to the short pulses, junction temperature is considered to have the same value (see chapters 3 and 4).

The relevance of the initial binning for diode operation in practice is examined as well. This means that voltage, flux, and colour values during steady-state operation on a fixed heat sink (350 mA current and about 330 to 350 K junction temperature) are registered and compared to the values obtained during pulsed operation. Indeed, the junction temperature difference between both conditions may possibly result in remarkably different output characteristics. Note however that colour binning relevance depends on the colour variation with viewing angle as well, even at constant current and temperature. This problem has been discussed in the preceding chapter 7 and will not be recurred here.

Warm, neutral, and cool white emitters of Cree, Nichia and Seoul Semiconductor have been selected in a way their respective colour bins overlapped as much as possible. Single-colour red LEDs have been added to the selection as well. Unfortunately however, acquiring research samples from the requested bins appeared to be very difficult and sometimes even impossible. At long last, twelve phosphor-white diode types from the three manufacturers have been obtained for the datasheet reliability discussion (see Table 8.1). Two types of single-colour red Cree LEDs could be added to the final selection.

Table 8.1: Overview of LED packages that have been measured for datasheet verification and examination of binning relevance. The column contents relate to Table A.1 in Appendix 1.

MFR	LED	colour
Cree	XCAN-1	4500 K
	XCAN-2	4500 K
	XCDM-1	3000 K
	XCDM-2	3000 K
	XEKP	8500 K
	XR2M-1	620 nm
	XR2M-2	620 nm
	XR3K	625 nm
Nichia	NSB3	7000 K
	NSC2-1	5000 K
	NSC2-2	5000 K
SSC	N42L-1	3000 K
	N42L-2	3000 K
	S42S-1	4000 K
	S42S-2	4000 K
	W42B-1	6300 K
	W42B-2	6300 K
	W42D-1	6300 K
	W42D-2	6300 K
	W42H-1	6300 K
	W42H-2	6300 K

For all figures with scaled axes in sections 8.2.2 and 8.2.3, the manufacturer's binning information is represented by a black rectangle (with exact values below). Saw tooth lines denote the measurements at pulsed operation for datasheet validation, while the black lines stand for the voltage and flux values for examination of the binning relevance during operation in practice (with exact values on top). Values are in volt and lumen, respectively. For the colour binning plots in section 8.2.4, square data points are used for the pulsed measurements, while triangles indicate the steady-state colour values.

8.2.2. Forward voltage binning

8.2.2.1. Cree

Surprisingly, manufacturer Cree provides a luminous flux and colour binning in its datasheets, but no forward voltage binning [Cree, 2006] [Cree, 2007]. A typical forward voltage value of 3.3 V at 350 mA and 25 °C junction temperature is however mentioned. Next to that, a temperature coefficient of -4.0 mV/K is claimed. Pulsed and steady-state forward voltage measurements have been compared for all Cree devices mentioned in Table 8.1. Deviations between both approaches have been found to amount about 8 % for the white, and 5 % for the red devices, corresponding to temperature coefficients of about -3.7 and -2.5 mV/K, respectively.

As a result, average steady-state forward voltage values amount 3.17 V for the white and 1.95 V for the single-colour devices.

Although not exactly the same devices have been studied, the temperature coefficients correspond very well to what can be expected from the modelling parameters in chapter 5. From the γ_P values in Table 5.2, forward voltage slopes of -3.5 and -2.4 mV/K can be derived for LED XREW and XRCR, respectively.

8.2.2.2. Nichia

Fig. 8.1 shows that both cool white Nichia device types show a very similar forward voltage behaviour. The voltage binning has been chosen rather wide (0.4 V), but nevertheless the pulsed binning is found to correspond very well to the manufacturer's specifications [Nichia, 2007]. At normal operating conditions however (at 330 K instead of 295 K junction temperature), forward voltage decreases by 0.35 V or 9 %. The forward voltage coefficient equals about -10 mV/K, which is relatively high in comparison with the other LEDs under consideration. Consequently, the forward voltage does no longer match the datasheet value during steady-state operation. Although not mentioned in Table 8.1, similar results have been obtained for LED types NCCW and NS6W.

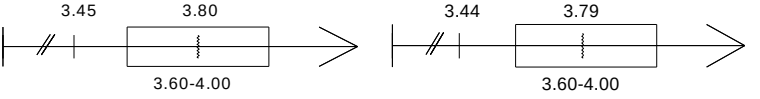

Fig. 8.1: Forward voltage bins and values for LED NSB3 (left) and NSC2-1 (right, similar for NSC2-2).

8.2.2.3. Seoul Semiconductor

Seoul Semiconductor uses 0.25 V forward voltage binning widths [SSC, 2007]. This is much smaller than the Nichia binning, but measurement results at pulsed conditions yet remain within their corresponding binning regions (see Fig. 8.2). Voltage decreases due to the increased junction temperature at steady-state operation amount about 3 % or 3 mV/K on average. This outcome is better than the temperature coefficients obtained for the white Cree and Nichia devices. As a result, depending on the initial voltage value, steady-state forward voltages of some LED types are still situated within the specified bin.

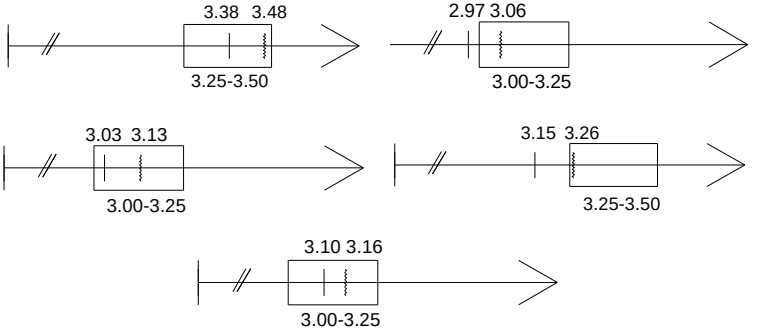

Fig. 8.2: Forward voltage bins and values for LED N42L-1 and 2 (top left), S42S-1 and 2 (top right), W42B-1 and 2 (middle left), W42D-1 and 2 (middle right), W42H-1 and 2 (bottom centre).

For LED W42D-1, a value of -4.3 mV/K can be obtained from its γ_P coefficient given in chapter 5, which is somewhat higher than the -3.7 mV/K obtained here. Note however that this slope value is determined from only two measurements here, while four temperatures had been selected for the power measurements described in chapter 5. The highest value is thus considered to be the most correct one.

8.2.3. Luminous flux binning

8.2.3.1. Cree phosphor-white

The Cree phosphor-white luminous flux values that have been determined for datasheet verification are very close to the upper edge of their respective luminous flux bin (see Fig. 8.3). Only for the XEKP device, the flux value at 300 K junction temperature matches with the datasheet specifications. By choosing very narrow luminous flux binning regions (width of 5 to 7 lm) in comparison with other manufacturers, Cree seems to be setting specification standards which are hard to fulfil by its own manufacturing process.

On the other hand, for steady-state operation on a fixed heat sink the luminous flux values have decreased by about 25 to 35 %, reaching a value far below the lower flux bin edge. Only at 305 to 310 K junction temperature values the luminous flux lies within the manufacturer's binning region. Unfortunately for Cree, this interval does not correspond to temperatures reached in practice.

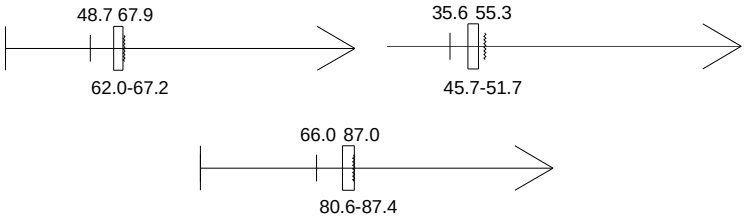

Fig. 8.3: Luminous flux bins and values for devices XCAN-1 and 2 (top left), XCDM-1 and 2 (top right), XEKP (bottom centre).

Note that the luminous flux variations presented here are more difficult to compare to the modelling coefficients in chapter 5 than the forward voltage changes with temperature. This is due to the additional spectrum peak frequency and spectrum width or skewness shifts (see chapter 6), making the luminous flux decreases significantly larger than the corresponding radiant flux decreases. This effect is even more important for single-colour LEDs.

8.2.3.2. Cree red

For both single-colour Cree LED types in Table 8.1 a luminous flux decrease of about 37 % between the pulsed and steady-state operating conditions has been measured (see Fig. 8.4). The flux values at 300 K junction temperature can be found at the low end within the binning regions specified by the datasheet; values at higher temperatures immediately drop out.

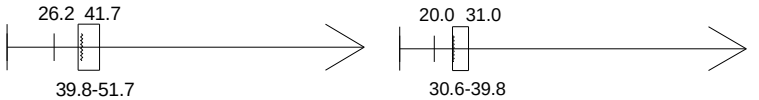

Fig. 8.4: Luminous flux bins and values for Cree red LEDs XR2M-1 and 2 (left) and XR3K (right).

8.2.3.3. Nichia

Although a flux binning width of 13 lm has been specified in the datasheets, Nichia encounters the same binning problem as Cree regarding phosphor-white emitters: Luminous flux values at pulsed operation are found above the datasheet bin, while during steady-state operation junction temperature fluxes decrease by roughly one third reaching a value below the bin (see Fig. 8.5).

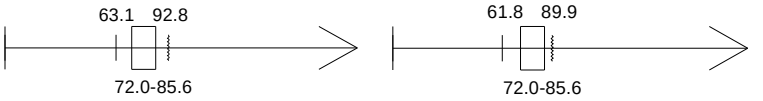

Fig. 8.5: Luminous flux bins and values for devices NSB3 (left) and NSC2-1, similar for NSC2-2 (right).

8.2.3.4. Seoul Semiconductor

Manufacturer Seoul Semiconductor provides luminous flux binning widths between about 10 and 25 lm. Even for the smallest bins, luminous flux values obtained for 300 K junction temperature conditions are situated within the specified binning regions. Seoul Semiconductor luminous flux binning is therefore considered to be better controlled than equivalent Cree and Nichia binning.

In comparison with their pulsed operating conditions, luminous flux values of all devices in Fig. 8.6 have decreased by 32, 30, 5, 26, and 19 %, respectively for steady-state operation at about 330 K junction temperature. Despite the occurrence of some (very) small flux decreases, all values at high temperature have fallen out of their corresponding bin. Nevertheless, in contrast with the other manufacturers under consideration flux decreases are sometimes of the same order or even smaller than the specified bin. The position of the initial luminous flux value thus determines whether the flux during steady-state operation will be situated within the bin or not.

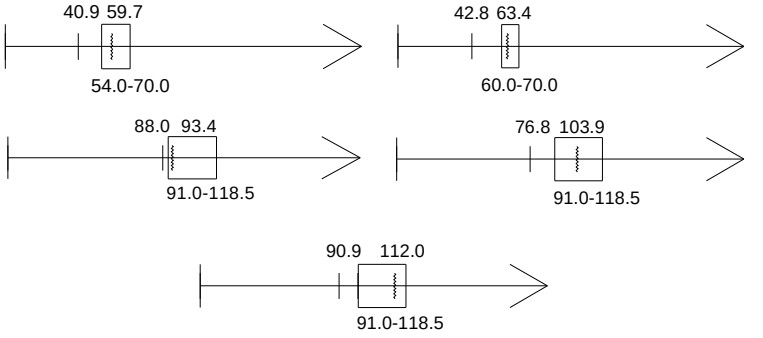

Fig. 8.6: Luminous flux bins and values for LEDs N42L-1 and 2 (top left), S42S-1 and 2 (top right), W42B-1 and 2 (middle left), W42D-1 and 2 (middle right), W42H-1 and 2 (bottom centre).

8.2.4. Colour binning

For the colour binning discussion, a somewhat different approach has been used. As devices have been selected according to their colour binning agreement, colour binning verification is grouped by device colour or CCT and not by manufacturer.

No colour binning is provided for the red Cree LEDs. For single-colour packages only a typical peak wavelength is mentioned in the datasheet.

8.2.4.1. Cool white LEDs

Two very cool white packages are included in the selection in Table 8.1, i.e. the Cree XEKP and the Nichia NSB3 LEDs, with a CCT of 8500 K and 7000 K, respectively. Surprisingly, the Cree and Nichia colour binning behaviour is different from their respective forward voltage and luminous flux binning performance. Indeed, although the colour shift is about four times larger for the Nichia device, both LEDs' colour coordinates for pulsed and steady-state operation can be found within the respective colour bins (see Fig. 8.7). This is in contrast with the voltage and flux binning which had been measured to be irrelevant during steady-state operation. The Nichia colour bin however sizes about twice the Cree bin.

Note that for both LED types the colour shifts towards lower CIE x and y values (or gets more bluish) with increasing junction temperature. This is due to a somewhat different pump and phosphor quantum efficiency decrease with temperature (see next paragraphs).

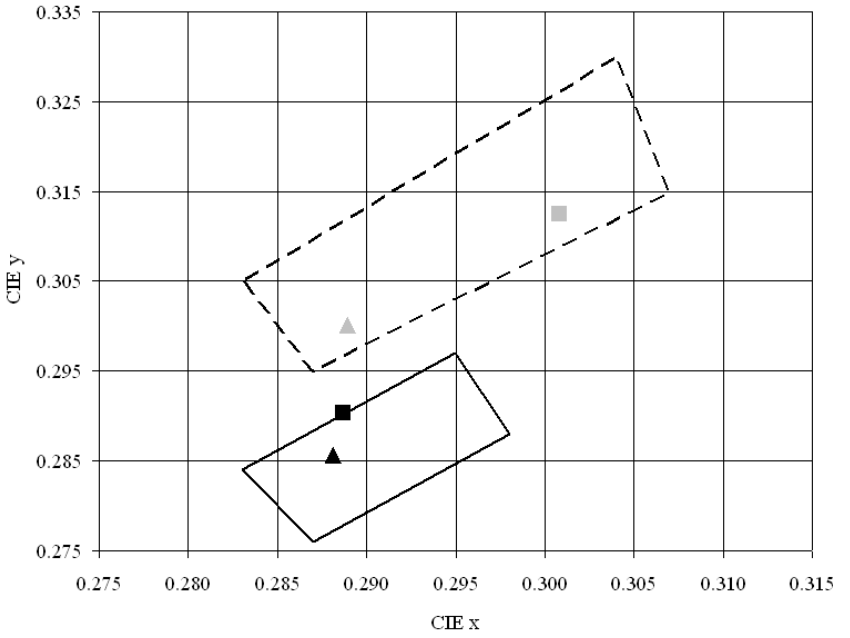

Fig. 8.7: Cree cool white binning (solid line) and Nichia cool white binning (dashed line) with inclusion of their respective LED types (XEKP in black and NSB3 in gray) operated using a pulse (squares) and at thermal steady-state (triangles).

The colour binning study of the Nichia and Seoul Semiconductor regular cool white LED types NSC2 and W42B, W42D, and W42H has been combined as well. As NSC2 and W42H bins overlap most, the measurement results of these devices are gathered in Fig. 8.8.

For both Nichia NSC2 packages comparable results as for the NSB3 device in Fig. 8.7 have been obtained. The CIE colour coordinates at 300 K junction temperature are situated within the specified bin. At higher junction temperatures reached during steady-state operation the colour has significantly shifted, but remains within or at least close to the initial colour bin. It is again remarkable that the SSC devices show a very small colour shift with temperature, but do not correspond to the related datasheet specifications. This is in contrast with the very good forward voltage and luminous flux binning results that have been obtained for this manufacturer. Most of the remaining SSC cool white packages showed similar colour binning properties. Only for LED W42B-1 the colour of both the pulsed and steady-state measurements are situated within the corresponding bin. Apparently, diode manufacturers do hardly succeed in fulfilling all three binning requirements simultaneously.

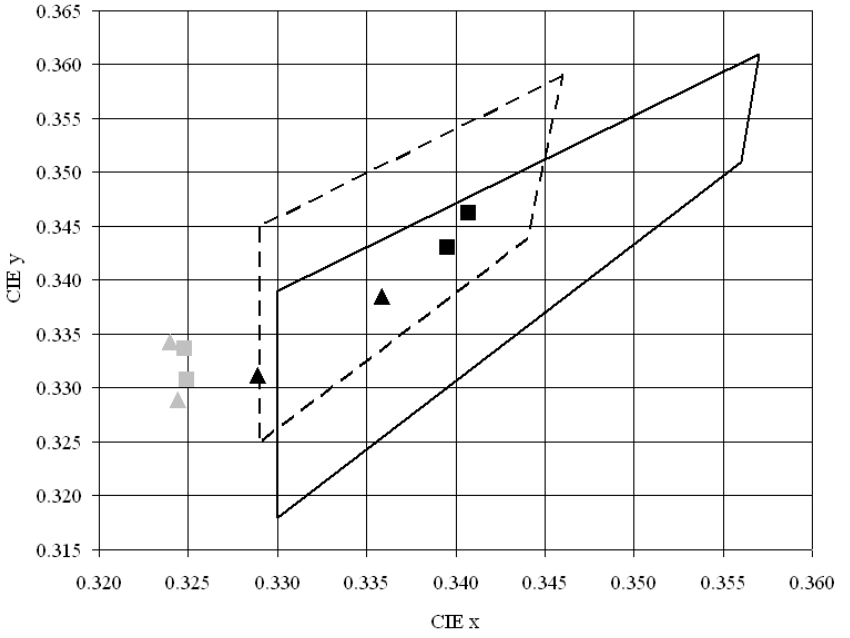

Fig. 8.8: Nichia cool white binning (solid line) and SSC cool white binning (dashed line) with inclusion of their respective LED types (NSC2 in black and W42H in gray) operated using a pulse (squares) and at thermal steady-state (triangles).

8.2.4.2. Neutral white LEDs

For the Cree XCAN (4500 K) and SSC S42S (4000 K) neutral white LEDs analogous results as for the cool white devices have been found. Colour shifts due to junction temperature increases are small, so the initial colour coordinates at low temperature typically indicate the binning agreement at high temperature as well (see Fig. 8.9). Again, the precise forward voltage and luminous flux binning by SSC seems to be compensated by important colour binning deviations, while for Cree the opposite is true.

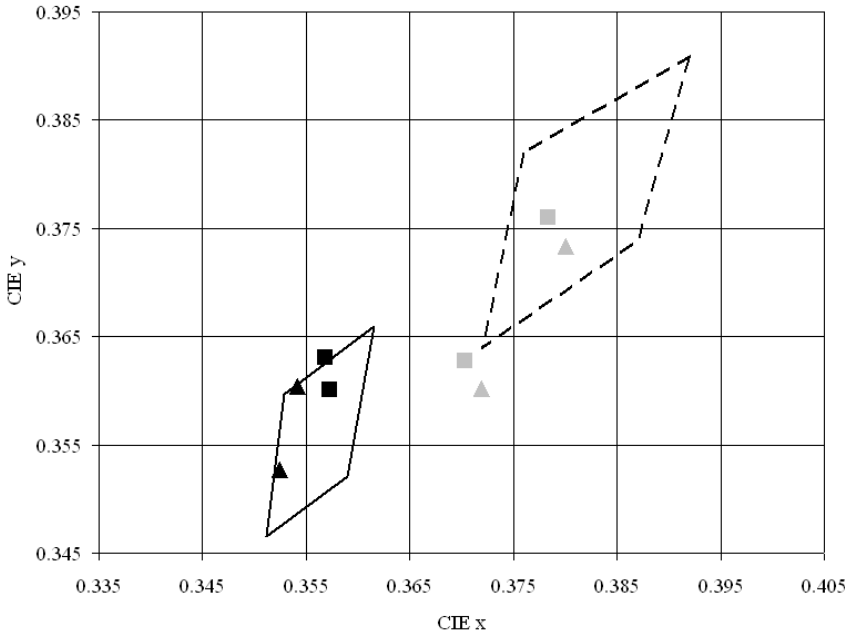

Fig. 8.9: Cree neutral white binning (solid line) and SSC neutral white binning (dashed line) with inclusion of their respective LED types (XCAN in black and S42S in gray) operated using a pulse (squares) and at thermal steady-state (triangles).

8.2.4.3. Warm white LEDs

Also for the warm white LEDs only Cree and Seoul Semiconductor packages could be considered. From these manufacturers, device types XCDM and N42L have been measured, respectively, both with an approximately 3000 K correlated colour temperature.

For all warm white LEDs the colour coordinates obtained during a short measurement pulse are positioned within their respective colour bin (see Fig. 8.10).

Although junction temperature dependent colour variations are of the same order of magnitude for both manufacturers, only the Cree device colour coordinates do not cross the bin edge during steady-state operation. Indeed, the Cree bin under consideration seems to be following the colour changes of the XCDM LED type, while the N42L devices show a larger colour change along the horizontal CIE chromaticity axis. These results once more confirm the conclusions that have been drawn in the preceding paragraphs.

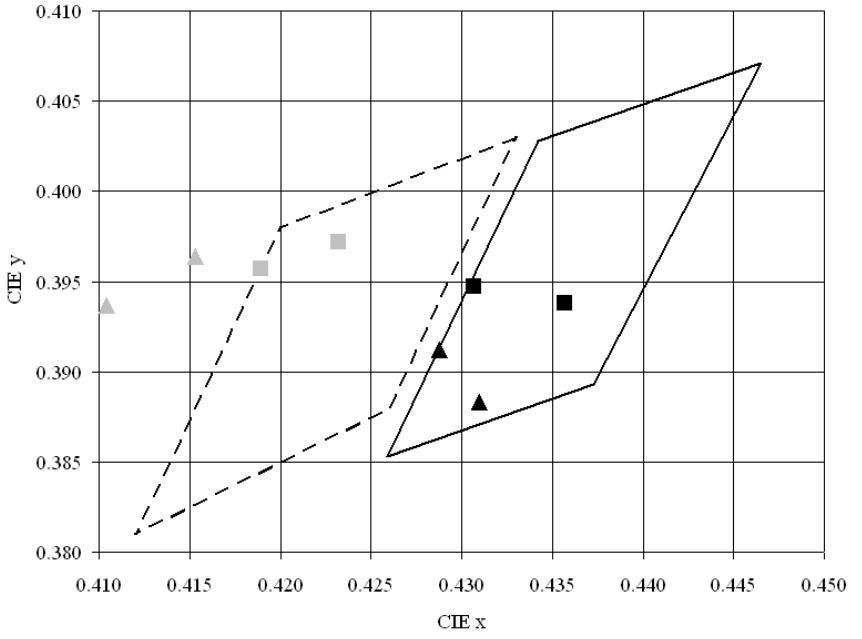

Fig. 8.10: Cree warm white binning (solid line) and SSC warm white binning (dashed line) with inclusion of their respective LED types (XCDM in black and N42L in gray) operated using a pulse (squares) and at thermal steady-state (triangles).

8.3. Power losses in LED applications

8.3.1. Efficiency scheme

An overview of all power losses in a general LED application can be found in Fig. 8.11. For vocabulary and notations CIE guidelines have been followed as much as possible [CIE, 1987].

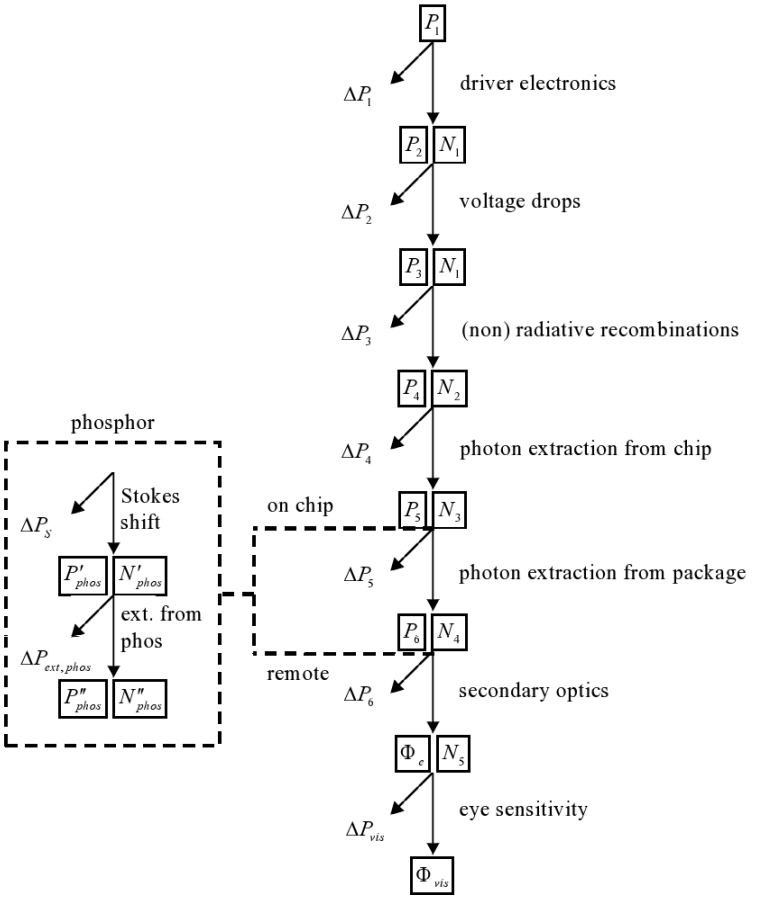

Fig. 8.11: Overview of power and particle losses in a general LED application.

In Fig. 8.11, P_1 corresponds to the total input power from the grid, also referred to as P_t. The subsequent power losses within a LED application are due to the following phenomena:

- Power conversion in the driver electronics (loss ΔP_1).
- Voltage drops in the wiring, the current spreading layer and (neutral regions in) the bulk semiconductor [Park, 2005], and voltage drops due to charge carrier relaxation in quantum wells by phonon emission [Schubert, 2006]. These losses can approximately be considered as voltage drops due to an overall internal series resistance (ΔP_2). Mark however that these losses are not only dissipated into the bulk or the diode junction.
- Non-radiative recombinations, such as Auger recombination or phonon creation near defects in the crystal structure or at surface dangling bonds (ΔP_3) [Schubert, 2006] [Heikkilä, 2009].

- Refractive index differences between diode chip and packaging on the one hand, and between packaging and air on the other, cause important photon absorption. Secondly, there is a chance that a photon travelling in the bulk of the device is absorbed in the cladding layers or in the current spreading window. Next to that, some photons can be absorbed in the active region, producing electron-hole pairs which afterwards recombine non-radiatively. Finally, since contacts are not very good reflectors, they decrease the photon extraction efficiency as well [Boroditsky, 1997]. These losses are combined in ΔP_4 and ΔP_5.
- An analogous photon extraction efficiency can be defined for the wavelength-converting phosphor, often referred to as quantum yield. For remote phosphors, this efficiency $\Delta P_{ext,phos}$ can be determined separately [de Mello, 1997]. The phosphor layer and its corresponding losses are missing for single-colour LEDs.
- Wavelength conversion in the phosphor – the Stokes shift – decreases the wavelength of an incoming pump photon, resulting in a photon energy loss ΔP_S [Schubert, 2006]. This energy is absorbed by the phosphor, thus increasing its temperature.
- Secondary optics, including additional reflectors or lenses constructing a complete luminaire (ΔP_6).
- The radiometric light output Φ_e will be visible for the human eye according to the spectral luminous efficiency $V(\lambda)$ [CIE, 1987]. This phenomenon is referred to as the eye sensitivity and corresponding loss ΔP_{vis}, and has nothing to do with heat dissipation into the diode package.

In practice, all power and efficiency values are current and junction temperature dependent. These dependencies will be included in the following sections.

For every step $s \rightarrow s+1$ in the efficiency scheme, the following equation is valid:

$$P_{s+1} = P_s - \Delta P_s \tag{8.1}$$

with P_s the useful power left at stage s and ΔP_s the power lost during the transition $s \rightarrow s+1$. Taking into account the energy conservation relation, one can therefore write for the complete scheme:

$$P_t = \Phi_{vis} + \sum_s \Delta P_s \tag{8.2}$$

Similar relations can be constructed for the respective numbers of particles N_s (electrons or photons). The corresponding efficiency η_s of each step $s \rightarrow s+1$ is defined by:

$$\eta_s = \frac{P_{s+1}}{P_s} \tag{8.3}$$

resulting in a total efficiency η_t given by:

$$\eta_t = \prod_s \eta_s \tag{8.4}$$

Note that the power loss ΔP_s can be calculated from the efficiency corresponding to the transition $s \rightarrow s+1$ and the resulting power P_{s+1} only. Combination of Eqs. (8.1) and (8.3) yields:

$$\Delta P_s = P_{s+1}\left(\eta_s^{-1} - 1\right) \tag{8.5}$$

A side remark on the calculation of thermal resistances can be made here. For calculation of this thermal resistance R_T for a light-emitting diode package, the dissipated power into the chip P_d has to be considered:

$$P_d \approx \sum_{s=2}^{4} \Delta P_s \tag{8.6}$$

by assuming that all voltage drops result in junction heating. As the package extraction efficiency is generally much higher (close to unity) than the die extraction efficiency, the dissipated power is often approximated by [Jayasinghe, 2006]:

$$P_d \approx \sum_{s=2}^{5} \Delta P_s \tag{8.7}$$

Consequently, for LED packages without secondary optics P_d can be easily determined by subtracting the radiant flux Φ_e from the package input power P:

$$P_d \approx P - \Phi_e \tag{8.8}$$

For diode chips covered by a proximate (on chip) phosphor, this difference includes the terms ΔP_S and $\Delta P_{ext,phos}$ as well. The phosphor of remote phosphor LEDs has to be removed before determining the radiant flux for Eq. (8.8). The junction-to-reference thermal resistance of a LED device can now be written as:

$$R_{T,j-r} \approx \frac{\Delta T_{j-r}}{P_d} \tag{8.9}$$

with ΔT_{j-r} the temperature difference between the diode junction and the reference point.

8.3.2. Power and efficiency calculations

High-power light-emitting diode efficiency strongly depends on the device type and operating conditions. Electrical and optical power measurements have therefore been performed on a selection of phosphor-white LEDs at a number of currents and temperatures. The results allow for a comparative evaluation of their dominant loss mechanisms.

This part of the work only concentrates on commercial LED packages, meaning that driver electronics and secondary optics are not taken into account. According to Eq. (8.2), the package input power P can then be written as:

$$P = \Delta P_R + \Delta P_{EQ} + \Delta P_{vis} + \Phi_{vis} \tag{8.10}$$

This equation is valid for single-colour LEDs. The power loss into the internal series resistance, eye sensitivity loss and visible flux are denoted as ΔP_R, ΔP_{vis} and Φ_{vis}, respectively. Power losses due to non radiative recombinations and due to photon absorption in chip and package are combined into a single term ΔP_{EQ} which is related to the total external quantum efficiency of the device.

For phosphor-white LEDs Eq. (8.10) becomes:

$$P = \Delta P_R + \Delta P_{EQ} + \Delta P_S + \Delta P_{vis} + \Phi_{vis} \tag{8.11}$$

where an extra power loss into the phosphor due to the Stokes shift ΔP_S is added. The phosphor's extraction efficiency is added to the total external quantum loss ΔP_{EQ}. All power losses on the right hand side of Eq. (8.11) are visualised in Fig. 8.12.

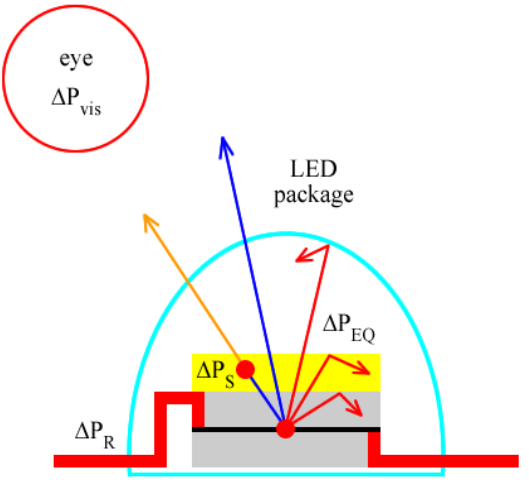

Fig. 8.12: Visualisation of power losses (marked in red) for a phosphor-white LED package. The flux has a pump (blue arrow) and proximate phosphor (orange arrow after Stokes shift) contribution.

The current and temperature dependent input power and power loss into the internal series resistance are given by

$$P(I,T) = IU_f(I,T) \tag{8.12}$$

and

$$\Delta P_R(I,T) = I^2 R_S(T) \tag{8.13}$$

respectively. The efficiency related to this internal series resistance η_R can thus be calculated as:

$$\eta_R(I,T) = 1 - \frac{IR_S(T)}{U_f(I,T)} \tag{8.14}$$

The overall external quantum efficiency $\eta_{EQ}(I,T)$ is calculated as the number of emitted photons divided by the number of injected electrons (with wavelengths λ in nm) [CIE, 1987]:

$$\eta_{EQ}(I,T) = \frac{\int_{380}^{780} \Phi_{e,\lambda}(I,T)\frac{\lambda}{hc}d\lambda}{I/e} \tag{8.15}$$

$\Phi_{e,\lambda}$, h, c, and e represent the spectral radiant flux, Planck constant, speed of light in vacuum and electron charge, respectively. Assuming that the energy of each photon created in the junction (hc/λ) on average equals the electron energy loss associated with the applied forward voltage ($E_g \approx eU_f$), the quantum efficiency related to particle numbers in Eq. (8.15) can be considered valid for the corresponding energy values as well [Schubert, 2006]. By use of Eq. (8.5), the power loss resulting from this external quantum efficiency then becomes:

$$\Delta P_{EQ}(I,T) = \frac{\Phi_{e,pump}(I,T)}{f_{pump}(I,T)}\left[\frac{1}{\eta_{EQ}(I,T)} - 1\right] \tag{8.16}$$

with $\Phi_{e,pump}$ the flux of the pump spectrum and f_{pump} the pump light leakage fraction:

$$f_{pump}(I,T) = \frac{\int_{380}^{780} \Phi_{e,\lambda,pump}(I,T)\,\lambda\,d\lambda}{\int_{380}^{780} \Phi_{e,\lambda}(I,T)\,\lambda\,d\lambda} \tag{8.17}$$

i.e. the number of photons emitted by the pump divided by the total number of emitted photons [Krames, 2007]. This fraction equals one for single-colour LEDs. In that case $\Phi_{e,pump}$ is replaced by the total radiant flux Φ_e in Eq. (8.16) as well. For all device types $\Phi_{e,pump}/f_{pump}$ thus equals the power of all photons in the measured flux spectrum before potential phosphor conversion. Radiant fluxes are determined as:

$$\Phi_e(I,T) = \int_{380}^{780} \Phi_{e,\lambda}(I,T)\,d\lambda \tag{8.18}$$

For remote phosphor type of LEDs, the phosphor's external quantum efficiency η_{phos} can be calculated separately as follows:

$$\eta_{phos} = \frac{\int_{380}^{780} \Phi_{e,\lambda,conv}\,\lambda\,d\lambda}{\int_{380}^{780} \Phi_{e,\lambda,init}\,\lambda\,d\lambda - \int_{380}^{780} \Phi_{e,\lambda,trans}\,\lambda\,d\lambda} \tag{8.19}$$

with $\Phi_{e,\lambda,conv}$, $\Phi_{e,\lambda,init}$ and $\Phi_{e,\lambda,trans}$ the phosphor-converted flux spectrum, initial pump flux spectrum and transmitted pump flux spectrum, respectively. A phosphor's quantum efficiency thus equals the number of converted and extracted photons with respect to the number of absorbed pump photons. When η_{phos} is

determined after integration of the phosphor into a practical application, Eq. (8.19) becomes the phosphor's effective quantum efficiency η_{eff} .

The efficiency of the Stokes shift is generally approximated by [Schubert, 2006]:

$$\eta_S(I,T) \approx \frac{E_{phos}}{E_{pump}} = \frac{\lambda_{pump}}{\lambda_{phos}} \tag{8.20}$$

Again using Eq. (8.5), this corresponds to a Stokes power loss:

$$\Delta P_S(I,T) \approx \Phi_{e,phos}(I,T)\left(\frac{\lambda_{phos}}{\lambda_{pump}} - 1\right) \tag{8.21}$$

with $\Phi_{e,phos}$ the fluorescence spectrum. However, taking into account the rather wide phosphor spectrum and the small blue spectrum, the power loss into the phosphor due to the Stokes shift can be calculated more accurately by adding the power losses of all phosphor wavelengths:

$$\Delta P_S(I,T) \approx \int_{380}^{780} \Phi_{e,\lambda,phos}(I,T)\left(\frac{\lambda}{\lambda_{pump}} - 1\right) d\lambda \tag{8.22}$$

The Stokes efficiency $\eta_S(I,T)$ then becomes:

$$\eta_S(I,T) \approx \frac{\int_{380}^{780} \Phi_{e,\lambda,phos}(I,T)\,\lambda_{pump}\; d\lambda}{\int_{380}^{780} \Phi_{e,\lambda,phos}(I,T)\,\lambda\; d\lambda} \tag{8.23}$$

The visible flux is determined by inserting the spectral luminous efficiency $V(\lambda)$ into Eq. (8.18):

$$\Phi_{vis}(I,T) = \int_{380}^{780} \Phi_{e,\lambda}(I,T)V(\lambda)\,d\lambda \tag{8.24}$$

The eye sensitivity loss ΔP_{vis} thus equals:

$$\Delta P_{vis}(I,T) = \int_{380}^{780} \Phi_{e,\lambda}(I,T)\left[1 - V(\lambda)\right] d\lambda \tag{8.25}$$

Eq. (8.24) shows that the visible flux also equals the luminous flux Φ_v divided by the maximum luminous efficacy of radiation K_m = 683 lm/W. Indeed, Φ_v is defined by:

$$\Phi_v(I,T) = K_m \int_{380}^{780} \Phi_{e,\lambda}(I,T) V(\lambda) d\lambda \tag{8.26}$$

The visibility efficiency η_{vis} equals:

$$\eta_{vis} = \frac{\Phi_{vis}}{\Phi_e} = \frac{K}{K_m} \tag{8.27}$$

by combining Eqs. (8.24) and (8.26), and with K the total luminous efficacy of radiation:

$$K(I,T) = \frac{\Phi_v(I,T)}{\Phi_e(I,T)} \tag{8.28}$$

Finally, the efficiency and luminous efficacy of a complete LED package are defined as:

$$\eta_e(I,T) = \frac{\Phi_e(I,T)}{P(I,T)} \tag{8.29}$$

and

$$\eta_v(I,T) = \frac{\Phi_v(I,T)}{P(I,T)} \tag{8.30}$$

respectively, meaning that $\eta_v = \eta_e K$.

In correspondence with Eq. (8.4), Eqs. (8.14), (8.15), (8.23), (8.27), (8.28), and (8.30) can be combined to the following formula, adapted from [Krames, 2007]:

$$\eta_v = \eta_R \ \eta_{EQ} \left[f_{pump} + (1 - f_{pump}) \eta_S \right] \eta_{vis} \ K_m \tag{8.31}$$

For $f_{pump} = 1$ the Stokes efficiency drops out and Eq. (8.31) becomes the efficiency equation for a single-colour LED.

8.3.3. Package efficiency measurements and results

Five commercial phosphor-white high-power LED packages have been selected for investigation through current-voltage and spectral radiant flux measurements at several forward current and junction temperature settings. At first, the current and junction temperature dependence of each power loss in Eq. (8.11) has been calculated by use of Eqs. (8.12) to (8.26) and examined at 300 K junction temperature and a 350 mA drive current, respectively (see Fig. 8.13).

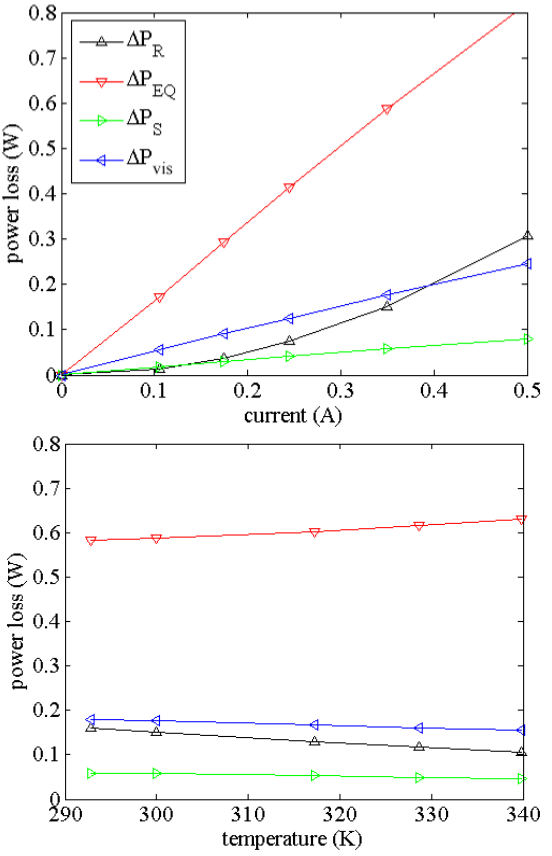

Fig. 8.13: Power losses as a function of current at 300 K (top), and temperature at 350 mA (bottom) for LED W42D-1.

With increasing current, the quantum, Stokes and visual losses increase quasi linearly. This means that the quadratic increase of the power loss into the internal series resistance forms the main reason for the decreasing diode efficiency with increasing current (see also chapter 4). On the other hand, the decreasing diode

efficiency with junction temperature is only due to the increasing external quantum loss with increasing temperature, as other losses slightly decrease.

All five terms on the right-hand side of Eq. (8.11) have been compared for all LEDs under consideration at normal operating conditions (350 mA and 330 K junction temperature) and per unit input power as well. From the data in Fig. 8.14, it is clear that the internal series resistance directly consumes about 10 to 20 % of the initial input power (see also chapter 4). As a result, the overall efficiency is remarkably higher for LEDs with a reduced resistance (e.g. W42D-1).

External quantum loss is clearly the dominant loss factor and can be related to the colour temperature of the LEDs (see also section 8.4.3). Indeed, W42D-1, XEKP, and LXML are cool white devices. The first two exhibit the smallest quantum losses. XCAN-1 is neutral white, while XCDM-1 is warm white. Non-fluorescent absorption in the phosphor seems to be more important for these warm white LEDs. For this reason, the LED efficiency is always higher for cool white LEDs [Schubert, 2006]. The Stokes shift losses equal about 2 to 5 % of the input power for all measured LEDs. Although the conversion loss per photon is larger for warm white LEDs, this effect seems to be compensated by the smaller number of emitted photons. The remaining visible flux part is always a few percent smaller than the visual loss for phosphor-white LED spectra.

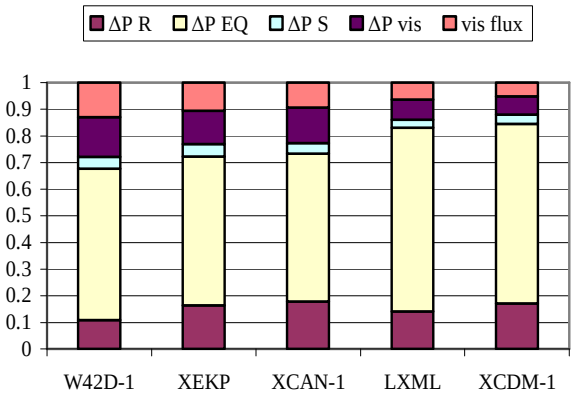

Fig. 8.14: Comparison of normalised power losses and flux for five LEDs at 350 mA and 330 K, sorted according to their visible flux per input power.

8.3.4. Phosphors' effective quantum efficiency

A lot of research is dedicated to determining the quantum efficiency of yellow phosphor powders for light-emitting diode applications, i.e. the number of converted photons relative to the number of absorbed blue pump photons [Narendran, 2005-2] [Winkler, 2007] [You, 2010]. The research however usually concentrates on

measuring the phosphor apart from its final application in a remote phosphor type of LED module. It is therefore appropriate to define the effective quantum efficiency η_{eff} as the quantum efficiency of a phosphor plate when integrated in a lighting application (see section 8.3.2). For the latter, all back-scattered photons are absorbed or redirected by the module, which may lead to different results in comparison with the quantum efficiency measurement setup for the phosphor powder.

If the pump light spectrum shape does not significantly change, the remote phosphor's effective quantum efficiency η_{eff} only depends on the temperature and excitation light density. The remote phosphor is thus firstly characterized by studying its temperature as a function of excitation light density and junction temperature. Afterwards, the effect of this phosphor temperature and excitation light density on effective quantum efficiency is determined.

The spectral radiant flux of a selection of three pump diode modules without phosphor plate has been determined for five forward currents (150, 250, 350, 500, and 700 mA) and five junction temperatures (300, 315, 335, 355, and 375 K) with a 1 m ambient-temperature-controlled integrating sphere connected to a CCD-array spectrometer with 3 nm bandpass. The same forward current and junction temperature settings have been used during a second spectral radiant flux measurement series with the remote phosphor plates remounted on their respective pump devices. The phosphor temperature has been recorded using a k-type thermistor connected with thermal paste. Combining the results of both measurement series allowed calculating the effective quantum efficiency of the phosphors afterwards.

Effective quantum efficiency values at 350 mA and 335 K junction temperature have been collected in Table 8.2. The corresponding phosphor temperature and excitation flux have been added as well. Fig. 8.15 shows the effective quantum efficiency for MOD1 as a function of phosphor temperature and pump flux.

Table 8.2: Phosphor temperature, pump flux, and effective quantum efficiency η_{eff} at 350 mA and 25 °C ambient for three remote phosphor devices.

	FOR1	MOD1	XIC4
T_{phos} (°C)	37.0	44.1	34.5
$\Phi_{e,pump}$ (W)	5.820	2.319	4.179
η_{eff} (%)	77.8	37.6	52.0

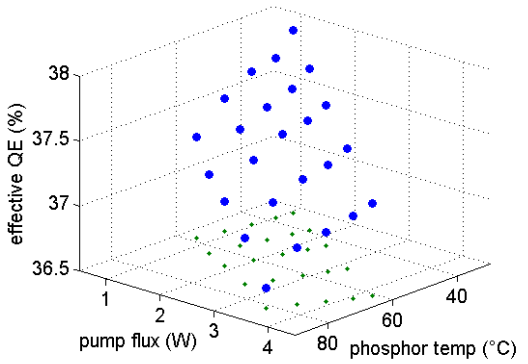

Fig. 8.15: Effective quantum efficiency for device MOD1 as a function of phosphor temperature and initial pump flux (large blue dots) and its projection in the horizontal plane (small green dots).

Although experimental results are not discussed in detail, phosphor temperature of a remote phosphor type of LED has been found to increase with increasing pump light flux and junction temperature. This increase largely depends on the phosphor's thermal resistance to the junction.

The steady-state effective quantum efficiencies in Table 8.2 roughly correspond to values reported in literature, but differ from efficiency values determined for non-integrated phosphors powders [Winkler, 2007] [Allen, 2008] [Hoelen, 2008]. Moreover, Fig. 8.15 shows that the effective quantum efficiency decreases with increasing phosphor temperature (about 0.03 %/K) and excitation light density (about 0.1 %/W). Within typical diode operation ranges, the pump flux effect is however negligible in comparison with the effect of temperature. Analogous results have been found for all devices under test. They correspond to phosphor powder efficiency behaviours that have been reported in literature [Zhang, 2008] [Setlur, 2009].

8.4. Efficiency comparison

Numbers quoted for luminous flux and efficiency of LEDs are very sensitive data as they are used to impress and push the LED market. Stated otherwise, the efficiency or luminous efficacy is the first quantity judged for light source comparison.

The efficiency comparison is divided into five parts. At first, the output of RGB and phosphor-white devices is compared, followed by a study of phosphor-white colour differences and luminous efficacy differences between manufacturers. After that, the possible benefits of using several dies instead of only one for creating high-power packages are examined. The comparison ends with an analysis of efficiencies obtained in practical applications.

8.4.1. RGB versus phosphor-white

Two types of LED configurations are used for white lighting applications. These are the combination of single-colour dies (typically red-green-blue), and phosphor conversion on top of a pump (typically blue) diode. The former could be expected to have a higher efficiency than phosphor-white LEDs due to the lack of phosphor losses and the use of lower currents per diode. However, as separate emitters or packages have to be used for one application, power losses may add up and the overall temperature of the application may be higher if no appropriate heat sink is installed. In order to know which configuration has the highest efficiency, this study focuses on the luminous efficacy comparison between phosphor-white and RGB LED devices for three manufactures. Two different approaches have been used:

The first approach consists of evaluating the luminous flux, CIE colour coordinates and electrical power of a phosphor-white LED at 350 mA and 300 K junction temperature, controlled by a Peltier element. Using custom-made software and the power models constructed in chapter 5, the currents necessary to obtain the same luminous flux and colour by combining the red, green, and blue diode at 300 K junction temperature are calculated afterwards. As a result, the efficiency of both approaches with identical flux and colour characteristics can be compared.

As the first approach is rather artificial, a second approach has been used as well. It takes into account the implementation of a LED in a practical setup, by putting the phosphor-white LED on a heat sink and evaluating its luminous flux, colour coordinates and electrical power during steady-state operation. The next step consists of reproducing the phosphor-white package's flux and colour coordinates by fine-tuning the red, green, and blue device currents for the RGB LED mounted on the same heat sink. Again, the efficiency of both approaches with identical flux and colour characteristics can be compared.

8.4.1.1. Comparison for a fixed junction temperature

Using the temperature-controlled heat sink mounted on the integrating sphere, the colour coordinates, luminous flux, and electrical power of cool white LEDs of Cree, Lumileds and Seoul Semiconductor (XEKP, LXML, and W42D-1, respectively) at 350 mA and 300 K junction temperature have been measured. The power models constructed in chapter 5 have been applied to determine the currents necessary to obtain the same luminous flux and colour by combining the red, green, and blue diode of each respective manufacturer at 300 K junction temperature afterwards. The RGB packages under consideration are XRC(RGB), LXR(RGB), and F51(RGB)-1 of Cree, Lumileds, and SSC, respectively. Input power and luminous efficacy results of both approaches are compared for each manufacturer in Table 8.3.

Table 8.3: Comparison of Cree, Lumileds, and SSC phosphor-white and RGB input powers and luminous efficacies for a 300 K constant junction temperature. For each manufacturer the same luminous flux and colour values have been considered for both the phosphor-white and RGB sources. The letters PW and S stand for phosphor-white and sum of RGB, respectively.

MFR	Φ_v (lm)	(x, y)	P (W) PW	η_v (lm/W) PW	P (W) R	P (W) G	P (W) B	P (W) S	η_v (lm/W) S
Cree	98.2	(0.310, 0.326)	1.19	82.5	0.49	-	0.25	-	-
Lum.	51.5	(0.324, 0.317)	1.08	47.7	0.50	1.62	0.43	2.55	20.2
SSC	107.5	(0.309, 0.326)	1.13	95.1	0.77	-	0.87	-	-

Most remarkably, the RGB currents necessary to reproduce the phosphor-white LEDs' flux and colour coordinates could not be calculated for manufacturers Cree and Seoul Semiconductor (dashes in Table 8.3). This is due to the high luminous flux and efficacy values of these phosphor-white emitters, while the green diode's light output reaches a maximum at about 0.54 and 0.72 A respectively, which has a value below the required flux value. This light output limit is a result of the quadratic flux variation with current, and is experimentally confirmed in literature [Hui, 2009].

Only for the green Lumileds diode LXRG the appropriate current could be reached, because of the rather low phosphor-white efficiency and the high flux peak value current for this green emitter. The Lumileds data in Table 8.3 show that the RGB efficacy is more than 50 % lower than the phosphor-white efficacy. This is due to the low quantum efficiency of the green emitter (more or less 10 %, see Fig. 8.16) in comparison with the quantum efficiency of blue (or pump in phosphor-white) and red emitters (30 to 50 %) [Schubert, 2006] [Krames, 2007] [Chen, 2008] [Mottier, 2009]. The electrical input power required for the Lumileds diode in Table 8.3 is indeed already higher than the electrical input power of the phosphor-white device. The power losses resulting from the Stokes shift and phosphor external quantum efficiency are thus relatively small in comparison with the losses related to the green LED's quantum efficiency (see sections 8.3.3 and 8.3.4).

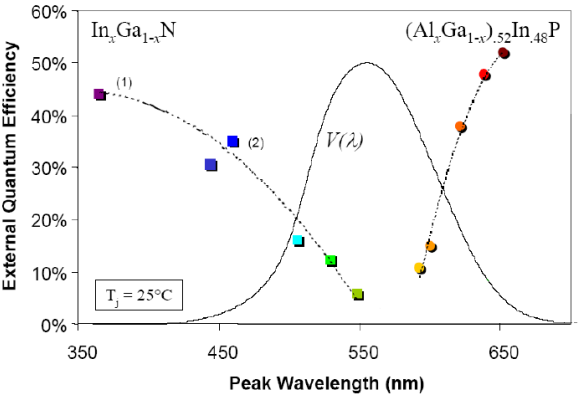

Fig. 8.16: External quantum efficiency of InGaN green and blue emitters (squares) and AlGaInP red diodes (circles) at about 300 K junction temperature [Liu, 2007]. The value of proportionality index x determines the compound semiconductor's peak wavelength.

8.4.1.2. Comparison for a fixed heat sink

As the RGB versus phosphor-white efficiency comparison at 300 K constant junction temperature is rather artificial and could not be performed for Cree and SSC, a second approach has been used as well. It takes into account the implementation of a LED in a practical setup, by putting the phosphor-white LED on a heat sink and evaluating its luminous flux, colour coordinates and electrical power during steady-state operation. The phosphor-white package's flux and colour coordinates are then reproduced by fine-tuning the red, green, and blue device currents for the RGB LED mounted on the same heat sink. The input powers and luminous efficacy values of both approaches are compared for each manufacturer in Table 8.4. For simplified comparison, the input powers are additionally visualized in Fig. 8.17.

Table 8.4: Comparison of Cree, Lumileds, and SSC phosphor-white and RGB input powers and luminous efficacies for devices mounted on a fixed heat sink. For each manufacturer the same luminous flux and colour values had been set for both sources. The letters PW and S stand for phosphor-white and sum of RGB, respectively.

MFR	Φ_v (lm)	(x, y)	P (W) PW	η_v (lm/W) PW	P (W) R	P (W) G	P (W) B	P (W) S	η_v (lm/W) S
Cree	84.1	(0.31, 0.33)	1.16	72.5	0.80	1.46	0.18	2.44	34.5
Lum.	45.9	(0.32, 0.33)	1.06	43.3	0.55	1.55	0.40	2.50	18.4
SSC	77.6	(0.30, 0.32)	1.11	69.9	0.48	1.76	0.37	2.61	29.7

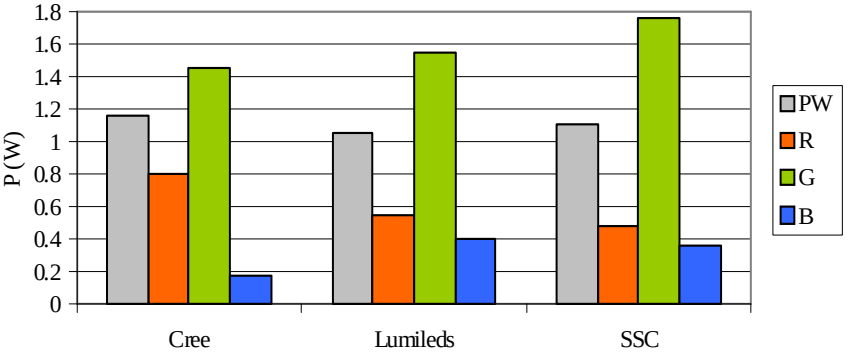

Fig. 8.17: Comparison of Cree, Lumileds, and SSC phosphor-white and RGB electrical input powers for devices mounted on a fixed heat sink. For each manufacturer the same luminous flux and colour values had been set for both sources. PW stands for phosphor-white.

The measurement data in Table 8.4 and Fig. 8.17 show that for the LEDs mounted on a fixed heat sink, sufficiently high luminous fluxes can be obtained for all green emitters to reproduce the corresponding phosphor-white diodes' flux and colour. The results confirm that the luminous efficacy of white devices equals more than twice the efficacy of the corresponding RGB combination for similar flux and colour characteristics, even in practical applications.

8.4.2. Phosphor-white colour differences

In section 8.3.3 the efficiency diversity between phosphor-white devices with different correlated colour temperatures has been pointed out already. Three commonly used colour temperature regions will be compared into more detail here. These regions are warm white with a CCT of 3000 K or below, neutral white with a CCT between 3000 and 5000 K, and cool white with a CCT of 5000 K or above. Efficiency differences have been studied through comparison of luminous flux values at 350 mA and 330 K junction temperature of cool, neutral, and warm white devices from two manufacturers, i.e. Cree and Seoul Semiconductor. For Cree, packages XEKP (cool), XCAN-1 (neutral), and XCDM-1 (warm) have been selected, while for SSC types W42H-1 (cool), S42S-1 (neutral), N42L-1 (warm) have been considered. Measurement results are gathered in Table 8.5.

Table 8.5: Input power, luminous flux, and luminous efficacy comparison of cool, neutral, and warm phosphor-white emitters from two manufacturers.

MFR	data type	cool	neutral	warm
Cree	CCT (K)	8500	4500	3000
	P (W)	1.19	1.06	1.14
	Φ_v (lm)	98.2	68.1	43.0
	η_v (lm/W)	82.5	63.9	37.8
SSC	CCT (K)	6300	4000	3000
	P (W)	1.09	1.06	1.12
	Φ_v (lm)	76.8	55.1	36.7
	η_v (lm/W)	70.5	52.0	32.8

Not taking into account the efficiency dissimilarity between Cree and SSC (see section 8.4.3) it is clear that large luminous efficacy differences exist for the three colour temperature regions. Cool white is most efficient for both manufacturers, while neutral white and warm white show a luminous efficacy value which is nearly 25 and 50 % lower, respectively.

The efficiency decrease with decreasing colour temperature can be explained from the normalized spectra of the Cree devices in Fig. 8.18. In order to obtain a lower correlated colour temperature, the relative phosphor contribution and the phosphor's peak wavelength both have to increase. Such increases correspond to a higher yellow-blue ratio (see chapter 7) and a more reddish phosphor colour, respectively. This means that more phosphor material has to be used, leading to lower external quantum efficiencies, and that on average more power is lost during each Stokes shift of the blue pump photon energy. The yellow-blue ratio approximately equals 0.5, 1, and 2 for cool, neutral, and warm white emitters, respectively (see also Fig. 8.18). According to Eq. (8.21), corresponding Stokes shifts convert about 19, 23, and 26 % of the initial pump photon power into heat. This means that the decreasing efficacy with decreasing colour temperature is mainly due to an increasing photon absorption in the phosphor.

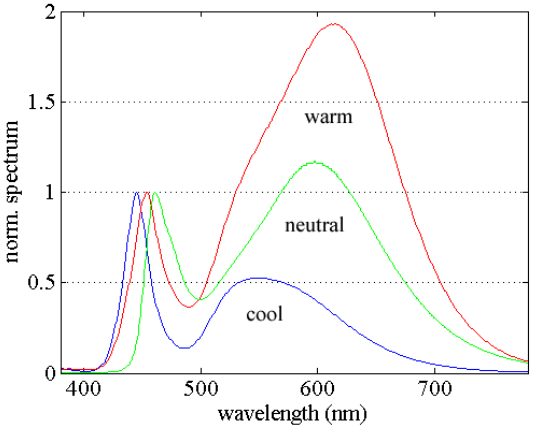

Fig. 8.18: Spectra of phosphor-white Cree devices XEKP (cool, blue line), XCAN-1 (neutral, green line), and XCDM-1 (warm, red line). For comparison of the phosphor contribution, spectra have been normalized to the pump peak value.

8.4.3. Differences between manufacturers

All luminous flux and power measurements performed for analysis throughout this work allowed comparing the luminous efficacy values of LED devices from different manufacturers as well. In order to perform this comparison as fair as possible, only single-die one watt packages driven with a 350 mA drive current and at a typical 330 K constant junction temperature have been considered. Moreover, as LED-technology and related efficiency values improve very rapidly, the selection has been divided into two levels corresponding to device production periods 2006-2007 and 2008-2009, respectively. The manufacturer selection is widest for the first period, but only cool phosphor-white LEDs are included in the comparison (see Table 8.6). Cool and warm white devices have been compared separately for the second period, but for three manufacturers only (see Tables 8.7 and 8.8). This selection is mainly a result of the research focus during the last two years. In each Table, devices are sorted by luminous efficacy.

Table 8.6: Luminous efficacy comparison of cool white LEDs (at 350 mA and 330 K) manufactured in 2006-2007.

MFR	LED	CCT (K)	P (W)	Φ_v (lm)	η_v (lm/W)
Cree	XREW	5700	1.12	71.7	64.0
SSC	W421	6300	1.07	66.0	61.7
Lum.	LW3C-1	5500	1.07	42.1	39.2
Osram	W5SM	5600	1.06	35.2	33.3
Nichia	NCCW-1	6600	1.20	34.5	28.8
Prol.	PG1A-1	6250	1.24	31.9	25.7

The data in the last column of Table 8.6 show that huge efficiency differences between manufacturers occur. The lowest luminous efficacy value of LED PG1A-1 of Prolight Opto equals about 40 % of the highest value obtained for the Cree XREW device. Although a rather large gap between the SSC and Lumileds values is observed, efficiencies of the other packages are more or less equally spread in between the two extreme values. In Tables 8.7 and 8.8, only the three highest efficacy manufacturers of 2006-2007 have been considered.

Table 8.7: Luminous efficacy comparison of cool white LEDs (at 350 mA and 330 K) manufactured in 2008-2009.

MFR	LED	CCT (K)	P (W)	Φ_v (lm)	η_v (lm/W)
SSC	W42D-1	6300	1.13	107.5	95.1
Cree	XEKP	8500	1.19	98.2	82.5
Lum.	PWC8	6500	1.13	74.9	66.1

Table 8.8: Luminous efficacy comparison of warm white LEDs (at 350 mA and 330 K) manufactured in 2008-2009.

MFR	LED	CCT (K)	P (W)	Φ_v (lm)	η_v (lm/W)
Lum.	LXML	3100	1.06	45.9	43.3
Cree	XCDM-1	3000	1.14	43.0	37.8
SSC	N42L-1	3000	1.12	36.7	32.8

The worldwide diode efficiency improvement research that is being conducted very intensively for years clearly pays. In comparison with the period 2006-2007, luminous efficacy values of cool phosphor-white diode packages of Cree, Lumileds and SSC have increased by roughly a third by 2008-2009 (see Table 8.7). An overview of LED technology developments and advances that made this increase possible is given in chapter 2. The much lower luminous efficacies that have been measured for the warm white devices in Table 8.8 are explained in section 8.4.2.

Even for some of the most famous LED package manufacturers nowadays, large discrepancies between their respective efficacy values have been found. The cool white Cree and Lumileds efficiencies amount about 87 and 70 % of the highest SSC luminous efficacy, respectively. On the other hand, the Lumileds warm white device scores best. For each subsequent manufacturer the luminous efficacy reduces by approximately 13 %.

Note that the values in Tables 8.6 to 8.8 have to be considered with certain scepticism. These values are indeed based on the measurement of individual packages. Next to that, the results in section 8.4.2 show that the small CCT differences manipulate the luminous efficacy comparison as well. Finally, measurement data are highly sensitive to the availability of research samples and their binning (see section 8.2). Unfortunately however, acquiring samples from specific bins appeared to be very difficult and sometimes even impossible.

8.4.4. Single-die versus multi-die

The supra-linear electrical input power and sub-linear radiant flux behaviour described in chapter 5 suggest that diode power losses increase with forward current. This statement has been confirmed in section 8.3.3. As a consequence, LED lighting applications could be made more efficient by replacing each package at normal drive current by a number of packages driven with a reduced forward current. Alternatively, a single-die package could be substituted by a multi-die package where the initial input power is shared by all dies. This approach totally differs from providing each die in a multi-die emitter with the normal input power of a single-die package. The latter does not cause any efficiency enhancement whatsoever.

First, a concrete efficiency improvement example is given. Simulation by use of the power models in chapter 5 show that LED W42D-1 has an input power of about 1.10 W, and a flux of 0.32 W at 350 mA normal drive current and 320 K junction temperature. Assuming an unchanged junction temperature, the same flux can be obtained by conducting three similar devices with a 100 mA drive current. The input power is then reduced to 0.3 W each, or 0.9 W in total. This corresponds to an 18 % efficiency increase. In practice however, the junction temperature decreases due to the decreased dissipated power, resulting in an additional efficiency augmentation, the possibility of using a smaller heat sink, and an extended light source lifetime (see section 8.5.2).

To our knowledge, so far only manufacturer Nichia provides this alternative multi-die approach in its LED gamma. Device type NCCW contains one diode chip, while NS6W incorporates six dies placed in a parallel connection. The devices compared in Table 8.9 were both manufactured in 2006, have a correlated colour temperature of 6600 K, and have been operated at 350 mA normal drive current and at 330 K constant (combined) junction temperature. As expected, the multi-die luminous efficacy is much higher than the single-die efficacy; the increase equals almost 50 %. Nevertheless, the cost versus gain question will as always determine the design approach in practice.

Table 8.9: Power, flux and efficacy of Nichia device NCCW-1 (1 die) and its multi-die alternative NS6W (6 dies).

	NCCW-1	NS6W
P (W)	1.20	1.10
Φ_v (lm)	34.5	52.7
η_v (lm/W)	28.8	47.9

8.4.5. Efficiency in practice

System efficiencies obtained in practical applications cannot lack in this efficiency comparison. The luminous flux of four LED lamps and six engines has been determined by use of an integrating sphere or spatial integration of goniophotometer intensity measurements (see Table A.2 in Appendix 1). For power supply and measurement of these devices, an Agilent 6813B Voltage Source with a typical 50 Hz sinusoidal input of 230 V (RMS) and a Voltech PM1000 Power Analyser have been used, respectively. In order to correspond to practical use, measurements have been performed during steady-state operation while mounted on their respective heat sinks. Diode junction temperatures in general amount between about 330 and 400 K.

On overview of the measured LED lamp efficiencies is given in Table 8.10. Except for MEG1 with GU10 fitting, all lamps have a standard E27 fitting. Luminous efficacy values have been found to amount between 35 and 45 lm/W, which is a rather limited range. The Megaman spot shows the highest efficacy, but this may be due to its higher colour temperature (neutral instead of warm white) and somewhat more recent production date as well. As expected, due to the use of additional narrowing optics, the Uniled spot ULS1 has a lower (by 10 %) luminous efficacy than the Uniled lamp ULL1. Of all LED lamps under test the Philips Pharox PHA1 is least efficient, but has to lowest CCT as well.

Table 8.10: Input power, luminous flux, and luminous efficacy comparison of commercial LED lamps.

LED	CCT (K)	P (W)	Φ_v (lm)	η_v (lm/W)
MEG1	4000	16.2	718	44.3
ULL1	3000	2.86	117	40.9
ULS1	3000	5.47	201	36.7
PHA1	2800	3.96	143	36.1

The power and efficacy measurement results of the selected LED engines with standard net plug are collected in Table 8.11. Luminous efficacy values of the phosphor-white devices are comparable to those for the LED lamps in Table 8.10. Only the Fortimo engine FOR1 shows a considerably higher efficiency of more than 50 lm/W. On the contrary, the Acriche package AW32 with integrated driver electronics has a luminous efficacy of 31.3 lm/W only, despite its high colour temperature and adequate 340 K junction temperature during measurement. However, this specific device has been manufactured in 2007 already, while the other engines have a more recent production date.

Table 8.11 also contains an overview of Philips Lexel luminous efficacies for full red, full green, full blue, and combined 4000 K white operation. The same heat sink as for FOR1 was attached during measurement. The obtained efficacy values confirm the conclusions of section 8.4.1, meaning that the RGB white efficacy equals roughly half the phosphor-white efficacy of device FOR1. Practical luminous efficacy values of individual colours are even lower. For the red and blue emitters

this is due to their marginal position with respect to the eye sensitivity function $V(\lambda)$, for the green LEDs the efficiency deficit is caused by the low external quantum efficiency of the InGaN compound semiconductor (see section 8.4.1.1).

Table 8.11: Input power, luminous flux, and luminous efficacy comparison of commercial phosphor-white LED engines (top) and one RGB engine (bottom).

LED	CCT (K)	P (W)	Φ_v (lm)	η_v (lm/W)
FOR1	4000	45.7	2356	51.5
FOS1	3000	21.5	849	39.4
XIC4	4000	23.4	886	37.9
XIC3	3000	23.8	795	33.4
AW32	6300	5.25	164	31.3

LED	CCT (K)	P (W)	Φ_v (lm)	η_v (lm/W)
LXLW	4000 K	30.05	856.7	28.5
LXLR	630 nm	16.07	344.8	21.5
LXLG	530 nm	18.68	387.3	20.7
LXLB	470 nm	13.62	119.4	8.8

The Luminous efficacy values in Tables 8.10 and 8.11 correspond very well to data found in non-commercial literature [Schubert, 2006] [Liu, 2007] [Navigant, 2009]. They indicate that practical efficacies of commercial LED lamps and engines are at present comparable with luminous efficacy values of compact fluorescent lamps (30 to 70 lm/W) [Schubert, 2006] [Mottier, 2009] [Navigant, 2009] [Bodart, 2010]. However, at this moment cool white package efficacies under normal operating conditions (see previous sections) are of the same order as fluorescent tube or HID efficacies (80 to 90 lm/W) [Chen, 2008] [Narukawa, 2008].

8.5. Light-emitting diode quality scale

8.5.1. Package quality control from measured diode characteristics

From the measurement and modelling efforts described in the previous chapters 4 to 7, ten parameters can be extracted which are determined by intrinsic diode properties and closely related to package quality. The parameters may therefore be utilized for LED comparison on a quality scale. Such a scale can be constructed for each parameter separately, or for a weighed function of a number of quality parameters. In order of appearance in text, the following quantities are taken into account:

- Ideality factor n. Ironically, despite its name the ideality factor is difficult to use for comparison as combination of multiple junctions enlarges the ideality factor, while diode performance might improve (see chapter 4).
- Internal series resistance at specific temperature $R_S(T_0)$, regarding junction heating.

- Slope γ_P of power decrease with temperature.
- Junction-to-board thermal resistance $R_{T,j-b}$, regarding junction heating.
- External quantum efficiency $\eta_{EQ}(I_0, T_0)$ at specific current and junction temperature (including effective phosphor efficiency).
- Slope α_F of external quantum efficiency decrease with current.
- Slope γ_F of external quantum efficiency decrease with temperature.
- Slope γ_p of peak frequency shift with temperature, regarding colour changes.
- Slope c_T of carrier temperature variation with junction temperature, regarding colour changes.
- Parameter C_1 of phosphor-white spatial colour variation.

The above quality parameters are evaluated for two single-die packages and one multi-die LED device from three different manufacturers in Table 8.12. The ideal value of each quality parameter is mentioned as well. For the multi-die package, all quantities have to be recalculated to allow fair chip-to-chip comparison.

Note that both γ_P and γ_p largely depend on the slope α' of $E_g(T)$. It is nevertheless appropriate to consider them as separate quality parameters. The latter equals α'/h and only depends on the compound semiconductor's energy gap variation with temperature, while the former contains an additional term including the ideality factor, forward current, and an unknown quasiconstant C_S (see Eqs. (5.3) and (5.5) in chapter 5). Their respective ideal values can therefore never be pursued simultaneously.

For white LEDs the CRI or a related quantity could be considered an additional quality parameter, determined by the LED's spectrum shape. However, the CRI is largely discussed and alternative colour rendering metrics are being constructed [Narendran, 2002] [Bodrogi, 2004] [Davis, 2010] [Smet, 2010]. CRI has therefore not been taken into account in this work.

Table 8.12: Comparison of ten LED package quality parameters for three commercial diodes. Units and ideal value of each parameter have been collected in column two and three, respectively. For multi-die package E3BN, quality parameters have been recalculated per die in the last column. Best values are marked with a gray background.

quality parameter	units	ideal value	XREW	PG1A-1	E3BN	E3BN per die
n	/	unity	1.83	3.49	8.68	1.45
$R_S(T_0)$	Ω	zero	1.00	2.37	2.91	0.49
γ_P	10^{-3} W/K	$\ll 0$	-1.20	-3.13	-2.23	-0.37
$R_{T,j-b}$	K/W	zero	3.35	4.32	3.64	=
$\eta_{EQ}(I_0,T_0)$	/	unity	30.1	14.5	14.7	=
α_F	W/A²	zero	-0.27	-0.28	-1.77	-0.30
γ_F	10^{-3} W/K	zero	-0.51	-0.40	-1.51	-0.25
γ_p	10^{10} Hz/K	zero	4.57	12.4	4.08	=
c_T	/	unity	1.32	1.71	1.56	=
C_1	/	below 0.6	0.82	0.81	0.82	=

For each quality parameter in Table 8.12 the best value of the three LEDs under consideration is marked with a gray background. Device PG1A-1 is plainly inferior to the XREW and E3BN packages. The latter both cover four out of ten best values. In practice however, the LED's external quantum efficiency might be considered of major importance for quality comparison. Type XREW would be preferred as a result. It is up to LED lighting designers to firstly select a number of device types based on design criteria, and then compare these components for each parameter separately or for a weighed function of a number of quantities.

8.5.2. Additional quality parameters

The above quality scale for LED packages could be completed by including the light output degradation and its current and temperature dependence. Related quality parameters can be extracted from L70 lifetime studies (also see chapter 3). Narendran *et al.* performed many experiments on this topic, both for low-power and high-power light-emitting diodes [Narendran 2004-1] [Narendran, 2004-2]. Under thermal steady-state operation, LED packages approximately show an exponential light output depreciation in time:

$$\Phi(t) \approx \Phi_0 \exp(-\alpha_l t) \tag{8.32}$$

with $\Phi(t)$ the radiometric or luminous flux as a function of time t, Φ_0 the flux for $t = 0$, and α_l the diode's degradation rate. As a result, the L70 lifetime t_l can be calculated as follows:

$$t_l = \left[\alpha_l \ln(0.7)\right]^{-1} \tag{8.33}$$

where in fact α_l depends on both forward current and junction temperature. As lifetime has been proven to decrease according to a power law of current [Levada, 2005] [Yanagisawa, 2005] and exponentially as a function of junction temperature [Chuang, 1997], the degradation rate can be expressed as:

$$\alpha_l(I,T) \approx C_l I^m \exp\left(\frac{T}{T_l}\right) \tag{8.34}$$

with C_l a constant degradation fitting parameter, m the power of the degradation rate variation with current, and T_l the characteristic temperature of light output degradation. T_l equals the ratio of the activation energy of the degradation reaction and the Boltzmann constant. Physically, this activation energy represents an effective energy barrier for defect reactions such as migration and creation of lattice imperfections [Chuang, 1997].

According to Eqs. (8.32) and (8.34), three parameters have to be added to the quality scale in order to fully take into account the LED light output degradation. These are the degradation constant C_l, the exponent m, and the characteristic temperature of degradation T_l (or degradation activation energy as an equivalent). In the ideal case C_l and m are as low as possible, while T_l should be as high as possible.

An extended experimental study of Narendran *et al.* examined the degradation rate into more detail for a large range of commercial high-power light-emitting diodes [Narendran, 2005-1]. In order to better understand the LED light output degradation, it seems useful to concisely mention the most important results of this study:

- The decay constant of high-power LEDs calculated from an exponential fit is most reliable when the initial 1000 h of data is omitted and a minimum of 5000 h of data beyond the initial 1000 h is used. This is possibly due to an annealing effect during the first 100 h to 1000 h of LED usage, often referred to as burn-in time. The annealing effect eliminates some defects in the chip, dominating the initial ageing process and thus causing an initial increase in light output [Hu, 2008].
- The main reason for the exponential LED lumen output decrease is the degradation of the semiconductor lattice (see degradation activation energy above). However, for phosphor-white LEDs, the decay constant clearly contains two aspects: semiconductor degradation and a similar exponential

phosphor degradation. The degradation of the protecting dome can be neglected in comparison with the degradation of diode chip and phosphor.
- Blue dies generally degrade faster than red ones. This means semiconductor degradation depends on the energy gap width. The larger the gap, the faster the degradation.
- Lots of variations exist between light output degradation rates of different commercial high-power LEDs.

A complete LED lighting system is not determined by intrinsic diode package properties only. The efficiency of driver electronics and secondary optics will have the biggest supplementary impact on system performance. These efficiencies can therefore be considered important quality parameters that obviously have to aim at high values (close to unity).

Finally, the total thermal resistance of a LED lamp or luminaire largely affects the junction temperature of incorporated diodes. In addition to the junction-to-board thermal resistance in Table 8.12, the board-to-ambient thermal resistance has to be as low as possible. If thermal resistances are summated, this brings the total number of parameters in the LED lighting quality scale to fifteen.

8.6. Best practice

When commercial purposes are concerned, LED technology evaluation will most probably be limited to reliability testing of binning by manufacturers (section 8.2) and comparison of device types on a light-emitting diode quality scale (section 8.5). Nevertheless, power losses and efficiency values (sections 8.3 and 8.4) can be calculated and compared from the same limited number of measurements as well.

Two integrating sphere measurements at different junction temperatures (one at 300 K) are necessary for the binning reliability testing of LED packages. The same experimental data can be used for all power loss calculations and their junction temperature dependence. At least one additional measurement at a different current is needed for additional knowledge of the power loss variation as a function of forward current (see chapter 5). These measurements have to be repeated for a selection of devices for the efficiency comparison described in section 8.4. Integrating sphere measurements can also be performed during steady-state operation on an appropriate heat sink. Current fine-tuning by use of three (or more) sources then allows comparing RGB and phosphor-white devices with equal luminous flux and colour characteristics. Power and flux measurements of LED lamps and wall-plug engines are generally performed during operation on their respective heat sinks as well.

The best practice sections in chapters 4 to 7 show that eight out of ten quality parameters in Table 8.12 can be determined from two current-voltage and three integrating sphere measurements only. Additionally, one power measurement and

two goniophotometer measurements allow calculating the junction-to-board thermal resistance and fitting parameter C_1 of the phosphor-white colour pattern, respectively. To extend the quality scale to LED lamps and engines, at least one extra integrating sphere measurement is needed to determine the efficiencies of driver electronics and secondary optics. A flux depreciation evaluation requires more complex experiments.

8.7. Summary and conclusions

Voltage, flux, and colour binning by manufacturers at the end of production lines has been verified by performing pulsed measurements at similar current and junction temperature conditions. The relevance of the initial binning for diode operation in practice is examined by performing identical measurements during steady-state operation on a fixed heat sink. Twelve phosphor-white diode types and two types of single-colour red LEDs from three manufacturers have been investigated. Although Cree provides no such binning, forward voltage regions have been successfully verified for all manufacturers. During steady-state operation however, only some Seoul Semiconductor packages remained within their specified voltage bin.

Luminous flux binning seems a difficult issue for SSL manufacturers. Due to the selection of very narrow flux bins, both Cree and Nichia packages did not pass the binning verification and binning relevance testing. Only fluxes of SSC devices during pulsed operation have been found to be situated within their respective binning regions. However, due to the LED light output reduction with junction temperature, these bins are not valid during steady-state operation in practice.

In contrast with the very good forward voltage and luminous flux results, it is remarkable that the SSC devices do not correspond to the datasheet colour specifications. On the other hand, Cree and Nichia colour coordinates are usually situated within the specified bins. Apparently, diode manufacturers hardly succeed in fulfilling all three binning requirements simultaneously. Nevertheless, LED colour changes due to rising junction temperatures have been found to be of the same order as typical compact fluorescent colour changes during stabilisation after switch-on [Bodart, 2010]. For phosphor-white LEDs, these colour shifts are often still smaller than the chromaticity differences due to spatial colour variations.

Several power loss mechanisms present in phosphor-white high-power LEDs have been evaluated at different operating conditions and mutually compared. Power loss in the internal series resistance has been found to amount 10 to 20 % of the initial input power and is the main reason for the decreasing diode efficiency with increasing current. External quantum losses areclearly the dominant loss factor and can be related to the colour temperature of the LEDs. Non-fluorescent absorption in the phosphor seems to be more important for warm white LEDs. The external quantum losses are also responsible for the efficiency decrease with junction

temperature. For this reason, the LED efficiency is always higher for cool white LEDs. The Stokes shift losses equal about 2 to 5 % of the input power for all measured LEDs. Although the conversion loss per photon is larger for warm white LEDs, this effect seems to be compensated by the smaller number of emitted photons. The remaining visible flux part is always a few percent smaller than the visual loss for phosphor-white LED spectra.

The phosphor temperature of a remote phosphor type of LED increases with increasing pump light flux and junction temperature. The increase depends on the phosphor's quantum efficiency and thermal resistance to the junction. The effective quantum efficiency of three LED modules has been calculated from spectral radiant flux measurements with and without the respective remote phosphor plates. The efficiencies correspond to values reported in literature, but differ from efficiency values determined for phosphors powders. Within typical diode operation ranges, the effective quantum efficiency decrease with pump flux (about 0.1 %/W) is negligible in comparison with the effect of an increasing phosphor temperature (about 0.03 %/K).

The LED efficiency comparison has been divided into five parts. Two approaches have been used to evaluate the efficiency of RGB and phosphor-white devices. At constant 300 K junction temperature, the green diode's luminous flux of only one out of three manufacturers could reach a sufficiently high value to simulate the corresponding phosphor-white's flux and colour coordinates. This is due to the low quantum efficiency of green emitters (more or less 10 %) in comparison with the quantum efficiency of blue (or pump in phosphor-white) and red emitters (30 to 50 %). The electrical input power required for the green Lumileds diode is already higher than the electrical input power of the phosphor-white device. The power losses resulting from the Stokes shift and phosphor external quantum efficiency are thus relatively small in comparison with the losses related to the green LED's quantum efficiency. For the LEDs mounted on a fixed heat sink, sufficiently high luminous fluxes could be obtained for all green emitters to reproduce the corresponding phosphor-white flux and colour. The results confirm that the luminous efficacy of white devices equals more than twice the efficacy of the corresponding RGB combination for similar flux and colour characteristics, even in practical applications.

The phosphor-white LED efficiency decrease with decreasing CCT has been explained from the related spectrum shapes. In order to obtain a lower correlated colour temperature, the relative phosphor contribution and the phosphor's peak wavelength both have to increase. This means that more phosphor material has to be used, leading to lower external quantum efficiencies, and that on average more power is lost during each Stokes shift of the blue pump photon energy.

In order to perform the manufacturer efficiency comparison as fair as possible, single-die one watt packages operated with a 350 mA drive current and at a typical 330 K constant junction temperature have been considered for device production

periods 2006-2007 and 2008-2009. Cool and warm white devices have been compared separately for the second period. In comparison with the period 2006-2007, luminous efficacy values of cool phosphor-white diode packages of Cree, Lumileds and SSC have increased by roughly a third by 2008-2009. Yet, even for some of the most famous LED package manufacturers nowadays, large discrepancies between their respective efficacy values have been found.

LED lighting applications could be made more efficient by replacing each package at normal drive current by a number of packages driven with a reduced forward current. Alternatively, a single-die package could be substituted by a multi-die package where the initial input power is shared by all dies. This statement has been validated by simulations and experiments.

The luminous flux of four LED lamps and six engines has been determined during steady-state operation while mounted on their respective heat sinks. For all LED lamps, luminous efficacy values have been found to amount between 35 and 45 lm/W. Phosphor-white LED engines have comparable efficacy values, which indicates that practical LED efficacies are at present comparable to luminous efficacies of compact fluorescent lamps (see chapter 2).

From the measurement and modelling efforts described in the previous chapters, ten parameters have been extracted which are determined by intrinsic diode properties and closely related to package quality. These quality parameters have been evaluated for two single-die packages and one multi-die device. For the multi-die package, all quantities had to be recalculated to allow for a fair chip-to-chip comparison. Three parameters have to be added to the quality scale in order to fully take into account the LED light output degradation. The efficiency of driver electronics and secondary optics will have supplementary impact on system performance. If thermal resistances are added, this brings the total number of parameters in the LED lighting quality scale to fifteen. It is up to future LED lighting designers to first select a number of device types based on design criteria, and then compare these components for each parameter separately or for a weighed function of a number of quantities.

Full LED package evaluation can be performed from two current-voltage, four integrating sphere (including a simple power measurement), and two goniophotometer measurements. To extend this evaluation to LED lamps and engines, at least one additional flux measurement is needed. The measurements can be repeated with the devices mounted on appropriate heat sinks, or for a selection of devices regarding efficiency comparison.

9. General conclusions

9.1. Scientific approach

The doctoral research at hand aimed at reducing the technological comprehension gap between high-power LED package manufacturers and application designers. For the scientific community, the most important contribution of this research is the construction of physics-based and experimentally validated light-emitting diode models. They allow product designers and luminaire manufacturers performing maximum LED characterization from a minimum of measurements and estimating diode performance in practical lighting applications.

By comparison with other modelling and simulation techniques, the gray-box modelling approach has been found to be the best option for the intended research contribution. Moreover, measurement results that have been used for model construction can be utilized for an extended evaluation of the present LED technology status as well. Integration of high-power LEDs in general lighting applications can thus be considered the final product of measurement, modelling, simulation, validation, and evaluation, in this specific order.

In combination with commercial electrical power source and measure equipment and an oven, two integrating sphere and two goniophotometer setups have been used for all experiments. The 50 cm diameter integrating sphere has been exclusively custom-made for this work and examined in detail. The typical hemispherical radiation pattern of high-power LEDs has been exploited to increase the accuracy of the flux determination. Recently proposed measurement techniques such as an external reference source and spectral detection have been combined with a specific port geometry of the sphere wall with minimum baffle area, showing a very uniform sphere response distribution function. The sphere response function has been modelled from the directional response of the detector. Luminous flux determination using spatial resolved goniometer measurements are in agreement with the results obtained with the integration sphere.

Current-voltage characteristics of ten commercial single-die high-power LEDs have been measured at six different temperatures ranging between 295 K and 400 K. For InGaN based emitters, three current regions are clearly distinguished. The intermediate current region is modelled with a generalized Shockley equation. The corresponding ideality factor has been determined to be quasi independent of junction temperature. As current-voltage characteristics could impossibly be explained and modelled by assuming a diffusion or recombination current mechanism only, the LED ideality factor has been explicitly introduced into the

expression of the saturation current. The adaptation can be considered in correspondence with the experimental Shockley equation. Additionally, the variation of the compound semiconductor band gap with temperature has been included. From this model, a linear behaviour between the forward voltage and the junction temperature can be expected, but only for a rather limited range of drive currents. These conclusions have been confirmed by measurements, with coefficients of determination exceeding 0.99 for all devices under test. Recording of current-voltage characteristics of ten multi-die LEDs at different ambient temperatures allowed verifying the forward voltage model using a generalized junction temperature. Light-emitting diode ideality factor and internal series resistance values of these multi-die packages have been related to those of individual dies.

For both single-die and multi-die packages, the initial forward voltage model has been extended with the temperature dependence of the diode's internal series resistance. Measurement results revealed that internal series resistances show a negative exponential junction temperature dependence, but in correspondence with the initial forward voltage model this behaviour is often approximated by a linear junction temperature dependence. Due to the internal resistance, about 10 to 35 % of the initial electrical input power is directly converted into heat at normal drive current. The internal series resistance has therefore been found to be the second biggest reason for junction heating in practical applications.

Partially based on the voltage-temperature modelling in chapter 4, a current-temperature relation has been constructed from the thermal resistance definition for LED packages. Electrical input power and optical radiant flux variations with current and temperature of nine commercial LED packages have been determined experimentally and modelled. For both input power and flux, a quadratic dependence on current and a linear dependence on junction temperature have been found with coefficients of determination exceeding 0.96. Combining these dependencies has lead to simple expressions for the electrical input power, radiant flux, and their difference as a function of forward current and junction temperature. These models can be used to simulate the junction temperature as a function of drive current and thermal resistance in practical applications. As a result, electrical input power and optical power can be calculated for each current as well. The method has been validated by comparing measured and simulated junction temperature and power values of two LEDs. Maximum deviations have been found to be of the order of a few percent.

The spectral radiant flux of seven commercial high-power light-emitting diode packages from two manufacturers has been measured with a custom made integrating sphere at different junction temperatures, ranging between 290 K and 340 K. Considering frequency instead of wavelength as the independent variable, a single-colour spectrum model for one particular temperature (300 K) has been constructed. Afterwards, the variation of the initial modelling parameters with

junction temperature has been examined. In contrast with a number of merely mathematical spectrum models proposed in literature, the Boltzmann exponential behaviour with carrier temperature variation and the band gap energy shift with junction temperature have been included explicitly. The absolute power variation with temperature has been recovered from the preceding chapter. For most of the fitting parameters, the values obtained for AlGaInP-based LEDs could be distinguished from the values obtained for InGaN-based emitters. A Gaussian function with temperature dependent peak value, peak frequency, and peak width appeared to be sufficient for modelling and simulation of fluorescence spectra. Very high coefficients of determination have been found, indicating a good agreement between the models and experimental data. Both models have been validated by comparing flux and colour coordinates of measured and simulated spectra at 340 K junction temperature. Except for one red LED showing a spectrum deficiency, flux and colour deviations between measurement and simulation have been found to be lower than 2.5 % and smaller than the radius of a three-step MacAdam ellipse, respectively.

Goniophotometer measurements have been performed on ten commercial LED packages incorporating a proximate or remote planar phosphor. Measurement results have been used to discuss and model the spatial colour distribution of these light sources. For all devices under test, the colour coordinates appeared on a single line in the CIE chromaticity diagram and have been found to increase with increasing viewing angle. As a result of these observations, modelling the spatial colour distribution has been reduced to modelling the yellow-blue ratio variation of the spectrum as a function of viewing angle. The YB variation has been modelled starting from its attribution to the relative apparent phosphor thickness change as a function of viewing angle, while Snellius' law has been included to connect internal and external light ray angles. Afterwards, a second parameter has been added to extend the initial model to phosphor-white LEDs with simple narrowing or widening optics. A very good agreement between measurement and simulation with all coefficients of determination exceeding 0.94 has been found.

The measurements and constructed model allowed evaluating the visibility of spatial colour differences and the relevance of colour binning measurements at the end of LED package production lines. Plain linear data fitting showed that a maximum colour difference corresponding to a four-step MacAdam ellipse is obtained when the primary modelling parameter equals 0.6.

A design proposal has been made to significantly increase the colour homogeneity of phosphor-white LEDs: Using remote spherical phosphors seems to be the best solution for obtaining minimal spatial colour variations.

Measurement results that have been used for model construction in chapters 4 to 7 have been utilized for an extended evaluation of the present LED technology status as well. This evaluation focussed on three major aspects, i.e. reliability testing of

datasheet information, extended evaluation of light-emitting diode power losses and efficiencies, and a proposal for a diode technology quality scale.

Voltage, flux, and colour binning by manufacturers at the end of production lines has been verified by performing pulsed measurements at similar current and junction temperature conditions. Twelve phosphor-white diode types and two types of single-colour red LEDs from three manufacturers have been investigated. Although Cree provides no such binning, forward voltage regions have been successfully verified for all manufacturers. During steady-state operation however, only some Seoul Semiconductor packages remained within their specified voltage bin.

Luminous flux binning seems a difficult issue for SSL manufacturers. Due to the selection of very narrow flux bins, both Cree and Nichia packages did not pass the binning verification and binning relevance testing. Only fluxes of SSC devices during pulsed operation have been found to be situated within their respective binning regions. However, due to the LED light output reduction with junction temperature, these bins were not valid during steady-state operation in practice.

In contrast with the very good forward voltage and luminous flux results, it is remarkable that the SSC devices do not correspond to the datasheet colour specifications. On the other hand, Cree and Nichia colour coordinates are usually situated within the specified bins. Apparently, diode manufacturers do hardly succeed in fulfilling all three binning requirements simultaneously. For phosphor-white LEDs, temperature induced colour shifts are often still smaller than the chromaticity differences due to spatial colour variations.

Several power loss mechanisms present in phosphor-white high-power LEDs have been evaluated at different operating conditions and mutually compared. Power loss in the internal series resistance has been found to be the main reason for the decreasing diode efficiency with increasing current. External quantum loss is clearly the dominant loss factor and could be related to the colour temperature of the LEDs. Non-fluorescent absorption in the phosphor seems to be more important for warm white LEDs. The external quantum loss is also responsible for the efficiency decrease with junction temperature. For this reason, the LED efficiency is always higher for cool white LEDs. The Stokes shift losses equal about 2 to 5 % of the input power for all measured LEDs. Although the conversion loss per photon is larger for warm white LEDs, this effect seems to be compensated by the smaller number of emitted photons. The remaining luminous flux part is always a few percent smaller than the visual loss for phosphor-white LED spectra.

The phosphor temperature of a remote phosphor type of LED increases with increasing pump light flux and junction temperature. The increase depends on the phosphor’s quantum efficiency and thermal resistance to the junction. The effective quantum efficiency of three LED modules has been calculated from spectral radiant flux measurements. Within typical diode operation ranges, the effective quantum

efficiency decrease with pump flux (about 0.1 %/W) is negligible in comparison with the effect of an increasing phosphor temperature (about 0.03 %/K).

The LED efficiency evaluation has been divided into five parts. Two approaches have been used to compare the efficiency of RGB and phosphor-white devices. Both the constant junction temperature and fixed heat sink approach showed that the luminous efficacy of phosphor-white LEDs equals more than twice the efficacy of the corresponding RGB combination for similar flux and colour characteristics.

The phosphor-white LED efficiency decrease with decreasing colour temperature has been explained from the related spectrum shapes. In order to obtain a lower correlated colour temperature, the relative phosphor contribution and the phosphor's peak wavelength both have to increase.

In order to perform the manufacturer efficiency comparison as fair as possible, single-die one watt packages driven with a 350 mA drive current and at a typical 330 K constant junction temperature have been considered for device production periods 2006-2007 and 2008-2009. In comparison with the period 2006-2007, luminous efficacy values of cool phosphor-white diode packages of Cree, Lumileds and SSC have increased by roughly a third by 2008-2009. Yet, even for some of the most famous LED package manufacturers nowadays, large discrepancies between their respective efficacy values have been found.

LED lighting applications could be made more efficient by replacing each package at normal drive current by a number of packages driven with a reduced forward current. Alternatively, a single-die package could be substituted by a multi-die package where the initial input power is shared by all dies. This statement has been validated by simulations and experiments.

The luminous flux of four LED lamps and six engines has been determined during steady-state operation while mounted on their respective heat sinks. For all LED lamps, luminous efficacy values have been found to amount between 35 and 45 lm/W. Phosphor-white LED engines have comparable efficacy values, indicating that practical LED efficacies are at present comparable with luminous efficacies of compact fluorescent lamps.

From preceding measurement and modelling efforts, ten parameters have been extracted which are determined by intrinsic diode properties and closely related to package quality. Three parameters have to be added to this quality scale in order to fully take into account the LED light output degradation. The efficiency of driver electronics and secondary optics has a supplementary impact on system performance. If thermal resistances are added, this brings the total number of parameters in the LED lighting quality scale to fifteen. It is up to future LED lighting manufacturers to first select a number of device types based on design criteria, and compare these components for each parameter separately or for a weighed function of a number of quantities.

9.2. Best practice

All modelling and evaluation work would be ineffectual if not applicable by those it is meant for. Therefore, at the end of each chapter a method for measurement and simulation or evaluation in practice has been proposed. This best practice usually consisted of a description of minimum model reconstruction, simulation and evaluation efforts, or guidelines for optimal device performance achievements. An overall best practice for integration of high-power light-emitting diodes in general lighting applications is added here.

Accurate junction temperature determination from forward voltage is only possible if at least two voltage-temperature calibration measurements are performed. In order to verify whether the measurement current lies within the intermediate current interval for all relevant temperatures, always two current-voltage measurements at about the most extreme relevant temperatures should be performed in practice.

Although less precise, a linear voltage-temperature behaviour can be applied at normal drive current as well. However, in order to obtain sufficiently high accuracies the measurement current generally differs from the normal current in practical applications. The drive current has to be lowered only for about a millisecond or less to minimize the influence of the forward voltage measurement on the junction temperature.

The junction temperature and electrical and optical power of integrated LED packages can also be determined from the forward current directly by performing four calibration measurements only. These consist of three integrating sphere measurements and one steady-state input power determination when the LED is placed on a fixed heat sink. However, LED performance prediction by application designers would be largely simplified if the power model parameters and thermal resistance values would be known in advance. Although some device manufacturers provide experimental figures of the input and output power variation with current and temperature already, explicit inclusion of the above power coefficients in datasheet specifications could be helpful.

Two spectral radiant flux measurements are needed to accurately model and simulate a diode spectrum at any temperature. The first serves as a reference. For single-colour LED spectra, four out of seven fitting parameters are determined from two separate exponential fits to the low energy and high energy tail of this reference spectrum. However, for the low energy slope fixed values of 22.5 10^{-14} Hz^{-1} and 7.5 10^{-14} Hz^{-1} could be used for AlGaInP-based and InGaN-based emitters, respectively. The difference between the combination of exponentials and the measured reference spectrum is modelled by a Gaussian function. Reference fluorescence spectra can be modelled by a Gaussian function directly.

As linear junction temperature dependencies appeared to be sufficiently accurate for modelling the temperature behaviour of all non-constant model parameters, one additional spectral radiant flux measurement allows calculating the variation of LED spectra with temperature.

Planar phosphor distributions in bichromatic white LEDs lead to an intrinsic and inevitable spatial colour variation due to the changing apparent phosphor thickness with viewing angle. In practice, two spectral radiant intensity measurements are sufficient to simulate the relative yellow-blue ratio or corresponding spatial colour variation of phosphor converted Lambertian LED devices. For phosphor-white LEDs with proportionally narrowing or widening optics, at least three spectral radiant intensity measurements are needed.

A high correlation between primary fitting parameter C_1 and the maximum CIE-$u'v'$ spatial colour difference ΔE_{uv} (R^2 = 0.92) has been observed. A maximum colour difference corresponding to a four-step MacAdam ellipse or typically one colour bin is obtained for $C_1 \approx 0.6$. This value can hence be used as a colour evaluation criterion. For LEDs with $C_1 > 0.6$, colour binning according to a four-step MacAdam ellipse can only be valid for part of the beam and is therefore inappropriate for the overall light output.

Spatial colour variations have been found to be remarkably smaller for remote phosphor devices in comparison with proximate phosphor distributions. Moreover, the most reasonable approach to avoid a changing apparent phosphor thickness as a function of viewing angle is the use of spherical phosphor distributions. Consequently, for phosphor-white LED devices the use of remote spherical phosphors seems to be the best solution for obtaining minimal spatial colour variations.

When commercial purposes are concerned, LED technology evaluation most probably will be limited to reliability testing of binning by manufacturers and comparison of device types on a light-emitting diode quality scale. Nevertheless, power losses and efficiency values can be calculated and compared from the same limited number of measurements as well.

Two integrating sphere measurements at different junction temperatures are necessary for the binning reliability testing of LED packages. The same experimental data can be used for all power loss calculations and their junction temperature dependence. At least one additional measurement at a different current is needed for additional knowledge of the power loss variation as a function of forward current. These measurements have to be repeated for a selection of devices for efficiency comparison. Integrating sphere measurements can also be performed during steady-state operation on an appropriate heat sink. Current fine-tuning using three (or more) sources then allows comparing RGB and phosphor-white devices with equal luminous flux and colour characteristics. Power and flux measurements

of LED lamps and wall-plug engines are generally performed during operation on their respective heat sinks as well.

Eight out of the ten selected quality parameters can be determined from two current-voltage and three integrating sphere measurements only. Additionally, one power measurement and two goniophotometer measurements allow calculating the junction-to-board thermal resistance and fitting parameter C_1 of the phosphor-white colour pattern, respectively. To extend the quality scale to LED lamps and engines, at least one extra integrating sphere measurement is needed to determine the efficiencies of driver electronics and secondary optics.

The preceding paragraphs show that all LED modelling, characterization, and evaluation can be achieved by performing a very limited number of experiments using only the measurement equipment described in chapter 3. If lighting designers tend to perform similar studies themselves based on the best practice guidelines, investments in appropriate tools will be required. Table 9.1 gives an overview of typical prices for the essential measurement equipment, taking into account a medium to high performance and commercial availability.

Table 9.1: Measurement equipment needed to perform the proposed LED testing with indication of its commercial price.

type of apparatus	price (€)
current-voltage source	10 000
active heat sink and driver	2500
integrating sphere	10 000
goniophotometer	20 000
spectrometer and CCD	15 000
calibration lamp and driver	3000

An oven for voltage-temperature calibrations is not included in Table 9.1. The necessity to control the ambient temperature for such measurements indeed becomes superfluous if the calibration method with active heat sink developed at the NIST (see section 3.7) is utilized, reducing the overall cost. The voltage-temperature calibration is in that case performed after the LED device has been mounted on the integrating sphere surface or goniophotometer.

According to the second column of Table 9.1, the initial price for purchasing all measurement equipment amounts about € 60 500. The current-voltage source is rather expensive due to its necessity to generate millisecond (or even shorter) current pulses. However, the integrating sphere can be left out of the list if a high-end goniophotometer with very accurate spatial integration is obtained. This option reduces the initial cost, by the expense of longer measurement times. Determining the spectral radiant flux of a light source takes about 15 minutes to half an hour, while obtaining the same quantity using a goniophotometer may take several hours.

An additional remark on the reproducibility of measurement results is highly valuable here. This reproducibility has a double meaning. On the one hand, it is

related to the variation between results for several measurements of the same device. This variation has been examined for each apparatus, resulting in an estimation of the related measurement error. As variations were always found to be smaller than 1 % in comparison with the values obtained for the measured quantities, these errors have not been taken explicitly into account in this work. Similar tests by laboratories of lighting designers are however necessary to assure the accuracy of the LED characterization for data publication or simulations.

On the other hand, reproducibility denotes the validity of measured quantities and model parameters for all LED devices from a single type or bin. Determination of the ideality factor and internal series resistance for example depends on the exponential current-voltage fitting within the Shockley-interval. The size of this interval may however fluctuate between LEDs of the same type, compromising their characterization. Although this kind of reproducibility has not been extensively addressed, measurement results indicate that relevant parameter differences may indeed occur between LED's of the same bin. Moreover, model parameters that are initially equal might become different after a certain burning time (see section 9.3). Application manufacturers should know this when selecting diode packages or when characterizing LED's for simulations.

Based on the research results discussed in this work, it is appropriate to provide the reader with further LED lighting design considerations. Luminous efficacy values of commercial LED lamps and engines have been found to be of the same order as compact fluorescent lamp efficacies. Moreover, diode chromaticity shifts due to rising junction temperatures are comparable with typical compact fluorescent colour changes during stabilisation after switch-on [Bodart, 2010]. Knowing that CRI values of both light source types are similar as well, one can thus state that compact fluorescent and light-emitting diode technologies are equally exploitable for general lighting applications at this moment. Of course, each technology will have its own best practice domains. Due to their decreasing performance with temperature, LED devices are for example preferred in cold environments. The superior qualities of light-emitting diodes for coloured indication or signal lighting applications had been proven before [Freyssinier, 2004].

A major drawback of present phosphor-white LED technology in comparison with compact fluorescent lighting is its often visible spatial colour variation during steady-state operation. The use of remote spherical phosphors seems to be the best solution for maximally reducing this shortcoming. Some LED lamp manufacturers have drawn the same conclusion and already have such improved LED lamp designs available, making the resemblance between LED and fluorescent lamp technology even bigger.

Despite its already rather satisfying output characteristics, it is very important to emphasis once again the diode's strongly reduced diode performance at drive currents specified in LED datasheets. The internal quantum efficiency significantly decreases with increasing current and about 10 to 35 % of the initial electrical input

power is directly converted into heat due to the internal series resistance. As a consequence, LED application efficiencies may be increased by 50 % or more, i.e. from compact fluorescent values to fluorescent tube, HID, or even higher efficiencies, by replacing each package at normal drive current by a number of packages driven with a reduced forward current. Alternatively, a single-die package could be substituted by a multi-die package where the initial input power is shared by all dies. As always, cost versus gain issues will determine the technology's manufacturing and application in the future.

9.3. Possibilities for improvements and future research

A lot of efforts have been made to perform the research described herein with maximum vigour. Perfectionism nevertheless remains a utopia. Beside an attempt to contribute to the present worldwide light-emitting diode research, the past four years have indeed been a great learning process as well. This process included device selection, measurement equipment construction and handling, application of the scientific method, critical interpretation of literature and results, and sharing these own results with peers in various ways. Looking back now to the outcome of this work, room for relevant improvement is distinguished on several aspects:

- The dependence of this study on the availability of commercial LED samples in a rapidly changing market can be considered somewhat unfortunate. The obtained samples have not always been selected from most recent fabrication stocks and were occasionally outdated by improved versions after a few months. Moreover, research samples were usually selected from those bins that are rather unpopular with application designers or luminaire manufacturers. The devices under test could therefore not always be considered the best representatives of the LED market at that time. Buying packages from specific bins would certainly reduce this problem, but manufacturers rarely allow purchasing just a few instead of hundreds to thousands of devices at once.

- Not only the availability of research samples could be improved, but if time allowed doing so the number of LED types per measurement series could be augmented as well. With an increased number of devices a more extended model validation through simulations and further comparison of LED packages on the proposed quality scale would have been possible. Especially the number of AC driven LED types should have been higher for fair technology evaluation. Only one AC package has been measured so far.

- Pulses of the order of a few hundred microseconds are sometimes recommended in literature for forward voltage measurements without affecting the junction temperature. However, the available Keithley source-measure tools only reached millisecond pulses at minimum. Although these pulse lengths have been verified not to significantly influence the junction temperature either, it would have been more correct to use specialized pulse generating equipment.

- The custom-made 50 cm diameter integrating sphere with temperature-controlled heat sink has been constructed from a first design edition. A number of improvements could be made to this apparatus: First, the power of the Peltier element attached to the sphere port mounting plate appeared to be insufficient to cover all typical junction temperature ranges (300 to 400 K). By using additional isolation between plate and sphere, and depending on the device type under test, extreme values of about 290 and 360 K could be reached. A commercially available temperature-controlled heat sink as used at the NIST would possibly have been a better solution for junction temperature control. Next to that, the fixed horizontal position of the sphere openings did not always allow performing flux measurements of LED engines in their natural air flow directions, which are mostly vertical. Rather recently, integrating spheres with a rotating horizontal axis are constructed in order to adopt the measurement configuration to the natural burning position of the LED device under test.

- A single Gaussian function with temperature dependent peak value, peak frequency, and peak width has been applied to model and simulate fluorescence spectra in chapter 6. More and more however, multiple phosphor types are combined in one LED to obtain a more uniform spectrum and thus higher CRI values. For such multi-phosphor devices, a sole Gaussian function will be insufficient for phosphor spectrum modelling. Although this has unfortunately not been tested yet, the sum of similar Gaussian fittings to each of the phosphor contributions should be able to model and simulate the complete fluorescence spectrum.

- The effective quantum efficiency of three remote phosphor types has been determined while mounted on their respective semiconductor pump devices. Values have been roughly validated through comparison with phosphor powder quantum efficiencies found in literature. Yet, it would have been better to measure the absolute quantum efficiency values of the non-integrated phosphor plates by use of an integrating sphere as well. This would allow calculating the additional power loss due to the incorporation of the phosphor in a LED application explicitly. Such a phosphor quantum

efficiency measurement setup is under construction in the Light & Lighting Laboratory at this moment.

In line of the LED technology research and its possible improvements as described in this text, a number of relevant future investigation directions can be proposed as well:

- Single-colour and phosphor-white diode spectra and their junction temperature dependence have been modelled in chapter 6. As a function of forward current on the other hand, the relative spectrum shape is known not to change drastically. This means that only the absolute radiant flux variation with current (from chapter 5) has to be introduced in the model to obtain a first approximation of the spectrum dependence on forward current. In practice, the single-colour and fluorescence spectrum will again have to be considered separately and small spectrum shape changes with current may occur. It would therefore be useful to perform additional research on this spectrum variation as a function of current. The effect of non-linear dimming methods (e.g. PWM) on LED output characteristics could in that case be included as well.

- The spatial colour distribution of high-power light-emitting diodes with planar phosphor has been examined and modelled. Although the colour pattern of single-colour packages is negligible, the chromaticity of multi-colour LEDs as RGB devices may vary significantly as a function of viewing angle due to chip shielding effects. The use of multi-die coloured diodes without strong diffusers is less relevant for general lighting applications [Mottier, 2009], but regarding signalization lighting or improved package design it might be constructive to study their complex colour distributions.

- The research in this work could be extended with a severe validation of the guidelines for best practice through simulation comparison with commercial software. The junction heating calculations in chapter 5 could for example be put side by side with thermal flow simulations using finite-element methods, or current and temperature dependent power values can be compared with those determined by internet tools using datasheet information. A more difficult task would be to evaluate the spatial colour distribution from ray-tracing simulations instead of using the model constructed in chapter 7. Note however that such comparisons do not only allow validating particular simulation tools. They also create deeper insights on possible technology improvements and their theoretical or practical limitations.

- As already mentioned before, the time dependence of LED output characteristics or corresponding model parameters is of major importance for diode performance and its simulation. The light output degradation of high-power diode packages is already studied quite intensively. In future research however, reliability testing of datasheet information and model parameters should be additionally focussed. This implies that related quantities are measured regularly in time and compared with their initial values. Large deviations should be taken into account for solid-state lighting evaluation and simulations.

- Finally, an overall technology comparison for general lighting applications could be performed. Based on the light-emitting diode evaluation here and in related works, and based on extended studies of other light source types, it would indeed be possible to make a selection of best applications (where and how) for each of these sources. The recent significant improvements of organic light-emitting diode devices (OLEDs) may thereby not be overlooked. Easily considered as point-like sources, LEDs are for example very suitable for directional lighting, while the planar OLEDs may be more convenient for illumination of large surfaces as backlighting or wall lighting applications. Next to that, the overall lighting technology comparison can examine the true benefit of LEDs' hemispherical light output, possibly from ray-tracing simulations. This benefit is already exploited in fluorescent tube replacement lamps with LEDs, but due to their only very recent appearance on the market (beginning of 2010) these devices have unfortunately not been included in this work's practical efficiency study. By now, a colleague has started a technology comparison for this type of LED lamps.

Bibliography

[Allen, 2008] S. C. Allen and A. J. Steckl, “A nearly ideal phosphor-converted white light-emitting diode,“ Appl. Phys. Lett., vol. 92, no. 143309, pp. 1-3, 2008.

[Amano, 1990] H. Amano, T. Asahi, and I. Akasaki, “Stimulated emission near ultraviolet at room temperature from a GaN film grown on sapphire by MOVPE using an AlN buffer layer,” Jpn. J. Appl. Phys., vol. 29, no. 2, pt. 2, pp. L205-L206, 1990.

[Bardeen, 1949] J. Bardeen and W. Brattain, “Physical principles involved in transistor action,” Phys. Rev., vol. 75, no. 8, pp. 1208-1225, 1949.

[Bardsley, 2009] Bardsley Consulting, Navigant Consulting, Inc., Radcliffe Advisors, Inc., SB Consulting, and SSLS, Inc., “Solid-state lighting research and development: manufacturing roadmap,” US Department of Energy Lighting Research and Development Building Technologies Program, 2009.

[Baureis, 2005] P. Baureis, “Compact modeling of electrical, thermal and optical LED behaviour,” Proc. ESSDERC, no. 1.D.3, pp. 145-148, 2005.

[Bierhuizen, 2007] S. Bierhuizen, M. Krames, G. Harbers, and G. Weijers, “Performance and trends of high-power light-emitting diodes,” Proc. SPIE, vol. 6669, no. 66690B, pp. 1-12, 2007.

[Bodart, 2010] M. Bodart, B. Roisina, P. D’Herdt, A. Keppens, P. Hanselaer, W. R. Ryckaert, and A. Deneyer, “Performances of compact fluorescent lamps with integrated ballasts and comparison with incandescent lamps,” Light & Eng., vol. 18, no. 2, pp. 83-98, 2010.

[Bodrogi, 2004] P. Bodrogi, P. Csuti, P. Hotváth, and J. Schanda, “Why does the CIE colour rendering index fail for white RGB LED light sources?” CIE Expert Symposium on LED Light Sources, 2004.

[Borbély, 2005] A. Borbély and S. G. Johnson, “Performance of phosphor-coated light-emitting diode optics in ray-trace simulations,” Opt. Eng., vol. 44, no. 11, pp. 1-4, 2005.

[Boroditsky, 1997] M. Boroditsky and E. Yablonovitch, “Light-emitting diode extraction efficiency,” Proc. SPIE, vol. 3002, pp. 119-122, 1997.

[Bullough, 2005] J. D. Bullough, “Recommendations for the definition and specification of useful life for light-emitting diode light sources,” Alliance for Solid-State Illumination Systems and Technologies (ASSIST), Lighting Research Center, Rensselaer Polytechnic Institute, 2005.

[Bürmen, 2008] M. Bürmen, F. Pernus, and B. Likar, “LED light sources: a survey of quality-affecting factors and methods for their assessment,” Meas. Sci. Technol., vol. 19, no. 122002, pp. 1-15, 2008.

[Carroll, 1961] F. W. Carroll, “A polynomial in each variable separately is a polynomial,” Am. Math. Monthly, vol. 68, no. 1, pp. 42, 1961.

[Chen, 2007] N. C. Chen, Y. K. Yang, W. C. Lien, and C. Y. Tseng, “Forward current-voltage characteristics of an AlGaInP light-emitting diode,” J. Appl. Phys., vol. 102, no. 4, 2007.

[Chen, 2008] G. Chen, M. Craven, A. Kim, A. Munkholm, S. Watanabe, M. Camras, W. Götz, and F. Steranka, “Performance of high-power III-nitride light-emitting diodes,” Phys. Stat. Sol. (a), vol. 25, no. 5, pp. 1086-1092, 2008.

[Chhajed, 2005-1] S. Chhajed, Y. Xi, Th. Gessmann, J.-Q. Xi, J. M. Shah, J. K. Kim, and E. F. Schubert, “Junction temperature in light-emitting diodes assessed by different methods,” Proc. SPIE, vol. 5739, pp. 16-25, 2005.

[Chhajed, 2005-2] S. Chhajed, Y. Xi, Y.-L. Li, Th. Gessman, and E. F. Schubert, “Influence of junction temperature on chromaticity and color-rendering properties of trichromatic white-light sources based on light-emitting diodes,” J. Appl. Phys., vol. 97, no. 054506, pp. 1-8, 2005.

[Chien, 2007] W.-T. Chien, C.-C. Sun, and I. Moreno, “Precise optical model of multi-chip white LEDs,” Opt. Express, vol. 15, no. 12, pp. 7572-7577, 2007.

[Cho, 2005] J. Cho, C. Sone, Y. Park, and E. Yoon, “Measuring the junction temperature of III-nitride light-emitting diodes using electro-luminescence shift,” Phys. Stat. Sol. (a), vol. 202, no. 9, pp. 1869-1873, 2005.

[Chonko, 2006] J. Chonko for Keithley Instruments Inc., “Using Forward Voltage to Measure Semiconductor Junction Temperature,” Application Note, 2006.

[Chou, 2008] H.-Y. Chou and T.-H. Yang, “Dependence of emission spectra of LEDs upon junction temperature and driving current,” J. Light & Vis. Env., vol. 32, no. 2, pp. 183-186, 2008.

[Chuang, 1997] S.-L. Chuang, A. Ishibashi, S. Kijima, N. Nakayama, M. Ukita, and S. Taniguchi, “Kinetic model for degradation of light-emitting diodes,” J. Quantum Elect., vol. 33, no. 6, pp. 970-979, 1997.

[CIE, 1987] CIE, “International lighting vocabulary,” CIE Publ. no. 17.4, 1987.

[CIE, 1989] CIE, “The measurement of luminous flux,” CIE Publ. no. 84, 1989.

[CIE, 2004] CIE, “Technical report – Colorimetry,” CIE Publ. no. 15:2004, 2004.

[CIE, 2007] CIE, “Measurement of LEDs,” CIE Publ. no. 127, 2007.

[Coltrin, 2007] M. E. Coltrin, J. Y. Tsao, and Y. Ohno, “Limits on the maximum attainable efficiency for solid-state lighting,” Proc. SPIE, vol. 6841, no. 684102, pp. 1-12, 2007.

[Cree, 2006] Cree, Inc., “Cree XLamp XR LED binning and labelling,” Application Note CLD-AP07.003, 2006.

[Cree, 2007] Cree, Inc., “Cree XLamp XR-E and XR-C LED binning and labelling,” Application Note CLD-AP12.002, 2007.

[Daintith, 2009] J. Daintith, ed., “Oxford dictionary of physics,” Oxford University Press, Oxford, 2009.

[Davis, 2010] W. Davis and Y. Ohno, “Color quality scale,” Opt. Eng., vol. 49, no. 033602, pp. 1-16, 2010.

[de Mello, 1997] J. C. de Mello, H. F. Wittmann, and R. H. Friend, “An improved experimental determination of external photoluminescence quantum efficiency,” Adv. Mater., vol. 9, no. 3, pp. 230-232, 1997.

[Deshayes, 2005] Y. Deshayes, L. Bechou, F. Verdier, and Y. Danto, “Long-term reliability prediction of 935 nm LEDs using failure laws and low acceleration factor ageing tests,” Qual. Rel. Eng. Int., vol. 21, pp. 571-594, 2005.

[DOE, 2010] U.S. Department of Energy and Next Generation Lighting Industry Alliance, “LED Luminaire Lifetime: Recommendations for Testing and Reporting,” first edition, 2010.

[Dupuis, 2008] R. D. Dupuis and M. R. Krames, “History, development, and applications of high-brightness visible light-emitting diodes,” J. Lightwave Technol., vol. 26, no. 9, pp. 1154-1171, 2008.

[Edison, 2007] Edison Opto Corporation, “50W Edistar,” Technical Datasheet version 1.0, 2007.

[Elation, 2006] Elation Professionals, “OPTI RGB powerful LED fixture – User instructions,” Instruction Manual, 2006.

[Freyssinier, 2004] J. P. Freyssinier, Y. Zhou, V. Ramamurthy, A. Bierman, J. D. Bullough, and N. Narendran, “Evaluation of light-emitting diodes for signage applications,” Proc. SPIE, vol. 5187, pp. 309-317, 2004.

[García, 2001] A. García-Botella, A. Alvarez Fernández-Balbuena, D. Vázquez-Moliní, and E. Bernabeu, “Thermal influences on optical properties of light-emitting diodes: a semi empirical model,” Appl. Opt., vol. 40, no. 4, pp. 533-537, 2001.

[Gessmann, 2003] Th. Gessmann, E. F. Schubert, J. W. Graff, K. Streubel, and C. Karnutsch, “Omni-directionally reflective contacts for light-emitting diodes,” Elect. Dev. Lett., vol. 24, pp. 683, 2003.

[Goebel, 1967] D. Goebel, “Generalized integrating-sphere theory,” Appl. Opt., vol. 6, nr. 1, pp. 125-128, 1967.

[Gu, 2004] Y. Gu and N. Narendran, “A non-contact method for determining junction temperature of phosphor-converted white LEDs,” Proc. SPIE, vol. 5187, pp. 107-114, 2004.

[Haitz, 1999] R. Haitz, F. Kish, J. Y. Tsao, and J. Nelson, “The case for a national research program on semiconductor lighting,” white paper for the Optoelectronics Industry Development Association (OIDA), 1999.

[Hanselaer, 1984] P. Hanselaer, W. H. Laflère, R. L. Van Meirhaeghe, and F. Cardon, “Current-voltage characteristic of Ti-pSi metal-oxide-semiconductor diodes,” J. Appl. Phys., vol. 56, no. 8, pp. 2309-2314, 1984.

[Harbers, 2007] G. Harbers, S. J. Bierhuizen, and M. R. Krames, “Performance of high-power light-emitting diodes in display illumination applications,” J. Disp. Technol., vol. 3, no. 2, pp. 98-109, 2007.

[Heikkilä, 2009] O. Heikkilä, J. Oksanen, and J. Tulkki, “Ultimate limit and temperature dependency of light-emitting diode efficiency,” J. Appl. Phys., vol. 105, no. 093119, 2009.

[Hino, 1979] I. Hino and K. Iwamoto, “LED pulse response analysis considering the distributed CR constant in the peripheral junction,” Trans. Elect. Dev., vol. 26, no. 8, pp. 1238-1242, 1979.

[Hoelen, 2008] C. Hoelen, H. Borel, J. de Graaf, M. Keupre, M. Lankhorst, C. Mutter, L. Waumans, and R. Wegh, “Remote phosphor LED modules for general illumination – towards 200 lm/W general lighting LED light sources,” Proc. SPIE, vol. 7058, no. 70580M, pp. 1-10, 2008.

[Holcomb, 2003] M. O. Holcomb, R. Mueller-Mach, G. O. Mueller, D. Collins, R. M. Fletcher, D. A. Steigerwald, S. Eberle, Y. K. Lim, P. S. Martin, and M. Krames, “The LED light bulb: Are we there yet? Progress and challenges for solid-state illumination,” Conference on Lasers and Electro-Optics (CLEO), no. CMQ2, 2003.

[Holonyak, 1962] N. Holonyak Jr. and S. F. Bevacqua, “Coherent (visible) light emission from Ga(AsP) junctions” Appl. Phys. Lett., vol. 1, pp. 82, 1962.

[Hong, 2004] E. Hong and N. Narendran, “A method for projecting useful life of LED lighting systems,” Proc. SPIE, vol. 5187, pp. 93-99, 2004.

[Hu, 2008] J. Hu, L. Yang, and M. W. Shin, “Electrical, optical and thermal degradation of high-power GaN/InGaN light-emitting diodes,” J. Phys. D: Appl. Phys., vol. 41, 2008.

[Huber, 2006] R. Huber for OSRAM Opto Semiconductors, “Thermal Management of Golden DRAGON LED,” Application Note, 2006.

[Hui, 2009] S. Y. Hui and Y. X. Qin, “A general photo-electro-thermal theory for light-emitting diode (LED) systems,” Trans. Power Elect., vol. 24, no. 8, pp. 1967-1976, 2009.

[Hunt, 1992] N. E. J. Hunt, E. F. Schubert, D. L. Sivco, A. Y. Cho, and G. J. Zydzik, “Power and efficiency limits in single-mirror light-emitting diodes with enhanced intensity,” Elect. Lett., vol. 28, no. 23, pp. 2169-2171, 1992.

[Hunt, 1998] R. W. G. Hunt, “Measuring colour – Third edition,” Fountain Press, Kingston-upon-Thames, pp. 58-59, 1998.

[Ishida, 2008] K. Ishida, I. Mitsuishi, Y. Hattori, and S. Nunoue, “A revised Kubelka-Munk theory for spectral simulation of phosphor-based white light-emitting diodes,” Appl. Phys. Lett., vol. 93, no. 241910, pp. 1-3, 2008.

[Jayasinghe, 2006] L. Jayasinghe, Y. Gu, N. Narendran, “Characterization of thermal resistance coefficient of high-power LEDs,” Proc. SPIE, vol. 6337, no. 63370V, pp. 1-7, 2006.

[Kang, 2006] D. Y. Kang, E. Wu, and D. M. Wang, “Modeling white light-emitting diodes with phosphor layers,” Appl. Phys. Lett., vol. 89, no. 231102, pp. 1-3, 2006.

[Kim, 2005] J. K. Kim, H. Luo, E. F. Schubert, J. Cho, C. Sone, and Y. Park, "Strongly enhanced phosphor efficiency in GaInN white light-emitting diodes using remote phosphor configuration and diffuse reflector cup," Jpn. J. Appl. Phys. – Express Letter, vol. 44, no. 649, 2005.

[Kittel, 1996] C. Kittel, "Introduction to Solid State Physics," John Wiley & Sons, Inc., New York, 1996.

[Knee, 1999] P. C. Knee, "Investigation of the uniformity and ageing of integrating spheres," Anal. Chimica Acta, vol. 380, nr. 2-3, pp. 391-399, 1999.

[Krames, 2007] M. R. Krames, O. B. Shchekin, R. Mueller-Mach, G. O. Mueller, L. Zhou, G. Harbers, and M. G. Craford, "Status and future of high-power light-emitting diodes for solid-state lighting," J. Disp. Technol., vol. 3, no. 2, pp. 160-175, 2007.

[Kuo, 2000] Y.-K. Kuo, J.-Y. Chang, K.-K. Horng, Y.-L. Huang, Y. Chang, and H.-C. Huang, "Temperature dependent optical properties of the InGaN semiconductor materials: experimental and numerical studies," Proc. SPIE, vol. 4078, pp. 579, 2000.

[Lee, 2004] C.C. Lee and J. Park, "Temperature Measurement of Visible Light-Emitting Diodes Using Nematic Liquid Crystal Thermography With Laser Illumination," Phot. Technol. Lett., vol. 16, no. 7, pp. 1706-1708, 2004.

[Lee, 2009] C.-Y. Lee, A. Su, Y.-C. Liu, W.-Y. Fan, and W.-J. Hsieh, "In situ measurement of the junction temperature of light-emitting diodes using a flexible micro temperature sensor," Sensors, vol. 9, pp. 5068-5075, 2009.

[Leloup, 2008] F. B. Leloup, S. Forment, P. Dutré, M. R. Pointer, and P. Hanselaer, "Design of an instrument for measuring the spectral bidirectional scatter distribution function," Appl. Opt., vol. 47, no. 29, pp. 5454-5467, 2008.

[Levada, 2005] S. Levada, M. Meneghini, G. Meneghesso, and E. Zanoni, "Analysis of DC current accelerated life tests of GaN LEDs using a Weibull-based statistical model," Trans. Dev. Mat. Rel., vol. 5, no. 4, pp. 688-693, 2005.

[Li, 2010] Z. Q. Li and Z. M. Simon Li, "Comprehensive modeling of super-luminescent light-emitting diodes," J. Quantum Elect., vol. 46, no. 4, pp. 454-461, 2010.

[Liu, 2007] M. Liu and B. Rong, "Evaluation of LED application in general lighting," Opt. Eng., vol. 46, no. 7, pp. 1-6, 2007.

[Liu, 2008-1] M.-Q. Liu, X.-L. Zhou, W.-Y. Li, Y.-Y. Chen, and W.-L. Zhang, "Study on methodology of LED's luminous flux measurement with integrating sphere," J. Phys. D: Appl. Phys., vol. 41, nr. 144012, 2008.

[Liu, 2008-2] Z. Liu, S. Liu, K. Wang, and X. Luo, "Optical analysis of color distribution in white LEDs with various packaging methods," Phot. Technol. Lett., vol. 20, no. 24, pp. 2027-2029, 2008.

[Liu, 2009-1] S. Liu, Z. Gan, X. Luo, K. Wang, X. Song, Z. Chen, H. Yan, Z. Liu, P. Wang, and W. Wei, "Muli-physics multi-scale modeling issues in LED," Proc. SPIE, vol. 7375, no. 737507, pp. 1-15, 2009.

[Liu, 2009-2] Z. Liu, S. Liu, K. Wang, and X. Luo, “Optical analysis of phosphor’s location for high-power light-emitting diodes,” Trans. Dev. Mat. Rel., vol. 9, no. 1, pp. 65-73, 2009.

[Lumileds, 2001] Lumileds Lighting, “Thermal Design Considerations for Luxeon Power Light Sources,” Application Note, 2001.

[Lumileds, 2007] Philips Lumileds Lighting Company, “Power light source Luxeon K2,” Technical Datasheet DS51, 2007.

[MacAdam, 1942] D. L. MacAdam, “Visual sensitivities to color differences in daylight,” J. Opt. Soc. Am., vol. 32, no. 5, pp. 247-274, 1942.

[Man, 2006] K. Man and I. Ashdown, “Accurate colorimetric feedback for RGB LED clusters,” Proc. SPIE, vol. 6337, no. 633702, 2006.

[Meneghini, 2007] M. Meneghini, L. Trevisanello, C. Sanna, G. Mura, M. Vanzi, G. Meneghesso, and E. Zanoni, “High temperature electro-optical degradation of InGaN/GaN HBLEDs,” Microelect. Rel., vol. 47, pp. 1625-1629, 2007.

[Miller, 2001] C. C. Miller and Y. Ohno, “Luminous flux calibration of LEDs at NIST,” Proc. 2nd CIE Expert Symposium on LED Measurement, 2001.

[Miller, 2004] C. C. Miller, Y. Zong, and Y. Ohno, “LED photometric calibrations at the National Institute of Standards and Technology and future measurement needs of LEDs,” Proc. SPIE, vol. 5530, pp. 69-79, 2004.

[Mirhosseini, 2009] R. Mirhosseini, M. Schubert, S. Chhajed, J. Cho, J. K. Kim, and E. F. Schubert, “Color rendering ability and luminous efficacy enhancements in white light-emitting diodes,” Proc. SPIE, vol. 7422, no. 742218, pp. 1-7, 2009.

[Moolman, 2009] M. C. Moolman, W. D. Koek, and H. P. Urbach, “A method towards simulating the total luminous flux of a monochromatic high-power LED operated in a pulsed manner,” Opt. Express, vol. 17, no. 20, pp. 17457-17450, 2009.

[Moreno, 2006] I. Moreno, “Spatial distribution of LED radiation,” Proc. SPIE, vol. 6342, no. 634216, pp. 1-7, 2006.

[Moreno, 2008] I. Moreno and C.-C. Sun, “Modeling the radiation pattern of LEDs,” Opt. Express, vol. 16, no. 3, pp. 1808-1819, 2008.

[Mottier, 2009] P. Mottier, ed., “LEDs for lighting applications,” ISTE Ltd. and John Wiley & Sons, Inc., London, 2009.

[Mueller, 2002] R. Mueller-Mach, G. O. Mueller, M. R. Krames, and T. Trottier, “High-power phosphor-converted light-emitting diodes base don III-nitrides,” J. Sel. Topics in Quantum Elect., vol. 8, no. 2, pp. 339-345, 2002.

[Nakamura, 1991] S. Nakamura, T. Mukai, and M. Senoh, “High-power GaN p-n-junction blue-light-emitting diodes,” Jpn J. Appl. Phys., vol. 30, no. 12A, pt. 2, pp. L1998–20011, 1991.

[Narendran, 2000] N. Narendran, N. Maliyagoda, A. Bierman, R. Pysar, and M. Overington, “Characterizing white LEDs for general illumination applications,” Proc. SPIE, vol. 3938, no. 39, pp. 1-9, 2000.

[Narendran, 2002] N. Narendran and L. Deng, “Color rendering properties of LED light sources,” Proc. SPIE, vol. 4776, no. 61, pp. 1-7, 2002.

[Narendran, 2004-1] N. Narendran, Y. Gu, J. P. Freyssinier, H. Yu, and L. Deng, “Solid-state lighting: failure analysis of white LEDs,” J. Christal Growth, vol. 268, no. 3-4, pp. 449-456, 2004.

[Narendran, 2004-2] N. Narendran, L. Deng, R. M. Pysar, Y. Gu, and H. Yu, “Performance characteristics of high-power light-emitting diodes,” Proc. SPIE, vol. 5187, pp. 267-275, 2004.

[Narendran, 2005-1] N. Narendran and Y. Gu, “Life of LED-based white light sources,” J. Disp. Technol., vol. 1, no. 1, pp. 167-170, 2005.

[Narendran, 2005-2] N. Narendran, Y. Gu, J. P. Freyssinier-Nova, and Y. Zhu, “Extracting phosphor-scattered photons to improve white LED efficiency,” Phys. Stat. Sol. (a), vol. 202, no. 6, pp. R60-R62, 2005.

[Narukawa, 2007] Y. Narukawa, M. Sano, M. Ichikawa, S. Minato, T. Sakamoto, T. Yamada, and T. Mukai, “Improvement of luminous efficiency in white light-emitting diodes by reducing a forward-bias voltage,” Jpn. J. Appl. Phys., vol. 46, no. 40, pp. L963-L965, 2007.

[Narukawa, 2008] Y. Narukawa, M. Sano, T. Sakamoto, T. Yamada, and T. Mukai, “Successful fabrication of white light-emitting diodes by using extremely high external quantum efficiency blue chips,” Phys. Stat. Sol. (a), vol. 205, no. 5, pp. 1081-1085, 2008.

[Navigant, 2009] Navigant Consulting, Inc., Radcliffe Advisors, Inc., and SSLS, Inc., “Solid-state lighting research and development,” Multi-year program plan FY’09-FY’15, 2009.

[Nichia, 2003] Nichia, “Thermal management design of LEDs,” Application Note, 2003.

[Nichia, 2007] Nichia Corporation, “Specifications for Nichia type white LED model: NS6W083AT,” Application Note STSE-CC7134A, 2007.

[Ohno, 1994] Y. Ohno, “Integrating sphere simulation – Application to total flux scale realization,” Appl. Opt., vol. 33, nr. 13, pp. 2637-2647, 1994.

[Ohno, 1995] Y. Ohno, “New method for realizing a luminous flux scale using an integrating sphere with an external source,” J. Illum. Eng. Soc., vol. 24, nr. 1, pp. 106-115, 1995.

[Ohno, 1998] Y. Ohno, “Detector-based luminous-flux calibration using the Absolute Integrating-Sphere Method,” Metrologia, vol. 35, pp. 473-478, 1998.

[Ohno, 1999] Y. Ohno and Y. Zong, “Detector-based integrating sphere photometry,” Proc. 24th Session of the CIE, pp. 155-160, 1999.

[Ohno, 2000] Y. Ohno, R. Köhler and M. Stock, “An ac/dc technique for the Absolute Integrating-Sphere Method,” Metrologia, vol. 37, pp. 583-586, 2000.

[Ohno, 2001] Y. Ohno and R. Daubach, “Integrating sphere simulation on spatial nonuniformity errors in luminous flux measurement,” J. IES, vol. 30, nr. 1, pp. 105-115, 2001.

[Ohno, 2005] Y. Ohno, “Spectral design considerations for white LED color rendering,” Opt. Eng., vol. 44, no. 11, 2005.

[Ohno, 2006] Y. Ohno, “Optical metrology for LEDs and solid state lighting,” Proc. SPIE, vol. 6046, nr. 604625, 2006.

[Ohno, 2007] Y. Ohno, “Colorimetry: understanding the CIE measurement system,” chap. 5, pp. 112, ed. J. Schanda, Wiley-Interscience, 2007.

[Park, 2005] J. Park and C. C. Lee, “An electrical model with junction temperature for light-emitting diodes and the impact on conversion efficiency,” Elect. Dev. Lett., vol. 26, no. 5, pp. 308-310, 2005.

[Pelka, 2003] D. G. Pelka and K. Patel, “An overview of LED applications for general illumination,” Proc. SPIE, vol. 5186, pp. 15-26, 2003.

[Perkins, 2009] J. Perkins, “LED manufacturing technologies and costs,” SSL Workshop, Fairfax, VA, 2009.

[Philips, 2009] Philips Electronics N.V., “Philips Fortimo LED downlight module system (DLM),” Design-in guide 3222 635 56401, 2009.

[Rea, 2000] M. S. Rea, “The IESNA lighting handbook – Reference and application – 9th edition,” Illuminating Engineering Society of North America, New York, 2000.

[Reifegerste, 2008] F. Reifegerste and J. Lienig, “Modelling of the temperature and current dependence of LED spectra,” J. Light & Vis. Env., vol. 32, no. 3, 2008.

[Rencz, 2004] M. Rencz and V. Székely, “Studies on the nonlinearity effects in dynamic compact model generation of packages,” Trans. Comp. Pack. Technol., vol. 27, no. 1, pp. 124-130, 2004.

[Riordan, 1997] M. Riordan and L. Hoddeson, “The origins of the p-n-junction,” Spectrum, vol. 34, no. 6, pp. 46–51, 1997.

[Ronchi, 2008] E. Ronchi, E. A. Sundén, S. Conroy, G. Ericsson, M. G. Johnson, J. Kallne, C. Hellesen, A. Hjalmarsson, H. Sjöstrand, M. Weiszflog, W. Puccio, L. Ahlén, and JET-EFDA contributers, “A bipolar LED drive technique for high performance, stability and power in the nanosecond time scale,” Nucl. Instr. Meth. Phys. Res. A, vol. 599, pp. 243-247, 2008.

[Round, 1907] H. J. Round, “A note on carborundum,” Elect. World, vol. 49, no. 309, 1907.

[Ryu, 2005] H.-Y. Ryu, K.-H. Ha, J.-H. Chae, O.-H. Nam, and Y.-J. Park, “Measurement of junction temperature in GaN-based laser diodes using voltage-temperature characteristics,” Appl. Phys. Lett., vol. 87, no. 093506, 2005.

[Ryu, 2009] H.-Y. Ryu, H.-S. Kim, and J.-I. Shim, “Rate equation analysis of efficiency droop in InGaN light-emitting diodes,” Appl. Phys. Lett., vol. 95, no. 081114, pp. 1-3, 2009.

[Salsbury, 2007] M. Salsbury and I. Ashdown, “A comprehensive model to predict solid state lighting performance,” Proc. SPIE, vol. 6669, no. 666919, pp. 1-9, 2007.

[Saucke, 2005] K. Saucke, G. Pausch, J. Stein, H.G. Ortlepp, and P. Schotanus, “Stabilizing Scintillation Detector Systems With Pulsed LEDs: A Method to Derive the LED Temperature From Pulse Height Spectra,” Trans. Nucl. Sc., vol. 52, no. 6, pp. 3160-3165, 2005.

[Schubert, 2006] E. F. Schubert, “Light-emitting diodes – Second edition,” Cambridge University Press, Cambridge, 2006.

[Schwegler, 1999] V. Schwegler, M. Seyboth, S. Schad, M. Scherer, C. Kirchner, M. Kamp, U. Stempfle, W. Limmer, and R. Sauer, “Temperature distribution in InGaN-MQW LEDs under operation,” Proc. MRS F99, no. W11.18, 1999.

[Setlur, 2009] A. A. Setlur, J. J. Shiang, M. E. Hannah, and U. Happek, “Phosphor quenching in LED packages: measurements, mechanisms, and paths forward,” Proc. SPIE, vol. 7422, no. 74220E, pp. 1-8, 2009.

[Shah, 2003] J. M. Shah, Y. L. Li, Th. Gessmann, and E. F. Schubert, “Experimental analysis and theoretical model for anomalously high ideality factors ($n \gg 2.0$) in AlGaN/GaN p-n junction diodes,” J. Appl. Phys., vol. 94, no. 4, pp. 2627-2630, 2003.

[Shaw, 2008] M. Shaw and T. Goodman, “Array-based goniospectroradiometer for measurement of spectral radiant intensity and spectral total flux of light sources,” Appl. Opt., vol. 47, nr. 14, pp. 2637-2647, 2008.

[Shockley, 1949] W. Shockley, “Theory of p-n-junctions,” Bell Syst. Tech. J., vol. 29, pp. 435–489, 1949.

[Smet, 2010] K. Smet, S. Jost-Boissard, W. R. Ryckaert, G. Deconinck, and P. Hanselaer “Validation of a colour rendering index based on memory colours,” CIE Lighting Quality & Energy Efficiency, 2010.

[Sommer, 2009] C. Sommer, J. R. Krenn, P. Hartmann, P. Pachler, M. Schweighart, S. Tasch, and F. P. Wenzl, “The effect of the phosphor particle sizes on the angular homogeneity of phosphor-converted high-power white LED light sources,” J. Sel. Topics in Quantum Elect., vol. 15, no. 4, pp. 1181-1188, 2009.

[SSC, 2007] Seoul Semiconductor Co., Ltd., “1W Z-POWER LED series binning and labelling (P4),” Application Note 1-1 Rev 01-2007/11, 2007.

[SSC, 2008] Seoul Semiconductor, “Specification AX32X1,” Technical Datasheet SSC-QP-7-07-25 (Rev. 00), 2008.

[Sunview, 2008] Sunview Lighting Co., Ltd., “High power LED spot light (PAR30-7W),” Technical Datasheet, 2008.

[Szylowski, 2006] M. Szylowski, M. Mossman, D. Barclay, and L. Whitehead, “Novel fibre-based integrating sphere for luminous flux measurements,” Rev. Sc. Instr., vol. 77, nr. 063102, pp. 1-7, 2006.

[Tamulaitis, 2004] G. Tamulaitis, P. Duchovskis, Z. Bliznikas, K. Breivé, R. Ulinskaité, A. Brazaityté, A. Novickovasa, A. Žukauskas, and M. S. Shur, "High-power LEDs for plant cultivation," Proc. SPIE, vol. 5530, pp. 165-173, 2004.

[Tsao, 2002] J. Y. Tsao, "Light-emitting diodes for general illumination," OIDA Technology Roadmap update, OIDA, 2002.

[Uchida, 2005] Y. Uchida and T. Taguchi, "Lighting theory and luminous characteristics of white light-emitting diodes," Opt. Eng., vol. 44, no. 12, pp. 1-9, 2005.

[Vaitonis, 2008] Z. Vaitonis, P. Vitta, and A. Zukauskas, "Measurement of the junction temperature in high-power light-emitting diodes from the high-energy wing of the electroluminescence band," J. Appl. Phys., vol. 103, no. 093110, pp. 1-7, 2008.

[Varshni, 1976] Y. P. Varshni, "Temperature dependence of the energy gap in semiconductors," Physica, vol. 34, no. 149, 1967.

[Wenzl, 2008] F. P. Wenzl, C. Sommer, L. Kuna, E. Zinterl, J. R. Krenn, P. Hartmann, P. Pachler, M. Schweighart, S. Tasch, and G. Leising, "Novel solutions towards improved high-power white LED light sources," Proc. SPIE, vol. 7138, no. 71382C, pp. 1-6, 2008.

[Winkler, 2007] H. Winkler, H. Enderle, C. Kuehn, R. Petry, and T. Vosgroene, "Advanced phosphors for LED applications," Proc. SPIE, vol. 6797, no. 67970A, pp. 1-12, 2007.

[Wyszecki, 2000] G. Wyszecki and W. S. Stiles, "Color science – Concepts and methods, quantitative data and formulae – Second edition," John Wiley & Sons, Inc., New York, 2000.

[Xi, 2004] Y. Xi and E.F. Schubert, "Junction-temperature measurement in GaN ultraviolet light-emitting diodes using diode forward voltage method," Appl. Phys. Lett., vol. 85, no. 12, pp. 2163-2165, 2004.

[Xi, 2005] Y. Xi, J.-Q. Xi, Th. Gessmann, J. M. Shah, J. K. Kim, E. F. Schubert, A. J. Fischer, M. H. Crawford, K. H. A. Bogart, and A. A. Allerman, "Junction and carrier temperature measurements in deep-ultraviolet light-emitting diodes using three different methods," Appl. Phys. Lett., vol. 86, no. 031907, pp. 1-4, 2005.

[Yam, 2005] F. K. Yam and Z. Hassan, "Innovative advances in LED technology," Microelect. J., vol. 36, pp. 129-137, 2005.

[Yanagisawa, 2005] T. Yanagisawa and T. Kojima, "Long-term accelerated current operation of white light-emitting diodes," J. Lum., vol. 114, pp. 39-42, 2005.

[You, 2010] J. P. You, N. T. Tran, and F. G. Shi, "Light extraction enhanced white light-emitting diodes with multi-layered phosphor-configuration," Opt. Express, vol. 18, no. 5, pp. 5055-5060, 2010.

[Yu, 2006] H. L. Yu, C. C. Hsiao, and W. C. Liu, “New apparatus, for haze measurement for transparent media,” Meas. Sci. Technol., vol. 17, pp. N29-N36, 2006.

[Zhang, 2008] Y. Zhang, L. Li, X. Zhang, and Q. Xi, “Temperature effects on photoluminescence of YAG:Ce3+ phosphor and performance in white light-emitting diodes,” J. Rare Earths, vol. 26, no. 3, pp. 446-449, 2008.

[Zong, 2004] Y. Zong, C. C. Miller, K. R. Lykke, and Y. Ohno, “Measurement of total radiant flux of UV LEDs,” Proc. CIE Expert Symposium on LED Light Sources, 2004.

[Zong, 2008] Y. Zong and Y. Ohno, “New practical method for measurement of high-power LEDs,” Proc. CIE Expert Symposium on Advances in Photometry and Colorimetry, vol. x033:2008, pp. 102-106, 2008.

List of publications

Journal papers:

A. Keppens, W. R. Ryckaert, G. Deconinck, and P. Hanselaer, "High-power light-emitting diode junction temperature determination from current-voltage characteristics," J. Appl. Phys., vol. 104, no. 093104, pp. 1-8, 2008.

P. Hanselaer, A. Keppens, S. Forment, W. R. Ryckaert, and G. Deconinck, "A new integrating sphere design for spectral radiant flux determination of light-emitting diodes (LEDs)," Meas. Sci. Technol., vol. 20, no. 095111, pp. 1-9, 2009.

M. Bodart, B. Roisina, P. D'Herdt, A. Keppens, P. Hanselaer, W. R. Ryckaert, and A. Deneyer, "Performances of compact fluorescent lamps with integrated ballasts and comparison with incandescent lamps," Light & Eng., vol. 18, no. 2, pp. 83-98, 2010.

A. Keppens, W. R. Ryckaert, G. Deconinck, and P. Hanselaer, "Modeling high-power light-emitting diode spectra and their variation with junction temperature," J. Appl. Phys., vol. 108, no. 043104, pp. 1-7, 2010.

A. Keppens, H. T. Chen, Y. J. Lu, Z. Chen, Y. L. Gao, G. Deconinck, and P. Hanselaer, "Light-emitting diode junction temperature and power determination from forward current," under review, Light & Eng., 2010.

Conference proceedings:

A. Keppens, D. De Smeyter, W. R. Ryckaert, G. Deconinck, and P. Hanselaer, "Thermal characterization of single-die and multi-die high-power light-emitting diodes," Proc. SPIE, vol. 7058, no. 70580H, pp. 1-12, 2008.

A. Keppens, W. R. Ryckaert, G. Deconinck, and P. Hanselaer, "Evaluation of current and temperature effects on high-power light-emitting diode efficiencies," Proc. CIE x034, no. PWSOI2, pp. 1-7, 2009.

W. R. Ryckaert, W. Hertog, K. Smet, A. Keppens, S. Herrebosch, G. Deconinck, and P. Hanselaer, "Counter lighting with fluorescent lamps and LEDs: a comparative study," Proc. Lux Europa, vol. 11, no. 51, pp. 535-540, 2009.

A. Keppens, S. Denijs, S. Wouters, W. R. Ryckaert, G. Deconinck, and P. Hanselaer, “Modelling the spatial colour distribution of phosphor-white high-power light-emitting diodes,” Proc. SPIE, vol. 7717, no. 771718, pp. 1-10, 2010.

Conference abstracts with (poster) presentation:

A. Keppens, Y. Zong, and Y. Ohno, “Characterization of remote phosphor type of LEDs,” CORM annual conference, 2010.

A. Keppens, P. C. Acuña, H. T. Chen, G. Deconinck, and P. Hanselaer, “Efficiency evaluation of phosphor-white high-power light-emitting diodes,” Proc. LS12-WLED3, no. 68, pp. 439-440, 2010.

A. Keppens, Y. Zong, Y. Ohno, G. Deconinck, and P. Hanselaer, “Determining phosphors’ effective quantum efficiency for remote phosphor type of LED modules,” Proc. CIE Tutorial and Expert Symposium on Spectral and Imaging Methods for Photometry and Radiometry, 2010.

Publications in national magazines:

A. Keppens and P. Hanselaer, “Light-emitting diodes, een inleiding…” Vlaams Elektro Innovatiecentrum (VEI), Nieuwe Lichtbronnen en Buitenverlichting, pp. 2-6, 2007.

A. Keppens, “Light-emitting diodes, in opmars…” Vlaams Elektro Innovatie-centrum (VEI), Technologiewacht – Licht, pp. 1-5, 2009.

A. Keppens, “LED – What’s in a name?” Vlaams Elektro Innovatiecentrum (VEI), Technologiewacht – Licht, pp. 1-4, 2010.

Brief biography

Arno Keppens was born on June 24, 1984 in Bornem, Belgium. Graduated as a Master in Physics from Gent University in 2006, he started a Ph.D. research project at the Light & Lighting Laboratory (Gent, Belgium) on the integration of high-power light-emitting diodes in general lighting. Today, this four-year project is still continued in cooperation with K.U.Leuven (Belgium) and four major luminaire manufacturers. Part of the doctoral research has been performed while working as a Guest Researcher at the National Institute of Standards and Technology (NIST, Gaithersburg, MD, USA). Arno has also been a guest lecturer at the National University of Colombia (Bogotá, Colombia) and at the Francisco José de Caldas District University (Bogotá, Colombia) for two weeks in 2008. By the end of 2010, government funding might result in a two-year postdoctoral mandate to extend the present LED-technology research.

While working as a doctoral researcher, Arno completed the Academic Specific Teacher Training and a one-year course on Present Science Philosophy, both at Ghent University. He is currently a member of the Belgian Physical Society, junior member of the International Society for Optical Engineering (SPIE), and member of Technical Committee 2-63 (Measurement of LEDs) of the International Commission on Illumination (CIE).

Thy golden light came down into my brain
And the grey rooms of mind LED-touched became
A bright reply to Wisdom's occult plane,
A calm illumination and a flame.

Adapted from a poem by Sri Aurobindo (Indian poet, 1872-1950)

Appendix 1

Table A.1 (next three pages): Overview of all light-emitting diode packages that have been selected for investigation: 92 devices from twelve different manufacturers in total. The information and measurement types that are shown for each measurable circuit are described in section 3.3.

MFR	date	part number	int. code	# dies	P (W)	colour	I-$U_f(T)$	$R_s(T)$	sphere	$T(I)$	gonio
Citizen Electr.	2007	CL-L100-C3N	CL3N	8 x 3 *	3	5000 K					
CREE	2008	XRCWHT-L1-4A-N4	XCAN-1	1	1	4500 K			1×1		
CREE	2008	XRCWHT-L1-4A-N4	XCAN-2	1	1	4500 K			2		
CREE	2008	XRCWHT-L1-7D-M3-0-01	XCDM-1	1	1	3000 K			4×4		
CREE	2008	XRCWHT-L1-7D-M3-0-01	XCDM-2	1	1	3000 K			2		
CREE	2008	XREWHT-L1-WK-P4-0-01	XEKP	1	1	8500 K			1×1		
CREE	2007	XR7090RD-L1-R2-M0	XR2M-1	1	1	620 nm			2		
CREE	2007	XR7090RD-L1-R2-M0	XR2M-2	1	1	620 nm			2		
CREE	2007	XR7090RD-L1-R3-K0	XR3K	1	1	625 nm			2		
CREE	2008	XRCBLU-L1-R250-00H01	XRCB	1	1	470 nm			1×1		
CREE	2008	XRCGRN-L1-R250-00N01	XRCG	1	1	530 nm			1×1		
CREE	2008	XRCRED-L1-R250-00M01	XRCR	1	1	625 nm			1×1		
CREE	2006	XR7090WT-L1	XREW	1	1	5700 K			3×2		
Edison Opto	2007	ENEW-05-0707-EB	ENEB	7 x 7	50	6000 K					
Hensel Int.	2006	HS-D20W3W	HSD2-1	2 x 1	3	7000 K					
Hensel Int.	2006	HS-D20W3W	HSD2-2	2 x 1	3	7000 K					
Lamina	2006	BL-33F0-0142	BL3B	39 x 2 *	8	470 nm					
Lamina	2006	BL-33F0-0142	BL3G	39 x 2 *	8	520 nm					
Lamina	2006	BL-33F0-0142	BL3R	39 x 2 *	6	624 nm					
Lamina	2008	BL-43F0-0305	BL4B	1 x 2	3	465 nm					
Lamina	2008	BL-43F0-0305	BL4G	1 x 2	3	525 nm					
Lamina	2008	BL-43F0-0305	BL4R	1 x 2	2	624 nm					
Lamina	2007	NT-52D0-0429	NT52	3 x 6	30	4700 K					
Lamina	2007	NT-53F0-0428	NT5B	3 x 3	15	460 nm					
Lamina	2007	NT-53F0-0428	NT5G	3 x 3	15	535 nm					
Lamina	2007	NT-53F0-0428	NT5R	3 x 3	10	629 nm					
Lumileds	2004	LXHL-FW3C	FW3C-1	1	3	5500 K					
Lumileds	2004	LXHL-FW3C	FW3C-2	1	3	5500 K					
Lumileds	2008	NL4052574	K2W7	1 x 7	21	6500 K					
Lumileds	2007	LXK2-PM12	LK2G-1	1	3	530 nm					

Lumileds	2007	LXK2-PM12	LK2G-2	1	3	530 nm					
Lumileds	2007	LXK2-PD12	LK2R-1	1	3	627 nm					
Lumileds	2007	LXK2-PD12	LK2R-2	1	3	627 nm					
Lumileds	2006	LXHL-LW3C	LW3C-1	1	3	5500 K			1		
Lumileds	2006	LXHL-LW3C	LW3C-2	1	3	5500 K					
Lumileds	2007	LXHL-LW6C	LW6C-1	2 x 2	5	5500 K			1×1		
Lumileds	2007	LXHL-LW6C	LW6C-2	2 x 2	5	5500 K					
Lumileds	2007	LXML-PWW1	LXML	1	3	3100 K			1×1		
Lumileds	2009	LXML-PB01	LXRB	1	3	470 nm					
Lumileds	2009	LXML-PM01	LXRG	1	3	530 nm					
Lumileds	2009	LXML-PD01	LXRR	1	3	627 nm					
Lumileds	2007	LXHL-MWGC	MWGC-1	1	1	3300 K					
Lumileds	2007	LXHL-MWGC	MWGC-2	1	1	3300 K					
Lumileds	2007	L2K2-MWW4-11-BT00	MWW4-1	1	3	3000 K					
Lumileds	2007	L2K2-MWW4-11-BT00	MWW4-2	1	3	3000 K					
Lumileds	2007	L2K2-MWW4-11-BT00	MWW4-3	1	3	3000 K					
Lumileds	2007	L2K2-MWW4-11-BT00	MWW4-4	1	3	3000 K					
Lumileds	2007	L2K2-MWW4-11-BT00	MWW4-5	1	3	3000 K			4×4		
Lumileds	2003	LXHL-NWG8	P1HW	1	1	3300 K			1		
Lumileds	2007	LXK2-PW14-U00	PW14-1	1	3	6500 K					
Lumileds	2007	LXK2-PW14-U00	PW14-2	1	3	6500 K					
Lumileds	2009	LXML-PWC1-0080	PWC8	1	3	6500 K			1		
Nichia	2006	NCCW023JE	NCCW-1	1	1	6600 K			1		
Nichia	2006	NCCW023JE	NCCW-2	1	1	6600 K					
Nichia	2006	NCCW023JE	NCCW-3	1	1	6600 K					
Nichia	2006	NS6W083T	NS6W	6 x 1*	1	6600 K			1		
Nichia	2007	NS6W083AT	NSB3	6 x 1*	1	7000 K			2		
Nichia	2007	NS6W083AT	NSC2-1	6 x 1*	1	5000 K			2		
Nichia	2007	NS6W083AT	NSC2-2	6 x 1*	1	5000 K			2		
Osram	2006	LEWE3B-NXQX-6K8L	E3BN	1 x 6	13	5600 K			1×1		
Osram	2006	LWW5SM-HYJZ-5K8L	W5SM	1	1	5600 K			1×1		

Philips	2009	LEDDLM2000/840	FOR1	2 x 9	32	4000 K			4×4×3		
Prolight Opto	2006	PG1A-1LWS-RX0	PG1A-1	1	1	6250 K			1×1		
Prolight Opto	2006	PG1A-1LWS-RX0	PG1A-2	1	1	6250 K					
Prolight Opto	2006	PG1N-1LVS-QQ0	PG1N-1	1	1	3400 K					
Prolight Opto	2006	PG1N-1LVS-QQ0	PG1N-2	1	1	3400 K					
Seoul Semic.	2007	AW3231	AW32	2 x 2	4	6300 K			1×1		
Seoul Semic.	2005	F50380	F50B	1	1	460 nm					
Seoul Semic.	2005	F50380	F50G	1	1	533 nm					
Seoul Semic.	2005	F50380	F50R	1	1	622 nm					
Seoul Semic.	2007	F50381	F51B-0	1	1	460 nm					
Seoul Semic.	2008	F50381	F51B-1	1	1	460 nm			1×1		
Seoul Semic.	2007	F50381	F51G-0	1	1	533 nm					
Seoul Semic.	2008	F50381	F51G-1	1	1	533 nm			1×1		
Seoul Semic.	2007	F50381	F51R-0	1	1	622 nm					
Seoul Semic.	2008	F50381	F51R-1	1	1	622 nm			1×1		
Seoul Semic.	2006	N11492-4K	N114-1	4 x 1	5	3000 K					
Seoul Semic.	2007	N42182-1L-SSKAI	N42L-1	1	1	3000 K			4×4		
Seoul Semic.	2007	N42182-1L-SSKAI	N42L-2	1	1	3000 K			2		
Seoul Semic.	2007	S42182-S	S42S-1	1	1	4000 K			2		
Seoul Semic.	2007	S42182-S	S42S-2	1	1	4000 K			2		
Seoul Semic.	2006	W11492-4A	W114	4 x 1	5	6500 K					
Seoul Semic.	2006	W42180-1H	W421	1	1	6300 K			1		
Seoul Semic.	2007	W42182-1B	W42B-1	1	1	6300 K			2		
Seoul Semic.	2007	W42182-1B	W42B-2	1	1	6300 K			2		
Seoul Semic.	2007	W42182-1D-USWOI	W42D-1	1	1	6300 K			2×2		
Seoul Semic.	2007	W42182-1D-USWOI	W42D-2	1	1	6300 K			2		
Seoul Semic.	2007	W42182-1H	W42H-1	1	1	6300 K			2		
Seoul Semic.	2007	W42182-1H	W42H-2	1	1	6300 K			2		
Xicato	2009	12B0-750	MOD1	2 x 6	14	3000 K			4×4×3		
Xicato	2009	XSM183080	XIC3	1 x 8	18	3000 K			1		
Xicato	2009	XSM184080	XIC4	1 x 8	18	4000 K			4×4×3		

Table A.2: Overview of ten LED lamps and engines from six different manufacturers. For these devices only one steady-state goniophotometer or integrating sphere measurement has been performed for efficiency evaluation.

MFR	date	part number	int. code	P (W)	colour
Lemnis Lighting	2008	PLS-E27/230-240/50-60	PHA1	4	2800 K
Megaman	2009	AR111-LR0115-50H	MEG1	15	4000 K
Philips	2009	LEDDLM2000/840	FOR1	32	4000 K
Philips	2010	LEDSLM1100/830	FOS1	23	3000 K
Philips	2009	LEDDLM1100/2700-6500	LXLB	14	470 nm
Philips	2009	LEDDLM1100/2700-6500	LXLG	20	530 nm
Philips	2009	LEDDLM1100/2700-6500	LXLR	16	630 nm
Philips	2009	LEDDLM1100/2700-6500	LXLW	30	4000 K
Seoul Semic.	2007	AW3231	AW32	4	6300 K
Uniled	2008	UNILED192	ULL1	3	3000 K
Uniled	2008	UNILED142	ULS1	6	3000 K
Xicato	2009	XSM183080	XIC3	18	3000 K
Xicato	2009	XSM184080	XIC4	18	4000 K

Appendix 2

Table B.1: Pictures of all devices that have been selected for investigation (second column), sorted according to the internal codes in Tables A.1 and A.2 in Appendix 1 (first column). For each manufacturer, devices with an identical design have been grouped. Picture sources are added in the third column.

LED	picture	source
AW32		Datasheet SSC-QP-7-07-25 Rev.00 (2008)
BL3RGB	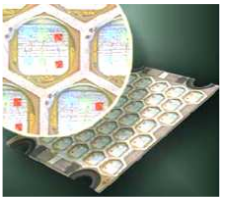	Datasheet BL-33F0-0142 Rev.01.20.05 (2005)
BL4RGB		Datasheet FM-0167 Rev.10.17.06 (2006)
CL3N		Datasheet CE-P160 (2007)
E3BN		Datasheet LEW E3B (2006)
ENEB	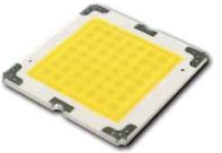	Datasheet 50W Edistar Version 1.0 (2007)

F50RGB F51RGB		Datasheet F50381 Rev.09 (2007)
FOR1 LXLRGB LXLW		Design-in guide Fortimo DLM 1100 (2009)
FOS1		Design-in guide Fortimo SLM 1100 (2010)
FW3C		Datasheet DS46 (2006)
HSD2	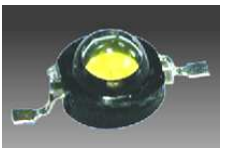	Datasheet HS-D20W3W (2006)
K2W7	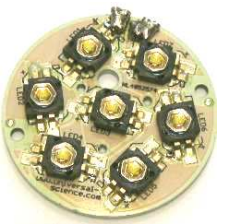	(own picture, 2009)
LK2R LK2G PW14 MWW4		Datasheet DS51 (2007)
LW3C		Datasheet DS46 (2006)

LW6C		Datasheet DS40 (2006)
LXML LXRRGB PWC8		Datasheet DS56 (2007)
MEG1		Datasheet MM01914 (2009)
MOD1 XIC3 XIC4		Datasheet XSM (2008)
MWGC		Datasheet DS47 (2006)
N114 W114		Datasheet X1149X Rev.07 (2006)
N42L S42S W421 W42B W42D W42H		Datasheet X42182 Rev.04 (2009)

NCCW	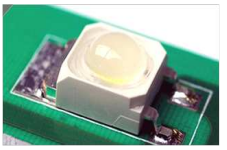	Datasheet STSE-CC5053A (2005)
NS6W NSB3 NSC2		Datasheet STSE-CC6065A (2005)
NT52 NT5RGB		Datasheet FM-0168 Rev.10.30.06 (2006)
P1HW	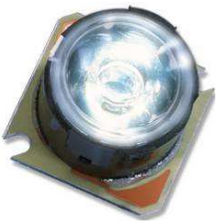	Datasheet DS47 (2006)
PG1A PG1N		Datasheet PG1A-1LXS Version 2.0 (2007)
PHA1		Datasheet Pharox LS (2008)
ULL1		Datasheet 192 (2007)

ULS1		(own picture, 2008)
W5SM		Datasheet LW W5SM (2009)
XCAN XCDM XEKP XR2M XR3K XRCRGB XREW		Datasheet CLD-DS10.007 (2007)